CZECH TECHNICAL UNIVERSITY IN PRAGUE
Faculty of Civil Engineering
Department of Mechanics

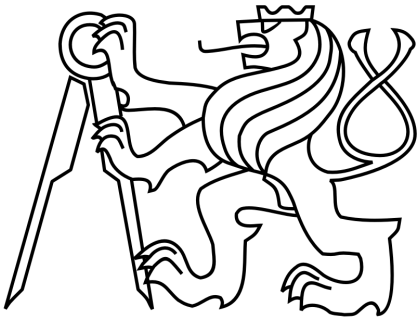

Application of Boundary Inverse Methods in Civil Engineering

DOCTORAL THESIS

Ing. Jan Havelka

Doctoral study program: Civil Engineering

Branch of study: Physical and Material Engineering

Doctoral thesis tutor: Ing. Jan Sýkora, PhD.

Prague, 2019

Název práce:	Aplikace hraničních inverzních metod ve stavebním inženýrství
Autor:	Ing. Jan Havelka
Vedoucí práce:	Ing. Jan Sýkora, Ph.D.
Studijní program:	Stavební inženýrství
Obor studia:	Fyzikální a materiálové inženýrství

Abstrakt

V určitých oblastech výzkumu, jako je například analýza historických budov, zobrazovací techniky v medicíně, materiálové inženýrství nebo geofyzika, je výhodné provádět pouze neintruzivní měření na hranici zkoumaného vzorku. Cílem těchto měření je získat detailní informace o materiálových vlastnostech uvnitř vzorku při jeho současném neporušení. Tato práce se věnuje právě takovým metodám, které spojují matematický model a inverzní metody využívající pouze hraniční měření. Celkem se zde uvažují tři výpočetní modely, které se zabývají elektrostatikou, ustáleným vedením tepla a časově závislým vedením tepla. Jednotlivé modely jsou diskretizovány pomocí metody konečných prvků. Pro identifikaci neznámých materiálových parametrů je využit nejprve standardní deterministický přístup modifikované regularizované Gauss-Newtonovy metody. Druhý přístup využívá pravděpodobnostní metodu založenou na Bayesově formulaci. V práci jsou popsány základní principy, detaily o implementaci a modifikace obecných omezení původně odvozených pro standardní Calderónův problém. Navržené identifikační postupy jsou následně výpočetně ověřeny pro širokou škálu materiálových parametrů, tvarů zkoumaných oblastí a okrajových podmínek.

Klíčová slova

Calderónův problém, metoda konečných prvků, difúzní rovnice, náhodné pole, Bayesovská statistika, hraniční inverzní metody, Neumann-to-Dirichlet mapa.

Title:	Application of Boundary Inverse Methods in Civil Engineering
Author:	Ing. Jan Havelka
Supervisor:	Ing. Jan Sýkora, Ph.D.
Doctoral programme:	Civil Engineering
Branch of study:	Physical and Material Engineering

Abstract

In specific fields of research such as treatment of historical structures, medical imaging, material science or geophysics, it is of particular interest to perform only a non-intrusive boundary measurement of the examined sample. The objective is then to obtain a comprehensive information about the material properties inside the sample, without damaging it or intervening in. This work is focused on such problems i.e. synthesising a physical model of interest with a boundary inverse techniques. In total, we consider three forward models, dealing with electrostatics, steady-state heat transfer and a transient heat transfer. Individual models are discretised with finite element method. We employ two approaches in order to recover the underlying material parameters. At first, we utilise a standard deterministic approach using a modified regularised Gauss-Newton method. The second approach utilises a probabilistic method based on a Bayesian inference. We provide a basic framework, implementation details and modification of general constrains originally derived for a standard setup of Calderón problem. The proposed model setup is numerically verified for various domains, load conditions and material field distributions.

Keywords

Calderón problem, finite element method, random field, Bayseian inference, diffusion equation, boundary inverse method, Neumann-to-Dirichlet map.

Declaration

Ph.D. student's name:	Jan Havelka
Title of the doctoral thesis:	Application of Boundary Inverse Methods in Civil Engineering

I hereby declare that this doctoral thesis is my own work and effort written under the guidance of the tutor Ing. Jan Sýkora, Ph.D. All sources and other materials used have been quoted in the list of references. The doctoral thesis was written in connection with research on the projects: GA15-07299S and GA18-04262S.

In Prague on 15. 5. 2019 Jan Havelka

Acknowledgements

In the first place, I would like to express my sincere gratitude to my supervisor Ing. Jan Sýkora, Ph.D., who has been always supportive during my studies for his immense patience, own time spent on consultations, possibilities of using the work space and finding the means without which this work could not be created.

Nevertheless, I am also grateful to Prof. Dr. Hermann G. Matthies from the Technische Universität Braunschweig, Germany, for bringing my attention to the Calderón's inverse problem, brilliant insight and an excellent ability to convey information about complex issues in an understandable way.

I thank my fellow doctoral students with whom I shared the woes and delights of my studies for the fruitful discussions, insightful comments, sharing ideas and of course friendship. In addition, I would like to express my gratitude to other members of the Department of Mechanics for valuable suggestions and advices for solving non-standard problems, always dedicated approach, creating a pleasant environment and time spent together.

Last but not least, I would like to thank my family and friends for their support during my studies.

This dissertation was supported by GA15-07299S and GA18-04262S.

Nomenclature

Abbreviations

CEM Complete Electrode Model

DTN Dirichlet-to-Neumann operator

EIT Electric Impedance Tomography

FEM Finite Element Method

GCV Generalised Cross-Validation

GN Gauss-Newton Method

GTM General Transport Model

LDM Lagged Diffusivity Method

LMR Levenberg-Marquardt regularisation

MCMC Markov chain Monte Carlo

NF Fixed Noise Figure

NM Nelder-Mead simplex method

NTD Neumann-to-Dirichlet operator

PDIPM Primal Dual-Interior Point Method

TV Total Variation

Other symbols

β line search parameter/s

κ hyper-parameter/s

Σ set of random elementary events ω

μ_g mean value of the random field g

ν smoothness parameter of the Matérn covariance function

Ω open bounded region

ω	elementary event
$\partial\Gamma_m$	observed part of the boundary $\partial\Omega$
$\partial\Omega$	boundary of the domain Ω
$\partial\Omega_D$	part of the boundary $\partial\Omega$ subjected to Dirichlet condition
$\partial\Omega_N$	part of the boundary $\partial\Omega$ subjected to Neumann condition
$\partial\Omega_T$	part of the boundary $\partial\Omega$ subjected to transfer condition
ρ	correlation length
σ_g	standard deviation of the random field g
ε	threshold error
ε_u	error on the measured system response (temperature)
ε_V	error on the measured system response (voltage)
ε_{λ_s}	error on the identified thermal conductivity coefficient
ε_σ	error on the identified electric capacity coefficient
ε_{c_v}	error on the identified volumetric capacity
ε_e	error on the identified thermal effusivity
φ	basis function
$\boldsymbol{\psi}$	eigenvector
ξ	random variable
ζ	eigennumber
m	number of distinct eigenmodes
m_h	number of distinct heaters
m_n	number of observed nodes
m_s	number of electrodes
m_t	number of time steps in the identification process
N_b	number of FE nodes located on the boundary $\partial\Omega$

N_e number of FE elements

N_n number of FE nodes

N_p number of distinct parameters

N_t total number of time steps

Mathematical operators

β single-parameter line-search step-size scale parameter

Λ_σ^{-1} Dirichlet-to-Neumann operator

Λ_σ Neumann-to-Dirichlet operator

$\mathbf{H}(\cdot)$ second-order differential operator

$\mathbf{L}$ single-parameter regularisation matrix

$\mathbf{R}$ multi-parameter regularisation matrix

$\otimes$ Kronecker product

$\boldsymbol{\beta}$ multi-parameter line-search step-size scale parameter matrix

$\boldsymbol{\delta}$ Kronecker delta

$\boldsymbol{\nabla}(\cdot)$ first-order differential operator

$F(\cdot)$ forward operator

$f(\cdot)$ objective function

$G(\cdot)$ regularisation operator

$L(\cdot)$ single-parameter regularisation operator

n outward pointing unit normal vector

$T_p^{\exp}(\cdot)$ exponential positivity operator

$T_c(\cdot)$ cap operator

$T_p(\cdot)$ positivity operator

Model parameters and variables

α heat transfer coefficient $[\mathrm{W} \cdot \mathrm{m}^{-2} \cdot \mathrm{K}^{-1}]$

Δt	time step	$[s]$
λ_s	thermal conductivity coefficient	$[\mathrm{W} \cdot \mathrm{m}^{-1} \cdot \mathrm{K}^{-1}]$
ρ_s	bulk density	$[\mathrm{kg} \cdot \mathrm{m}^{-3}]$
σ	electrical conductivity	$[\mathrm{A} \cdot \mathrm{V}^{-1}]$
τ	time integration parameter	$[-]$
$\mathbf{\Phi}$	matrix containing material parameters	
$\boldsymbol{\phi}$	vector within $\mathbf{\Phi}$ containing a single material parameter	
$\mathbf{\Phi}'$	vectorised form of $\mathbf{\Phi}$	
$\mathbf{\Theta}$	matrix containing transformed material parameters $\mathbf{\Phi}$	
$\boldsymbol{\theta}$	vector within $\mathbf{\Theta}$ containing a single material parameter	
$\mathbf{\Theta}'$	vectorised form of $\mathbf{\Theta}$	
c_p	specific heat capacity	$[\mathrm{J} \cdot \mathrm{kg}^{-1} \cdot \mathrm{K}^{-1}]$
c_v	volumetric heat capacity	$[\mathrm{J} \cdot \mathrm{m}^{-3} \cdot \mathrm{K}^{-1}]$
d_s	thermal diffusivity	$[\mathrm{m}^2 \cdot \mathrm{s}^{-1}]$
e_s	thermal effusivity	$[\mathrm{W} \cdot \mathrm{s}^{1/2} \cdot \mathrm{m}^{-2}\mathrm{K}^{-1}]$
f_D	prescribed temperature	$[^o\mathrm{C}]$
f_N	prescribed heat flux	$[\mathrm{W} \cdot \mathrm{m}^{-2}]$
f_T	prescribed transfer heat flux	$[\mathrm{W} \cdot \mathrm{m}^{-2}]$
I_s	s-th current pattern	$[\mathrm{A}]$
r	heater contact resistance coefficient	$[\mathrm{K} \cdot \mathrm{W}^{-1}]$
t	time	$[s]$
T_e	temperature of an active heater	$[^o\mathrm{C}]$
T_h	h-th stimulation pattern	$[^o\mathrm{C}]$
t_s	final time of the computation	$[s]$
u	temperature potential	$[^o\mathrm{C}]$

u_0	environment temperature	[^{o}C]
v	electrostatic potential	[V]
V_s	s-th electrode potential	[V]
z	contact impedance	[Ω]

Contents

1 Introduction

Numerical methods have become an inherent part of engineering designs. Not only they serve as a prediction of the system behaviour but are also able to provide a complex information about the genuine interaction of individual components. Together with the ever increasing computer performance it opens up the possibilities for an extensive optimisation based designs resulting into energy, material, human resources and time savings. However, the precision of a model response compared to the real observations often varies to some extent. Since every mathematical model is a collection of theoretical knowledge and principles, errors due to an approximation on the physical phenomena level, material description, load conditions etc. contribute to the gap between the actual observation and the model prediction. In a pursuit of matching the relation between reality and the model response, one can find several ways for eliminating the observable discrepancy. Each direction inevitably induces another trade off to harness embodied in a balance between the computational complexity, model simplicity, number of parameters and additional decision making whether the increased complexity is worth the effort. Despite the difficulties, however, the trend is today in favour of more complex models due to the progress in manufacturing precision, profound development in numerical procedures, accurate measurement techniques and increasing computational power. Some of the main options for improving the model precision in order to better reflect the real physical processes are briefly outlined in the following paragraphs. Although numerical methods represent widespread tool used in many areas, this thesis interest is mostly concerned with models applicable in civil engineering, e.g problems mainly governed by elliptic or parabolic partial differential equations (PDEs) with defined geometry, load and material properties.

The first strategy treats the fundamental model description by examining various environmental factors and their interactions. The result of including new relations can be represented by a coupled models, e.g. fire-structure analysis [85], moisture-heat transport [56], climate models [33] and other multi-physics problems. Another example of modification at the level of governing equations can be introduction of geometric non-linearity, which can occur due to large displacements, strains, rotations, etc. The second option is to modify the constitutive law, i.e. to treat the relations on material description level. This includes a wide area of application ranging from modelling unsaturated environment in a ground water flow [112] through damage [10] and plasticity [118, 49] to various forms of ageing like creep or relaxation [11] in structures. Since the material property often depends on state variables, the model itself becomes non-linear. The third strategy combines

the outer effects, i.e. the boundary or load conditions, together with the problem of handling errors due to the physical domain deviations, discrepancy between the real and simulated load conditions, material properties, etc. This frequently involves the probabilistic approach [35, 69], admitting the randomness to occur on all aforementioned levels allowing to study the impact of many sources of uncertainties on the model response.

Essentially, the majority of foregoing strategies enriches the model with additional information by increasing the number of input parameters and thus the computational complexity. When using such models one is required to have a profound knowledge and understanding of the input parameters which is often accomplished by in many cases expensive and complex experiments. This work is focused on the identification techniques of input parameters for various computational models applicable in civil engineering. Special focus is devoted to non-destructive parameter identification technique based merely on the boundary observations of the object of interest. This approach brings practical benefits such as the ability to maintain the sample object under consideration intact meanwhile providing comprehensive information about the parameter distribution inside the observed object. Methods dealing with such problems are being utilised in many disciplines ranging from geophysics to medicine. Although the first signs of similar work on this subject date back to the 1930s in geophysics [65, 96], the principle of identifying material parameters from boundary measurements is often associated with the name of Argentine mathematician Alberto Calderón, who first formed his thoughts in a foundational paper [21] published in 1980. Nowadays one of the most common application utilising Calderón problem principles is represented by Electrical Impedance Tomography (EIT). As a medical imaging technique it was proposed earlier in 1978 by John G. Webster [43]. The first tomogram was constructed later in 1983 by David C. Barber and Brian H. Brown and described in their joint work in 1984 [8]. This non-invasive and painless method has gained its popularity mainly due to its inexpensiveness, portability and the ability of obtaining real time images, which is achieved by a high scanning speed that can result in up to 1000 frames per second [115]. As a medical imaging technique it is used e.g. for lung examination and respiratory problems [19, 66], as an alternative technique to mammography [27, 26], monitoring brain activity [109, 3], etc. The ultimate goal of EIT is to determine an electric conductivity field inside an object of interest using only boundary measurements. The basic idea of this method lies in the difference of surface measurements due to variations in the subsurface conductivity distribution. Single set of surface measurements for a given load conditions might result in a number of possible conductivity fields. Calderón surpassed this problem by sequentially implying multiple load conditions, for

which the system responses have the potential to contain the complete information about the underlying conductivity distribution. The major downside of this method lies in its spatial resolution which is several orders of magnitude lower in comparison to other non-invasive imaging techniques such as Computed Tomography (CT) or Magnetic Resonance Imaging (MRI). Another criterion for considering the use of this method is the need of additional data processing in order to recover the final image and the necessity to handle deviations between the real and simulated boundary shape etc. The crucial part of successful material field recovery is then a precise placement of measurement electrodes together with knowledge of the boundary shape and load conditions, i.e. knowing the impedance and current flux.

A straightforward analogy to the EIT utilising a direct instead of alternating electric current is, for example, Electrical Capacitance Tomography (ECT) [117] or Electrical Resistivity Tomography (ERT) also known as Electrical Resistivity Imaging (ERI). For both ECT and ERT the mathematical formulation and the inverse procedure are identical to the one utilised in EIT. The ERT is essentially a direct current method utilised in geophysics where the electrodes are usually inserted into vertical boreholes filled with water. A modern concept of ERT is used to capture the fluid movement in porous [32, 31] and fractured [95] media. Another interesting application of this method is in archaeology [83], where it is used to roughly locate the possible findings. On the other side the potential of ECT is in industry for monitoring and analysing pneumatic conveying systems, i.e. gas-solid flow [48], measurement of the flow of fluids in pipes [46] and a measurement of the concentration of one fluid in another, or the distribution of a solid in a fluid.

In civil engineering problems, thermal tomography approaches have been used, see [6], in order to recover thermal spatially distributed parameters, i.e. thermal conductivity and volumetric heat capacity, from non-destructive imaging surface temperatures. In practice, a domain being analysed is sequentially subjected to different loading states and corresponding temperature responses are collected on the boundary layer. Consequently, the true material field distribution is identified based on the knowledge of the load conditions and the boundary observations. This problem has been studied during past few years from several perspectives. Spatially distributed thermal conductivity for steady-state heat equation was first estimated from boundary observations in [50]. The defects and/or inhomogeneities in the thermal conductivity fields were presented in [6] and [45]. In [59], authors demonstrated the feasibility of thermal tomography for more complex approach focused on the transient problem, i.e. identifying the thermal conductivity and also the volumetric heat capacity. Furthermore, the methodology

has been extended in [110] towards the practical problems considering the boundary heat flux as unknown and introducing the heat transfer coefficient as an additional field that needs to be recovered. The three dimensional aspects of parameter estimation and Bayesian inference for stationary and non-stationary heat problem was proposed in [111].

The ongoing research whether for medical, geophysical or civil engineering purposes focusses essentially on two main problems. The first is the possibility of recovering an anisotropic conductivity tensor field which in a standard settings can not be uniquely determined by boundary data, see [38, 103]. This can be, however, remedied by a sufficient a priori knowledge, see [67]. A different approach to solve the problem concerning anisotropy can be found in the following papers [4, 40]. Another important direction of the development is the work on reconstruction algorithms and advanced numerical methods, which are generally not limited to EIT application. The development concerns the improvement of algorithms in the field of the overall accuracy, computational demands and the trade-off of choosing one over another. Particular strategies utilised in EIT-like problems are outlined in the following text of this work.

All of the aforementioned methods are built upon the foundational research conducted by A. Calderón in [22], following the same principles, taking into account only preconfigured load conditions mediated by devices such as electrodes or heaters. Although the technical design of EIT suits well in use with electricity, the direct use[1] in civil engineering practise is moderately cumbersome. The problem in using the same technique, although for different physical phenomena, lies in the fact that while in the electricity the rate in which one is able to change the system state, i.e. to alter boundary conditions and wait until the steady-state is reached in the body, is limited by the technical possibilities of the particular equipment being used[2]. Heat propagation across the body, however, has inherently a longer time horizon of getting into its steady-state and the ability to quickly alter boundary conditions with simultaneous measurement collection becomes irrelevant. Other influences, such as environmental instability and the possibility that the temperature in the body at the time of measurement has not yet reached the steady-state, are starting to play a significant role in a successful identification of the material field. Therefore, one of the goals of this thesis is to

[1] In sense of using heaters instead of electrodes and sequentially turning on and off individual heaters in order to invoke different boundary conditions meanwhile capturing the system response for each load condition.

[2] In EIT specifically, the equipment is represented by a digital to analogue converters (DACs), multiplexers and finally an ad-hoc device, e.g. a full desktop computer, computing the inversion in order to visualise the results.

develop a novel paradigm for introducing new load cases in thermal tomography along with practical measurement setup which takes into account the time dependency of the phenomena and other problems that might arise in common building structures. Compared to the laboratory environment, in real world situations it is not an easy task to maintain boundary conditions unchanged during the observation period, which gives the possibility to ask whether an utilisation of the sequential pre-defined load is at all necessary or at least beneficial in the task of the parameter identification. It is therefore appropriate to study the effect of load variability over time and its influence on identified parameters. The resulting variance in the load and therefore in the system response may consist of two components, where the first might be represented by the inevitable and unknown measurement error. The second component might constitute deliberate introduction of variability in load over time that could be treated as a potential source of new information rather than another measurement error. Thus the importance of this thesis lies in the theoretical findings applicable in practical situations by changing the premise of sequentially altering the load conditions in the context of introduction of new information into the system. Practical implications of the proposed methodology arise in the reduction of requirements for load specifications and in the demands on technical equipment settings.

In general, the estimation of thermal properties from boundary measurements is an ill-posed problem because of issues related to the existence of a solution and uniqueness. Small variations in measured data can also result in large changes in a solution and this affects the stability of a problem, see [73]. Traditional approaches have used regularisation methods to impose well-posedness and to search for deterministic solutions, mostly by employing optimisation techniques, see [42]. Another possibility is casting the inverse problem in a probabilistic setting, see [87]. The thesis addresses both deterministic and probabilistic formulation of the problem. Each approach has its advantages and disadvantages, and accordingly, the individual models in this thesis are solved with either the first, the second or, in some cases, by both methods. The probabilistic approach has the edge in treating the ill-posedness of the inverse problem due to its self-regularisation property while at the same time the very same property ensures the inevitable error in measurements is also included in the calculation. Virtually also other influences are involved in this error, such as fluctuations that are below the resolution of the measuring technique or the model inaccuracy. On the other hand, the deterministic approach constitutes a traditional procedure used in inverse problems and offers a straightforward representation of the results with predictable and consistently repeatable outputs. Moreover the sheer volume of variants and sophisticated algorithm modifications developed in the past of-

fers great flexibility and one has the possibility to choose an algorithm which meets their specific needs, e.g. identification of non-differentiable fields, non-smooth transitions, detection of defects, etc.

The thesis is structured as follows: the next section comprises a survey of utilised forward models with a thorough description of the physical meaning of individual elements, measuring procedure, boundary conditions and numerical solutions. Specifically it includes a standard version of electrostatic EIT / ERT using electrodes on the surface of the object as a measuring and loading devices, a steady-state as well as transient variant of model used in thermal tomography. The third section discusses common approaches to solve inverse problems. Then it narrows to two specific methods from deterministic and probabilistic point of view, comprising all of the numerical details of the algorithms that are applied in the next chapter. The representative of deterministic approach is embodied in an iterative method utilising modified regularised Gauss-Newton algorithm. The probabilistic approach is carried out by a Bayesian inference from which the posterior distribution is recovered by the Markov chain Monte Carlo (MCMC) method. The fourth section gives an overview of the identification algorithm performance, considering various scenarios, i.e domain shapes, material distributions, load conditions and limited number of measurement points. The work is then summarised in the last section.

The thesis presents a detailed insight into the concept of non-invasive parameter identification with primary focus on models utilised in civil engineering concerning heat transport. The emphasis is put on the practicality of the proposed solution and the demands for technical equipment. Moreover, the proposed methodology considering a transient heat transport is designed to be an external load-free method, i.e. it completely relies on the environmental factors as a source of changes which are necessary in order to identify the material properties inside the domain. All of the proposed models and identification methods are supported by numerical calculations with artificial or semi-artificial data[3] for various domain shapes, material fields and load conditions. All examples are processed in two-dimensions, providing convenient presentation of the results while keeping the computational complexity low. Furthermore, the extension to three-dimensional space is straightforward in terms of both the computational model and the identification algorithm.

[3]Part of the measurements comes from real observation while the rest of available data, e.g. domain shape or dimensions, the true material distribution, etc., is simulated.

2 Forward models

This thesis considers basically three numerical models which are based on a diffusion equation. Computational models play a fundamental role since each is repeatedly used in the inverse process and also for simulating the error-less data. Numerical solutions for each model are always based on the finite element method (FEM). The space and time discretisation and other specifications are briefly outlined for each model within its section. All relevant information regarding the derivation, implementation and relationships of FEM principles proposed in this paper can be for example found in [9] and the literature therein.

Even though this thesis is mainly concerned with time-dependent heat related processes in civil engineering, the main ideas are created upon the foundational research conducted in [25], where the boundary inversion was proposed and experimentally validated. The aforementioned paper, however, deals with electrostatics instead of heat transfer. Therefore, this thesis is in the first place concerned with the principles of EIT in order to describe the foundations and basic features of boundary inversion.

2.1 Electrical Impedance Tomography

There exist a number of established forward models whether for direct or alternating current, assuming various simplifications with a different computational complexity. In this thesis we mainly concentrate on direct current models as they are closely related to the processes in civil engineering environment. The simplest models can be represented by a *continuum*, *shunt* or *gap model*, which are sometimes referred to as a non-physical, due to the simplification in modelling the electrode as a perfectly conducting single point, e.g. there is no transition impedance between the skin and the actual electrode [93].

Due to a more accurate physical representation, a *Complete Electrode Model* (CEM) is now mostly used in practice. It allows to consider electrodes actual physical size and introduces a contact impedance layer between the skin and the electrode. The model was introduced and experimentally validated in 1989 by K. S. Chen [25]. Further proof for CEM solution uniqueness under assumptions 1 was given by E. Somersalo, et al. in 1992 [98]. Significant contributions to the theory were papers [20, 105] proving the solution is uniquely determined in dimension $n \geq 3$ for complete DTN eq. (3.3) or NTD eq. (3.2) data. Unlike in $n \geq 3$, in dimension $n = 2$ the problem is undetermined and the solution was proved to be unique up to a change of coordinates [104, 80].

Further in this thesis we consider only a CEM model, which is defined in the following way [98]

$$\begin{cases} \nabla \cdot (\sigma(x)\nabla v(x)) = 0, & x \in \Omega \\ \int_{e_s} \sigma(x)\dfrac{\partial v}{\partial n}(x)\mathrm{d}S = I_s, & s = 1, \dots, m_s \\ \sigma(x)\dfrac{\partial v}{\partial n}(x) = 0, & x \in \partial\Omega \setminus \bigcup\limits_{s=1}^{m_s} e_s \\ v(x) + z_s\sigma(x)\dfrac{\partial v}{\partial n}(x) = V_s, & x \in e_s, s = 1, \dots, m_s, \end{cases} \tag{2.1}$$

where $\Omega \subseteq \mathbb{R}^d$, $d = 2$, is a bounded domain with a piecewise smooth boundary. The outward unit normal vector to the boundary is denoted by n. A known electrical conductivity field σ is given on the closure of Ω. The model consists of m_s electrodes $(e_s)_{s=1}^{m_s}$ modelled as a part of the surface $\partial\Omega$, each with known contact impedances $(z_s)_{s=1}^{m_s} \in \mathbb{R}_+$ that are assumed to be constant. The current pattern applied to the electrodes is denoted by $(I_s)_{s=1}^{m_s} \in \mathbb{R}$. The electrostatic potential field within the domain is denoted by $v(x)$. The model conditions introduced in eq. (2.1) can be translated as follows: the first term is the governing equation, the second condition indicates that the current flux is averaged across each electrode e_s and gives rise to a known (measured) constant current I_s. The third condition implies that there is no current leakage through the bare skin, assuming that the air is an insulator and the last term is a Robin condition, which includes z_s, a skin-electrode contact impedance. The problem in eq. (2.1) determined by the first three equalities is solvable under some natural assumptions such as the positiveness of σ and $\sum_{s=1}^{m_s} I_s = 0$. The latter condition also has a physical justification as conservation of charge. The fourth equality in eq. (2.1) shows how the potential v determines an electrode potential V_s on each electrode e_s. Motivated by physical considerations, we can expect that V_s are constants. A question arises, whether problem 2.1 with unknown constants V_s has a solution. That is, whether a function v and a vector from $\mathbb{R}^{m_s}$ exist such that they solve eq. (2.1).

In [98], the weak formulation of eq. (2.1) was presented and the proof of the existence of a solution formed by $\mathbf{v}$ and $\mathbf{V} = (V_1, \dots, V_{m_s})$ was given under the following assumptions.

Assumption 1. *The conductivity σ, the contact impedances z_s and the current pattern I_s satisfy*

(i) $\quad \sigma \in L^\infty(\Omega; \mathbb{R}), \quad \inf\limits_{x\in\Omega} \sigma(x) = \sigma_- > 0,$

(ii) $\quad 0 < z_- \leq z_s \leq z_+ < \infty, \quad s = 1, \ldots, m_s,$

(iii) $\quad \sum_{s=1}^{m_s} I_s = 0.$

However, the solution is only defined up to addition of a constant to both v and V. It is proved in [98] that the uniqueness of the solution is ensured if $\sum_{s=1}^{m_s} V_s = 0$. By virtue of the linearity of eq. (2.1), this condition can be used (a) for the *ex post* normalisation of v and V, (b) in the definition of a vector subspace where V is searched for, or (c) in the setting of the reference potential if the electrode voltages are measured as in identification problems. More information and different perspective of the model description and its treatment can be found in [113, 25, 114] and the literature therein.

Overall the inputs for this model are the conductivity field $\sigma(x)$, current patterns $(\mathbf{I}_s)_{s=1}^{m_s} \in \mathbb{R}^{m_s}$ and contact impedances $(z_s)_{s=1}^{m_s} \in \mathbb{R}_+$. The model output consists of a measurement set $(\mathbf{V}_s)_{s=1}^{m_s} \in \mathbb{R}^{m_s}$ and a potential field $u(x)$, see eq. (2.4).

While contact impedances z_s are to some extent given or measured a priori and the conductivity field $\sigma(x)$ is a matter of the identification algorithm, practically the only adjustable variable is represented by the choice of current patterns, where one can choose from variety of approaches, see [113]. Although there are various current pattern strategies, it is sufficient to choose only $m_s - 1$ linearly independent load conditions to generate measurements comprising all possible information[4] due to the linear relationship between current and potential. In our case, the current patterns $\mathbf{I} = (I_s)_{s=1}^{L-1} \in \mathbb{R}^{L\times(L-1)}$ takes following form

$$\mathbf{I} = C \times \begin{bmatrix} +1 & 0 & \cdots & 0 \\ -1 & +1 & \cdots & 0 \\ 0 & -1 & \ddots & 0 \\ \vdots & \vdots & \ddots & +1 \\ 0 & 0 & 0 & -1 \end{bmatrix}, \tag{2.2}$$

where $C \in \mathbb{R}$ [A] is a constant regarding to applied current and each column represents a single load condition. Note also that each load condition has to sum up to zero, satisfying the condition (iii) in assumption 1, with a physical meaning of conservation of charge.

In short, the identification algorithm works as follows. The model eq. (2.1) is provided with the measured input data, i.e. the fluxes I_s, impedances z_s,

[4] In case of admitting errors in measurements, redundant current patterns can actually provide additional information.

along with a chosen estimate of the conductivity field σ. The part of the model output which we are interested in is primarily the set of electrical potentials V_s for particular choice of the field σ. The identification algorithm then adjusts the field σ in such a way to minimise an appropriate norm of the difference $(V_s - W_s)$[5], where W_s represents the error-less (measured) data stemming from an experiment, see Sec. 3.

Numerical solution of the forward model

The additional complexity in solving the CEM forward model lies in the property of each electrode, i.e. including the impedance layer and its actual physical size. Since the currents are transmitted through each electrode which is departed from the object via impedance layer, one have to adopt some technique or incorporate a virtual electrode nodes to the FE problem in order to obtain the full solution, i.e. the vector $\mathbf{u}$ and $\mathbf{V}$ for each loading case. In this thesis we follow the usual way of solving this problem which is the latter. The solution of eq. (2.9) is obtained using finite element method. The domain is discretised into N_e disjoint triangular elements with N_n nodes. The solution is approximated with $\varphi_i(x)$ for $i = 1, \ldots, N_n$ linear basis functions. The parameter $\sigma(x)$ is approximated by an element-wise constant functions and can be identified with a vector $\boldsymbol{\sigma} \in \mathbb{R}^{N_e}$. The forward operator is then constructed in the following way

$$F(\boldsymbol{\sigma}) = \mathbf{V}, \quad \mathbf{V} \in \mathbb{R}^{m_s \times (m_s - 1)}, \tag{2.3}$$

where $\mathbf{V}$ is a matrix containing m_s measurements, i.e. voltages, for $(m_s - 1)$ individual current stimulation patterns. The set of measurements $\mathbf{V}$ is obtained by solving following set of equations

$$\begin{bmatrix} \mathbf{K} + \mathbf{K}_{uu} & \mathbf{K}_{uv} \\ \mathbf{K}_{uv}^T & \mathbf{K}_{vv} \end{bmatrix} \begin{bmatrix} \mathbf{v} \\ \mathbf{V} \end{bmatrix} = \begin{bmatrix} \mathbf{0} \\ \mathbf{I} \end{bmatrix}, \tag{2.4}$$

where $\mathbf{v} \in \mathbb{R}^{N_n \times (m_s - 1)}$ is a solution matrix of potentials in Ω, $\mathbf{I} \in \mathbb{R}^{m_s \times (m_s - 1)}$ is a matrix of current stimulation patterns, $\mathbf{0} \in \mathbb{R}^{N_n \times (m_s - 1)}$ is a matrix of zeros and the individual system matrices are calculated in a following way

$$K_{ij} = \int_\Omega \sigma \nabla \varphi_i \cdot \nabla \varphi_j \, \mathrm{d}A \qquad i, j = 1 \ldots N_n, \tag{2.5}$$

$$K_{uu,ij} = \sum_{s=1}^{m_s} \int_{e_s} \frac{1}{z_s} \varphi_i \varphi_j \, \mathrm{d}S \qquad i, j = 1 \ldots N_n, \tag{2.6}$$

[5] In the following text we denote these variables as follows: $V_s = F(\boldsymbol{\sigma})$ and $W_s = \mathbf{v}_m$.

$$K_{uv,is} = -\sum_{s=1}^{m_s} \int_{e_s} \frac{1}{z_s} \varphi_i \, \mathrm{d}S \qquad i = 1 \dots N_n,\ s = 1 \dots m_s, \tag{2.7}$$

$$K_{vv,ks} = \int_{e_s} \frac{1}{z_s} \, \mathrm{d}S = \frac{|e_s|}{z_s} \delta_{ks} \qquad k, s = 1 \dots m_s, \tag{2.8}$$

where N_n is a number of linear FE basis functions φ, $|e_s|$ is the electrode length and δ_{ks} is Kronecker delta.

The in-depth derivation of individual terms can be for example found in [113, 25, 114] and the literature therein.

2.2 General Transport Model (GTM)

Following the same principles, one can generalise the concept for arbitrary transport process governed by a diffusion equation. For the purpose of civil engineering application, we shall consider a steady-state heat equation with its boundary conditions in the following form

$$\begin{cases} \nabla \cdot (\lambda_s(x) \nabla u_h(x)) = 0, & x \in \Omega \\ \lambda_s(x) \dfrac{\partial u_h}{\partial n}(x) = f_N(x), & x \in \partial\Omega_N \backslash e_h \\ \alpha \left(u_h(x) - u_0(x) \right) = \lambda_s(x) \dfrac{\partial u_h}{\partial n}(x), & x \in \partial\Omega_T \backslash e_h \\ u_h(x) + r_h \lambda_s(x) \dfrac{\partial u_h}{\partial n}(x) = T_h, & x \in e_h,\ h = 1, \dots, m_h \end{cases} \tag{2.9}$$

$$\partial\Omega = \partial\Omega_T \cup \partial\Omega_N.$$

The formulation of eq. (2.9) considers m_h solutions of the governing equation on the first line, which is a response to m_h different boundary conditions, i.e. individual heaters, represented by the Robin condition on the last line. In contrast to EIT, the potential $u_h(x)$ [K] represents here the temperature field for h-th load condition, thus the electrodes e_h now transform into heaters which are capable of changing their temperature instead of the electric current[6]. The other variables include the thermal conductivity field $\lambda_s(x)$, the outward pointing unit normal vector n and the constants r_h and T_h representing the heater resistance coefficient and the heater temperature of the h-th loading state, respectively. The environmental factors are α being the constant heat transfer coefficient, $u_0(x)$ is the environmental temperature

[6]By using Robin condition together with the heater temperature T_h and transfer coefficient r_h, one can still employ the Neumann-To-Dirichlet map for GTM model, see Sec. 3.

and $f_N(x)$ [$\mathrm{W} \cdot \mathrm{m}^{-2}$] is the prescribed flux. The $\partial\Omega$ is a boundary of the domain Ω. Note that T_h is a single constant for the h-th out of m_h loading states indicating our intention to utilise a stimulation pattern in which only the h-th heater is active while the others are inactive.

The inputs for this model are then the conductivity field $\lambda_s(x)$, the stimulation temperatures $(T_h)_{h=1}^{m_h}$, the contact resistances $(r_h)_{h=1}^{m_h}$ and the environmental factors α, $u_0(x)$ and $f_N(x)$. Subsequently, the model output consists of the temperature field $u(x)$ with its trace on the boundary $\partial\Omega$. In the numerical settings, m_h heaters are attached to the boundary $\partial\Omega$, whereas only one is active at a time. For each active heater we capture the temperature in m_n measurement nodes on the boundary $\Gamma_m \subseteq \partial\Omega$ forming a vector containing $m_h m_n$ values.

By simplifying Assumption 1, the existence and uniqueness of the solution of the weak form of eq. (2.9) is proved under following assumptions, see [86]

Assumption 2. *The conductivity $\lambda_s(x)$, the contact resistances r_h and the transfer coefficients α satisfy the following conditions*

(i) $\lambda_s \in L^\infty(\Omega;\mathbb{R}), \quad \inf_{x\in\Omega} \lambda_s(x) = \lambda_s^+ > 0,$

(ii) $0 < r_h^- \leq r_h \leq r_h^+ < \infty, \quad h = 1, \ldots, m_h,$

(iii) $0 < \alpha^- \leq \alpha \leq \alpha^+ < \infty.$

Note that in comparison to Assumption 1 there is no parallel to the condition for conservation of charge, i.e. $\sum I_s = 0$. By application of the second and the third equation in eq. (2.9) the solution of the problem is unique and there is no need to introduce an analogy to the condition $\sum V_s = 0$ in CEM.

Unlike in EIT, where the measurements are conducted only by electrodes that are not active in particular loading state, one can actually choose all accessible parts of the boundary $\partial\Omega$, which can be understood as taking a thermal camera images. Since the stimulation temperatures T_h and resistances r_h for each heater are known a priori, the last equation in eq. (2.9) can be interpreted as a prescribed flux with a reference temperature T_h, thus preserving the principle of loading with flux and measuring the potential at the boundary as it is common in EIT. The previously mentioned *current stimulation pattern* from EIT now translates into the *temperature stimulation pattern*, which can take nearly arbitrary form.

Another beneficial aspect in GTM is that in oppose to EIT at least two electrodes in each loading state must be active concurrently due to the third condition in Assumption 1. GTM is always provided with the reference

temperature T_h due to the third equation in eq. (2.9), so one can stimulate the construction with just a single heater at time without having to solve a problem with the existence of a solution, which is also the case in our numerical examples.

The stimulation pattern can be then expressed in the following way

$$\boldsymbol{T} = \begin{bmatrix} T_1 & \emptyset & \cdots & \emptyset \\ \emptyset & T_2 & \cdots & \emptyset \\ \vdots & \vdots & \ddots & \emptyset \\ \emptyset & \emptyset & \emptyset & T_h \end{bmatrix}, \tag{2.10}$$

where T_1, T_2, $\ldots T_h$ [K] are constant temperatures of active heaters. Each load condition is aligned in a column and the symbol $\emptyset$ indicates that the boundary condition for a given part of the boundary e_h in particular loading state is substituted by the third condition from eq. (2.9) which is present in the close surrounding of the edge e_h.

Numerical solution of the forward model

The solution of eq. (2.9) is obtained using finite element method. The domain is discretised into N_e disjoint triangular elements with N_n nodes. The solution is approximated with $\varphi_i(x)$ for $i = 1, \ldots, N_n$ linear basis functions. The parameter $\lambda_s(x)$ is approximated by an element-wise constant function and can be identified with a vector $\boldsymbol{\lambda}_s \in \mathbb{R}^{N_e}$. We assume nodes located on Γ_m that coincide with active heaters not visible by the thermal camera and therefore are excluded from the observation. Let us define the dependence of the nodal temperatures $u_h|_{\Gamma_m}$ on the parameter $\boldsymbol{\lambda}_s$ by the following forward operator

$$F(\boldsymbol{\lambda}_s) = \mathbf{u}_r, \quad \mathbf{u}_r \in \mathbb{R}^{m_n \cdot m_h}, \tag{2.11}$$

where $\mathbf{u}_r$ is the vector containing the temperatures on the boundary $\Gamma_m \subseteq \partial\Omega$ that is subjected to measurement, m_n is the cardinality of the discrete form of Γ_m, i.e. the number of finite element nodes located on Γ_m and m_h is the number of heaters.

The full solution vector for the h-th active heater $\mathbf{u}_h \in \mathbb{R}^{N_n}$, containing all temperatures in Ω is obtained in the following way

$$(\mathbf{K} + \mathbf{K}_t + \mathbf{K}_{e,h})\, \mathbf{u}_h = \mathbf{f}_t + \mathbf{f}_{e,h} + \mathbf{f}_n, \tag{2.12}$$

where the particular system matrices and corresponding right-hand side vectors are computed in the following way

$$K_{jk} = \int_\Omega \lambda_s \nabla\varphi_j \cdot \nabla\varphi_k \,\mathrm{d}A \qquad j, k = 1 \ldots N_n, \tag{2.13}$$

$$K_{t,hjk} = \int_{\partial\Omega_T \setminus e_h} \alpha \varphi_j \varphi_k \,\mathrm{d}S \qquad j,k = 1 \dots N_n,\ h = 1, \dots m_h, \tag{2.14}$$

$$K_{e,hjk} = \int_{e_h} \frac{1}{r_h} \varphi_j \varphi_k \,\mathrm{d}S \qquad j,k = 1 \dots N_n,\ h = 1, \dots m_h, \tag{2.15}$$

$$f_{t,hj} = \int_{\partial\Omega_T \setminus e_h} \alpha u_0 \varphi_j \,\mathrm{d}S \qquad j = 1 \dots N_n,\ h = 1, \dots m_h, \tag{2.16}$$

$$f_{e,h} = \int_{e_h} \frac{1}{r_h} T_h \,\mathrm{d}S \qquad h = 1 \dots m_h, \tag{2.17}$$

$$f_{n,hj} = -\int_{\partial\Omega_N \setminus e_h} f_N \varphi_j \,\mathrm{d}S \qquad j = 1 \dots N_n,\ h = 1, \dots m_h. \tag{2.18}$$

2.3 Transient model

In real conditions it is, however, not an easy task to sustain a stable and steady state conditions. Not only the surrounding temperature u_0 fluctuates even in a laboratory environment, but for standard building materials like bricks, concrete, wood, etc. the steady state can be reached after several hours or days depending on the volumetric capacity, heat conductivity and material thickness. Therefore, we intend to apply the identical principles used in a Calderón problem for time dependent models.

To describe a time dependent heat transfer, one can adopt following set of equations

$$\begin{cases} \rho_s(x) c_p(x) \dfrac{\partial u}{\partial t}(x,t) - \nabla \cdot (\lambda_s(x) \nabla u(x,t)) = 0, & x,t \in \Omega \times (0, t_s)\,, \\ \lambda_s(x) \dfrac{\partial u}{\partial n}(x,t) = f_N(x,t), & x \in \partial\Omega_N, \\ \alpha(u(x,t) - u_0(x,t)) = \lambda_s(x) \dfrac{\partial u}{\partial n}(x,t), & x \in \partial\Omega_T, \\ \partial\Omega = \partial\Omega_N \cup \partial\Omega_T, \quad u(x,0) = 0 \text{ for } x \in \Omega. \end{cases} \tag{2.19}$$

where $\rho_s(x)$ $[\mathrm{kg} \cdot \mathrm{m}^{-3}]$ is the volumetric mass density, $c_p(x)$ $[\mathrm{J} \cdot \mathrm{kg}^{-1} \cdot \mathrm{K}^{-1}]$ is the specific heat capacity, $\lambda_s(x)$ $[\mathrm{W} \cdot \mathrm{m}^{-1} \cdot \mathrm{K}^{-1}]$ is the thermal conductivity. t_s [s] is the final time of the simulation, $\Omega \subseteq \mathbb{R}^2$ is the open bounded region and $\partial\Omega_{(N,T)}$ are the non-intersecting subsets of the boundary $\partial\Omega$ with corresponding environmental factors being the ambient temperature $u_0(x,t)$ [K], the heat transfer coefficient α $[\mathrm{W} \cdot \mathrm{m}^{-2} \cdot \mathrm{K}^{-1}]$ and the prescribed heat flux $f_N(x,t)$ $[\mathrm{W} \cdot \mathrm{m}^{-2}]$. The existence of a solution and uniqueness of the weak form of eq. (2.19) can be found in [63]. For computational purposes in

the identification process, the volumetric heat capacity $c_v(x)$ $[\mathrm{J}\cdot\mathrm{m}^{-3}\cdot\mathrm{K}^{-1}]$ is introduced in heat balance equation as

$$c_v(x) = \rho_s(x) c_p(x). \tag{2.20}$$

In the definition of this model in eq. (2.19) one can notice that there is no mention of electrodes or heaters indicating our intention not to consciously intervene in the system itself, but only to rely on external influences and a natural fluctuation of the temperature. In situations, where the boundaries $\partial\Omega$ are not exposed to different external influences, one can adapt a similar techniques to GTM and CEM, i.e. to equip the boundary with a heater and/or cooler or control the ambient temperature using the second or the third condition in equation eq. (2.19). From a practical point of view a special feature of this model lies in its independence on the excitation device, i.e. stimulation electrodes or heaters, which manifests itself in a smaller requirements on the measuring equipment, i.e. the full measurement setup consists only of thermometer arrays and/or thermal cameras.

Numerical solution of the forward model

The discretisation and approximation correspond to the previous model with the extension to the volumetric capacity $c_v(x)$ which is approximated by piecewise constant functions on each element forming a vector $\boldsymbol{c}_v \in \mathbb{R}^{N_e}$. The forward operator F then consists of two independent parameters and solves the system for chosen time steps m_t at once, giving a rise to the following formulation

$$F(\boldsymbol{\lambda}_s, \boldsymbol{c}_v) = \mathbf{u}_r, \qquad \mathbf{u}_r \in \mathbb{R}^{m_n \cdot m_t}, \tag{2.21}$$

where the inputs are the thermal conductivity $\boldsymbol{\lambda}_s$ and the volumetric capacity $\boldsymbol{c}_v$ vectors. The output $\mathbf{u}_r$ of the forward operator is acquired as a vectorised subset of a full solution matrix[7] $\mathbf{u}_{\mathrm{sol}} = [\mathbf{u}_1, \mathbf{u}_2, \ldots, \mathbf{u}_{N_t}] \in \mathbb{R}^{N_n \times N_t}$, were N_t is the number of total time steps of the simulation. The individual vectors $\mathbf{u}_i$ are obtained from the following set of linear equations

$$\begin{aligned} \mathbf{K}_C \mathbf{u}_{i+1} = &\left(\mathbf{K}_C - \Delta t \widetilde{\mathbf{K}}\right) \mathbf{u}_{i-1} + \ldots \\ &\Delta t \left((1-\tau)\mathbf{f}_{n,i-1} + \tau \mathbf{f}_{n,i}\right) + \ldots \\ &\Delta t \left((1-\tau)\mathbf{f}_{t,i-1} + \tau \mathbf{f}_{t,i}\right), \end{aligned} \tag{2.22}$$

$$\widetilde{\mathbf{K}} = \mathbf{K} + \mathbf{K}_t, \tag{2.23}$$

$$\mathbf{K}_C = \mathbf{C} + \tau \Delta t \widetilde{\mathbf{K}}, \tag{2.24}$$

[7] From which $m_n < N_n$ and $m_t \leq N_t$ numbers are utilised in the identification process.

where $\Delta t = t_{i+1} - t_i$ is the time step, and $\tau \in \langle 0; 1 \rangle$ is an implicitness parameter[8], the system matrices and right hand side vectors are computed in the following way

$$K_{jk} = \int_\Omega \lambda_s \nabla \varphi_j \cdot \nabla \varphi_k \, \mathrm{d}A \qquad j, k = 1 \ldots N_n, \tag{2.25}$$

$$C_{jk} = \int_\Omega \rho_s c_p \varphi_j \varphi_k \, \mathrm{d}A \qquad j, k = 1 \ldots N_n, \tag{2.26}$$

$$K_{t,jk} = \int_{\partial\Omega_T} \alpha \varphi_j \varphi_k \, \mathrm{d}S \qquad j, k = 1 \ldots N_n, \tag{2.27}$$

$$f_{t,ji} = \int_{\partial\Omega_T} \alpha u_{0,i} \varphi_l \, \mathrm{d}S \qquad i = 1 \ldots N_t,\ j = 1 \ldots N_n, \tag{2.28}$$

$$f_{n,ji} = -\int_{\partial\Omega_N} f_N(t_i) \varphi_j \, \mathrm{d}S \qquad i = 1 \ldots N_t,\ j = 1 \ldots N_n. \tag{2.29}$$

For detailed information and derivation of individual terms, the interested reader is referred to [9, 47, 101, 118] and literature therein.

[8] The foregoing computations were calculated using Crank-Nicolson scheme, i.e. $\tau = 0.5$.

3 Inverse problem

In a classical concept of numerical analysis, one is often provided with an appropriate physical model and a certain surrounding environment, i.e. a set of possible causes with a knowledge of the system behaviour, determining the required model responses. Such procedure is called a forward model and is opposite to the inverse problem, for which the main objective is to determine the cause from a given set of observations. Generally, the majority of forward models for physical situations lead to the well-posed problems in the sense of Hadamard, see [39], for which the conditions can be stated as

- for all admissible data the solution exists (existence),
- for all admissible data there is at most one solution of the problem (uniqueness),
- the solution depends continuously on the data (stability).

However, inverse problems do not necessarily have the aforementioned properties. Solution of such problems might therefore not be unique or stable and even small changes in the input data can result into a large changes in the solution violating the third condition, thus the problem can be recognised as ill-posed, see [113, 53]. Another criterion that comes into consideration is uniqueness of the solution which can be better understood as a possible information shortage or data insufficiency stemming from inadequate number of measurements, poor measurement accuracy or the data could be partially missing. Although lack of the information cannot be remedied by any mathematical treatment, see [64], stability of the solution can be treated by various mathematical procedures. In case that the instability is intrinsic property of the system itself and the problem cannot be reformulated, one needs to provide additional assumptions, e.g. some prior information, enforcing smoothness, preferring solution with the smallest norm, provide bounds to the unknown entity, set a de-noising filter or an approximation of what the missing data could be etc. Procedures for determining such constraints and/or additional requirements on the solution are generally called regularisation methods and within this thesis are categorised as deterministic and stochastic with a brief overview of frequently used methods in the following subsections.

An inverse problem has many applications and can be viewed from many perspectives. On one hand it can represent a task of finding a match between the measured data, resulting from an experiment, with the response of the forward model. As a result, the set of parameters, e.g. a distribution of the

material field, is obtained for a given forward model corresponding to the experiment. Another category consists of tasks looking for an optimal distribution of parameters by modifying e.g. a mass distribution, stiffness, spatial arrangement of individual components and/or a combination of multiple parameters. The result is then an original design which is yet to be manufactured and experimentally verified. Further, our intention is inclined towards boundary inverse which is mathematically related to Calderón inverse problem, representing a non-linear and severely ill-posed problem (see [79]) of recovering the coefficient of divergence σ in a system of elliptic partial differential equations. For electrostatic EIT the problem is modelled by the generalised Laplace equation with the following boundary conditions

$$\begin{cases} \nabla \cdot (\sigma \nabla v) = 0, & \text{in } \Omega \\ \sigma \nabla v \cdot n = g, & \text{on } \partial\Omega \end{cases} \tag{3.1}$$

satisfying the conservation of charge $\int_{\partial\Omega} g \, \mathrm{d}S = 0$ and choice of the reference voltage $\int_{\partial\Omega} v \, \mathrm{d}S = 0$ providing the solution existence and uniqueness respectively, see [86]. The term $g \in H^{-1/2}(\partial\Omega)$ is a given current flux on the Lipschitz boundary $\partial\Omega$ and the induced potential lying in the Sobolev space $u \in H^1(\Omega)$ uniquely solves the Neumann boundary value problem in a bounded domain $\Omega \subseteq \mathbb{R}^2$. The electrical conductivity $\sigma \in L^\infty(\Omega)$ is assumed to be scalar valued, strictly positive and bounded in Ω and n is the outward pointing unit normal vector.

The knowledge of the resulting trace of the potential $v \in H^{1/2}(\partial\Omega)$ then gives rise to the Neumann-to-Dirichlet (NTD) $\Lambda_\sigma : H^{-1/2}(\partial\Omega) \to H^{1/2}(\partial\Omega)$ map, which can be formally defined as

$$\Lambda_\sigma : (\sigma \nabla v) \cdot n|_{\partial\Omega} \mapsto v|_{\partial\Omega}. \tag{3.2}$$

In general it is also possible to proceed in the opposite way, i.e. to prescribe the Dirichlet boundary condition $v|_{\partial\Omega}$ in eq. (3.1) and infer the current flux $(\sigma \nabla v) \cdot n|_{\partial\Omega}$. Following such procedure, one can define a Dirichlet-to-Neumann (DTN) $\Lambda_\sigma^{-1} : H^{1/2}(\partial\Omega) \to H^{-1/2}(\partial\Omega)$ map as

$$\Lambda_\sigma^{-1} : v|_{\partial\Omega} \mapsto (\sigma \nabla v) \cdot n|_{\partial\Omega}. \tag{3.3}$$

With this definition Λ_σ and Λ_σ^{-1} are bounded linear maps though non-linearly depending on the conductivity σ. The physical representation of NTD map can be interpreted as a knowledge of the resulting potential distribution on $\partial\Omega$ corresponding to given flux distribution on $\partial\Omega$.

The problem of interest is then to ask whether the Cauchy data, i.e. the pair of potentials and fluxes on the boundary, determine the conductivity

σ in Ω uniquely. The injectivity of the forward map and uniqueness were proven under variety of assumptions in [105, 80, 20] and states following

$$\Lambda_{\sigma_1} = \Lambda_{\sigma_2} \Rightarrow \sigma_1 = \sigma_2. \tag{3.4}$$

For detailed information about DTN and NTD maps, see [106].

From a practical point of view the recovery process suffers from limited number of independent measurements, its accuracy and large number of degrees of freedom of the discretised parameter/s to be identified. Although the solution stability has been studied from various perspectives [1, 90], partial data recovery still remains to be an opened question [51, 54, 52] and a chosen set of examples is numerically studied in the section Sec. 4. Another substantial subject of research is limited ability to identify anisotropic fields, see [38, 103, 67, 4, 40].

Despite the aforementioned difficulties and serious open questions, inverse problems represent one of the most important topics in mathematics and science and have a wide range of applications in medical imaging [109, 3, 27, 26, 8, 43], geophysics [83, 32, 115, 65, 95, 96], machine learning [97, 107], acoustics [91, 28, 107], signal processing [84], radar [16], optics [7], astronomy [29, 71] and many other fields.

3.1 General procedure

In relation to the previous text, the inverse problem or identification methods can be in principle represented by optimisation algorithms which utilise mathematical methods that explore the available search space[9] in order to find an optimal or near-optimal solution of a problem of interest with regard to predetermined goals and constraints. The primary step is the choice of a metric representing a measure of optimality that operates with the forward model response and optionally also with experimental data. The metric most often takes the form of a transformation f of a given data $\mathbf{\Phi}$ into a scalar quantity, i.e. $f : \mathbf{\Phi} \to \mathbb{R}$, where $\mathbf{\Phi}$ represents a general multi-parameter set. Such transformation is usually referred to as an objective, cost or loss function when the functional f is being minimised or fitness or a utility function if the functional is being maximised. The input data $\mathbf{\Phi}$ may also be further subjected to variety of constraints, e.g. one can provide $\mathbf{\Phi}$ with lower and/or upper bounds, restrict the parameter to lie on a positive real axis, etc. In a probabilistic settings the transformation may be represented by a likelihood

[9] The search space is represented by the span of free parameters, i.e. the domain of $\mathbf{\Phi}$, which in practical settings can take a form of a range of values of the material property in particular area, geometrical parameters, etc.

function, see eq. (3.62). In the deterministic case it usually corresponds to a p-norm and can be written in the following way

$$f(\boldsymbol{\Phi}) = \arg\min_{\boldsymbol{\Phi}} \|\mathbf{u}_m - F(\boldsymbol{\Phi})\|_p, \tag{3.5}$$

where $F(\cdot)$ is the forward operator, $\mathbf{u}_m$ represents error-less data, i.e. a priori measured data from a real or a synthetic experiment, and the p-norm is minimised over the domain of all possible solutions of $\boldsymbol{\Phi}$. In a sense of norms in vector spaces the metric can be then interpreted for example as a distance[10] from the true solution or as a measure of similarities between solutions.

Although it might be undemanding to examine what are the implications of employing particular choice of p-norm for the identified variable, i.e. for example $p = 0$ is typical to prefer sparse solutions, for $p = 1$ the solution is allowed to incorporate non-smooth transitions [5, 44] or $p = 2$ for the preference of smooth solutions, the actual implementation of some norms into the algorithm can often lead to intractable problem due to combinatorial increase in the number of local minima as the number of candidate basis vectors increases [116]. Selecting the right metrics is therefore not straightforward and depends not only on requirements on the accessible computational resources, but also on the available mathematical tools to solve such optimisation task and on the problem itself. Therefore we employ only metrics that leads to more tractable computational methods, such as $p = 2$. The aim of this thesis focuses merely on parameter identification, where the free parameters are represented by the material field/s and therefore the multi-parameter set $\boldsymbol{\Phi} = [\boldsymbol{\phi}_1, \ldots, \boldsymbol{\phi}_{N_p}] \in \mathbb{R}^{N_e \times N_p}$ containing N_p independent parameters, which further constitute for example an electrical conductivity $\boldsymbol{\Phi} = [\boldsymbol{\phi}_1] = \boldsymbol{\sigma}$, thermal conductivity coefficient together with volumetric capacity, i.e. $\boldsymbol{\Phi} = [\boldsymbol{\phi}_1, \boldsymbol{\phi}_2] = [\boldsymbol{\lambda}_s, \boldsymbol{c}_v]$, etc. Moreover, in the numerical settings, we make use of the vectorised form of $\boldsymbol{\Phi}$ which is denoted in the following way

$$\boldsymbol{\Phi}' = \mathrm{vec}(\boldsymbol{\Phi}) = \begin{bmatrix} \boldsymbol{\phi}_1 \\ \boldsymbol{\phi}_2 \\ \vdots \\ \boldsymbol{\phi}_{N_p} \end{bmatrix} \in \mathbb{R}^{N_e \cdot N_p}. \tag{3.6}$$

Note that $\boldsymbol{\Phi} \in \mathbb{R}^{N_e \times N_p}$ refers to the situation after discretisation. The case before the problem is discretised is only distinguished by the change in parameter dimensions and constitute only N_p elements, i.e. $\boldsymbol{\Phi} \in \mathbb{R}^{N_p}$.

[10] This is valid for a case of $p = 2$ being the shortest distance between two points or for $p = 1$ being the ℓ_1 or Manhattan distance.

3.2 Deterministic methods

Such methods represent a traditional approach for solving a wide range of problems. The extent of use and independence of the particular method used on a specific problem make deterministic methods a relatively well-researched and ever expanding discipline. The identification methods in various fields are pursuing different objectives, e.g. the interest in non-iterative methods is mostly driven by the necessity of fast and reliable identification algorithms generating real time visualisations in medical imaging [40, 99], whereas in geophysics [23, 65, 44], iterative algorithms providing generally refined solutions are more preferred. Since numerical procedures for solving ill-posed and non-linear problems are mathematically identical for various tasks, boundary inverse methods can therefore be solved in a number of ways. Representative iterative methods are for example moment methods [2], Calderón's approach [15], back-projection [92, 12] and in general various modifications of Newton's iteration algorithms [14, 78, 24]. A different approach is represented by non-iterative fully non-linear methods, from which the layer stripping method [99] was introduced as the first one. A more recent development is then devoted to scattering transform, i.e. D-Bar or $\bar{\partial}$ methods [94, 55], due to its ability to accurately recover the absolute conductivity field and handle various noise levels. Furthermore the method was extended to the third dimension [13].

The problem addressed in this thesis is inherently time dependent and relatively slow, so we do not pursue real time imaging, but rather prefer more precise solution which is in our case provided by iterative Newton-type methods based on the assumption of small perturbations of the parameter field. The traditional approach is to linearise the problem and subsequently use a regularisation method to stabilise the solver. The resulting system can be updated iteratively by one from the family of Newton-type methods. The opportunity to perform regularisation of the problem prior to the linearisation or vice versa opens up a wide range of possible ways to solve such problem. The minimisation problem is often stated as follows, with the first term representing the cost function and the second term being the regularisation penalty

$$\boldsymbol{\Phi}_{\text{rec}} = \arg\min_{\boldsymbol{\Phi}} \|\mathbf{u}_m - F(\boldsymbol{\Phi})\|_p + G(\boldsymbol{\Phi}). \tag{3.7}$$

We call $F(\cdot)$ a forward operator containing the model responses for all loading states on the observed part of the boundary, $\mathbf{u}_m$ represents the error-less system response[11], p indicates ℓ_p-norm, $G(\boldsymbol{\Phi})$ is the regularisation functional

[11] By this we mean that we utilise only virtual measurements calculated with a given material distribution $\boldsymbol{\Phi}_{\text{true}}$ which is then unknown in the identification procedure, i.e. $\mathbf{u}_m = F(\boldsymbol{\Phi}_{\text{true}})$.

introducing additional constraints to the solution and $\mathbf{\Phi}_{\text{rec}}$ is the set of parameters being identified.

A typical choice of the regularisation penalty term for multiple parameters in (3.7) is of the following form [113]

$$G(\mathbf{\Phi}) = \kappa^2 \|(\mathbf{1} \otimes L)\mathbf{W}(\mathbf{\Phi}' - \mathbf{\Phi}'_r)\|_{\ell_2}, \tag{3.8}$$

where the hyper-parameter κ, i.e. regularisation parameter, is controlling the trade-off between solution stability, given constrains and a distance from the true solution. The symbol $\otimes$ is a Kronecker product and $\mathbf{1} \in \mathbb{R}^{N_p \times N_p}$ is an identity matrix indicating the mutual spatial independence of parameters $\mathbf{\Phi}' = [\phi_1, \ldots, \phi_{N_p}]^T \in \mathbb{R}^{N_p}$ and $\mathbf{W} \in \mathbb{R}^{N_p \times N_p}$ is a diagonal weighting matrix which without any knowledge can be set to an identity matrix. An additional constraint $\mathbf{\Phi}'_r \in \mathbb{R}^{N_p}$ represents some known and possibly non-smooth behaviour of the unknown parameter [44]. A straightforward way of explaining the regularisation operator L is such that it draws the solution towards its null space, i.e. $\ker(L)$. It might take form of a discrete approximation to the Laplacian[12] of a piecewise constant functions on the finite element mesh [114], a weighted diagonal matrix to promote a sparse solution [30], Gaussian smoothing filter [18] or without any knowledge of the system, the operator is often left to be an identity.

The probably best known and understood methods are iterative algorithms which often make use of Tikhonov regularisation. In a classical settings, the penalty term takes a following form

$$G(\mathbf{\Phi}) = \kappa^2 \|(\mathbf{1} \otimes L)\mathbf{W}\mathbf{\Phi}'\|_{\ell_2}. \tag{3.9}$$

For the convenience of computational purposes and preference of smooth solutions, see [72, 44], both terms in (3.7) are preferred to be ℓ_2-norm. A different approach is to use so called Total Variation (TV) functional in the penalty term, i.e. to replace ℓ_2-norm with ℓ_1-norm:

$$G(\mathbf{\Phi}) = \kappa \|(\mathbf{1} \otimes L)\mathbf{W}(\mathbf{\Phi}' - \mathbf{\Phi}'_r)\|_{\ell_1} \tag{3.10}$$

With a following consequences regarding the solution: the resulting parameter $\mathbf{\Phi}$ is more strictly tightened to the exact solution, allowing to preserve sharp edges, represent piece-wise constant solutions and other desirable properties, e.g. handling a moderate levels of noise [89, 17]. However implementation of TV functional is not straightforward due to its non-

[12]The null space of such operator is any constant field or more precisely the solution is pushed towards $\mathbf{\Phi} = \mathbf{\Phi}_r + c$, where $c \in \mathbb{R}$ is constant shift of the whole field in any direction.

differentiability [72], requiring to use a non-standard solvers, e.g. deterministic Lagged Diffusivity Method (LDM) using a hybrid ℓ_1/ℓ_2, the Primal Dual-Interior Point Method (PDIPM) [72] using a true ℓ_1 or probabilistic methods such as Markov chain Monte Carlo (MCMC) [58, 100] algorithm.

Despite nearly every regularisation technique requires a choice of a hyper-parameter, there is not yet a rigorous formulation with guaranteed convergence and stability. However there are various ad-hoc methods, e.g. heuristic selection, L-Curve method, Generalised Cross-Validation (GCV), Fixed Noise Figure (NF), discrepancy principle or Greferer/Raus method, see [113, 37].

3.2.1 Numerical solution of the inverse problem

All results for deterministic calculations in Sec. 4 share the same regularised Gauss-Newton (GN) iteration scheme [36, 41, 44] in the form of eqs. (3.19) and (3.32). Also the numerical procedures within this section and Sec. 4 refers to the situation after discretisation. In our settings, both terms in eq. (3.7) are preferred to be ℓ_2-norm due to the convenience for computational purposes and the preference of smooth solutions, see [72, 44]. In such case, by combining the minimisation scheme eq. (3.7) for $p = 2$ with the penalty term eq. (3.8) one can obtain a following objective function

$$f(\boldsymbol{\Phi}) = \|\delta\mathbf{u}(\boldsymbol{\Phi})\|_{\ell_2} + \|(\boldsymbol{\kappa} \otimes \mathbf{L})\mathbf{W}(\boldsymbol{\Phi}' - \boldsymbol{\Phi}'_r)\|_{\ell_2}, \tag{3.11}$$

where $\boldsymbol{\Phi} = [\boldsymbol{\phi}_1, \dots, \boldsymbol{\phi}_{N_p}] \in \mathbb{R}^{N_e \times N_p}$ represents N_p material parameters sorted in columns each with a constant value on each element, $\delta\mathbf{u}(\boldsymbol{\Phi})$ is the vector containing the difference between the model response and error-less data, see eq. (3.13), $\boldsymbol{\kappa} \in \mathbb{R}^{N_p \times N_p}$ is a diagonal matrix containing the hyper-parameters $\kappa_1, \dots, \kappa_{N_p}$ for individual parameters in $\boldsymbol{\Phi}$, $\mathbf{W} \in \mathbb{R}^{(N_e \cdot N_p) \times (N_e \cdot N_p)}$ is a diagonal weighting matrix after discretisation containing spatial distribution of weights for individual parameters $\mathbf{W} = \mathrm{diag}([\mathbf{w}_{\phi_1}, \dots, \mathbf{w}_{\phi_{N_p}}])$. Note that the matrix $\mathbf{W}$ has the ability to spatially increase or decrease the effect of regularisation which can be beneficial in parts of the domain, where the parameters being identified is not sensitive to measurements. The last term $\mathbf{L} \in \mathbb{R}^{N_e \times N_e}$ represents the discrete counterpart of the operator L from eq. (3.8) and is obtained in the following way

$$L_{ij} = \begin{cases} -N_e^{(i)} & \text{if } i = j, \\ 1 & \text{if } \mathrm{conn}(i,j) \wedge i \neq j \quad \text{for } i,\, j = 1, \dots, N_e, \\ 0 & \text{otherwise,} \end{cases} \tag{3.12}$$

where $N_e^{(i)}$ is the number of elements attached by an edge to the i-th element and function $\mathrm{conn}(i,j)$ is true if and only if the i-th and j-th element share

the same edge.

$$\delta \mathbf{u}(\mathbf{\Phi}) = \mathbf{u}_m - \mathrm{F}\left(\mathbf{\Phi}\right) \in \mathbb{R}^{m_n \cdot v}, \tag{3.13}$$

where $F(\mathbf{\Phi}) \in \mathbb{R}^{m_n \cdot v}$ represents the discrete NTD forward operator with m_n being the number of measurement points, i.e. the number of nodes of the FE mesh on a subset Γ_m of the boundary $\partial\Omega$ that is being observed and v is the number of distinct loading states[13]. The quantity containing the error-less data is stored in a vector $\mathbf{u}_m \in \mathbb{R}^{m_n \cdot v}$.

There exist several approaches to derive an iterative algorithm based on Gauss-Newton approximation of Newton-Raphson multi-variable method. In this work we derive the iterative scheme with help of the Taylor expansion, which is utilised in order to approximate the objective function $f(\mathbf{\Phi}) \approx \widetilde{f}(\mathbf{\Phi})$ from eq. (3.11) in a given point $\mathbf{d}$. The second-order approximation in a point $\mathbf{d}$ takes the following form

$$f(\mathbf{\Phi}) \approx \widetilde{f}(\mathbf{\Phi}) = f(\mathbf{d}) + \left(\boldsymbol{\nabla} f(\mathbf{d})\right)^T \left(\mathbf{\Phi}' - \mathbf{d}\right) + \frac{1}{2}(\mathbf{\Phi}' - \mathbf{d})^T \mathbf{H}(f(\mathbf{d}))(\mathbf{\Phi}' - \mathbf{d}), \tag{3.14}$$

where $\boldsymbol{\nabla}$ is the gradient operator and $\mathbf{H}$ is a Hessian containing the second-order partial derivatives of the objective function f, see Appendix B. In order to find an extreme of the function $\widetilde{f}$, one is required to find a point $\mathbf{\Phi}_{st}$ satisfying the following condition

$$\boldsymbol{\nabla} \widetilde{f}(\mathbf{\Phi}_{\mathrm{st}}) = \mathbf{0}, \tag{3.15}$$

where the gradient of the quadratic approximation of $\widetilde{f}$ takes the following form

$$\begin{aligned} \boldsymbol{\nabla} \widetilde{f}(\mathbf{\Phi}) &= \boldsymbol{\nabla}[f(\mathbf{d}) + \left(\boldsymbol{\nabla} f(\mathbf{d})\right)^T \left(\mathbf{\Phi}' - \mathbf{d}\right) + \ldots \\ &\quad + \frac{1}{2}(\mathbf{\Phi}' - \mathbf{d})^T \mathbf{H}(f(\mathbf{d}))(\mathbf{\Phi}' - \mathbf{d})], \\ &= \boldsymbol{\nabla} f(\mathbf{d}) + \mathbf{H}\left(f(\mathbf{d})\right)\left(\mathbf{\Phi}' - \mathbf{d}\right). \end{aligned} \tag{3.16}$$

By combining the expression on the last line of eq. (3.16) with eq. (3.15) one can acquire the point $\mathbf{\Phi}'_{\mathrm{st}}$ in the following way

[13]For the steady-state model v corresponds to the number of heaters m_h, whereas for the transient model v is equal to the number of chosen time steps m_t.

$$
\begin{aligned}
\boldsymbol{\nabla} f(\mathbf{d}) + \mathbf{H}\left(f(\mathbf{d})\right)\left(\boldsymbol{\Phi}'_{\mathrm{st}} - \mathbf{d}\right) &= 0, \\
\mathbf{H}\left(f(\mathbf{d})\right)\left(\boldsymbol{\Phi}'_{\mathrm{st}} - \mathbf{d}\right) &= -\boldsymbol{\nabla} f(\mathbf{d}), \\
\left(\boldsymbol{\Phi}'_{\mathrm{st}} - \mathbf{d}\right) &= -\Big[\mathbf{H}\left(f(\mathbf{d})\right)\Big]^{-1}\boldsymbol{\nabla} f(\mathbf{d}), \\
\boldsymbol{\Phi}'_{\mathrm{st}} &= \mathbf{d} - \Big[\mathbf{H}\left(f(\mathbf{d})\right)\Big]^{-1}\boldsymbol{\nabla} f(\mathbf{d}), \\
\boldsymbol{\Phi}'_{\mathrm{st}} &= \mathbf{d} + \delta\mathbf{d},
\end{aligned}
\tag{3.17}
$$

$$
\delta\mathbf{d} = -\Big[\mathbf{H}\left(f(\mathbf{d})\right)\Big]^{-1}\boldsymbol{\nabla} f(\mathbf{d}), \tag{3.18}
$$

where $\delta\mathbf{d}$ represents the best[14] one-step update from the given point $\mathbf{d}$ in the direction $\delta\mathbf{d}$ towards an extreme of the function f. However, due to the imperfection of the second-order approximation of the function f, the newly acquired point $\boldsymbol{\Phi}'_{\mathrm{st}}$ does not necessarily end up at the actual stationary point of the objective function $f(\boldsymbol{\Phi})$. The point is thus successively updated and one obtains the following iterative formula

$$
\boldsymbol{\Phi}'_{k+1} = \boldsymbol{\Phi}'_k + \delta\boldsymbol{\Phi}'_k, \tag{3.19}
$$

which is repeated until some convergence criterion is met, see eqs. (3.52) to (3.54). Note that symbols $\mathbf{d}$ and $\delta\mathbf{d}$ in eq. (3.17) have been replaced by $\boldsymbol{\Phi}_k$ and $\delta\boldsymbol{\Phi}_k$ respectively to make the continuity of iterations and repeatability of the resulting algorithm more apparent.

In order to compute the one-step update $\delta\boldsymbol{\Phi}'_k$ in eq. (3.19), one is required to evaluate the gradient and Hessian of the objective function f in eq. (3.11), in a given point $\boldsymbol{\Phi}_k$. The function in eq. (3.11) rewritten into the matrix format has the following form

$$
f(\boldsymbol{\Phi}) = \delta\mathbf{u}(\boldsymbol{\Phi})^T\delta\mathbf{u}(\boldsymbol{\Phi}) + (\boldsymbol{\Phi}' - \boldsymbol{\Phi}'_r)^T\mathbf{W}(\boldsymbol{\kappa}\otimes\mathbf{L})^T(\boldsymbol{\kappa}\otimes\mathbf{L})\mathbf{W}(\boldsymbol{\Phi}' - \boldsymbol{\Phi}'_r) \tag{3.20}
$$

$$
= \delta\mathbf{u}(\boldsymbol{\Phi})^T\delta\mathbf{u}(\boldsymbol{\Phi}) + (\boldsymbol{\Phi}' - \boldsymbol{\Phi}'_r)^T\mathbf{R}(\boldsymbol{\kappa})(\boldsymbol{\Phi}' - \boldsymbol{\Phi}'_r), \tag{3.21}
$$

where the term $\mathbf{W}(\boldsymbol{\kappa}\otimes\mathbf{L})^T(\boldsymbol{\kappa}\otimes\mathbf{L})\mathbf{W}$ in eq. (3.20) is abbreviated by the matrix $\mathbf{R}(\boldsymbol{\kappa}) \in \mathbb{R}^{(N_e\cdot N_p)\times(N_e\cdot N_p)}$ in eq. (3.21), which is composed from the regularisation operator $\mathbf{L}$ in the following way

$$
\begin{aligned}
\mathbf{R}(\boldsymbol{\kappa}) &= \mathbf{W}(\boldsymbol{\kappa}\otimes\mathbf{L})^T(\boldsymbol{\kappa}\otimes\mathbf{L})\mathbf{W}, && (3.22)\\
&= \mathbf{W}(\boldsymbol{\kappa}^2\otimes\mathbf{L}^T\mathbf{L})\mathbf{W}, && (3.23)\\
&= \mathbf{W}(\boldsymbol{\kappa}^2\otimes\mathbf{L}\mathbf{L})\mathbf{W}. && (3.24)
\end{aligned}
$$

[14] It stems from utilisation only a second-order approximation of f.

Note that nesting of $\boldsymbol{\kappa}$ into the matrix $\mathbf{R}$ makes sense later in text since a different hyper-parameter is utilised for each of N_p parameter fields. In case a single hyper-parameter is used, the formula can be simplified in the following way $\boldsymbol{\kappa} = \kappa\mathbf{1}$, where the term $\mathbf{1} \in \mathbb{R}^{N_p \times N_p}$ is an identity matrix.

Particular choice of the weighting matrix $\mathbf{W}$ employed in our calculations is of the following form

$$\mathbf{W} = \operatorname{diag}\left(\frac{1}{\mathbf{w}_1}, \ldots, \frac{1}{\mathbf{w}_{N_p}}\right) \in \mathbb{R}^{(N_e \cdot N_p)\times(N_e \cdot N_p)}, \tag{3.25}$$

where $\mathbf{w}_i \in \mathbb{R}^{N_e}$ and $i = 1, \ldots, N_p$ are the sensitivity maps for each individual parameter, which are obtained in the following way

$$\widetilde{\mathbf{w}} = \sum_{i=1}^{m_n \cdot v} |J_{ij}| = \sum_{r=1}^{m_n} \sum_{s=1}^{v} \left[\overbrace{\frac{\partial u_{rs}}{\boldsymbol{\phi}_1}}^{\substack{\mathbf{w}_1 \\ j=1}} \quad \overbrace{\frac{\partial u_{rs}}{\boldsymbol{\phi}_2}}^{\substack{\mathbf{w}_2 \\ j=2}} \quad \cdots \quad \overbrace{\frac{\partial u_{rs}}{\boldsymbol{\phi}_{N_p}}}^{\substack{\mathbf{w}_{N_p} \\ j=N_p}} \right]. \tag{3.26}$$

With the formula in eq. (3.25) we intend to obtain weights including all $m_n \cdot v$ measurements with respect to $N_e \cdot N_p$ parameters. This reveals areas in the domain that are generally less sensitive to all measurements with almost no computational effort. One can notice that the sum of absolute values $\mathbf{w}_j = \sum_i |J_{ij}|$ appears in denominator. This means that locations with the highest overall sensitivity is regularised the least, meanwhile locations with the lowest sensitivity is regularised more aggressively with weights greater than one. Note the weighting matrix emphasises the operator $\mathbf{L}$ which penalises spatial fluctuations. However, due to large variations in terms $\mathbf{w}_j$, we restrict the weighting matrix to the scale from 1 to 1.5. Particular examples of $\mathbf{W}$ are depicted for selected cases in Sec. 4.

In order to compute the one-step update, one is required to evaluate the first and second order derivatives of the objective function in eq. (3.21), which can be expressed in the following way

$$\boldsymbol{\nabla} f(\boldsymbol{\Phi}) = 2\left(-\mathbf{J}^T \delta\mathbf{u}(\boldsymbol{\Phi}) + \mathbf{R}(\boldsymbol{\kappa})(\boldsymbol{\Phi}' - \boldsymbol{\Phi}'_r)\right), \tag{3.27}$$

$$\mathbf{H} f(\boldsymbol{\Phi}) = 2\left(-\boldsymbol{\nabla}\left(\mathbf{J}^T\right)\delta\mathbf{u}(\boldsymbol{\Phi}) + \mathbf{J}^T\mathbf{J}\right) + 2\mathbf{R}(\boldsymbol{\kappa}), \tag{3.28}$$

where the second derivatives of the residuum $\delta\mathbf{u}$ in Gauss-Newton method is assumed to be approximately zero, i.e. $\boldsymbol{\nabla}\left(\mathbf{J}^T\right) \approx 0$ (see [36, 41]) and therefore the expression in eq. (3.28) takes the following form

$$\mathbf{H} f(\boldsymbol{\Phi}) \approx 2\left(\mathbf{J}^T\mathbf{J} + \mathbf{R}(\boldsymbol{\kappa})\right). \tag{3.29}$$

The Jacobian matrix $\mathbf{J} \in \mathbb{R}^{(m_n \cdot v) \times (N_e \cdot N_p)}$ is numerically calculated by perturbing the value of Φ_{ij} for all indices ij in the following way

$$J_{rs,ij} = \frac{\partial F(\mathbf{\Phi})_{rs}}{\partial \Phi_{ij}} = \frac{\partial u_{rs}}{\partial \Phi_{ij}} \qquad \text{for} \quad \begin{array}{l} r = 1, \ldots, m_n, \\ s = 1, \ldots, v, \\ i = 1, \ldots N_e, \\ j = 1, \ldots N_p. \end{array} \tag{3.30}$$

Indices r and s correspond to the measurement nodes and loading states respectively. Index i identifies the parameter change on i-th FE element while j distinguishes distinct parameters, i.e. for example $\boldsymbol{\phi}_{j=1} = \boldsymbol{\lambda}_s$ and $\boldsymbol{\phi}_{j=2} = \mathbf{c}_v$. For convenience of the calculation the Jacobian is matricised along indices rs and ij. The final structure of the Jacobian matrix is of the following form

$$\mathbf{J} = \left[\begin{array}{cccc} \dfrac{\partial \mathbf{u}}{\partial \boldsymbol{\phi}_1} & \dfrac{\partial \mathbf{u}}{\partial \boldsymbol{\phi}_1} & \cdots & \dfrac{\partial \mathbf{u}}{\partial \boldsymbol{\phi}_{N_p}} \end{array} \right], \tag{3.31}$$

where the particular term $\frac{\partial \mathbf{u}}{\partial \boldsymbol{\phi}_1} \in \mathbb{R}^{(m_n \cdot v) \times N_e}$ for $\boldsymbol{\phi}_1 = \boldsymbol{\lambda}_s$[15] is further expanded in eq. (3.34). Note that the distinct loading states $s = 1, \ldots, v$ in the expanded equation are vertically aligned and consist of $(m_n \times N_e)$ blocks.

By combining eq. (3.18), eq. (3.27) and eq. (3.29) one can obtain the k-th iteration update, which is of the following form

$$\delta \mathbf{\Phi}'_k = \left(\mathbf{J}_k^T \mathbf{J}_k + \mathbf{R}(\boldsymbol{\kappa}_k) \right)^{-1} \left(\mathbf{J}_k^T \delta \mathbf{u} - \mathbf{R}(\boldsymbol{\kappa}_k) \left(\mathbf{\Phi}'_k - \mathbf{\Phi}'_r \right) \right), \tag{3.32}$$

where $\mathbf{J}_k \in \mathbb{R}^{(m_n \cdot v) \times (N_e \cdot N_p)}$ is the Jacobian evaluated at $\mathbf{\Phi}'_k \in \mathbb{R}^{N_e \cdot N_p}$, $\delta \mathbf{u} \in \mathbb{R}^{m_n \cdot v}$ is a vector containing the difference between the model response and error-less data, see eq. (3.13). If not mentioned otherwise, the reference field $\mathbf{\Phi}_r$ is dropped out by setting it to zero and the iteration starts with a unit vector $\mathbf{\Phi}_0 \in \mathbb{R}^{N_e \times N_p}$.

In computations, where the hyper-parameter κ_k is a constant, it is modified in each iteration k as follows

$$\kappa_k = \max_j \sum_{i=1}^{m_n \cdot v} J_{k,ji} J_{k,ij} \quad \text{for} \quad j = 1, \ldots N_e \cdot N_p, \tag{3.33}$$

[15] The index s in λ_s belongs to the name of the particular variable and is not a sequence index.

$$\frac{\partial \mathbf{u}}{\partial \boldsymbol{\phi}_1} = \frac{\partial \mathbf{u}}{\partial \boldsymbol{\lambda}_s} = \left[\begin{array}{ccc} \frac{\partial u_{11}}{\partial \lambda_{s,1}} & \frac{\partial u_{11}}{\partial \lambda_{s,2}} & \cdots \quad \frac{\partial u_{11}}{\partial \lambda_{s,N_e}} \\ \vdots & \vdots & \vdots \\ \frac{\partial u_{m_n 1}}{\partial \lambda_{s,1}} & \frac{\partial u_{m_n 1}}{\partial \lambda_{s,2}} & \cdots \quad \frac{\partial u_{m_n 1}}{\partial \lambda_{s,N_e}} \end{array}\right] \left.\vphantom{\begin{array}{c} a \\ a \\ a \end{array}}\right\} \begin{array}{l} \text{loading state} \\ s = 1 \end{array}$$

$$\left[\begin{array}{ccc} \frac{\partial u_{12}}{\partial \lambda_{s,1}} & \frac{\partial u_{12}}{\partial \lambda_{s,2}}, & \cdots \quad , \frac{\partial u_{12}}{\partial \lambda_{s,N_e}} \\ \vdots & \vdots & \vdots \\ \frac{\partial u_{m_n 2}}{\partial \lambda_{s,1}} & \frac{\partial u_{m_n 2}}{\partial \lambda_{s,2}} & \cdots \quad \frac{\partial u_{m_n 2}}{\partial \lambda_{s,N_e}} \end{array}\right] \left.\vphantom{\begin{array}{c} a \\ a \\ a \end{array}}\right\} \begin{array}{l} \text{loading state} \\ s = 2 \end{array} \tag{3.34}$$

$$\left[\begin{array}{ccc} \vdots & \vdots & \vdots \end{array}\right]$$

$$\left[\begin{array}{ccc} \frac{\partial u_{1v}}{\partial \lambda_{s,1}} & \frac{\partial u_{1v}}{\partial \lambda_{s,2}} & \cdots \quad \frac{\partial u_{1v}}{\partial \lambda_{s,N_e}} \\ \vdots & \vdots & \vdots \\ \frac{\partial u_{m_n v}}{\partial \lambda_{s,1}} & \frac{\partial u_{m_n v}}{\partial \lambda_{s,2}} & \cdots \quad \frac{\partial u_{m_n v}}{\partial \lambda_{s,N_e}} \end{array}\right] \left.\vphantom{\begin{array}{c} a \\ a \\ a \end{array}}\right\} \begin{array}{l} \text{loading state} \\ s = v \end{array}$$

In this work we also consider a variant where the hyper-parameter is searched for individual parameters $[\boldsymbol{\phi}_1, \boldsymbol{\phi}_2, \ldots, \boldsymbol{\phi}_{N_p}]$ in each iteration. The criterium is for particular choice of the hyper-parameters is of the following form

$$\boldsymbol{\kappa}_{k,\min} = \min_{\kappa_1,\ldots,\kappa_{N_p}} f(\boldsymbol{\Phi}_k + \delta\boldsymbol{\Phi}_k(\boldsymbol{\kappa})). \tag{3.35}$$

The minimisation problem consists of finding N_p values of the diagonal matrix $\boldsymbol{\kappa}_k$ in k-th iteration. In such case the problem is solved by means of Nelder-Mead method.

Additional numerical treatment

The Gauss-Newton iteration scheme presented in eq. (3.32) is relatively simple and does not contain natural constraints to ensure that conditions in Assumption 1 are satisfied. The most critical condition for solving the forward model, that is not treated in the basic iteration scheme in eq. (3.32), is the condition of positive parameters, e.g. electrical conductivity coefficient σ, heat conductivity coefficient λ_s, volumetric capacity c_v and others. Since

the inverse problem is inherently non-linear and the iteration proceeds with non-restricted linear steps, the second problem, which can be treated within eq. (3.32) is the step size which needs to be constrained in order to mitigate the deviation from linearity. The aforementioned problems are addressed by introducing two operators and/or a line-search [82] algorithm to prevent divergence, which reduce the impact or completely eliminate the unwanted phenomena that might occur during the iteration and therefore increases stability and robustness of the identification algorithm.

The constraint defined for strict positivity of the parameter field during the iteration gives rise to a *positivity operator* T_p and is treated in two variants: the first is processed with an ad-hoc algorithm which is not allowing for the occurrence of negative numbers in the solution. They are replaced with a small positive number $\hat{\varepsilon}_j$, see eq. (3.36). This operator is in the following text denoted simply by T_p. The operator evaluated for individual components of $\boldsymbol{\Phi} \in \mathbb{R}^{N_e \times N_p}$ is defined by the following formula

$$T_p(\Phi_{ij}) = \begin{cases} \Phi_{ij} & \text{if } \Phi_{ij} > 0, \\ \hat{\varepsilon}_j & \text{if } \Phi_{ij} \leq 0, \end{cases} \quad \text{for} \quad \begin{matrix} i = 1, \dots, N_e, \\ j = 1, \dots, N_p, \end{matrix} \tag{3.36}$$

where $\hat{\varepsilon}_j = 0.01 \cdot \bar{\phi}_j \in \mathbb{R}_+$ is chosen to be sufficiently small so it does not cause numerical problems and $\bar{\phi}_j$ is the arithmetic mean of the j-th parameter of the starting vector, i.e. the initial expert estimate of the j-th parameter.

A different approach regarding the positivity of parameters is treated by transforming the identified variables. The particular transformation in this thesis is denoted by $T_p^{\exp}$ and takes the following form

$$\boldsymbol{\Phi} = T_p^{\exp}(\boldsymbol{\Theta}) = \exp(\boldsymbol{\Theta}), \tag{3.37}$$

where $\boldsymbol{\Theta} = [\boldsymbol{\theta}_1, \dots, \boldsymbol{\theta}_{N_p}] \in \mathbb{R}^{N_e \times N_p}$ represents the parameters that are actually being identified, which are after applying the operator $T_p^{\exp}(\cdot)$ transformed into the desired quantity $\boldsymbol{\Phi}$, i.e. the material parameters with an actual physical meaning. The idea is that individual components of $\boldsymbol{\Theta}$ can in essence acquire arbitrary values, but they remain positive after the transformation.

The *cap operator* T_c limiting the maximal step size is defined similarly for both operators T_p and T_p^{exp} and differs only in the choice of the cap $\bar{c}$.

$$T_c(\delta\phi_i) = \begin{cases} \operatorname{sign}(\delta\Phi_{ij}) \cdot \bar{c} & \text{if } |\delta\Phi_{ij}| > \bar{c}_j, \\ \delta\Phi_{ij} & \text{if } |\delta\Phi_{ij}| \leq \bar{c}_j, \end{cases} \quad \text{for} \quad \begin{matrix} i = 1, \dots, N_e, \\ j = 1, \dots, N_p, \end{matrix} \tag{3.38}$$

where the coefficient $\bar{c}_j$ is the maximum step size for the j-th parameter. In the numerical examples we set the coefficient to $\bar{c}_j = 0.5 \cdot \bar{\phi}_j$ for T_p and

$\bar{c}_j = 0.5$ for T_p^{exp}. The reason for different choice of the cap $\bar{c}$ for T_p and T_p^{exp} becomes apparent when analysing the behaviour of positivity operators. As long as the input of T_p stays positive it acts as an identity operator and therefore has the ability of preserving the properties of addition, i.e. with the assumption that a, $\delta a \in \mathbb{R}$ and $b \in \mathbb{R}_+$ one can simply omit the operator:

$$b = T_p(a + T_c(\delta a)) = a + T_c(\delta a). \tag{3.39}$$

As a result, one needs to provide the cap operator in T_p with a reference value to a, which is in our case represented by the arithmetic average of the individual identified field $\boldsymbol{\phi}_j$.

However in case of the exponential positivity operator T_p^{exp} the sum of a and δa is inseparable and takes the following form, see eq. (3.43)

$$b = T_p^{exp}(a + T_c(\delta a)) = T_p^{exp}(a) T_p^{exp}\left(T_c(\delta a)\right). \tag{3.40}$$

One can see that T_p^{exp} transforms addition into multiplication and therefore performs as a scaling operator which naturally incorporates the reference value a by its structure. Note also that in a region of small numbers that are equivalent to the chosen cap $\bar{c}$, the operator T_p^{exp} retains a relatively good linearity, see Fig. 1. In a sense of outcome after applying the particular choice of positivity operator, the cap $\bar{c}$ in both cases has virtually identical effect. In eq. (3.41) it restricts the change in a single iteration to 50% of the $\bar{\boldsymbol{\Phi}}_0$ and in eq. (3.42) the change is restricted to roughly 50% of the values in the last iteration $\boldsymbol{\Theta}_{k-1}$.

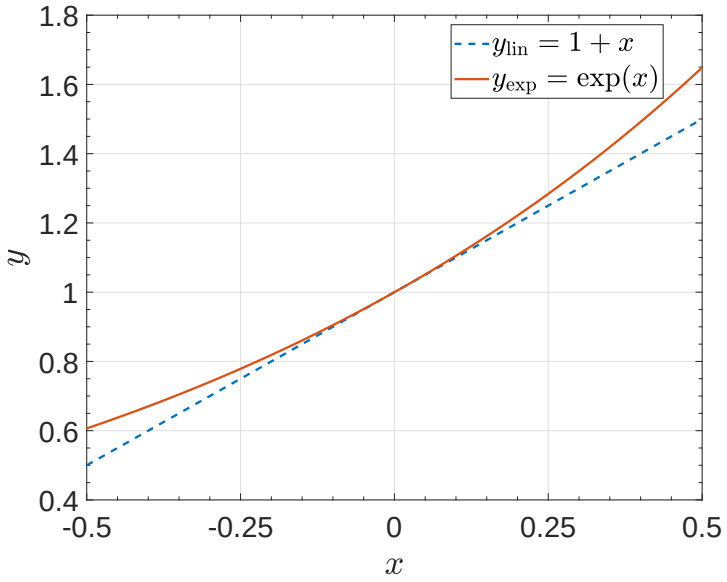

Figure 1: Deviation from linearity when using T_p^{exp} operator in one-dimensional case.

The modified Gauss-Newton iteration scheme for the first variant, after applying eq. (3.36) and eq. (3.38) to eq. (3.19), is expressed as

$$\boldsymbol{\Phi}_{k+1} = T_p\left(\boldsymbol{\Phi}_k + T_c\left(\delta\boldsymbol{\Phi}_k\right)\right). \tag{3.41}$$

In the second variant, it is desirable to separate the expert estimate from the identified parameter by adding a constant $\tilde{\boldsymbol{\Theta}}$ into the iteration scheme. Then, after applying eq. (3.37) and eq. (3.38) to eq. (3.19), the iteration scheme is of the following form

$$\boldsymbol{\Phi}_{k+1} = T_p^{exp}\left(\tilde{\boldsymbol{\Theta}} + \boldsymbol{\Theta}_k + T_c\left(\delta\boldsymbol{\Theta}_k\right)\right). \tag{3.42}$$

By abbreviating application of the cap operator to $\delta\boldsymbol{\Theta}_k^c = T_c\left(\delta\boldsymbol{\Theta}_k\right)$, one can expand the expression eq. (3.42) into the following form

$$\begin{aligned}
T_p^{exp}\left(\tilde{\boldsymbol{\Theta}} + \boldsymbol{\Theta}_k + \delta\boldsymbol{\Theta}_k^c\right) &= \exp\left(\tilde{\boldsymbol{\Theta}} + \boldsymbol{\Theta}_k + \delta\boldsymbol{\Theta}_k^c\right), \\
&= \exp(\tilde{\boldsymbol{\Theta}})\exp(\boldsymbol{\Theta}_k)\exp\left(\delta\boldsymbol{\Theta}_k^c\right), \\
&= \exp(\tilde{\boldsymbol{\Theta}})\exp\left(\delta\boldsymbol{\Theta}_k^c\right)\exp\left(\delta\boldsymbol{\Theta}_{k-1}^c\right)\ldots\exp\left(\delta\boldsymbol{\Theta}_0^c\right), \\
&= \boldsymbol{\Phi}_0\exp\left(\delta\boldsymbol{\Theta}_0^c\right)\exp\left(\delta\boldsymbol{\Theta}_1^c\right)\ldots\exp\left(\delta\boldsymbol{\Theta}_k^c\right), \\
&= \boldsymbol{\Phi}_0\prod_{i=0}^{k}\exp\left(\delta\boldsymbol{\Theta}_i^c\right) \approx \boldsymbol{\Phi}_0\prod_{i=0}^{k}\left(\mathbf{1} + \delta\boldsymbol{\Theta}_i^c\right),
\end{aligned} \tag{3.43}$$

where the initial expert estimate is contained in $\tilde{\boldsymbol{\Theta}} = \log\left(\boldsymbol{\Phi}_0\right) \in \mathbb{R}^{N_e \times N_p}$ and the iteration starts with $\boldsymbol{\Theta}_0 = \mathbf{0} \in \mathbb{R}^{N_e \times N_p}$. The expression on the last line then makes it possible to circumvent the additional non-linearity caused by the transformation of parameters in eq. (3.37) and possibly broaden the range $\bar{c}$ of the cap operator. However the linearisation is kept as an option for further improvement and is not implemented in this thesis. A key feature justifying particular choice of the transformation eq. (3.37) is utilised in multi-parameter models. Beside the apparent property of non-negativity, the transformation is beneficial when the parameters being identified are of different orders of magnitude, e.g. a thermal conductivity λ_s and volumetric capacity c_v which are for common building materials like concrete six orders of magnitude apart. In particular case the matrix being inverted in eq. (3.32) takes the following form

$$\mathbf{J}_k^T\mathbf{J}_k + \mathbf{R}(\boldsymbol{\kappa}_k) = \begin{bmatrix} \dfrac{\partial\mathbf{u}}{\partial\boldsymbol{\lambda}_s}^T\dfrac{\partial\mathbf{u}}{\partial\boldsymbol{\lambda}_s} & \dfrac{\partial\mathbf{u}}{\partial\boldsymbol{\lambda}_s}^T\dfrac{\partial\mathbf{u}}{\partial\boldsymbol{c}_v} \\ \dfrac{\partial\mathbf{u}}{\partial\boldsymbol{c}_v}^T\dfrac{\partial\mathbf{u}}{\partial\boldsymbol{\lambda}_s} & \dfrac{\partial\mathbf{u}}{\partial\boldsymbol{c}_v}^T\dfrac{\partial\mathbf{u}}{\partial\boldsymbol{c}_v} \end{bmatrix} + \begin{bmatrix} \kappa_{1,k}^2\mathbf{L}^T\mathbf{L} & \mathbf{0} \\ \mathbf{0} & \kappa_{2,k}^2\mathbf{L}^T\mathbf{L} \end{bmatrix} \tag{3.44}$$

where the block $\frac{\partial \mathbf{u}}{\partial \boldsymbol{\lambda}_s}^T \frac{\partial \mathbf{u}}{\partial \boldsymbol{\lambda}_s} \in \mathbb{R}^{N_e \times N_e}$ typically contains much larger numbers than $\frac{\partial \mathbf{u}}{\partial \boldsymbol{c}_v}^T \frac{\partial \mathbf{u}}{\partial \boldsymbol{c}_v} \in \mathbb{R}^{N_e \times N_e}$. This leads to ill-conditioning of the resulting matrix in eq. (3.44) and related numerical issues. On one hand this can be treated by varying κ_k, which emphasises the regularisation and disrupts the dependence between $\boldsymbol{\lambda}_s$ and $\boldsymbol{c}_v$. Another option is preconditioning which increases computational demands. Alternative workaround for this issue is the transformation T_p^{exp} that adjusts the proportions between individual parameters, which can be also understood as a mutual parameter normalisation. Mutual proportionality between parameters $[\boldsymbol{\theta}_1, \ldots, \boldsymbol{\theta}_{N_p}]$ during the iteration eq. (3.42) is then only affected by their spatial distribution and the initial estimate $\tilde{\boldsymbol{\Theta}}$. Another aspect that is not addressed by the transformation is the intrinsic insensitivity of the parameters to the model response, which can in turn also cause numerical problems.

Another way of improving the fidelity of the identified fields and also prevent the iterative algorithm in eq. (3.41) or eq. (3.42) from divergence can be achieved by the adoption of line-search method, which can be applied nearly seamlessly in accordance with the aforementioned techniques. This method is applicable whether the $\boldsymbol{\Theta}$ and $\boldsymbol{\Phi}$ is being identified. In our case, we proceed from the parameter set $\boldsymbol{\Phi}$. However, the resulting equations could also be derived directly for the transformed parameter set $\boldsymbol{\Theta}$. At the same time the method is not computationally demanding, requiring only a few evaluations of the objective function $f(\cdot)$, and hence the additional complexity is in most cases worth the effort.

Newton's method and its modifications generally determines both direction and the step size. Validity of the step size, however, goes only as far as the quadratic model in a given point $\boldsymbol{\Phi}_k$ accurately describes the underlying objective function $f(\cdot)$ from eq. (3.11). The basic principle of the line-search algorithm lies in adjusting the step size in a given descent direction $\delta\boldsymbol{\Phi}_k$ previously acquired by the Gauss-Newton method, i.e. it allows to stretch out or shorten the step size by a factor of $\beta \in \mathbb{R}$ in order to minimise the function $f(\cdot)$ along the given direction $\delta\boldsymbol{\Phi}_k$. This can be done by solving a one-dimensional minimisation problem in the following form

$$\beta_{\mathrm{k,min}} = \min_{\beta} f(\boldsymbol{\Phi}_k + \beta\delta\boldsymbol{\Phi}_k), \tag{3.45}$$

which can be solved by a minimisation algorithm of interest.

In our case we adopt a modification of the line-search algorithm allowing it not only to stretch out or shorten the step size by the factor of β, but also to deviate from the given direction $\delta\boldsymbol{\Phi}_k$. The necessity for altering the direction is caused by limitation of the quadratic approximation of the Newton's method for which not only the step size loses its validity, but also the

direction might deviate from the true solution as one moves away from the point $\mathbf{\Phi}_k$ in which the quadratic approximation was constructed. Correction of the direction is achieved by altering the step size for each individual parameter separately, i.e. we untie the mutual dependence between individual parameters $[\delta\boldsymbol{\phi}_1, \ldots, \delta\boldsymbol{\phi}_{N_p}]$, which was introduced by the off-diagonal blocks in eq. (3.44) and look for the step size factors $\beta_1, \ldots, \beta_{N_p}$ for each parameter, virtually modifying the overall direction of $\delta\mathbf{\Phi}_k$. This can be achieved by multiplying the descent direction $\delta\mathbf{\Phi}_k$ from right with a matrix $\boldsymbol{\beta} \in \mathbb{R}^{N_p \times N_p}$ containing the factors $\beta_1, \ldots, \beta_{N_p}$ on a diagonal, see eqs. (3.46) and (3.47).

$$\boldsymbol{\beta} = \begin{bmatrix} \beta_1 & 0 & \ldots & 0 \\ 0 & \beta_2 & \ldots & 0 \\ \vdots & \vdots & \ddots & \vdots \\ 0 & 0 & \ldots & \beta_{N_p} \end{bmatrix} \in \mathbb{R}^{N_p \times N_p}. \tag{3.46}$$

$$\begin{aligned} \delta\mathbf{\Phi}\boldsymbol{\beta} &= \begin{bmatrix} \delta\phi_{11} & \delta\phi_{12} & \ldots & \delta\phi_{1,N_p} \\ \delta\phi_{21} & \delta\phi_{22} & \ldots & \delta\phi_{2,N_p} \\ \vdots & \vdots & \ddots & \vdots \\ \delta\phi_{N_e,1} & \delta\phi_{N_e,2} & \ldots & \delta\phi_{N_e,N_p} \end{bmatrix} \begin{bmatrix} \beta_1 & 0 & \ldots & 0 \\ 0 & \beta_2 & \ldots & 0 \\ \vdots & \vdots & \ddots & \vdots \\ 0 & 0 & \ldots & \beta_{N_p} \end{bmatrix} \\ &= \begin{bmatrix} \beta_1\delta\boldsymbol{\phi}_1 & \ldots & \beta_{N_p}\delta\boldsymbol{\phi}_{N_p} \end{bmatrix}. \end{aligned} \tag{3.47}$$

As a result one needs to solve N_p dimensional minimisation problem given by the following formula

$$\boldsymbol{\beta}_{\min} = \min_{\beta_1,\ldots,\beta_{N_p}} f(\mathbf{\Phi} + \delta\mathbf{\Phi}\boldsymbol{\beta}), \tag{3.48}$$

which is still fairly tractable and computationally efficient. The minimisation problem is solved by means of a Newton's, Nelder-Mead method [81, 57] or a compass search [57] method.

Adopting the line-search algorithm in combination with the positivity operator T_p^{exp} requires to determine the true descent direction $\delta\mathbf{\Phi}$, which can be with the help of eq. (3.43) and eq. (3.19) expressed in the following way

$$
\begin{aligned}
\delta\boldsymbol{\Phi}_k &= \boldsymbol{\Phi}_{k+1} - \boldsymbol{\Phi}_k, \\
&= \exp\Big(\tilde{\boldsymbol{\Theta}} + \boldsymbol{\Theta}_k + T_c(\delta\boldsymbol{\Theta}_k)\Big) - \boldsymbol{\Phi}_k, \\
&= \exp\Big(\tilde{\boldsymbol{\Theta}} + \boldsymbol{\Theta}_k\Big)\exp\left(\delta\boldsymbol{\Theta}_k^c\right) - \boldsymbol{\Phi}_k, \\
&= \boldsymbol{\Phi}_k \exp\left(\delta\boldsymbol{\Theta}_k^c\right) - \boldsymbol{\Phi}_k, \\
&= \boldsymbol{\Phi}_k \left(\exp\left(\delta\boldsymbol{\Theta}_k^c\right) - 1\right),
\end{aligned}
\tag{3.49}
$$

where the term $T_c(\delta\boldsymbol{\Theta}_k)$ on the second line is for clarity abbreviated to $\delta\boldsymbol{\Theta}_k^c$. One can also notice that the expression on the last line attains negative values for $\delta\boldsymbol{\Theta}_k^c < 0$ and hence positivity of the parameter $\boldsymbol{\Phi}$ in a combination with some matrix $\boldsymbol{\beta}$ is not guaranteed any more. For this reason a regular positivity operator T_p is utilised and the final iterative scheme combining the positivity operator T_p^{exp} and the line-search algorithm is of the following form

$$
\begin{aligned}
\boldsymbol{\Phi}_{k+1} &= T_p\Big(\boldsymbol{\Phi}_k + \delta\boldsymbol{\Phi}_k\boldsymbol{\beta}_{\min}\Big), \\
&= T_p\Big(\boldsymbol{\Phi}_k + \boldsymbol{\Phi}_k\Big\{\exp\left(\delta\boldsymbol{\Theta}_k^c\right) - 1\Big\}\boldsymbol{\beta}_{\min}\Big), \\
&= T_p\Big(\boldsymbol{\Phi}_k\Big[1 + \Big\{\exp\left(\delta\boldsymbol{\Theta}_k^c\right) - 1\Big\}\boldsymbol{\beta}_{\min}\Big]\Big), \\
&= \boldsymbol{\Phi}_k T_p\Big(1 + \Big\{\exp\left(\delta\boldsymbol{\Theta}_k^c\right) - 1\Big\}\boldsymbol{\beta}_{\min}\Big),
\end{aligned}
\tag{3.50}
$$

where individual components $\beta_{1,\min}, \ldots, \beta_{N_p,\min}$ of the diagonal matrix $\boldsymbol{\beta}_{\min}$ (see eq. (3.47)) are obtained from the following minimisation problem

$$
\boldsymbol{\beta}_{\min} = \min_{\beta_1,\ldots,\beta_{N_p}} f\left(\boldsymbol{\Phi}_k T_p\Big(1 + \Big\{\exp\left(\delta\boldsymbol{\Theta}_k^c\right) - 1\Big\}\boldsymbol{\beta}\Big)\right). \tag{3.51}
$$

In order to keep the calculation efficient, the identification algorithm stops when the maximum number of iterations is reached or one of the following convergence criteria is satisfied

$$
\frac{\|\mathbf{u}_m - F(\boldsymbol{\Phi}_k)\|_2}{\|\mathbf{u}_m\|_2} \leq \varepsilon, \tag{3.52}
$$

$$
\frac{\|F(\boldsymbol{\Phi}_{k-1}) - F(\boldsymbol{\Phi}_k)\|_2}{\|F(\boldsymbol{\Phi}_k)\|_2} \leq \varepsilon, \tag{3.53}
$$

$$
\frac{\|\boldsymbol{\Phi}'_{k-1} - \boldsymbol{\Phi}'_k\|_2}{\|\boldsymbol{\Phi}'_k\|_2} \leq \varepsilon, \tag{3.54}
$$

where $\boldsymbol{\Phi}_k$ is the material field in the k-th iteration. The stopping conditions can be translated as follows: in eq. (3.52), one evaluates the relative error on

the measured error-less data with the model response. The second condition in eq. (3.53) says that if the relative change of the model response for two consecutive parameter field iterations does not change significantly, the first condition will probably not be met and the algorithm will stop. The last condition in eq. (3.54) is analogous to the previous one except that sufficient change on the identified parameters in between the iteration is required. From our experience we set the maximum number of iterations to 15 and the threshold error $\varepsilon = 5 \times 10^{-3}$.

3.3 Probabilistic methods

Although the models that are utilised in this thesis are not considered to be strictly random in nature, one can still benefit from recasting the deterministic problem into the stochastic one by treating the individual unknown parameters as random variables, i.e. reformulating the problem to a form of stochastic inference. The parameter randomness represents an extension to the traditional deterministic approach and can be viewed as the uncertainty to its true value expressed by the means of a probability distribution. Most often the stochastic inference is based on the notion of conditional probabilities which are exploited in the implementation of the Bayesian approach in a following form

$$p(\mathbf{m}|\mathbf{z}) = \frac{p(\mathbf{z}|\mathbf{m})}{p(\mathbf{z})} \cdot p(\mathbf{m}), \tag{3.55}$$

where solution is the *posterior* probability distribution $p(\mathbf{m}|\mathbf{z})$ of the unknown parameter $\mathbf{m}$ conditioned on the provided measurements $\mathbf{z}$, $p(\mathbf{z}|\mathbf{m})$ is the *likelihood*, i.e. the conditional probability of $\mathbf{z}$ assuming that $\mathbf{m}$ is given. The *evidence* $p(\mathbf{z})$ represents the probability of observing $\mathbf{z}$ and the *prior* $p(\mathbf{m})$ relates to what is known prior to observing the data $\mathbf{z}$ [75]. Once knowing the posterior density, one can obtain several forecasts of the unknown parameters by evaluating the point estimates, i.e. mean, median, maximum, etc.

Taking the mean estimate, one obtain a Minimum Mean Square Estimation (MMSE) enforcing the minimisation of the square norm of estimate error, i.e.

$$\tilde{\mathbf{m}}_{MS}(\mathbf{z}) = \arg\min_{\tilde{\mathbf{m}}} \mathbb{E}\left\{\|\mathbf{m} - \tilde{\mathbf{m}}(\mathbf{z})\|_2\right\}, \tag{3.56}$$

where an estimator $\tilde{\mathbf{m}}(\mathbf{z})$ of $\mathbf{m}$ is any function of the measurement $\mathbf{z}$. With the help of Bayesian cost method [76] the MMSE can be obtained as a con-

ditional expectation of $\mathbf{m}$ given the measurements $\mathbf{z}$, i.e. the estimator is given by the posterior mean of the parameter to be estimated.

$$\tilde{\mathbf{m}}_{MS} = \int_{-\infty}^{\infty} \mathbf{m} p(\mathbf{m}|\mathbf{z}) \mathrm{d}\mathbf{m} = \mathbb{E}\{\mathbf{m}|\mathbf{z}\} \tag{3.57}$$

In Maximum Likelihood Estimation (MLE) one is trying to find a set of parameters $\mathbf{m}_{MLE}(\mathbf{z})$ for given data $\mathbf{z}$ such that the maximum likelihood satisfy

$$p(\mathbf{z}|\mathbf{m}_{MLE}) \geq p(\mathbf{z}|\mathbf{m}), \tag{3.58}$$

i.e. $\mathbf{m}_{MLE}$ makes the observation $\mathbf{z}$ the most probable and maximises the likelihood function $p(\mathbf{z}|\mathbf{m})$ [113, 76].

In Maximum a Posteriori (MAP) an estimation is based on maximum of the posterior conditional density $p(\mathbf{m}|\mathbf{z})$ which is obtained by integrating conditional expectation which, especially for large parameter spaces, often make use of Monte Carlo (MC) methods, such as Markov chain Monte Carlo (MCMC). With Gaussian assumptions of prior and likelihood, the MAP estimator is identical to MMSE and ML.

3.4 The Bayesian inference

When identifying the thermal properties of a system one deals with a situation where the observable quantity, i.e. the temperature on the boundary, is measured and the goal is to find the corresponding model parameters $\boldsymbol{q} = [\boldsymbol{\lambda}_s^{\mathrm{T}}, \boldsymbol{c}_v^{\mathrm{T}}]$. In the Bayesian setting of parameter identification, the uncertainty in observations is combined together with prior expert knowledge about the parameter values for estimation of the so-called posterior probabilistic description of identified parameters together [34, 87]. To begin with a priori knowledge, both the thermal conductivities $\boldsymbol{\lambda}_s$ and volumetric heat capacities $\boldsymbol{c}_v$, cannot be negative in civil engineering problems; hence, lognormal distribution is more suitable for their description. Therefore, q_i is considered to be independent lognormally distributed with the probability density function

$$p_i(q_i) = \frac{1}{q_i \sqrt{2\pi\sigma_g^2}} \exp\left\{ -\frac{(\ln q_i - \mu_g)}{2\sigma_g^2} \right\}, \tag{3.59}$$

where parameters μ_g and σ_g are, respectively, the mean and standard deviation of the variable's natural logarithm. The joint prior density function is then defined as

$$p_q(\boldsymbol{q}) = \prod_{i=1}^{N_q} p_i(q_i)\,, \tag{3.60}$$

where N_q is the number of parameters.

The observations $\boldsymbol{z}$ differ from the modelled values $\boldsymbol{u}_r$ because of model imperfection and measurement error. Hence, $\boldsymbol{z} = \boldsymbol{u}_r + \boldsymbol{\varepsilon}$, where $\boldsymbol{\varepsilon}$ includes both of the aforementioned errors. To keep the presentation of different numerical aspects of particular methods clear and transparent, a quite common and simple case is assumed where modelling imperfections are neglected and measurement errors are modelled as zero-mean Gaussian random variables with the probability density function

$$p_j(\varepsilon_j) = \frac{1}{\sqrt{2\pi\sigma_\varepsilon^2}} \exp\left\{-\frac{\varepsilon_j^2}{2\sigma_\varepsilon^2}\right\}, \tag{3.61}$$

where σ_ε^2 is the measurement error variance. Assuming the measurement errors in particular observations to be independent, the likelihood function $L(\boldsymbol{q})$ is subsequently expressed, see [62], as

$$L(\boldsymbol{q}) = \prod_{j=1}^{N_\varepsilon} p_j(\varepsilon_j) = \prod_{j=1}^{N_\varepsilon} p_j(z_j - F_j(\boldsymbol{q}))\,. \tag{3.62}$$

where N_ε is the number of independent observations; in our case, $N_\varepsilon = m_n \cdot m_t$. The result of the probabilistic identification procedure comes with the posterior state of information given by the conjunction of the prior information and the information obtained from measurements, see [108], as

$$\pi(\boldsymbol{q}) = \varpi p_q(\boldsymbol{q}) L(\boldsymbol{q})\,, \tag{3.63}$$

where ϖ is a normalisation constant. The primary computational challenge in Bayesian inference is based on extracting information from the posterior density. Most estimates take the form of expectations w.r.t. the posterior. These expectations, mathematically integrals, may be numerically evaluated via asymptotic, deterministic, or sampling methods. Nowadays, Markov chain Monte Carlo (MCMC) methods remain the most general, flexible, and wide-spread techniques employed. To be more specific, the Metropolis-Hastings algorithm is the most common method for obtaining a sequence of random samples from a probability distribution, see [34]. The basic principle relies on performing a random walk, which would sample the prior probability distribution and then apply an appropriate probabilistic rule to accept or reject samples in order to obtain the resulting set of accepted walks sampling the posterior distribution, see [62].

3.4.1 Random field

In the area of numerical modelling of a heterogeneous material, the random field theory is a widely accepted methodology for describing the spatial

variability of material parameters. The definition of lognormal random field $q(\boldsymbol{x}, \omega)$ starts from the definition of Gaussian random field $g(\boldsymbol{x}, \omega)$, which is expressed by its mean

$$\mu_g(\boldsymbol{x}) = \mathbf{E}[g(\boldsymbol{x}, \omega)] = \int_\Sigma g(\boldsymbol{x}, \omega)\, \mathbf{P}(\mathrm{d}\omega) \tag{3.64}$$

and its covariance

$$\begin{aligned} C_g(\boldsymbol{x}, \boldsymbol{x}') &= \mathbf{E}[(g(\boldsymbol{x}, \omega) - \mu_g(\boldsymbol{x}))(g(\boldsymbol{x}', \omega) - \mu_g(\boldsymbol{x}'))] \\ &= \int_\Sigma (g(\boldsymbol{x}, \omega) - \mu_g(\boldsymbol{x}))(g(\boldsymbol{x}', \omega) - \mu_g(\boldsymbol{x}'))\, \mathbf{P}(\mathrm{d}\omega)\,, \end{aligned} \tag{3.65}$$

where Σ is a set of random elementary events ω together with a σ-algebra $\mathscr{S}$ to which a real number in the interval [0, 1] may be assigned, the probability of occurrence - mathematically a measure $\mathbf{P}$. Some non-Gaussian fields may be synthesised as non-linear functions of Gaussian fields [74, 88]. The lognormal random field $q(\boldsymbol{x}, \omega)$ is obtained as

$$q(\boldsymbol{x}, \omega) = \exp(g(\boldsymbol{x}, \omega))\,. \tag{3.66}$$

When the lognormal prior distribution is prescribed in terms of its mean μ_q and variance σ_q^2 instead of the mean μ_g and variance σ_g^2 of the variable's natural logarithm, then the latter moments can be then obtained from the former ones according to the following relations, see [88],

$$\sigma_g^2 = \ln\left(1 + \left(\frac{\sigma_q}{\mu_q}\right)^2\right), \quad \mu_g = \ln \mu_q - \frac{1}{2}\sigma_g^2\,. \tag{3.67}$$

The Karhunen-Loève expansion is an extremely useful tool representing the stochastic process as an infinite linear combination of orthogonal functions. Based on the spectral decomposition of covariance function $C_g(\boldsymbol{x}, \boldsymbol{x}')$ and the orthogonality of eigenfunctions ψ_i, the random field $g(\boldsymbol{x}, \omega)$ can be written as

$$g(\boldsymbol{x}, \omega) = \mu_g + \sigma_g \sum_{k=0}^{\infty} \sqrt{\varsigma_k}\xi_k(\omega)\psi_k(\boldsymbol{x}), \tag{3.68}$$

where $\boldsymbol{\xi}(\omega)$ is a set of standard i.i.d. random variables. Since the covariance $C_g(\boldsymbol{x}, \boldsymbol{x}')$ is symmetric and positive definite, it can be expanded in the series

$$C_g(\boldsymbol{x}, \boldsymbol{x}') = \sum_{k=1}^{\infty} \varsigma_k \psi_k(\boldsymbol{x})\psi_k(\boldsymbol{x}'). \tag{3.69}$$

However, computing the eigenfunctions analytically is usually not feasible. Therefore, one discretises the covariance spatially according to chosen

grid points (usually corresponding to nodes of finite element mesh) and the solution of the problem turns into the series of eigenvalues ς_k and eigenvectors $\boldsymbol{\psi}_k$. The Karhunen-Loève expansion $\hat{\boldsymbol{g}}(\omega)$ of random field $g(\boldsymbol{x}, \omega)$ is then expressed as

$$\hat{\boldsymbol{g}}(\omega) = \mu_g + \sigma_g \sum_{k=0}^{m} \sqrt{\varsigma_k} \xi_k(\omega) \boldsymbol{\psi}_k, \tag{3.70}$$

where the number m ($m \leq N_n$ in case of nodal discretisation) is chosen such that the above equation gives a good approximation, i.e. it captures a high proportion of the total variance. Higher values of m yield better descriptions of a random field, smaller values lead to more significant dimensionality reduction a computation acceleration. Taking into account a lognormal distribution of the parameters, the final formulation of the random field describing the parameter q_i then becomes

$$\hat{\boldsymbol{q}}_i(\omega) = \exp\left(\mu_g + \sigma_g \sum_{k=0}^{m} \sqrt{\varsigma_k} \xi_k(\omega) \boldsymbol{\psi}_k\right). \tag{3.71}$$

Note that the covariance and eigenvectors discretised to finite element nodes also provide nodal discretisation of parameter q_i, which needs to be further mapped into the centroids by means of finite element basis functions before applying eqs. (2.25) and (2.26).

It is obvious that the covariance function plays a key role in the construction of the random field. Therefore, from a group of commonly-used isotropic covariance functions the Matérn covariance function is introduced for two points separated by the distance $d = \|\boldsymbol{x} - \boldsymbol{x}'\|_2$ as

$$C(d) = \frac{2^{1-\nu}}{\Gamma(\nu)} \left(\sqrt{2\nu}\,\frac{d}{\rho}\right)^{\nu} K_\nu \left(\sqrt{2\nu}\,\frac{d}{\rho}\right), \tag{3.72}$$

where $\Gamma(\nu)$ is the gamma function, K_ν is the modified Bessel function of the second kind, and ρ and ν are non-negative parameters of the covariance. The parameter ρ represents a measure of how the correlation decreases with the distance d, and ν is the smoothness parameter, see [77]. As $\nu \to 1/2$, the Matérn covariance function turns into the exponential covariance function and another limit case is obtained for $\nu \to \infty$, where the function turns into the Gaussian covariance function. Note that the determination of correlation lengths is generally not obvious. However, in material modelling, one possible way to estimate the correlation length is to utilise image analysis as described in [70]. A numerical study for various numbers of eigenmodes m included in the Karhunen-Loève expansion is presented, for example, in [61].

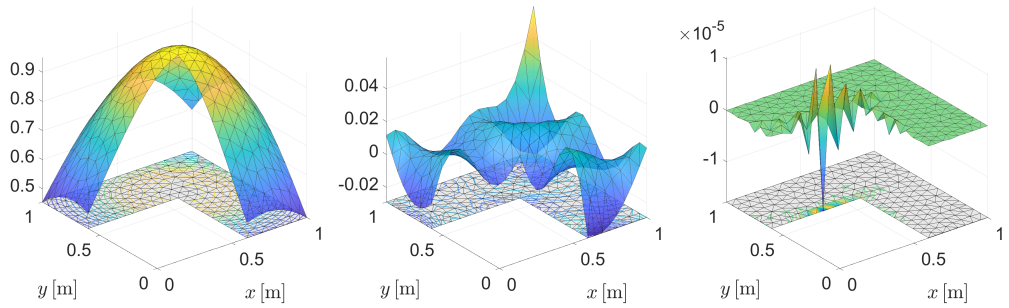

(a) (b) (c)

Figure 2: Eigenfunctions of the Matérn covariance function evaluated for $\rho = 0.25$ and $\nu = 5$: (a) $m = 1$; (b) $m = 20$; (c) $m = 216$.

For illustration, several eigenmodes computed with the help of eq. (3.72) for $\rho = 0.25$ and $\nu = 5$ are depicted in Fig. 2. One can see the low oscillation of the first eigenmode, while the last eigenmode clearly describes higher frequencies. It is worth mentioning that each eigenmode is weighted in the Karhunen-Loève expansion with a different eigenvalue, i.e. the influence of each subsequent eigenmode on a resulting random field has a decreasing tendency. This effect can be also seen in Fig. 3 which shows dimensionless random fields constructed for various numbers of eigenmodes. It is apparent from the reported figures that the last two random fields ($m = 20$ and $m = 216$) are visually similar.

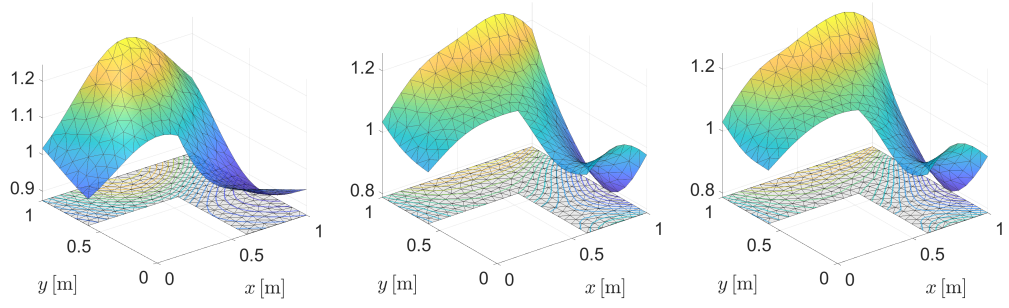

(a) (b) (c)

Figure 3: Dimensionless random fields constructed for (a) 5 eigenmodes; (b) 20 eigenmodes; (c) 216 eigenmodes.

4 Results

In this section we provide an insight into the performance of the proposed identification algorithms under various conditions, i.e. considering domains of different shapes, limited number of measurements and/or load conditions, partial data identification and distinct material properties. We first examine single-parameter models, i.e. EIT and GTM, utilising the most basic iterative scheme (see eq. (3.19)) of the Gauss-Newton regularised method. The results obtained for EIT and GTM are of illustrative nature and the emphasis is put on the transient model, where we also treat individual influences causing a potential solver instability. Although it is virtually impossible to accurately describe particular phenomena, we resort to a set of examples for each case in order to cover the particular issue as broadly as possible. However, separation of individual issues will inevitably lead us to deliberately commit an *inverse crime*, see [28, 44, 68], in order to eliminate most of the other influences that are not part of the phenomenon being investigated. Due to the ill-posed nature of the problem it is expected that distinct approaches and modifications of the identification algorithm will fail in certain situations where the others might excel and vice versa. For this reason we distinguish several possible causes leading to increased error or identification algorithm failure. For each cause we set up multiple scenarios, which will be used as a diagnostic procedure for the algorithm performance.

All measurements, i.e. $\mathbf{V}_m$ for EIT or $\mathbf{u}_m$ for rest of the models, in the following examples are obtained from synthetic computer generated experiments utilising either the same or more accurate finite element mesh than the one used in the identification process. For this purpose, we need to generate a $\boldsymbol{\Phi}_{\text{true}}$, i.e. a spatial distribution of true parameter fields. Note that we do not utilise distributions that correspond to a real building material. In most cases we deliberately choose fields that are either difficult to identify or that have specific properties, e.g. omni-directional variations in space, clearly defined inclusions, fluctuations with a certain frequency or non-differentiability. Their mathematical formulations evaluated on corresponding domains are shown in appendix A.

In sections 4.3.3 and 4.3.2 we also perform computations based on different modifications of the identification algorithms presented in Sec. 3. Distinct approaches are distinguished as follows

Abbreviation	Method description
basic	Iteration scheme with positivity operator T_p and cap operator T_c, see eq. (3.41).
Θ	Iteration scheme with positivity operator $T_p^{\exp}$ and cap operator T_c, see eq. (3.42).
Θ_0 $\Theta_{0,NM}$ $\Theta_{0,C}$	Iteration scheme with positivity operator $T_p^{\exp}$ and cap operator T_c, see eq. (3.42). In this case, prior to the Gauss-Newton iteration a constant field $\tilde{\boldsymbol{\Theta}}$ is being searched by means of a Nelder-Mead (NM), compass (C) or Newton's ( ) method.
LS^1 LS^1_{NM} LS^1_C	Iteration scheme with positivity operator $T_p^{\exp}$ and cap operator T_c, see eq. (3.42). In this case a line-search algorithm is applied in the form of eq. (3.45), where one looks for a single scaling constant β in order to scale the actual update direction $\delta\boldsymbol{\Theta}_k$, and is solved by means of a Nelder-Mead (NM), compass (C) or Newton's ( ) method.
LS^2 LS^2_{NM} LS^2_C	Iteration scheme with positivity operator $T_p^{\exp}$ and cap operator T_c, see eq. (3.42). In this case a line-search algorithm is applied in the form of eq. (3.48), where one looks for a multiple scaling constants $\boldsymbol{\beta}$ in order to scale the actual update direction $\delta\boldsymbol{\Theta}_k$, and is solved by means of a Nelder-Mead (NM), compass (C) or Newton's ( ) method.
LS^2_0 $LS^2_{0,NM}$ $LS^2_{0,C}$	Iteration scheme with positivity operator $T_p^{\exp}$ and cap operator T_c, see eq. (3.42). Prior to the Gauss-Newton iteration a constant field $\tilde{\boldsymbol{\Theta}}$ is being searched by means of a Nelder-Mead (NM), compass (C) or Newton's ( ) method. In addition to this a line-search algorithm is applied in the form of eq. (3.48), where one looks for a multiple scaling constants $\boldsymbol{\beta}$ in order to scale the actual update direction $\delta\boldsymbol{\Theta}_k$, and is solved by means of a Nelder-Mead (NM), compass (C) or Newton's ( ) method.
$LSH^2_{0,NM}$	Iteration scheme with positivity operator $T_p^{\exp}$ and cap operator T_c, see eq. (3.42). Prior to the Gauss-Newton iteration a constant field $\tilde{\boldsymbol{\Theta}}$ is being searched by means of a Nelder-Mead (NM) method. In addition to this a line-search algorithm is applied in the form of eq. (3.48), where one looks for a multiple scaling constants $\boldsymbol{\beta}$ in order to scale the actual update direction $\delta\boldsymbol{\Theta}_k$, and is solved by means of a Nelder-Mead (NM) method. On top of this, the hyper-parameter $\boldsymbol{\kappa}$ in each iteration is being searched by means of a Nelder-Mead method.

Table 1: Method abbreviations with description.

4.1 Electrical Impedance Tomography

In foregoing examples, we assume the classical settings of CEM model, where the electrode impedance, applied currents and domain dimensions with electrode placement, see Fig. 4 and Fig. 7, are known. In the first case, we study the reconstruction algorithm performance for limited number of electrodes with a smooth (Fig. 5) and a non-differentiable (Fig. 6) true parameter field.

The identification algorithm performance is evaluated for two error measures. Since we perform only synthetic experimental measurements and the true parameter field $\boldsymbol{\sigma}_{\text{true}} \in \mathbb{R}^{N_e}$ is actually known, one can evaluate the error between the output of the identification algorithm, i.e. $\boldsymbol{\sigma}_{\text{rec}} \in \mathbb{R}^{N_e}$, and the true parameter field in the following way

$$\varepsilon_\sigma = \frac{\|\boldsymbol{\sigma}_{\text{rec}} - \boldsymbol{\sigma}_{\text{true}}\|_2}{\|\boldsymbol{\sigma}_{\text{true}}\|_2}, \tag{4.1}$$

However, in real conditions the true parameter field is not known and the only quantity one can manipulate with is the difference between experimental measurements $\mathbf{v}_m \in \mathbb{R}^{m_s \cdot (m_s - 1)}$ and the model output $\mathbf{V} = F(\boldsymbol{\sigma}_{\text{rec}}) \in \mathbb{R}^{m_s \cdot (m_s - 1)}$. The error on measured quantity is denoted as ε_V and is of the following form

$$\varepsilon_V = \frac{\|\mathbf{V}_{\text{rec}} - \mathbf{v}_m\|_2}{\|\mathbf{v}_m\|_2}, \tag{4.2}$$

where $\mathbf{V}_{\text{rec}}$ is a vectorised form of the forward operator in eq. (2.3).

All examples consider the same electrode properties, i.e. the impedance z_s and applied current C (see eq. (2.2)), which are set in the following way

$$\begin{aligned} &z_s = 1, \text{ for } s = 1, \ldots, m_s, \\ &C = 1. \end{aligned} \tag{4.3}$$

The first set of examples comprises results assuming the L-shaped domain (see Fig. 4), which represents a part of the building construction, where one is interested in examining the electrical conductivity in the body. The domain is divided into $N_e = 360$ finite elements with $N_n = 216$ nodes. As a result one needs to identify 360 conductivity coefficients assorted in a vector $\boldsymbol{\Phi} = \boldsymbol{\sigma} \in \mathbb{R}^{360}$.

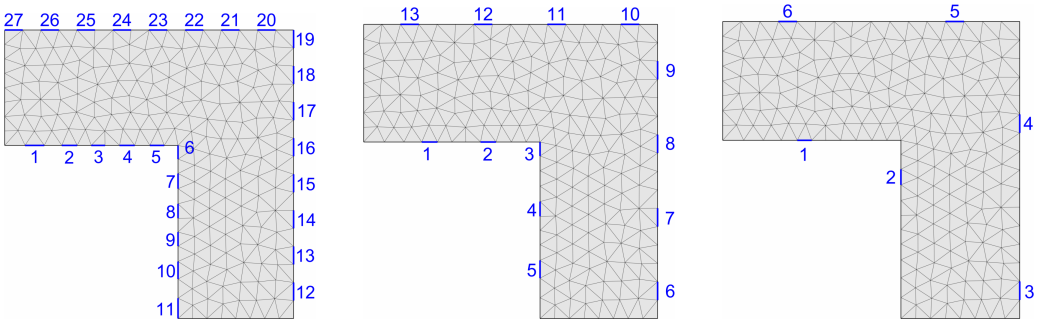

(a) $m_s = 27$ (b) $m_s = 13$ (c) $m_s = 6$

Figure 4: Domain electrode setups with electrodes denoted by blue lines.

The first set of examples comprises results for the field with smooth transitions. The identified fields corresponding to the given electrode setup in Fig. 4a to 4c are shown in the following figures

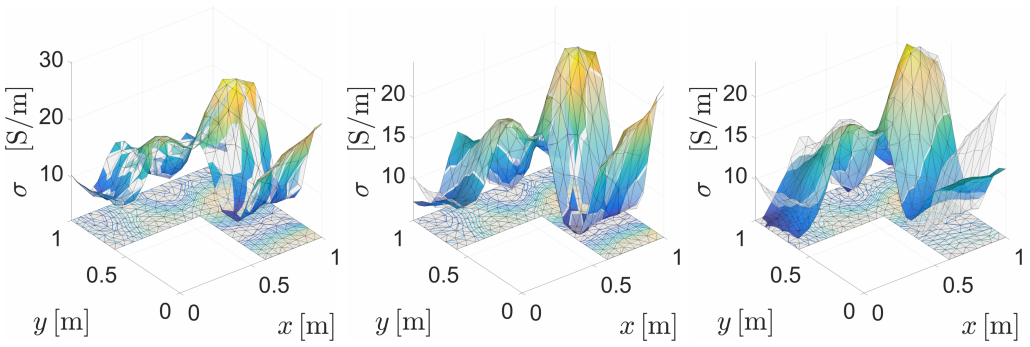

(a)
$\varepsilon_\sigma = 0.0117$,
$\varepsilon_V = 1.63 \times 10^{-7}$

(b)
$\varepsilon_\sigma = 0.0387$,
$\varepsilon_V = 6.25 \times 10^{-7}$

(c)
$\varepsilon_\sigma = 0.1658$,
$\varepsilon_V = 1.59 \times 10^{-7}$

Figure 5: Identified parameter fields with smooth material field (a) $m_s = 27$, (b) $m_s = 13$, (c) $m_s = 6$ electrodes. In colour: σ_{rec}, in transparent: σ_{true}.

In Fig. 5a, one can notice a very close match between the true and identified parameter field even though two parts of the boundary were not fitted with electrodes. However, quality of the identification deteriorates rapidly with decreasing number of electrodes. The mismatch between the true and the identified field appears not only in areas where electrodes are not physically located, but also in the places with faster parameter changes. The capability of capturing faster fluctuations therefore decreases with the number of electrodes, as can be observed in the case of identifying the non-differentiable field in the following figures

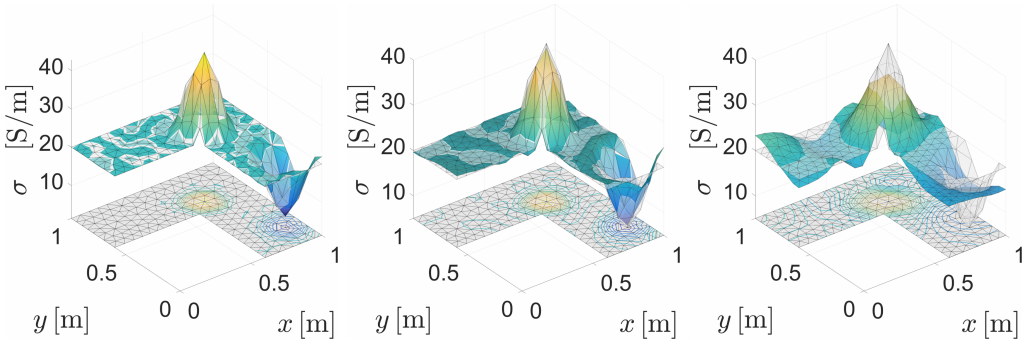

(a) $\varepsilon_\sigma = 0.0315$, $\varepsilon_V = 7.98 \times 10^{-7}$

(b) $\varepsilon_\sigma = 0.054$, $\varepsilon_V = 6.19 \times 10^{-8}$

(c) $\varepsilon_\sigma = 0.1608$, $\varepsilon_V = 2.71 \times 10^{-7}$

Figure 6: Identified parameter fields with non-differentiable material field (a) $m_s = 27$, (b) $m_s = 13$, (c) $m_s = 6$ electrodes. In colour: σ_{rec}, in transparent: σ_{true}.

In comparison to the smooth material field Fig. 5, one can notice that the identification process for non-differentiable field in Fig. 6 suffers from insufficiency of data, i.e. non-differentiability and sharp transitions in the material field raise a need for more data in order to achieve the same precision in terms of the error ε_σ. In our case, this is mainly caused by the chosen solver, which favours smooth solutions and even with a lot of data it tends to round up the identified fields. One can also notice the error ε_σ in case of $m_s = 6$ electrodes is lower for non-differentiable field. This is due to fact, that the field in Fig. 6c is mostly constant, which is in general not problematic to identify and the error is mostly concentrated in the region of the spikes, whereas the field in Fig. 5c contains various frequency fluctuations and the error on the identified field is more evenly distributed in the domain. However, in both cases the identification deviates from the true solution most on the edges where no electrode is present.

A different set of benchmark examples is dealing with material inclusions (Fig. 7a), partial data reconstruction (Fig. 7b) and a combination of both (Fig. 7c). In the case of Fig. 7a, the domain is a circle with radius of $r = 0.5\,\text{m}$ divided into $N_e = 574$ finite elements with $N_n = 318$ nodes and comprises $m_s = 8$ mostly evenly distributed electrodes. As one can see from Fig. 8, results for the circular domain are reaching the lowest error of $\varepsilon_\sigma = 0.0569$ from the given example set. This is due to utilisation of sufficient amount of electrodes which are conveniently placed all over the domain boundary. However, it is noticeable that the spatial distribution of error is accumulated in the close neighbourhood of the inclusions similarly to the previous example

shown in Fig. 6.

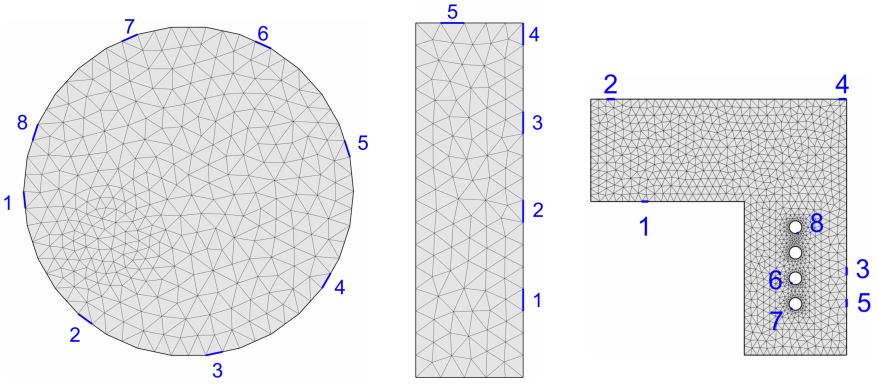

(a) $N_e = 574$, $N_n = 318$

(b) $N_e = 194$, $N_n = 119$

(c) $N_e = 926$, $N_n = 536$

Figure 7: Domain set with limited number of electrodes.

The example in Fig. 7b is a rectangle of sides 0.3 m and 1 m representing a wall section, where an electrode on some parts of the boundary can not be placed. It is divided into $N_e = 194$ finite elements, $N_n = 119$ nodes and comprises $m_s = 5$ electrodes distributed only on the right and top boundaries, while the rest of the boundary is assumed to be inaccessible. The resulting identified field is shown in Fig. 8b and one can see it noticeably suffers from data insufficiency with an error reaching a value of $\varepsilon_\sigma = 0.379$, making the identification useless in terms of the description accuracy of the underlying true parameter field. The identification algorithm is only controlled by difference of electrode potentials $\mathbf{V}_s - \mathbf{W}_s$[16]. In this example error on the observed quantity is very low at $\varepsilon_V = 3.05 \times 10^{-7}$, which is still much higher than in Fig. 8a or Fig. 8c, but for practical purposes the error is under the resolution of measuring devices. It is apparent that the parameter field in region close to the boundary with no electrodes has little to no influence on the electrode potentials $\mathbf{V}_s$ and therefore can acquire nearly arbitrary values. Nonetheless this example shows that one can not expect the identification to perform well in regions where electrodes are missing and/or are distant from parts of the boundary with electrodes, but for given electrode setup there exist multiple compliant fields for which the error on electrode potentials is almost zero.

[16]In our case $\mathbf{V}_s$ represents the model response and $\mathbf{W}_s$ represents the error-less data from a synthetic experiment.

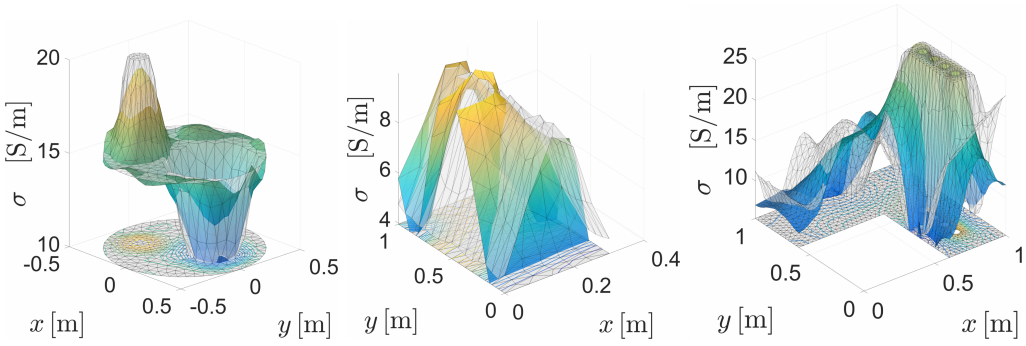

(a)
$\varepsilon_\sigma = 0.0569$,
$\varepsilon_V = 7.49 \times 10^{-10}$

(b)
$\varepsilon_\sigma = 0.379$,
$\varepsilon_V = 3.05 \times 10^{-7}$

(c)
$\varepsilon_\sigma = 0.187$,
$\varepsilon_V = 6.75 \times 10^{-8}$

Figure 8: Parameter field identification for various material fields and domain shapes. In colour: σ_{rec}, in transparent: σ_{true}.

The last example shown in Fig. 7c represents a more complex geometry combining partial data identification with non-smooth parameter field transitions. The domain is divided into $N_e = 926$ finite elements, $N_n = 536$ nodes and there are in total $m_s = 8$ electrodes. Overall, the result in Fig. 8c duplicates the experience from previous examples. For instance in the area of electrodes number 1, 2 and 4 the identified field accuracy deteriorates due to insufficiency of data and the resulting field is smoothed out, whereas in the region surrounded by electrodes number 6, 7 and 8 the parameter field is identified sufficiently well.

4.2 General Transport Model

The following model could be already employed in civil engineering as it solves the stationary heat transfer in the construction. It is based on the same diffusion equation as in the CEM with modified boundary conditions. In our settings, heaters only serve to excite different boundary conditions and do not collect any kind of data. This makes it more clear when it comes to studying the influence of incompleteness of measurements and the effect of sensor distribution on the boundary $\partial\Omega$. We put emphasis on the obstacles arising in civil engineering problems such as a limited number of measurement nodes on the boundary, reduced number of heaters and/or discontinuous or non-differentiable material fields.

The m_n measurement nodes representing the boundary Γ_m are labelled by red asterisks, see for example Figs. 9, 16 and 12a. In each of the following examples we consider one observation of Γ_m for each of the m_h different heaters.

The collection of error-less data, i.e. the vector $\mathbf{u}_m = F(\boldsymbol{\lambda}_{s,\text{true}}) \in \mathbb{R}^{m_n \cdot m_h}$ in eq. (3.7), is assumed to be conducted by a thermal camera and/or by an array of discrete thermometers with an appropriate interpolation providing continuous surface data. The first iteration starts with a spatially uniform thermal conductivity $\lambda_s = 1\,[\,\mathrm{W} \cdot \mathrm{m}^{-1} \cdot \mathrm{K}^{-1}\,]$.

Similarly to the previous model, we evaluate an error on the identified field, i.e. ε_{λ_s}, in the following way

$$\varepsilon_{\lambda_s} = \frac{\|\boldsymbol{\lambda}_{s,\text{rec}} - \boldsymbol{\lambda}_{s,\text{true}}\|_2}{\|\boldsymbol{\lambda}_{s,\text{true}}\|_2}, \tag{4.4}$$

where $\boldsymbol{\lambda}_{s,\text{rec}} \in \mathbb{R}^{N_e}$ is the identified conductivity field obtained from the simplest iterative formula in eq. (3.19). The error on temperature takes the following form

$$\varepsilon_u = \frac{\|\mathbf{u}_r - \mathbf{u}_m\|_2}{\|\mathbf{u}_m\|_2}, \tag{4.5}$$

where $\mathbf{u}_r \in \mathbb{R}^{m_n \cdot m_h}$ is output of the forward operator (see eq. (2.11)) for given conductivity field $\boldsymbol{\lambda}_{s,\text{rec}}$. Note that the error is evaluated only for the observed quantity $u|_{\Gamma_m}$, i.e. it does not take into account temperatures on the whole boundary $\partial\Omega$ or in the domain Ω.

The heater properties in the next example are set in the following way

$$\begin{aligned} r_h &= 0.01, \\ T_h &= 10, \text{ for } h = 1, \ldots, m_h. \end{aligned} \tag{4.6}$$

In the first set of examples with domain, measurements and the placement of heaters shown in Fig. 9, we assume the following boundary conditions

$$\begin{aligned} \lambda_s \frac{\partial u}{\partial n}(x)|_{\partial\Omega_1} &= 10 \cdot (u(x) - 30)\,, \\ \lambda_s \frac{\partial u}{\partial n}(x)|_{\partial\Omega_2} &= 10 \cdot (u(x) - 15)\,, \\ \lambda_s \frac{\partial u}{\partial n}(x)|_{\partial\Omega_3} &= 0, \end{aligned} \tag{4.7}$$

where the boundary $\partial\Omega_2$ belongs to the outer corner and $\partial\Omega_1$ belongs to the inner corner of the L-shaped domain in Fig. 9. The transfer boundary condition, i.e. the third line in eq. (2.9), is defined on $\partial\Omega_T = \partial\Omega_1 \cup \partial\Omega_2$ and zero flux, which corresponds to the second line in eq. (2.9), is defined on rest of the free boundary $\partial\Omega_3 = \partial\Omega \backslash \partial\Omega_T$.

The following examples are configured in such a way to verify the performance and stability when the model is subjected to substantially constrained measurements with two different material fields. In Fig. 9 the observed boundaries are emphasised with red asterisks, whereas heaters are displayed as blue lines. There are only $m_h = 2$ heaters, resulting into two distinct loading states and therefore only two measurements along the boundary Γ_m are collected. The total number of measured values for each experiment in Fig. 9 is equal to $m_h m_n = 2m_n$ numbers. Corresponding results for smooth and non-differentiable material fields are shown in Fig. 10 and Fig. 11, respectively.

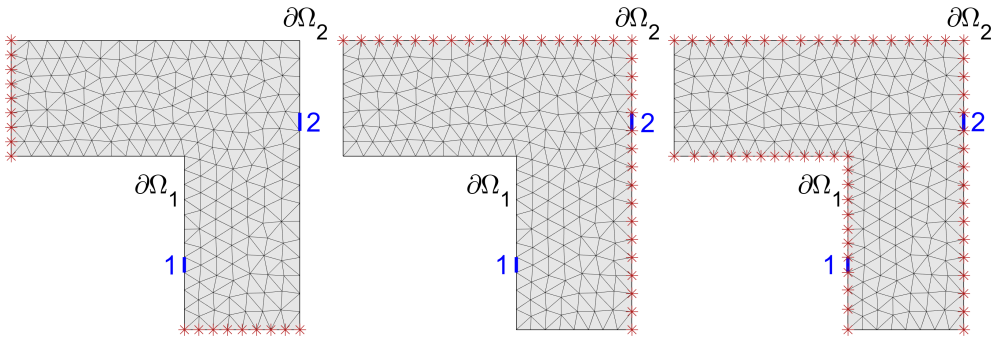

(a) $m_n = 18$ (b) $m_n = 33$ (c) $m_n = 54$

Figure 9: L-shaped domain discretised into $N_e = 360$ finite elements and $N_n = 216$ nodes. The two heaters are denoted by blue lines and observed boundaries by red asterisks.

Regardless of what kind of the material field is identified, numerical experiments are performed without any additional error included in the calculation and the identification procedure is executed with an identical finite element mesh discretisation as in the case of the synthetic experiment. The free boundary that could be subjected to measurements comprises in total $N_b = 70$ nodes and the percentage representation of free boundary subjected to measurement in experiments Fig. 9a to 9c is therefore 25.7%, 47.1% and 77.1%, respectively.

The first example (see Fig. 9a) is deliberately set to be extremely difficult for the identification procedure as only 25.7% of the boundary included in the measurements is located along the sides $\partial\Omega_3$. This overall counts $m_h m_n = 2 \cdot 18 = 36$ measurement numbers. In the resulting field (see Fig. 10a), one can notice a previously observed phenomenon, that the area in a close surrounding of the observed boundary is tightened closer to the true values.

This is due to higher sensitivity of the parameters to the system response around the measured boundary. The identified parameter field in the area of the corner is, however, not even close to the true spatial distribution.

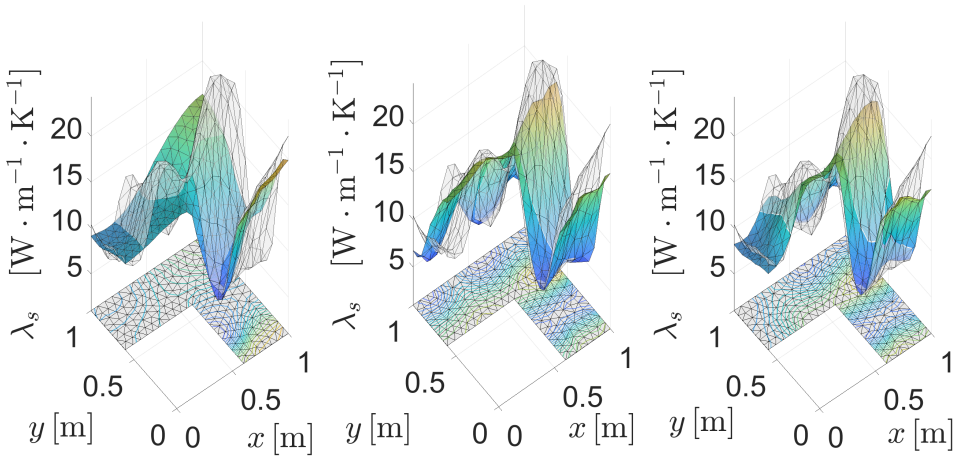

(a)
$\varepsilon_{\lambda_s} = 0.3747$,
$\varepsilon_u = 3 \times 10^{-4}$

(b)
$\varepsilon_{\lambda_s} = 0.1836$,
$\varepsilon_u = 9 \times 10^{-4}$

(c)
$\varepsilon_{\lambda_s} = 0.1506$,
$\varepsilon_u = 23 \times 10^{-4}$

Figure 10: Identified material fields for smooth field. In colour: $\lambda_{s,\text{rec}}$, in transparent: $\lambda_{s,\text{true}}$.

The most interesting result is that there is visually almost no difference between Fig. 10c and Fig. 10b although the latter employs nearly half the measurement nodes and the information about the temperature on $\partial\Omega_1$ is completely missing. The difference is most apparent on the left side of the inner corner, where in the case of Fig. 10c, the additional measurements at the boundary $\partial\Omega_1$ do not allow for higher deviations from the true distribution of the field.

Similar conclusions can be made from observing the results shown in Fig. 11 for non-differentiable fields. One can notice that both errors, i.e. ε_{λ_s} and ε_u, are in comparison to Fig. 10 lower in each case. This is due to the constant distribution of the true field on the left side of the structure, which is generally easier to identify. However, one can notice a significant deterioration in the area of the spikes.

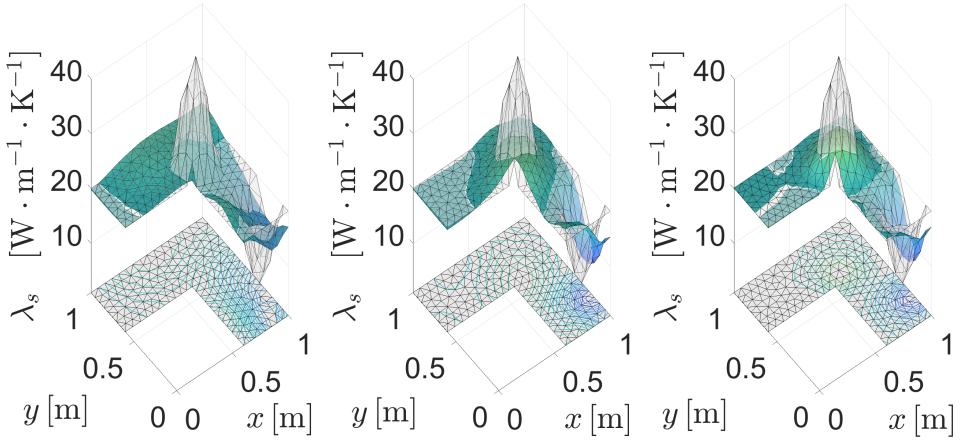

(a) $\varepsilon_{\lambda_s} = 0.2110$, $\varepsilon_u = 1 \times 10^{-4}$

(b) $\varepsilon_{\lambda_s} = 0.1674$, $\varepsilon_u = 3 \times 10^{-4}$

(c) $\varepsilon_{\lambda_s} = 0.1427$, $\varepsilon_u = 4 \times 10^{-4}$

Figure 11: Identified material fields for non-differentiable field. In colour: $\lambda_{s,\text{rec}}$, in transparent: $\lambda_{s,\text{true}}$.

Another interesting phenomenon is that, although with increasing number of measurements the error on the identified field ε_{λ_s} decreases, the error on the monitored quantity ε_u increases, which can be observed on both set of results in Fig. 10 and Fig. 11. This can be explained by the following considerations. For example, if only one point on the domain is observed, then there exist many field realisations for which the error on the monitored temperature ε_u is small and the identification algorithm simply falls into one of the closest local minima, which is not necessarily the true parameter field. On the other hand, when all points on the boundary are observed, the range of possible field realisations is narrowed because the wider area of the domain to which the measurements are sensitive is covered. As a result, one can get possibly closer to the true parameter field with a narrower set of possible realisations. However, as there are infinitely many field realisations that lead to better solutions[17], one is not guaranteed to always perform better with higher number of measurements[18]. This claim can be supported by the following example, in which we take the same amount of measurement nodes as we do in the case of Fig. 9a, i.e. $m_n = 18$, but the measurement nodes are distributed more uniformly on the boundary, see Fig. 12a.

[17]The set of possible realisations always includes the true solution.

[18]The variables influencing the overall quality of the identified field consist from the choice of solver, number and placement of measurement nodes, initial value for the identified field, domain geometry, etc.

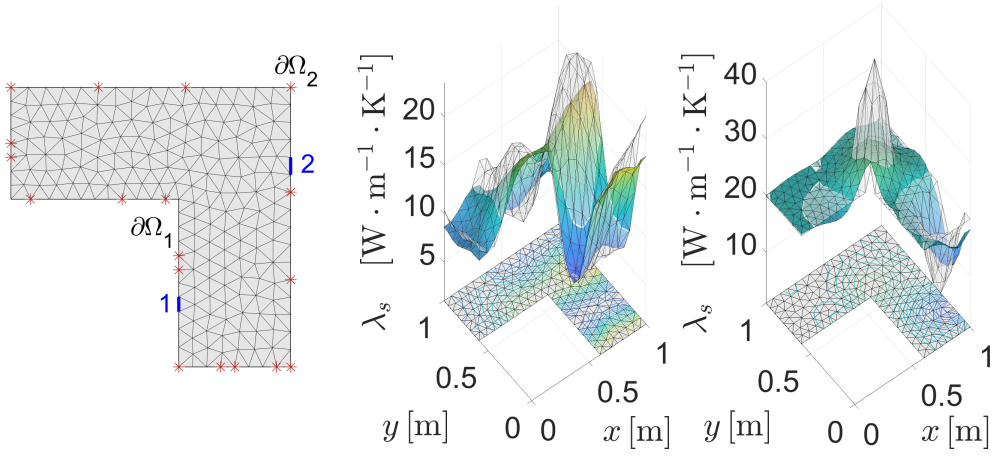

(a) $m_n = 18$

(b) $\varepsilon_{\lambda_s} = 0.1539$, $\varepsilon_u = 15 \times 10^{-4}$

(c) $\varepsilon_{\lambda_s} = 0.1599$, $\varepsilon_u = 2 \times 10^{-4}$

Figure 12: Distribution of the measurement nodes and heaters (a) and the identified material fields for smooth (b) and non-differentiable (c) material field. In colour: $\lambda_{s,\text{rec}}$, in transparent: $\lambda_{s,\text{true}}$.

Overall, it can be inferred from results above that error on the identified field ε_{λ_s} decreases with higher number of measurement nodes. However, it depends on other parameters such as the distribution of measurement nodes along the boundary, number and distribution of heaters or the shape of the field being identified, i.e. the rate of fluctuations. The error on temperature ε_u is also dependent on multiple factors, where one effect is the mutual distance between individual measurement nodes. In case the measurement nodes are grouped at a specific location, the overall error ε_u tends to be lower and vice versa. This is because the temperatures in points to that are geometrically close together have nearly the same temperature, no matter what the underlying conductivity λ_s is[19]. It can be accounted to the smoothing effect of the governing equation in eq. (2.9). An example of this phenomenon is the difference between results shown in Fig. 10a and Fig. 12b or Fig. 11a and Fig. 12c, where the number of measurement nodes, placement of heaters, domain and boundary conditions are the same and the only difference is in the placement of measurement nodes, which are in case of Fig. 12 further apart. In this example, despite having better fit on the identified parameter, i.e. lower error of ε_{λ_s}, one can notice higher error on the temperature ε_u.

Another set of examples comprises a partial data reconstruction on a circular shape domain with two inclusions (see Fig. 13a), a directionally

[19]The major difference is observable in heat fluxes, which are calculated as $\lambda_s \frac{\partial u}{\partial x}$.

biased partial data identification (see Fig. 13b) and a more complex geometry (see Fig. 13c). In case of the circular domain in Fig. 13a, we consider the following boundary conditions

$$\begin{aligned} \lambda_s \frac{\partial u}{\partial n}(x)|_{\partial\Omega_1} &= \ 10 \cdot (u(x) - 30)\,, \\ \lambda_s \frac{\partial u}{\partial n}(x)|_{\partial\Omega_2} &= \ 10 \cdot (u(x) - 15)\,, \end{aligned} \tag{4.8}$$

where $\partial\Omega = \partial\Omega_T = \partial\Omega_1 \cup \partial\Omega_2$. The part $\partial\Omega$ coincide with the observed boundary Γ_m and contains $m_n = 26$ nodes out of $N_b = 60$, which means that 43.3% of the whole boundary is being observed. Radius of the domain is set to $r = 0.5\,m$ and contains two material inclusions of a circular shape which are highlighted with a bold outline. Radius of the small inclusion is set to $r_1 = 0.1\,m$, whereas the second inclusion has a radius of $r_2 = 0.2\,m$.

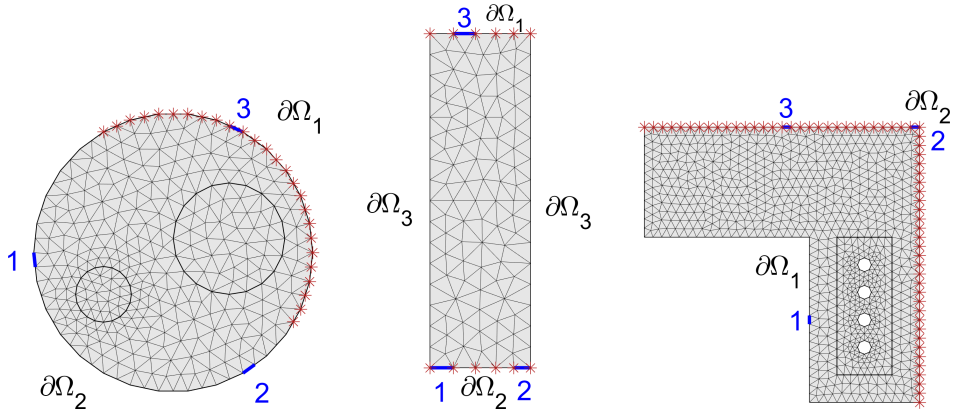

(a) $N_e = 574$, $N_n = 318$

(b) $N_e = 190$, $N_n = 117$

(c) $N_e = 926$, $N_n = 536$

Figure 13: Domain set with three heaters (blue) and observed boundaries (red).

In Fig. 14a one can notice that combination of particular domain shape with a choice of measurement nodes can be of critical importance. Even though approximately 43% of boundary is observed, the smaller material inclusion could not be fully recovered and is smoothed out, whereas the larger inclusion is identified sufficiently well. This is, however, not because of the size of inclusion, but rather because the larger inclusion is closer and more surrounded by the measuring points.

In case of the long wall and L-shaped domain in Fig. 13b and 13c the boundary conditions for both examples are set in the following way

$$
\begin{aligned}
\lambda_s \frac{\partial u}{\partial n}(x)|_{\partial\Omega_1} &= 10 \cdot (u(x) - 30)\,, \\
\lambda_s \frac{\partial u}{\partial n}(x)|_{\partial\Omega_2} &= 10 \cdot (u(x) - 15)\,, \\
\lambda_s \frac{\partial u}{\partial n}(x)|_{\partial\Omega_3} &= 0,
\end{aligned}
\tag{4.9}
$$

where the transfer boundary condition is defined on $\partial\Omega_T = \partial\Omega_1 \cup \partial\Omega_2$, whereas zero heat flux is defined on $\partial\Omega_3$. In case of the L-shaped domain part of the boundary $\partial\Omega_3$ is defined as follows $\partial\Omega_3 = \partial\Omega \backslash \partial\Omega_T$.

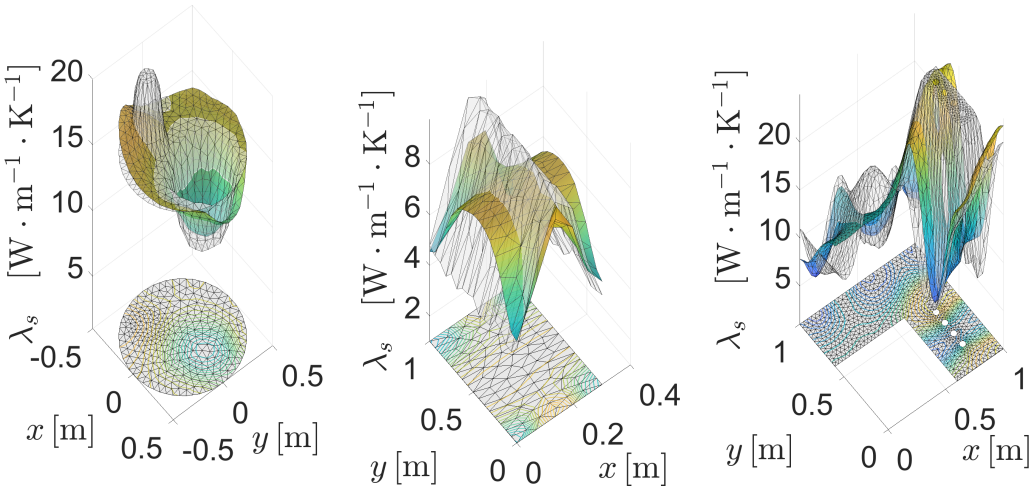

(a) $\varepsilon_{\lambda_s} = 0.0844$, $\varepsilon_u = 1 \times 10^{-4}$

(b) $\varepsilon_{\lambda_s} = 0.2493$, $\varepsilon_u = 9 \times 10^{-4}$

(c) $\varepsilon_{\lambda_s} = 0.3454$, $\varepsilon_u = 7 \times 10^{-4}$

Figure 14: Identified material fields for various domain shapes. In colour: $\lambda_{s,\mathrm{rec}}$, in transparent: $\lambda_{s,\mathrm{true}}$.

The example of a straight long wall in Fig. 13b comprises $m_h = 3$ heaters and $m_n = 12$ measurement nodes, which are located at the boundaries $\partial\Omega_1$ and $\partial\Omega_2$. The total number of nodes on the boundary $\partial\Omega$ is $N_b = 42$ and the representation of the measurement nodes is therefore 28.6%. The observed boundary $\Gamma_m = \partial\Omega_1 \cup \partial\Omega_2$ together with $m_h = 3$ heaters and load conditions were aligned in such a way that they could provide an information about the underlying field $\lambda_{s,\mathrm{true}}$ only in a single direction. Because of this, the parameter can not be identified properly. In the resulting field (see Fig. 14b) one can notice a relatively good approximation to the true field near the boundaries $\partial\Omega_1$ and $\partial\Omega_2$ since both are part of the observed boundary Γ_m.

However, information about the material distribution in a section in the middle of a domain parallel to the x axis is almost completely lost and nearly a constant field is obtained from the identification algorithm. Identified and true field cross sections at the mentioned locations on the construction are shown in the following figures

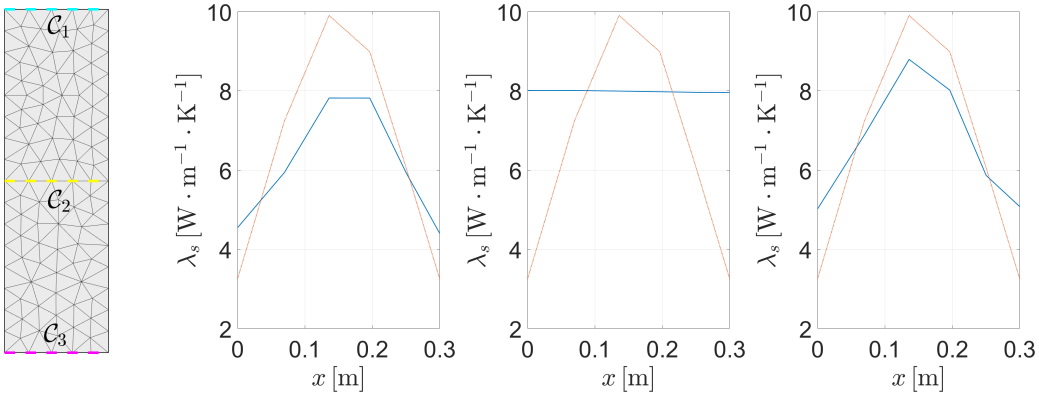

(a) (b) $\mathcal{C}_1$ (c) $\mathcal{C}_2$ (d) $\mathcal{C}_3$

Figure 15: Identified and true material field cross sections. In blue: $\lambda_{s,\mathrm{rec}}$, in red: $\lambda_{s,\mathrm{true}}$.

Notice that the identification algorithm achieved better results in section $\mathcal{C}_3$ (see Fig. 15d) than in section $\mathcal{C}_3$. This is due to the fact that in section $\mathcal{C}_3$ there are two heaters, which are providing additional data about true distribution of the underlying conductivity.

The resulting field of the L-shaped domain example in Fig. 14c represents an analogy to the Fig. 10b with a more complex geometry and material distribution. The synthetic experiment consists of $m_h = 3$ heaters and $m_n = 61$ measurement nodes which take place on the boundary $\Gamma_m = \partial\Omega_2$. The free boundary $\partial\Omega$ including four holes in the right section of the domain consists of $N_b = 154$ nodes. Therefore, representation of the observed boundary Γ_m to the $\partial\Omega$ corresponds to 39.6%. When comparing the results in Fig. 14c and Fig. 10b, it can be seen that despite reaching a lower error on the monitored temperature ε_u, which is achieved inter alia by a higher number of heaters, the overall error on the identified field is much higher. This is mainly due to the material complexity as in the case of Fig. 10b the identification algorithm found a better solution with less data.

In previous examples, we studied behaviour of the identification method in cases of limited number measurements for various domain shapes and distributions of material parameters. However, in each case we have committed

an *inverse crime* by not incorporating the error into measurement $\mathbf{u}_m$, computing the synthetic experiment on the same finite element mesh as in the identification algorithm, etc. In the following examples we make the identification task more realistic by introducing a more accurate model, which in our case is represented by a finer FE mesh.

However, the difference in FEM meshes for the error-less data and the identification process might cause the vector dimension mismatch. In case of the measured quantity, i.e. system responses and output of the forward operator from eq. (2.11), the measurement nodes coincide for both meshes and hence output of the forward operator $F(\boldsymbol{\lambda}_s)$ and the error-less data $\mathbf{u}_m$ are of same dimensions. For the parameter being identified a known function f, e.g. $\lambda_s(\mathbf{x}) = f(\mathbf{x})$, is utilised. To obtain the vector of error-less data $\lambda_{s,\text{true}}$ on a mesh, we simply take $\lambda_{s,i} = f(\mathbf{x}_{c,i})$, where $\mathbf{x}_{c,i}$ are the centroid coordinates for i-th element. The identification algorithm is run on a different, coarser mesh. In order to compare the identified piecewise constant $\lambda_{s,\text{rec}}$ with the true values $\lambda_{s,\text{true}}$ in eq. (4.4), f at the centroids of the coarse mesh is evaluated[20].

We utilise two geometrical domains, i.e circular and L-shaped domain, with their finite element discretisation, measurement nodes and positions of heaters are shown in Fig. 16. Measurement nodes are marked as asterisks and $m_h = 3$ heaters placed on the external side of the boundary are labelled by numbers from 1 to 3. The boundary conditions for circular domain according to the third equation in eq. (2.9) are set in the following way

$$\begin{aligned} \lambda_s(x)\frac{\partial u}{\partial n}(x)|_{\partial\Omega_1} &= 10 \cdot (u(x) - 30)\,, \\ \lambda_s(x)\frac{\partial u}{\partial n}(x)|_{\partial\Omega_2} &= 10 \cdot (u(x) - 15)\,, \end{aligned} \tag{4.10}$$

where $\partial\Omega = \bigcup_{i=1}^{2} \partial\Omega_i$ and the number of measurement nodes is $m_n = 52$, which corresponds to 43.3% of the total number of nodes on the boundary $\partial\Omega$. For the L-shaped domain, the boundary conditions are set in the following way

$$\begin{aligned} \lambda_s(x)\frac{\partial u}{\partial n}(x)|_{\partial\Omega_1} &= 10 \cdot (u(x) - 30)\,, \\ \lambda_s(x)\frac{\partial u}{\partial n}(x)|_{\partial\Omega_2} &= 10 \cdot (u(x) - 15)\,, \\ \lambda_s(x)\frac{\partial u}{\partial n}(x)|_{\partial\Omega_3} &= 0, \end{aligned} \tag{4.11}$$

[20]By assumption this we introduce a negligible additional error.

where $\partial\Omega_T = \bigcup_{i=1}^{2} \partial\Omega_i$ is the union of the outer and inner corner segment of the boundary, $\partial\Omega_3 = \partial\Omega \backslash \partial\Omega_T$ and the number of the measurement nodes is $m_n = 81$, which corresponds to 50.6% of the total number of nodes on the boundary $\partial\Omega$. The heater properties are expressed for both examples as follows

$$\begin{aligned} T_i &= 5 \quad [\,^{\circ}\mathrm{C}\,], \\ r_i &= 0.01 \quad [\,\mathrm{m}\cdot\mathrm{K}\cdot\mathrm{W}^{-1}\,], \quad \text{for} \quad i = 1,2,3, \\ l_i &= 0.1 \quad [\,\mathrm{m}\,], \end{aligned} \tag{4.12}$$

where l_i is the length of the individual heater. In both examples the true parameter field represents an artificial material distribution. For the circular domain it contains two inclusions, see Fig. 16c, and in the case of L-shaped domain the material distribution has smooth transitions, see Fig. 16f.

The resulting fields showing the difference between the true and the identified thermal conductivity are depicted in Fig. 17, where corresponding errors ε_{λ_s} and ε_u obtained from eq. (4.4) and eq. (4.5), respectively, are also presented. Moreover, notice the errors ε_u are much smaller than ε_{λ_s} due to the smoothing effect of the stationary heat model. It can be seen that the obtained fields roughly correspond with the true fields. The most recognisable inaccuracies in the identified thermal conductivity field can be once again found in the close neighbourhood of the discontinuities and in general in regions with high frequency oscillations due to the smoothing effect of the governing equation, concrete choice of the operator L and the norm $p = 2$ in eq. (3.7) which prefers smooth fields. In case of the circular domain in Fig. 17a the smaller of inclusions merge into one large cluster and it is virtually impossible to locate it without a prior knowledge.

In order to evaluate the impact of different FE mesh, both examples were performed again with a coarse FE mesh for either the identification algorithm and a synthetic experiment. In case of the circular domain, the error obtained on the parameter field was $\varepsilon_{\lambda_s} = 0.0723$ and on the temperatures $\varepsilon_u = 5 \times 10^{-4}$. This corresponds approximately to 12% of the error increase on ε_{λ_s} and 19% of the error increase on ε_u when a different FE mesh is utilised. The resulting errors for the L-shaped domain were $\varepsilon_{\lambda_s} = 0.1482$ on the parameter field and $\varepsilon_u = 23 \times 10^{-4}$ on the temperatures, which corresponds to approximately 8% increase of the error on the parameter field and 8% on the temperatures. From obtained results it can be seen the particular problem is moderately case dependent. While in some cases a perfect model, which is in our case represented by the same FE mesh utilised in the synthetic experiment, carries a significant portion of information about the underlying parameter field (a circular domain in our case) in other cases the difference is not so significant (the L-shaped domain). Possibly interesting study would

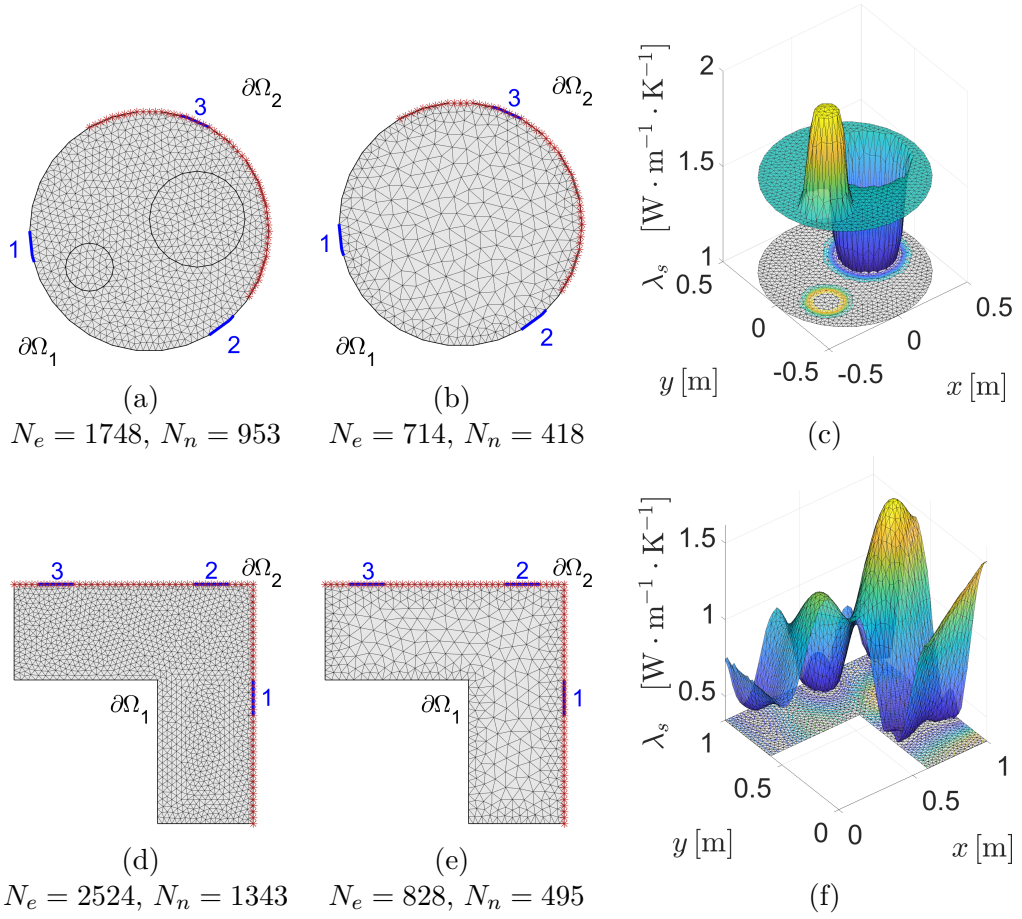

(a) $N_e = 1748$, $N_n = 953$ (b) $N_e = 714$, $N_n = 418$ (c)

(d) $N_e = 2524$, $N_n = 1343$ (e) $N_e = 828$, $N_n = 495$ (f)

Figure 16: (a,d) Domain discretisation utilised for simulating the experiment, (b,e) domain discretisation used in the identification algorithm, (c,f) spatial distribution of the true material - thermal conductivity $\lambda_{s,\text{true}}$.

be to utilise two different meshes, which share the same number of nodes N_n and elements N_e, but would not be nested.

Note that for increasing number of measurements m_n and loading states m_h, the identified parameter field numerically converges to the true material field as it was shown in Fig. 10 and 11. However, a more advanced study is not the intent of present work and we refer the interested reader to [60].

We can finally conclude that calculated results promote the capability of the proposed methodology to identify the material field from the boundary measurements for steady-state model.

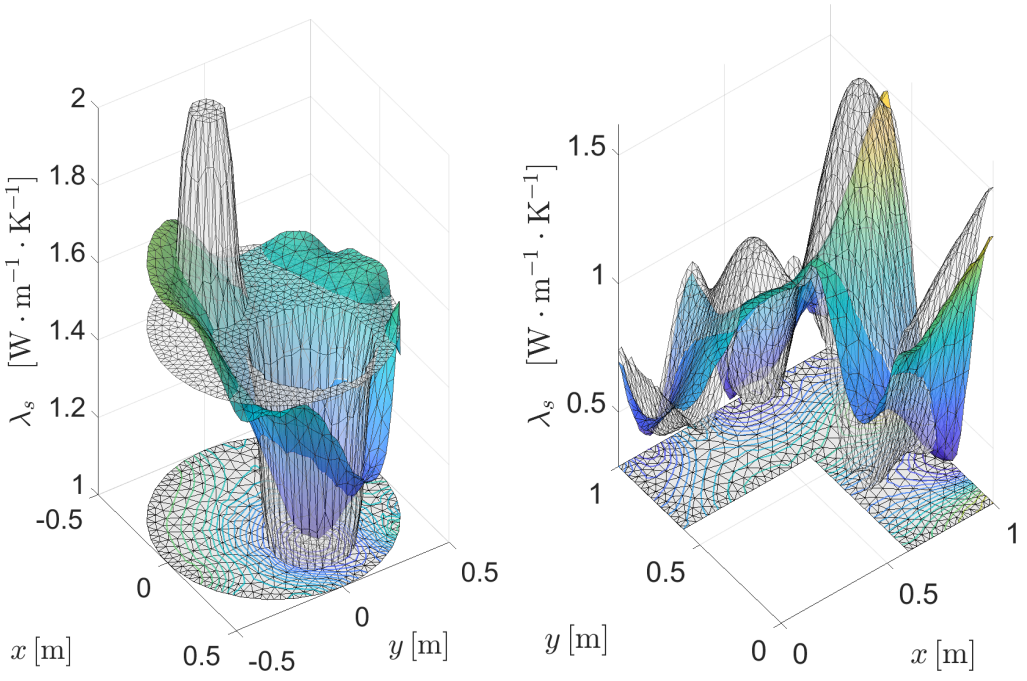

(a) $\varepsilon_{\lambda_s} = 0.0820$, $\varepsilon_u = 7 \times 10^{-4}$

(b) $\varepsilon_{\lambda_s} = 0.1606$, $\varepsilon_u = 26 \times 10^{-4}$

Figure 17: Comparison of the true (transparent) and the identified (opaque) thermal conductivity field: (a) circular domain and (b) L-shaped domain.

4.3 Transient model

From a practical point of view, more interesting problem is represented by the time dependent heat equation, which can describe even sudden changes in external factors, i.e. u_0 and α from the third equation in eq. (2.19), and load conditions during the observation. In order to capture the transition from a steady-state heat transport to a transient problem, in the following example we put these two physical models in similar situation in terms of boundary conditions, domain shape with discretisation and heater properties. By this we mean that we will virtually simulate a GTM experiment by a transient model, i.e. as it would be performed in the laboratory settings.

In order to quantify the identification performance, we evaluate the error ε_u representing the mismatch between the model response $\mathbf{u}_r = \mathrm{F}(\mathbf{\Phi}) \in \mathbb{R}^{m_n \cdot m_t}$ (see eq. (2.21)) and the measured temperatures $\mathbf{u}_m \in \mathbb{R}^{m_n \cdot m_t}$ in the following way

$$\varepsilon_u = \frac{\|\mathbf{u}_r - \mathbf{u}_m\|_2}{\|\mathbf{u}_m\|_2}. \tag{4.13}$$

Since the transient model constitutes two individual parameters $\boldsymbol{\Phi} = [\boldsymbol{\phi}_1, \boldsymbol{\phi}_2]$, we also examine the error separately for each parameter field, i.e. $\boldsymbol{\phi}_1 = \boldsymbol{\lambda}_{s,\cdot} \in \mathbb{R}^{N_e}$ and $\boldsymbol{\phi}_2 = \mathbf{c}_{v,\cdot} \in \mathbb{R}^{N_e}$ in the following way

$$\varepsilon_{\lambda_s} = \frac{\|\boldsymbol{\lambda}_{s,\mathrm{rec}} - \boldsymbol{\lambda}_{s,\mathrm{true}}\|_2}{\|\boldsymbol{\lambda}_{s,\mathrm{true}}\|_2}, \tag{4.14}$$

$$\varepsilon_{c_v} = \frac{\|\mathbf{c}_{v,\mathrm{rec}} - \mathbf{c}_{v,\mathrm{true}}\|_2}{\|\mathbf{c}_{s,\mathrm{true}}\|_2}. \tag{4.15}$$

In some cases we also need to evaluate the thermal effusivity, which is defined as $e_s = \sqrt{\lambda_s \cdot c_v}$, and the corresponding error in the following way

$$\varepsilon_{e_s} = \frac{\|\mathbf{e}_{s,\mathrm{rec}} - \mathbf{e}_{s,\mathrm{true}}\|_2}{\|\mathbf{e}_{s,\mathrm{true}}\|_2}. \tag{4.16}$$

The examined L-shaped domains with measurement nodes, heaters and discretisation are depicted in Fig. 18a and 18b. Spatial distributions of the true materials are shown in Fig. 18c and 18d. Boundary conditions according to the second and the third equation in eq. (2.19) are set in the following way

$$\begin{aligned} \lambda_s(x)\frac{\partial u}{\partial n}(x,t)|_{\partial\Omega_1} &= 10 \cdot (u(x,t) - 25)\,, \\ \lambda_s(x)\frac{\partial u}{\partial n}(x,t)|_{\partial\Omega_2\setminus(e_1\cup e_2)} &= 10 \cdot (u(x,t) - 5)\,, \\ \lambda_s(x)\frac{\partial u}{\partial n}(x,t)|_{\partial\Omega_3} &= 0, \end{aligned} \tag{4.17}$$

where $\partial\Omega_T = \partial\Omega_1 \cup \partial\Omega_2$ is also used as the observed part of the boundary Γ_m, i.e. $\Gamma_m = \partial\Omega_T$, and contains $m_n = 117$ nodes and $\partial\Omega_3 = \partial\Omega \setminus \partial\Omega_T$. The starting fields in the identification process are set as follows: $\lambda_s = 1\,\mathrm{W}\cdot\mathrm{m}^{-1}\cdot\mathrm{K}^{-1}$ and $c_v = 1 \times 10^6\,\mathrm{J}\cdot\mathrm{m}^{-3}\cdot\mathrm{K}^{-1}$. The heater properties are set equivalently for both models. In particular, for steady-state model are defined as

$$\begin{aligned} T_i &= 10 \quad [\,^{\mathrm{o}}\mathrm{C}\,], \\ r_i &= 0.1 \quad [\,\mathrm{m}\cdot\mathrm{K}\cdot\mathrm{W}^{-1}\,], \quad \text{for} \quad i = 1, 2, \\ l_i &= 0.1 \quad [\,\mathrm{m}\,], \end{aligned} \tag{4.18}$$

whereas for the transient model are set as follows

$$\begin{aligned} \lambda_s(x)\frac{\partial u}{\partial n}(x,t)|_{e_1} &= 10 \cdot (u(x,t) - T_1(t))\,, \\ \lambda_s(x)\frac{\partial u}{\partial n}(x,t)|_{e_2} &= 10 \cdot (u(x,t) - T_2(t))\,. \end{aligned} \tag{4.19}$$

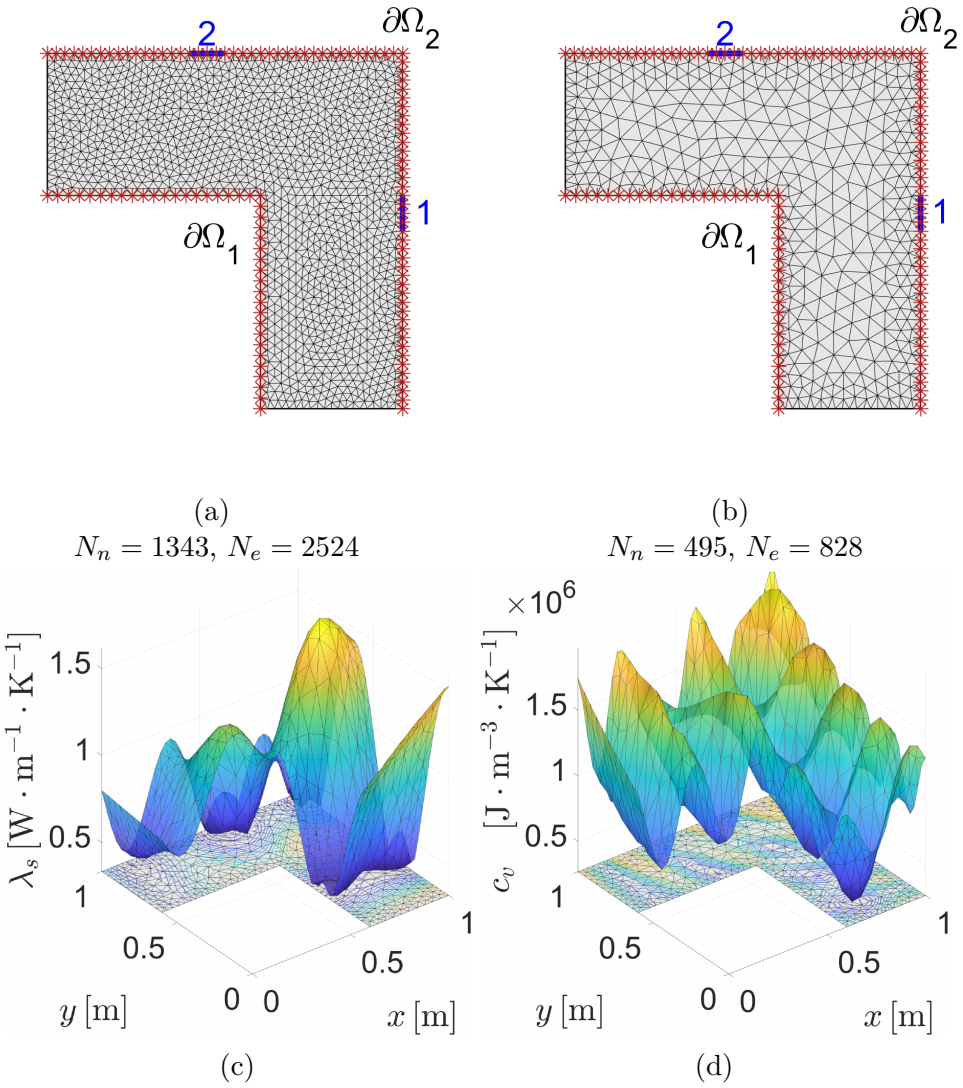

Figure 18: L-shaped domain with discretisation utilised for (a) simulating real measurement and (b) for the identification, (c) distribution of the true thermal conductivity $\lambda_{s,\mathrm{true}}$, (d) distribution of the true volumetric heat capacity $c_{v,\mathrm{true}}$.

Evolution of the temperature of individual heater T_i and the corresponding model response u_i in the domain underneath each heater is depicted in Fig. 19. This graphs primarily describe the temperature stimulation pattern employed for the transient problem. Each heater is consecutively excited to 10 ^{o}C for a single day with 12 hours shift between each load condition, while the second heater is inactive. The collection of data starts from day two when the stationary state in Ω is approximately reached, i.e. the ob-

servation period lasts 3 days and a measurement of the temperature on the boundary Γ_m is recorded every two hours, i.e. $m_t = 36$, which overall yields $m_n \cdot m_t = 36 \cdot 117 = 4212$ values.

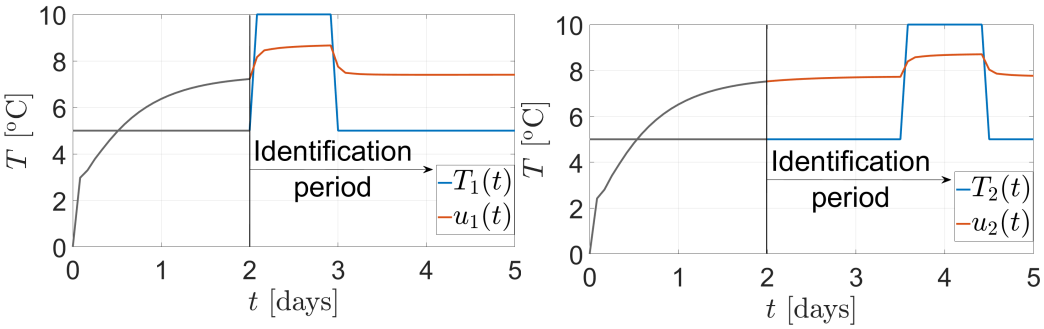

(a) (b)

Figure 19: Prescribed temperatures for (a) the first and (b) the second heater.

Results for the stationary model are shown in Fig. 20a, while the identified fields for the time dependent model are shown in Fig. 20b and 20c. The identified fields visually correspond to the true fields and in particular the conductivity $\lambda_{s,\mathrm{rec}}$ for both models appears to be similar. However, both errors, i.e. ε_{λ_s} and ε_u, are lower in the case of transient model in comparison to GTM. Better identification performance in case of the transient model can be understood from the following considerations. In this specific settings the aforementioned experiment evaluated by GTM is provided with two stationary states $\mathbf{u}_m^{\mathrm{GTM}} \in \mathbb{R}^{2\cdot 117}$, i.e. a single system response for each heater. On the other hand, transient model was provided with $m_t = 36$ time steps, where at least two of them are approximately equal to $\mathbf{u}_m^{\mathrm{GTM}}$. Meaning that in this specific case the transient model not only includes the two steady-states, which are also part of the GTM identification, but additionally contains further data of the temperature evolutions in time on Γ_m before the stationary states are reached.

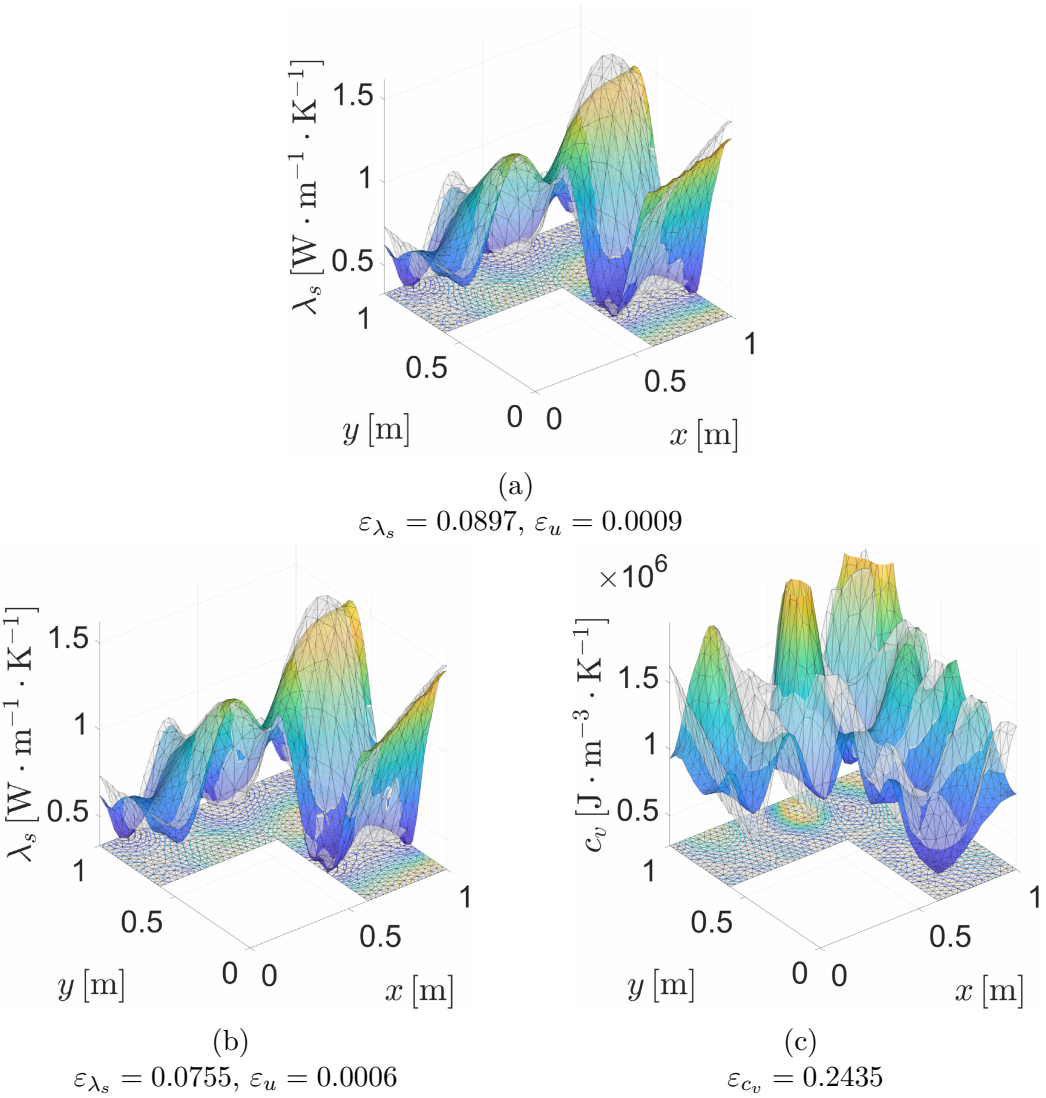

(a)
$\varepsilon_{\lambda_s} = 0.0897$, $\varepsilon_u = 0.0009$

(b)
$\varepsilon_{\lambda_s} = 0.0755$, $\varepsilon_u = 0.0006$

(c)
$\varepsilon_{c_v} = 0.2435$

Figure 20: Comparison of the true (transparent) and the identified (opaque) field: (a) stationary problem - thermal conductivity field, (b) transient problem - thermal conductivity field, (c) transient problem - volumetric heat capacity.

In the next example, we take a look at a situation where the transient model is subjected to constant boundary conditions over time given by eq. (4.21) for such a period of time for which a steady-state in the domain Ω is approximately reached. Performing particular experiment provides us with data that contains the time evolutions of the observed temperatures $\mathbf{u}_m$ on the boundary Γ_m leading to only one stationary state. Note that one could

possibly argue the initial condition $u(x, t = 0) = u_c(x, t = 0) = \tilde{c} \in \Omega$[21], where $\tilde{c} \in \mathbb{R}$, also corresponds to another stationary state included in the data. However, it does not in fact contain any information about the underlying parameter field. This can be proven by simply plugging the initial condition into the governing equation in eq. (2.19) as follows

$$\rho_s(x)c_p(x)\frac{\partial u_c}{\partial t}(x, t = 0) - \nabla \cdot (\lambda_s(x) \underbrace{\nabla u_c(x, t = 0)}_{\mathbf{0}}) = 0. \tag{4.20}$$

As a result the aforementioned equation is satisfied for any value of $\lambda_s(x)$ and hence such state does not carry any information about the underlying parameter $\lambda_{s,\text{true}}$. The zero information content can be in our case generalised from requiring $u(x, t = 0) = u_c(x, t = 0) = \tilde{c}$ for $x \in \Omega$ to $u(x, t) = u_{cb}(x, t) = \tilde{c}$ for $x, t \in \partial\Omega \times (0, t_s)$. This can be understood from an example in which one extend the vector of error-less data[22] $\mathbf{u}_m \in \mathbb{R}^{N_n \cdot m_t}$ by a discretised form of u_{cb}, i.e. $\mathbf{u}_{cb} = \tilde{c} \cdot \mathbf{1}$, where $\mathbf{1} \in \mathbb{R}^{N_n}$ is a vector full of ones. Such state corresponds to a Dirichlet boundary condition with prescribed temperature $\tilde{c}$ on the whole boundary $\partial\Omega$, which ultimately leads to a constant solution $u(x, t) = u_c(x, t) = \tilde{c} \in \Omega$ of the weak form of the governing equation in eq. (2.19) and eq. (4.20) can be utilised to prove the zero information content again.

In the following example, we analyse the ability of the identification algorithm to reconstruct the underlying true fields λ_s and c_v if only the first n_t from the total of N_t time steps are available for the identification. The experiment is set in the following way: we use identical domain[23], discretisation, measurement nodes and the true material field distribution as shown in Fig. 18. The observation period starts from day 0 with an initial condition $u(x, t = 0) = 0$ for $x \in \Omega$ and lasts 2 days with 2 hour intervals, i.e. the total number of time steps is $N_t = 24$.

$$\begin{aligned}
\lambda_s(x)\frac{\partial u}{\partial n}(x, t)|_{\partial\Omega_1} &= 10 \cdot (u(x, t) - 25)\,, \\
\lambda_s(x)\frac{\partial u}{\partial n}(x, t)|_{\partial\Omega_2} &= 10 \cdot (u(x, t) - 5)\,, \\
\lambda_s(x)\frac{\partial u}{\partial n}(x, t)|_{\partial\Omega_3} &= 0.
\end{aligned} \tag{4.21}$$

As a measure of how close the data are to the stationary state, we utilise the

[21] In our case we simply put $\tilde{c} = 0$.

[22] It is necessary to set $\Gamma_m = \partial\Omega$ in order to make a general claim.

[23] With exception of heaters, which are not utilised in this example.

following formula

$$c_{st} = 1 - \frac{\|\mathbf{u}_s - \mathbf{u}_{n_t}\|_2}{\|\mathbf{u}_s\|_2}, \tag{4.22}$$

where $\mathbf{u}_s \in \mathbb{R}^{N_n}$ is the full solution vector calculated for the steady-state heat equation, N_n is the number of finite element nodes and $\mathbf{u}_{n_t} \in \mathbb{R}^{N_n}$ is the solution vector for the transient model evaluated at time step n_t. Most importantly both vectors are evaluated for the true, i.e. error-less material parameters. The coefficient c_{st} serves only as an indication of how close the data from transient model are to the steady-state.

The following figure shows the relation between the error for both parameter fields calculated using eqs. (4.14) and (4.15) and the number of time steps $m_t = n_t$ given to the identification algorithm. It can be seen that involving more time steps into the identification is beneficial and any additional information leads to a more accurate identification of both fields. On the other hand, as the temperature develops over the time and approaches the steady-state, the error decreases more slowly, which is more pronounced in the error ε_{c_v} for the volumetric capacity. This is due to the fact that a successful identification of volumetric capacity mainly depends on the time change of the temperature field, which becomes negligible towards the steady-state. Moreover, one can notice that even in the early stages of the evolution process, i.e. $m_t \leq 5$, the algorithm performs surprisingly well and despite only limited number of observations m_t it is able to identify at least a rough distribution of the true fields. The amount of errors for given number of time steps n_t is shown in Fig. 21, whereas the identified fields for selected n_t are shown in Fig. 22.

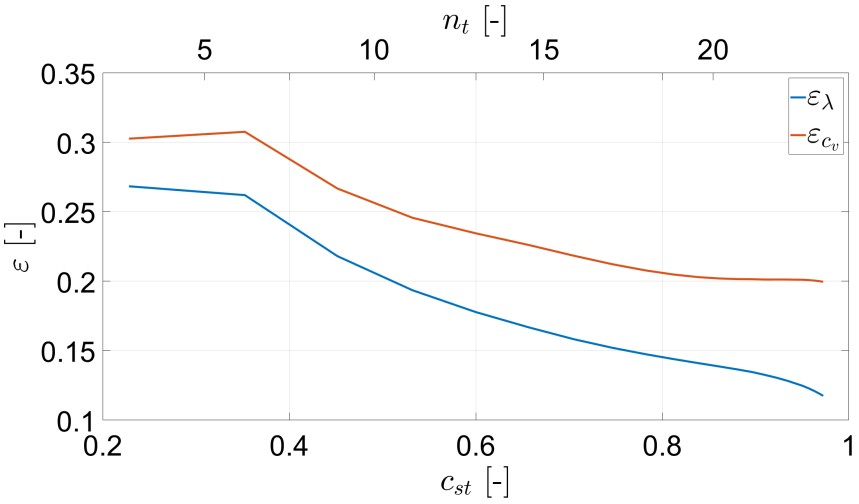

Figure 21: Material field errors calculated for different number of time steps involved in the calculation.

The last example presents the capability of the identification framework when simulating the time dependent problem. We utilise identical domain shape and discretisation as in the previous example, see Fig. 18b. In order to simulate a realistic environmental conditions and capture the temperature fluctuations in the interior and exterior, the heater elements in Fig. 18b are omitted and a measurement using an arduino based weather station is conducted. The environment is in total monitored for eleven consecutive days at minute intervals. For computational purposes the data are further sparsified to one hour intervals which satisfy both sufficient precision in describing the temperature curve and reasonable computational load. The resulting graphs without any additional processing are displayed in Fig. 23.

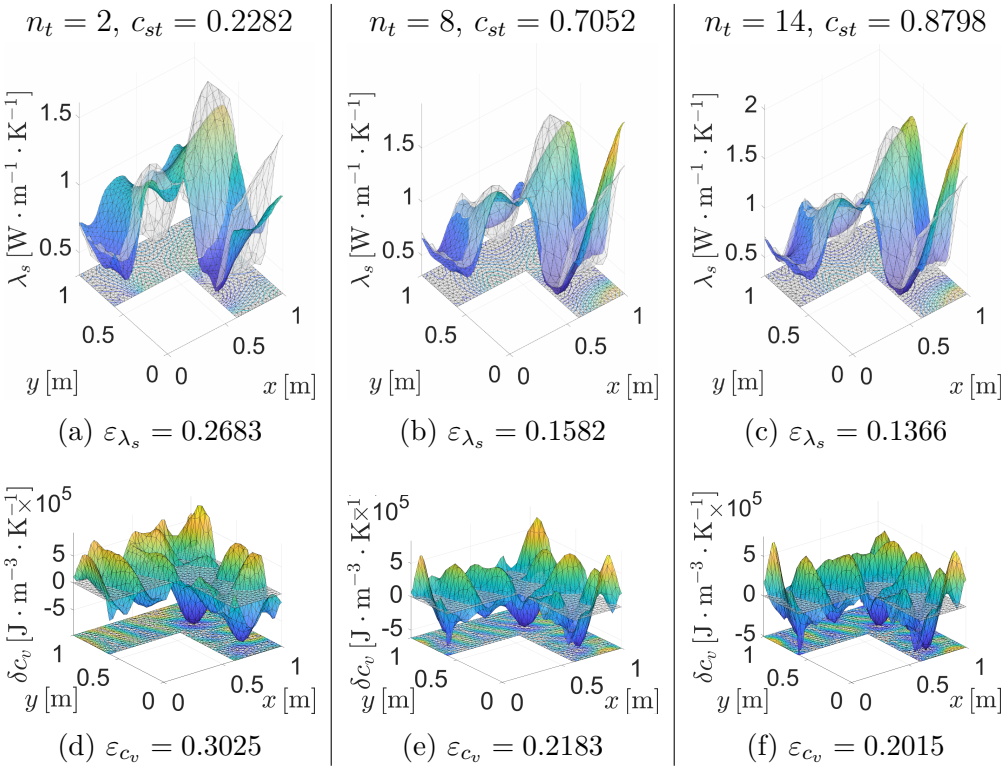

(a) $\varepsilon_{\lambda_s} = 0.2683$ (b) $\varepsilon_{\lambda_s} = 0.1582$ (c) $\varepsilon_{\lambda_s} = 0.1366$

(d) $\varepsilon_{c_v} = 0.3025$ (e) $\varepsilon_{c_v} = 0.2183$ (f) $\varepsilon_{c_v} = 0.2015$

Figure 22: Samples of identified fields for 2, 8 and 14 time steps $m_t = n_t$. The second row shows the difference between the true (see Fig. 18d) and the identified field.

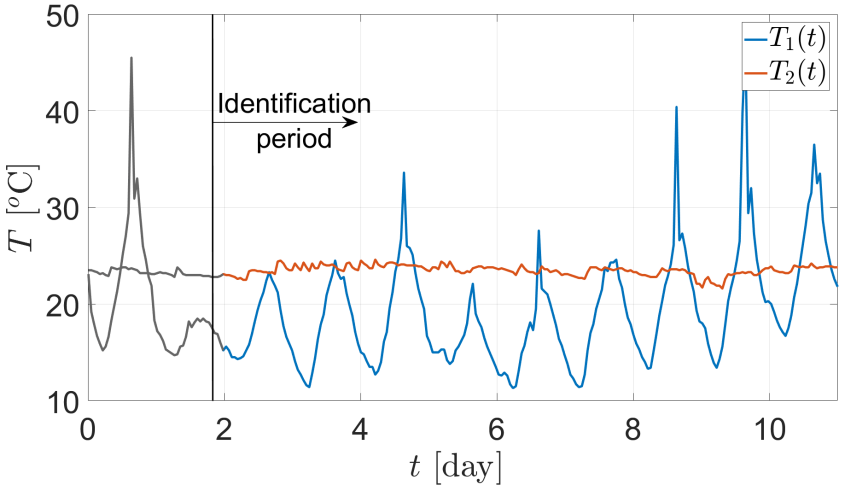

Figure 23: Interior (T_2) and exterior (T_1) temperatures, data included in the calculation spans from day 2 to 11.

The boundary conditions are set in the following way

$$\begin{aligned}
\lambda_s(x)\frac{\partial u}{\partial n}(x,t)|_{\partial\Omega_1} &= 10\cdot(u(x,t)-T_1(t))\,,\\
\lambda_s(x)\frac{\partial u}{\partial n}(x,t)|_{\partial\Omega_2} &= 10\cdot(u(x,t)-T_2(t))\,,\\
\lambda_s(x)\frac{\partial u}{\partial n}(x,t)|_{\partial\Omega_3} &= 0,
\end{aligned} \tag{4.23}$$

where the environmental temperatures $T_1(t)$ and $T_2(t)$ are shown in Fig. 23. Since the true material fields are identical to the ones in the previous example, see Fig. 18c and 18d, the starting fields for the first iteration are set in the same way, i.e. $\lambda_s = 1\,[\,\mathrm{W}\cdot\mathrm{m}^{-1}\cdot\mathrm{K}^{-1}\,]$ and $c_v = 1\times10^6\,[\,\mathrm{J}\cdot\mathrm{m}^{-3}\cdot\mathrm{K}^{-1}\,]$. The observation period lasts 9 days and starts from day two with hourly intervals which yields $m_t = 216$ observations. The observed part of the boundary Γ_m coincides with $\partial\Omega_1$ and $\partial\Omega_2$ and contains in total $m_n = 117$ nodes. The resulting identified fields are shown in the following figure

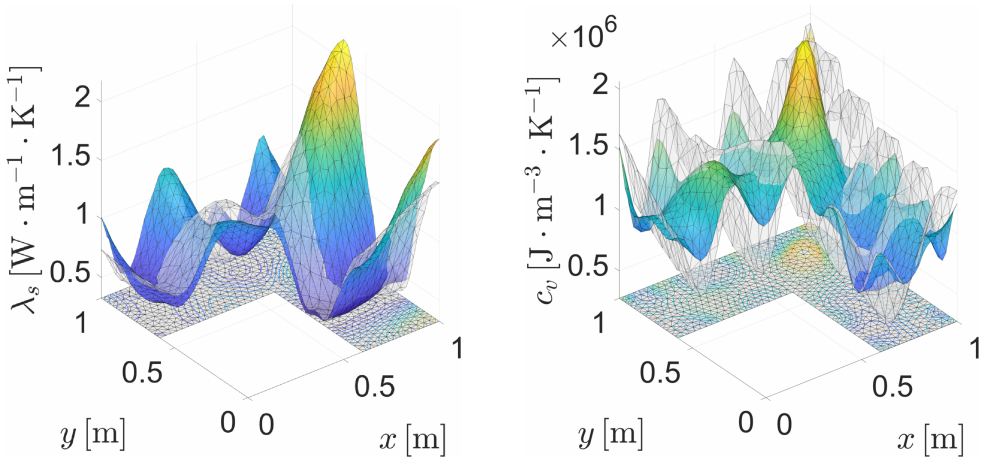

(a) $\varepsilon_{\lambda_s} = 0.2074$

(b) $\varepsilon_{c_v} = 0.2792$

Figure 24: (a) Comparison of the true (transparent) and the identified (opaque) thermal conductivity field with error on the temperatures $\varepsilon_u = 0.0010$, (b) comparison of the true and the identified volumetric heat capacity.

4.3.1 Probabilistic approach

In this section we use a probabilistic method in order to solve the inverse problem. The numerical example supporting the proposed identification strategy is identical to the previous one except for the finite element discretisation. Due to the higher computing complexity in case of the probabilistic method we employ a coarser finite element mesh which is divided into $N_e = 360$ triangular elements with $N_n = 216$ nodes, see Fig. 25a. Also, in this case the same finite element mesh is simultaneously employed for generating error-less data and in the identification algorithm.

Real climatic changes in temperature are imposed on the observed part of the boundary over several days. Measurements are assumed to be conducted by a thermal camera and/or by an array of discrete thermometers with an appropriate interpolation providing continuous surface data. The observation period lasts 9 days and starts on Day Two with hourly intervals. This yields $m_t = 216$ time observations, see Fig. 23. The boundary conditions are defined as

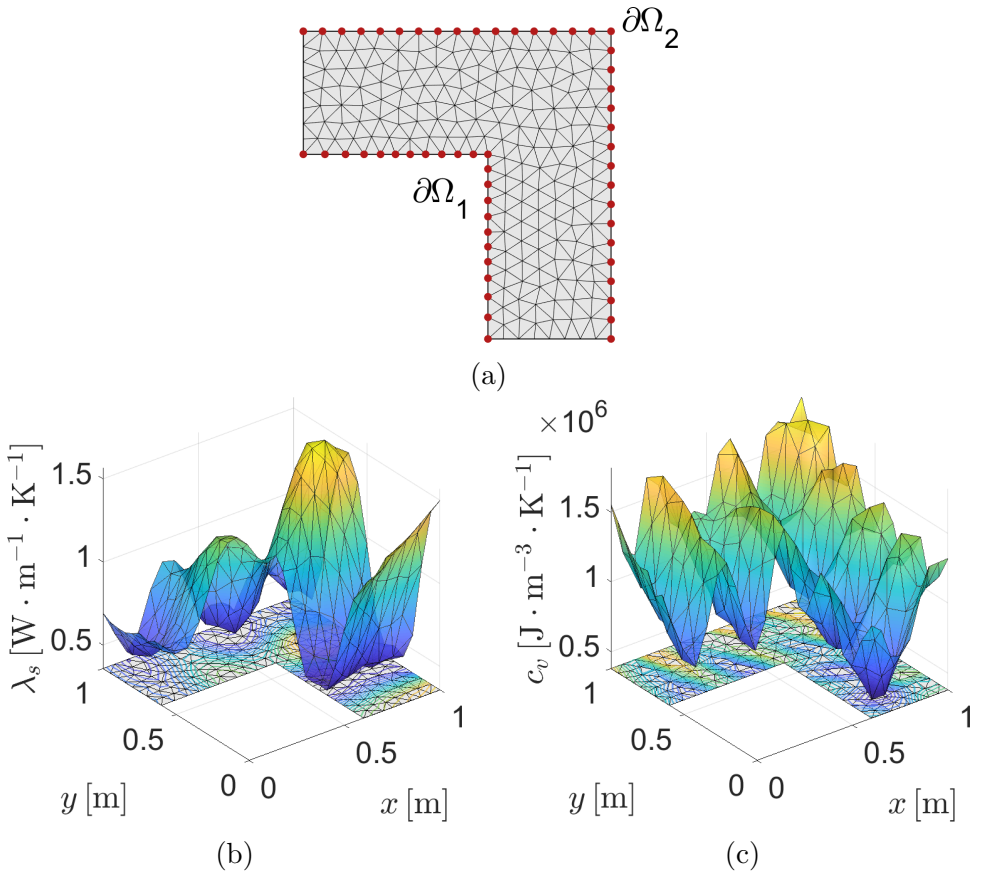

Figure 25: (a) Geometrical L-shaped domain with highlighted boundary conditions; (b) True material field - thermal conductivity; (c) True material field - volumetric heat capacity.

$$\begin{aligned}
\lambda_s \frac{\partial u}{\partial n}(\boldsymbol{x}, t)|_{\partial\Omega_1} &= \alpha \cdot (u(\boldsymbol{x}, t) - T_1(t)), \\
\lambda_s \frac{\partial u}{\partial n}(\boldsymbol{x}, t)|_{\partial\Omega_2} &= \alpha \cdot (u(\boldsymbol{x}, t) - T_2(t)), \\
\lambda_s \frac{\partial u}{\partial n}(\boldsymbol{x}, t)|_{\partial\Omega_3} &= 0,
\end{aligned} \tag{4.24}$$

where the environmental temperatures $T_1(t)$ and $T_2(t)$ are shown in Fig. 23 and where $\alpha = 10\,\mathrm{Wm^{-2}K^{-1}}$. The observed part of the boundary coincides with $\partial\Omega_1$ and $\partial\Omega_2$ ($\partial\Omega_T = \partial\Omega_1 \cup \partial\Omega_2$) and contains $m_n = 56$ nodes. The third condition in eq. (4.24) represents the insulated part of the boundary, i.e. $\partial\Omega_3 = \partial\Omega \backslash \partial\Omega_T$, which corresponds to the rest of the boundary in Fig. 25a.

The prior information about material parameters, both the thermal con-

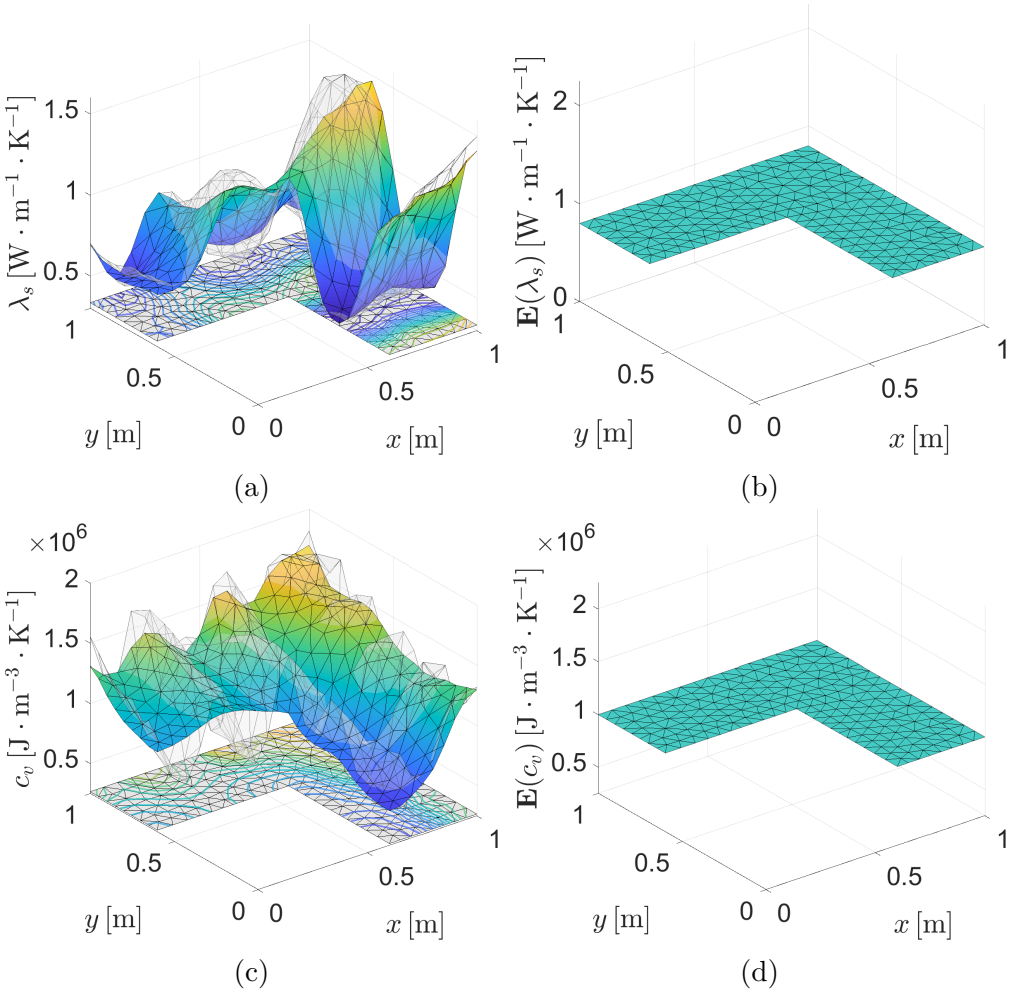

Figure 26: (a) Comparison of true thermal conductivity field with deterministic solution; (b) Mean of prior distribution of thermal conductivity; (c) Comparison of true volumetric heat capacity field with deterministic solution; (d) Mean of prior distribution of volumetric heat capacity.

ductivity λ_s and volumetric heat capacity c_v are considered to be lognormally distributed with the mean and standard deviation given in Tab. 2. The mean values represent typical values for materials in civil engineering, with a standard deviation of 30% of the mean values. As the prior distribution of ξ_k in eq. (3.71) is considered to be standard Gaussian with a zero mean, the mean of prior fields $\boldsymbol{q}_i$ is constant, see Fig. 26b and 26d.

The Bayesian update was performed using the Metropolis algorithm (see [34]) with Gaussian proposal distribution and a standard deviation $\sigma_0 = 0.0025$. Overall $100,000$ samples were generated in order to sample the

	Thermal conductivity λ_s [$\mathrm{Wm^{-1}K^{-1}}$]	Volumetric heat capacity c_v [$\mathrm{Jm^{-3}K^{-1}}$]
μ_q	0.8	$1.0 \cdot 10^6$
σ_q	0.24	$0.3 \cdot 10^6$

Table 2: Statistical moments of prior distributions.

posterior densities according to eq. (3.63) combining eqs. (3.60)-(3.62) with $\sigma_\varepsilon^2 = 0.09°\mathrm{C}$.

As outlined in Section 3.4.1, the spatial variability of each material field is approximated by a Karhunen-Loève expansion depending on a limited number m ($m < N_n$) of random variables to be identified. This is the principal difference between our proposed approach and the classical Calderón inverse problem where the material field is modelled using the N_n random variables defined in all nodes of finite element mesh. The resulting material fields are, of course, influenced also by parameters of chosen approximation, namely (i) m - number of eigenmodes and (ii) parameters of the covariance function (ρ, ν) entering the Karhunen-Loève expansion through eigenvalues and eigenmodes. The selection of appropriate values for these parameters is, however, a non-trivial task. Since ν is the smoothness parameter, its impact on the shape of the random field is rather low. In the following numerical study, its value is fixed to $\nu = 5$. The effect of correlation length ρ is, on the contrary, significant. From the definition of the Karhunen-Loève expansion, see eq. (3.71), it can be seen that the correlation length does not enter the expansion directly but rather through the spectral decomposition of the covariance matrix, see eq. (3.69). Its estimation is thus a very complex task. Therefore, a numerical study was performed for a number of eigenmodes $m = [1, \ldots, 50]$ and covariance lengths $\rho = [0.1, 0.25, 0.5, 1.0, 2.5, 5.0, 7.5, 10.0]$ to demonstrate the significance and role of these parameters. The methodology for estimation of correlation length from the experimental data is out of the scope of this paper, but an interested reader is referred to Lombardo et al. [70], which discusses its estimation using image analysis.

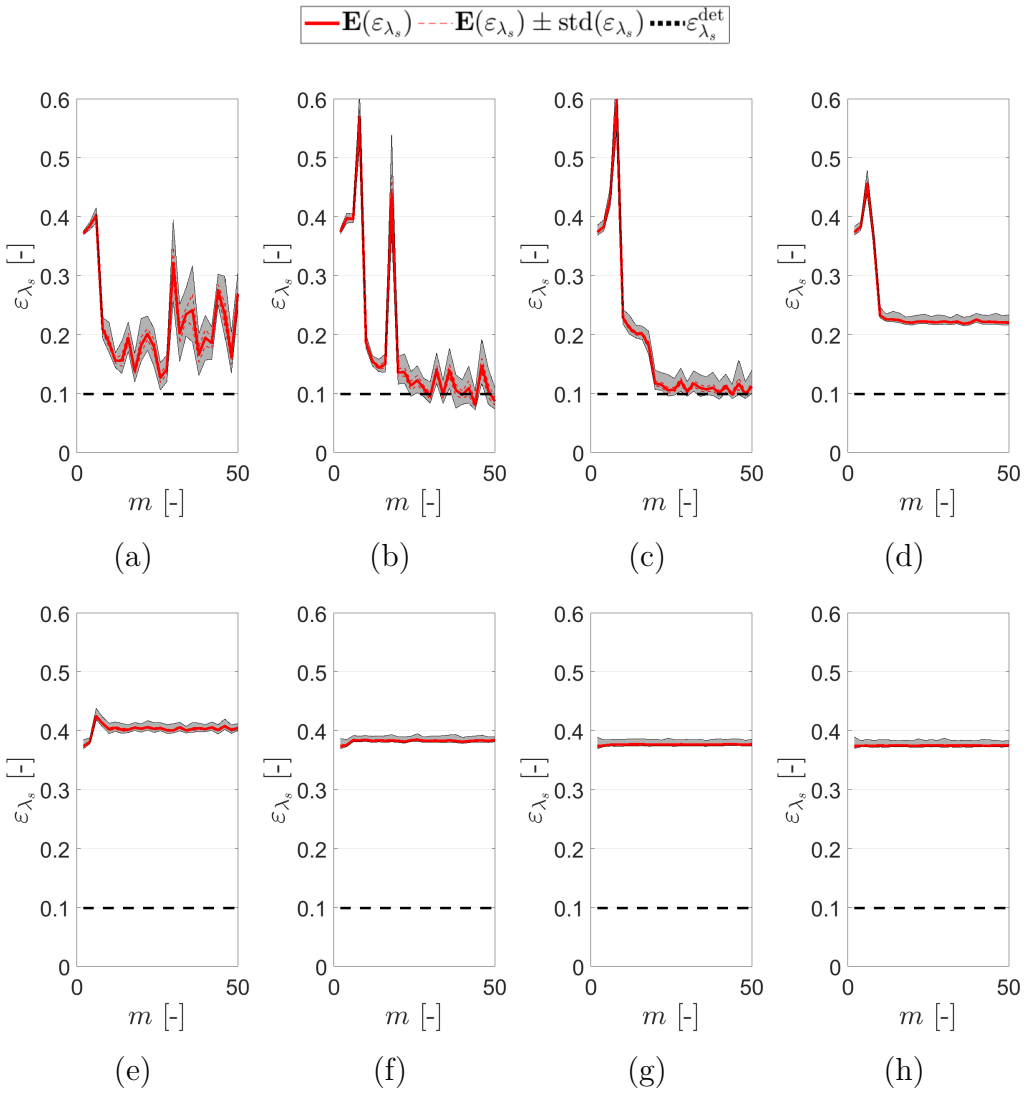

Figure 27: Resulting errors of thermal conductivity ε_{λ_s} as a function of the number of eigenmodes m; study performed for following correlation lengths: (a) $\rho = 0.10$; (b) $\rho = 0.25$; (c) $\rho = 0.50$; (d) $\rho = 1.00$; (e) $\rho = 2.50$; (f) $\rho = 5.00$; (g) $\rho = 7.50$; (h) $\rho = 10.00$.

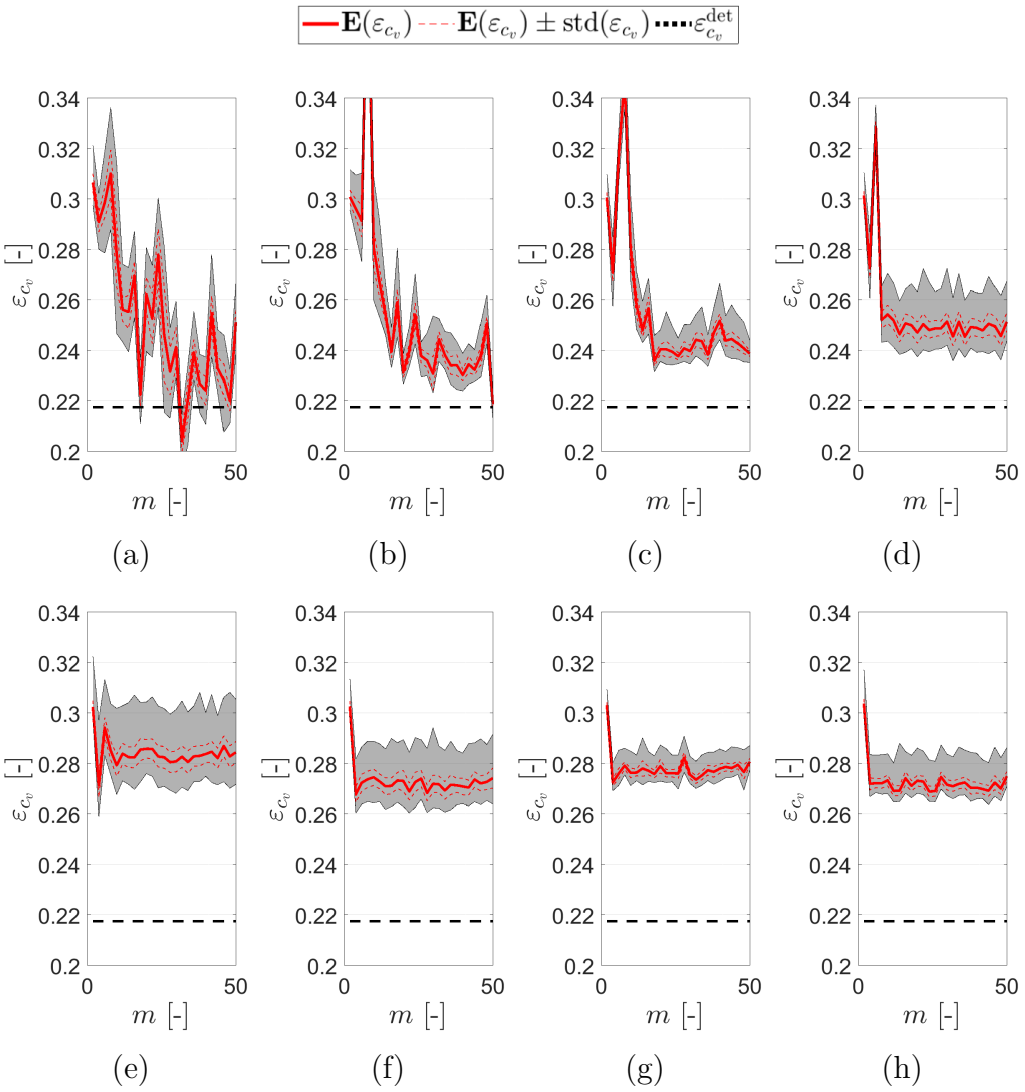

Figure 28: Resulting errors of volumetric heat capacity ε_{c_v} as a function of the number of eigenmodes m; study performed for following correlation lengths: (a) $\rho = 0.10$; (b) $\rho = 0.25$; (c) $\rho = 0.50$; (d) $\rho = 1.00$; (e) $\rho = 2.50$; (f) $\rho = 5.00$; (g) $\rho = 7.50$; (h) $\rho = 10.00$.

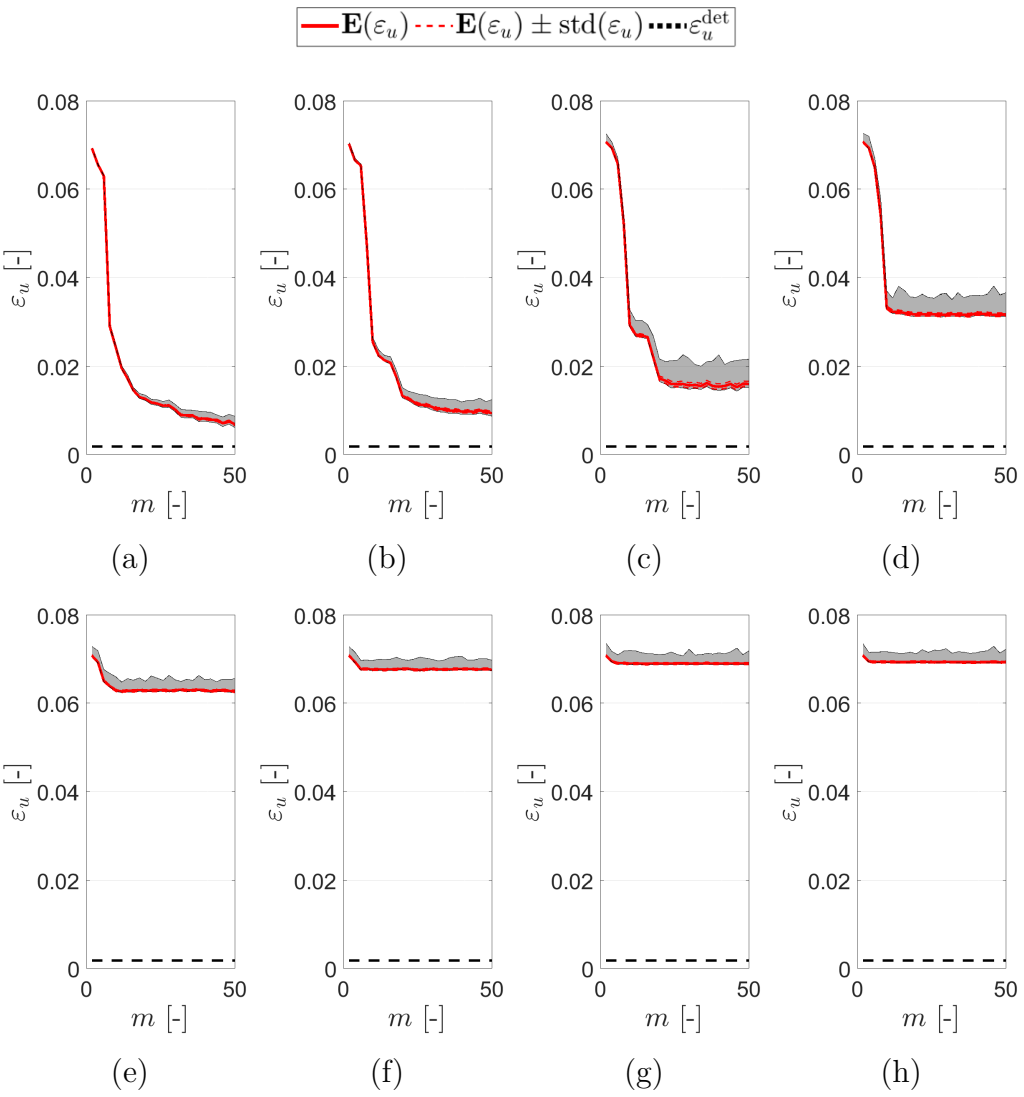

Figure 29: Resulting errors of temperature ε_u as a function of the number of eigenmodes m; study performed for following correlation lengths: (a) $\rho = 0.10$; (b) $\rho = 0.25$; (c) $\rho = 0.50$; (d) $\rho = 1.00$; (e) $\rho = 2.50$; (f) $\rho = 5.00$; (g) $\rho = 7.50$; (h) $\rho = 10.00$.

The resulting errors of thermal conductivity ε_{λ_s}, volumetric heat capacity ε_{c_v}, and temperature ε_u as a function of the number of Karhunen-Loève eigenmodes m are depicted in Figs. 27-29. The grey surface on these figures represents the errors calculated for all posterior samples. The bold red line is the mean value and the standard deviation is represented by a red dashed line. Moreover, the black dashed line represents the values of errors obtained by the deterministic identification scheme without considering random fields or measurement errors in the calculations, see our previous work [42]. To be more specific, the desired parameter fields are recovered using a Calderón problem which is numerically solved by means of a regularised Gauss-Newton method, see eq. (3.19). The achieved values were: (i) $\varepsilon_{\lambda_s}^{\text{det}} = 0.0950$, (ii) $\varepsilon_{c_v}^{\text{det}} = 0.2175$, and (iii) $\varepsilon_u^{\text{det}} = 0.0018$. Comparison with these errors derived from deterministic solutions gives us the opportunity to see the performance of our technique based on the dimensionality reduction. Note the difference in deterministic results in this section and the previous one can be accounted to the finite element mesh discretisation. Overall results in terms of the error magnitudes for the deterministic identification are in favour of this section due to two factors: first is the fact we utilised the same finite element meshes for the synthetic experiment and also for the identification process. The second factor is the use of a coarser mesh that has fewer degrees of freedom, which has a positive effect on the solution.

Very good results are achieved for values of correlation length $\rho < 1.0$, where the amount of error still decreases with an increasing number of eigenmodes in the description of random fields. The mean of corresponding posterior fields for $m = 50$ eigenmodes is depicted in Fig. 30. It is interesting that while the amount of error in temperature fields in Fig. 29 decreases relatively smoothly with increasing number of eigenmodes, the errors in the parameter fields oscillate significantly, see Figs. 27 and 28. This means that a better description of the measured temperature field can be obtained for parameter fields, which differs more from the true ones. This is visible also in Fig. 30, while the smallest amount of error in temperature field is achieved for correlation length $\rho = 0.10$ and the smallest amount of error in conductivity and capacity fields is obtained for $\rho = 0.25$. It is not very surprising that the inaccuracy in approximation with a limited number of eigenmodes may cause convergence of the identification process to an incorrect solution. More interesting is that including an additional eigenmode into the approximation, i.e. one additional degree of freedom, allows for improvement of the temperature field, but may lead to significantly worse representation of the parameter fields. This is probably caused by the fact that particular eigenmodes were not constructed from the correct covariance kernel corresponding to the true fields and thus such eigenmodes do not ensure smooth monotonic conver-

gence. Moreover, the plots in Figs. 27 and 28, namely Fig. 27a suggest that the amount of error is not converging towards the error of a deterministic solution at all and not even including all eigenmodes allow for achieving the amount of error of a deterministic solution. On the other hand, covariance kernel with correlation lengths $\rho = 0.25$ or $\rho = 0.50$, see Figs. 27b and 27c, seems to better represent the covariance structure of the true conductivity field indicated by more smooth convergence of the error as well as by its proximity to the deterministic error.

Regarding higher values of ρ ($\rho \geq 1.0$), the convergence graphs of error values in the parameters fields are already also relatively smooth, especially

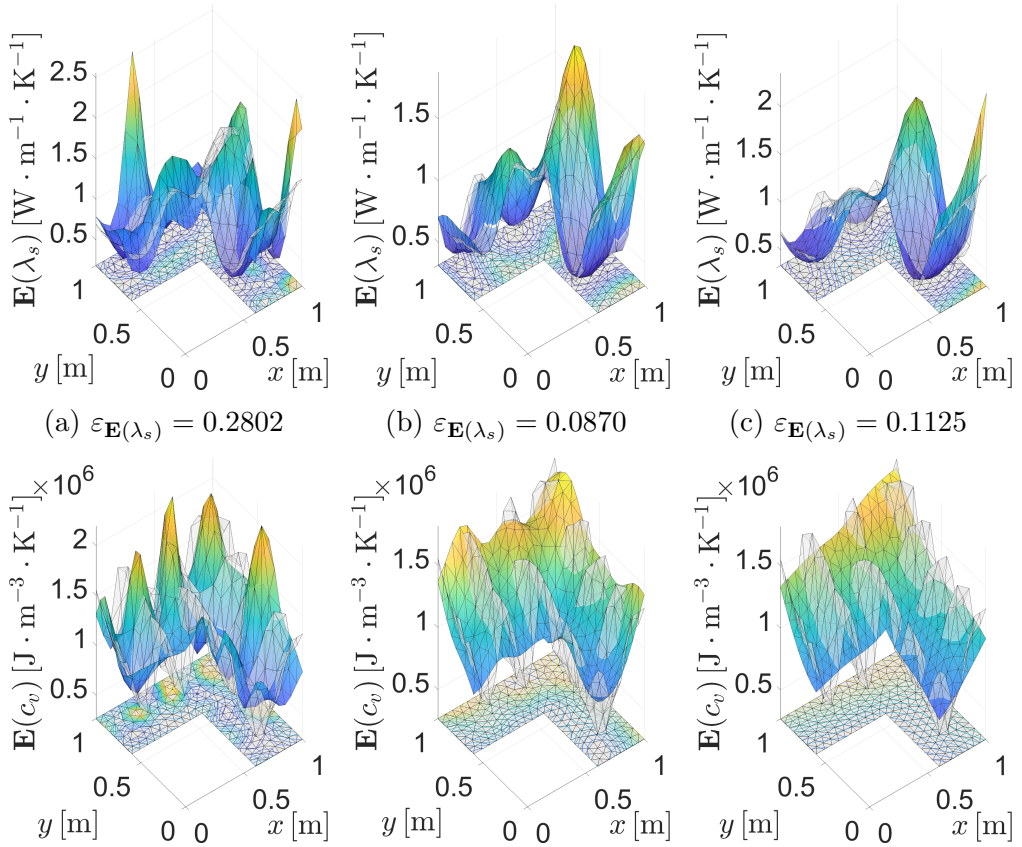

(a) $\varepsilon_{\mathbf{E}(\lambda_s)} = 0.2802$ (b) $\varepsilon_{\mathbf{E}(\lambda_s)} = 0.0870$ (c) $\varepsilon_{\mathbf{E}(\lambda_s)} = 0.1125$

(d) $\varepsilon_{\mathbf{E}(c_v)} = 0.2514$ (e) $\varepsilon_{\mathbf{E}(c_v)} = 0.2208$ (f) $\varepsilon_{\mathbf{E}(c_v)} = 0.2388$

Figure 30: Comparison of true fields with mean of posterior fields constructed using the 50 eigenmodes: (a) Thermal conductivity, $\rho = 0.10$; (b) Thermal conductivity, $\rho = 0.25$; (c) Thermal conductivity, $\rho = 0.50$; (d) Volumetric heat capacity, $\rho = 0.10$; (e) Volumetric heat capacity, $\rho = 0.25$; (f) Volumetric heat capacity, $\rho = 0.50$.

in case of thermal conductivity, see Figs. 27d – 27h. These graphs also clearly show that the error values quickly start to stagnate, and inclusion of additional eigenmodes does not bring any improvement. Moreover, the stagnation appears not only in the convergence graph of error in thermal conductivity or volumetric heat capacity fields, but also in the temperature fields, see Figs. 29d – 29h. This can be explained by the fact that high correlation lengths in the covariance kernel do not allow for description of higher frequencies in eigenmodes. This is connected to a ill-conditioned covariance matrix, which can be almost singular up to some numerical error amounts, and solution of the eigenvalue problem results in a very fast decay in eigenvalues suggests that only a few eigenvalues explain almost whole the variance of a random field, see Fig. 32. The remaining eigenvalues are nearly zero and thus the addition of corresponding eigenvectors to the Karhunen-Loève expansion brings no improvement to the quality of the random field approximation.

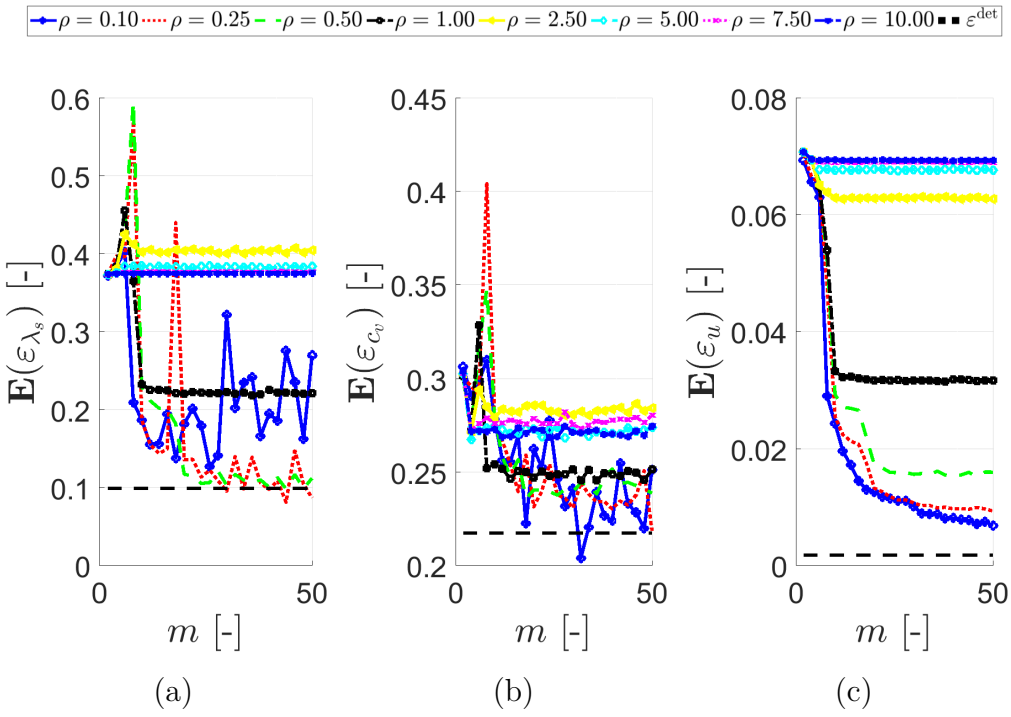

Figure 31: Final comparison: (a) Averaged errors of thermal conductivity ε_{λ_s} as a function of the number of eigenmodes m and ρ; (b) Averaged errors of volumetric heat capacity ε_{c_v} as a function of the number of eigenmodes m and ρ; (c) Averaged errors of temperature ε_u as a function of the number of eigenmodes m and ρ.

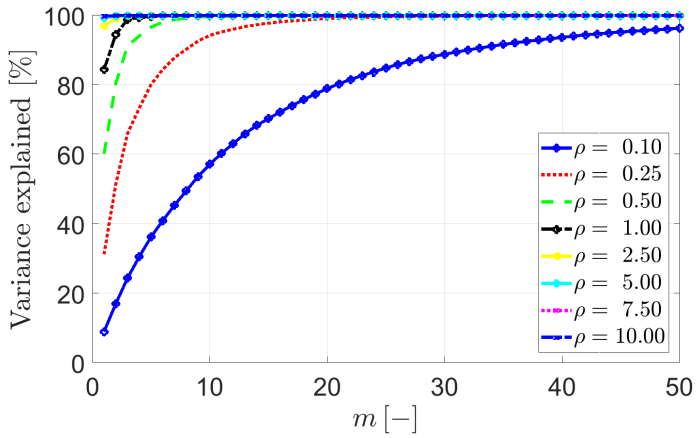

Figure 32: Decay of eigenvalues with different prior correlation lengths. Vertical axis shows the fraction of the prior variance explained by m eigenmodes.

4.3.2 Loading related issues

In an experimental setup one might encounter problems with accessibility of certain parts of the boundary where, although their dimensions or approximate boundary conditions are known, a sensor can not be placed. On these parts of the structure it is therefore not possible to acquire any measurements and at the same time one have to make an estimate for the boundary conditions. Both of these effects, i.e. missing measurements and possibly incorrect boundary conditions, can potentially contribute greatly to the inaccuracy of the identified fields. In a civil engineering an example of this kind can be represented by a long wall from which only a small section is intended to be examined, see Fig. 43. Another example can be represented by a chimney shaft or other technical facilities in buildings, where dimensions as well as the boundary conditions are approximately known, but a placement of the sensor might be problematic. For such kind of tasks we compare the performance of various algorithm modifications described in Tab. 1.

First, we examine an L-shaped domain where certain parts of the boundary are not accessible. As a consequence, measurements can not be conducted on such boundaries and one also have to come up with an approximate assumptions on the boundary conditions. The domain and its discretisation that is utilised to generate error-less data is shown in Fig. 33a whereas the domain with its discretisation used in the identification process is shown in Fig. 33b. In addition to different discretisation, the domain in Fig. 33a is extended by 1 m on two sides, which is essentially utilised in order to model non-zero fluxes at the boundary where zero flux is considered for the domain used to identify the parameters. In order to address solely the effect of additional fluxes on the identification algorithm performance, the results are compared to an identical experiment evaluated on a non-extended mesh, see

Fig. 34. Although we use different geometrical domains in both examples, see Fig. 33 and Fig. 34, parts of the domain that match dimensionally have identical discretisation. Therefore one can attribute the difference in results to the inexact assumptions on boundary conditions.

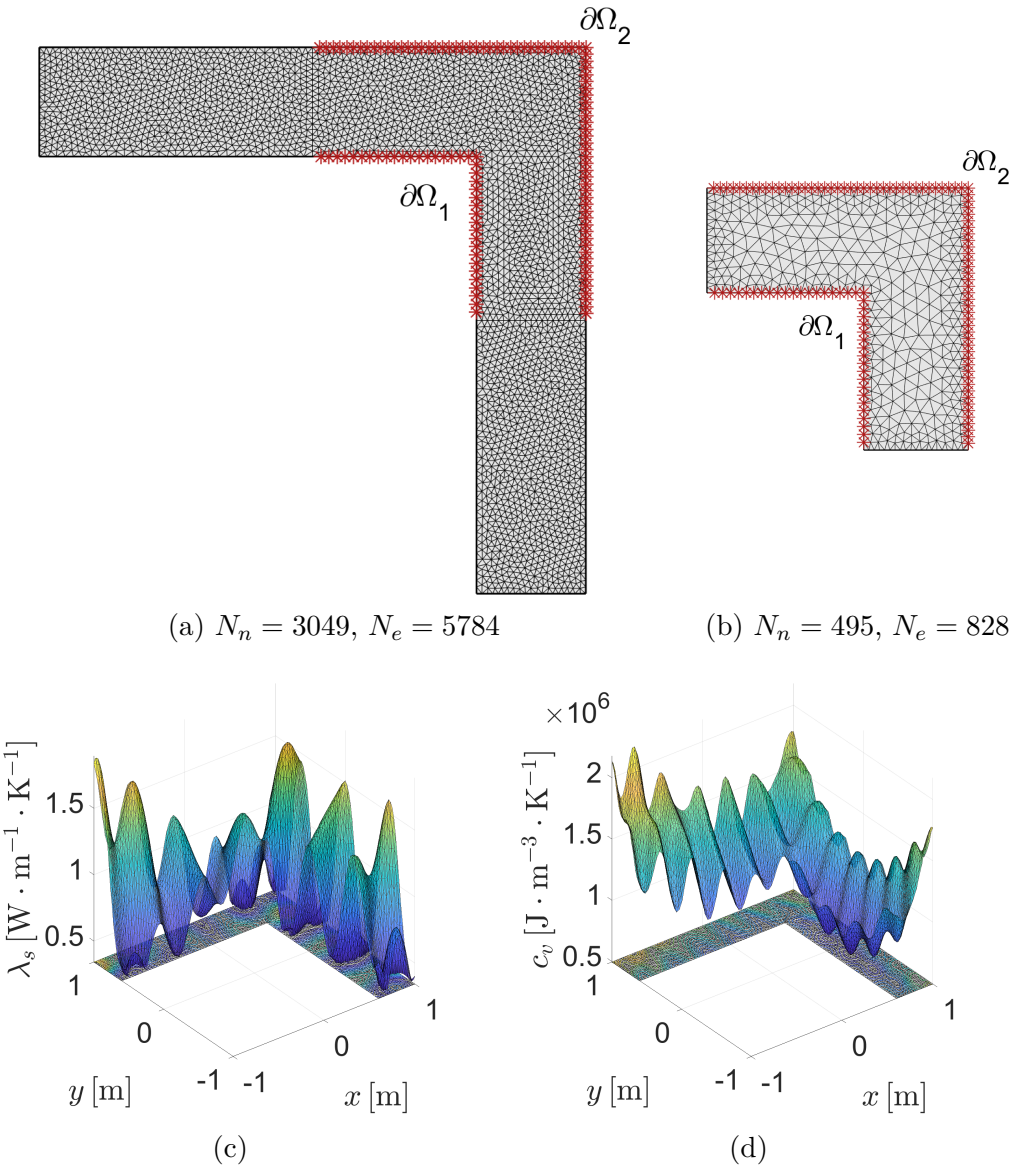

(a) $N_n = 3049$, $N_e = 5784$ (b) $N_n = 495$, $N_e = 828$

(c) (d)

Figure 33: L-shaped domain with discretisation utilised for (a) simulating real measurement and (b) for the identification, (c) distribution of the true thermal conductivity $\lambda_{s,\mathrm{true}}$, (d) distribution of the true volumetric heat capacity $c_{v,\mathrm{true}}$.

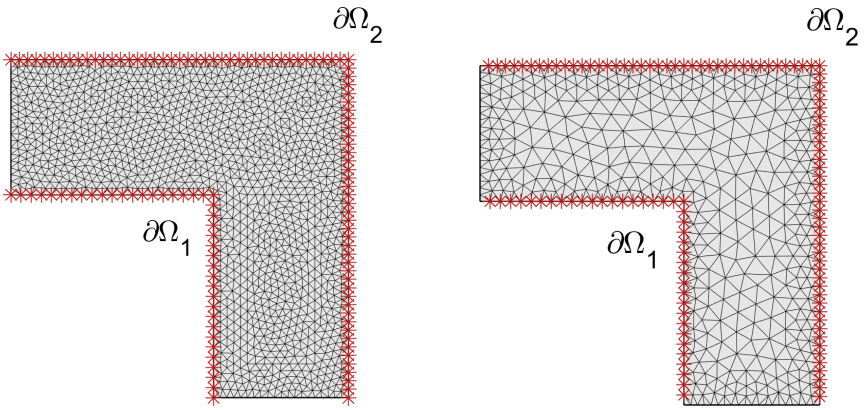

(a) $N_n = 1343$, $N_e = 2524$ (b) $N_n = 495$, $N_e = 828$

Figure 34: The reference L-shaped domain with discretisation utilised for (a) simulating real measurement and (b) for the identification.

In total there are $m_n = 118$ measurement nodes which with respect to the finite element mesh shown in Fig. 33b correspond to 73.75% representation of the whole boundary $\partial\Omega$. Boundary conditions correspond to a realistic environment with $m_t = 216$ observations and are set in the following way

$$\begin{aligned} \lambda_s(x)\frac{\partial u}{\partial n}(x,t)|_{\partial\Omega_1} &= 10 \cdot (u(x,t) - T_1(t))\,, \\ \lambda_s(x)\frac{\partial u}{\partial n}(x,t)|_{\partial\Omega_2} &= 10 \cdot (u(x,t) - T_2(t))\,, \\ \lambda_s(x)\frac{\partial u}{\partial n}(x,t)|_{\partial\Omega_3} &= 0, \end{aligned} \tag{4.25}$$

where the environmental temperatures $T_1(t)$ and $T_2(t)$ are shown in the following figure.

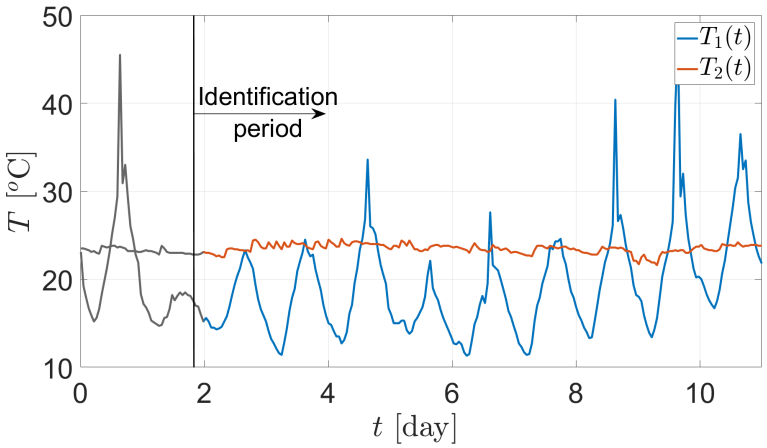

Figure 35: Interior (T_2) and exterior (T_1) temperatures, data included in the calculation spans from day 2 to 11.

In order to visualise the magnitude of fluxes in each direction in particular section of the domain, we employ the following formula

$$\begin{bmatrix} q_n(t) \\ q_t(t) \end{bmatrix} = \mathbf{q}(t) = \oint_{\mathcal{C}} -\mathbf{W}_{\mathcal{C}} \left(\lambda_s(\mathbf{x}) \boldsymbol{\nabla} u(\mathbf{x}, t)\right) \mathrm{d}\mathbf{x}, \tag{4.26}$$

where fluxes in $\mathbf{q}$, i.e. its normal (q_n) and tangent (q_t) components, are obtained as line integrals evaluated along the curve $\mathcal{C}$, which is in our case represented by a section $\mathcal{C}_1$ or $\mathcal{C}_2$, see Fig. 37a. The matrix $\mathbf{W}_{\mathcal{C}}$ is of the following form

$$\mathbf{W}_{\mathcal{C}} = \begin{bmatrix} \mathbf{n}^T \\ \mathbf{t}^T \end{bmatrix}, \tag{4.27}$$

where $\mathbf{n} \in \mathbb{R}^2$ and $\mathbf{t} \in \mathbb{R}^2$ are unit normal and tangent vectors with respect to the given section $\mathcal{C}$. Note that in our case $\mathbf{W}_{\mathcal{C}}$ is independent of spatial coordinates since either $\mathcal{C}_1$ or $\mathcal{C}_2$ are straight lines and the vectors $\mathbf{n}$ and $\mathbf{t}$ are constant along the sections $\mathcal{C}_1$ and $\mathcal{C}_2$.

In Fig. 36 one can see that the evolution of fluxes in time in particular cuts, whereas in Fig. 37, one can see that the distribution of fluxes for each separate direction in domain in time $t = 10.6$ days. The important remark here is that $q_n(t)$ in Fig. 36 is relatively small to $q_t(t)$ but non-zero, which addresses the mismatch between the synthetic reality and assumption in a non-extended domain. Figures in 37 provide an illustration of relative flux magnitudes in each direction. Although the tangential flux is of vague physical meaning, with the assumption that fluxes q_t perpendicular to the particular section $\mathcal{C}$ are not changing significantly, which is true in our case, it can be imagined as an average flux in the perpendicular section of the same length.

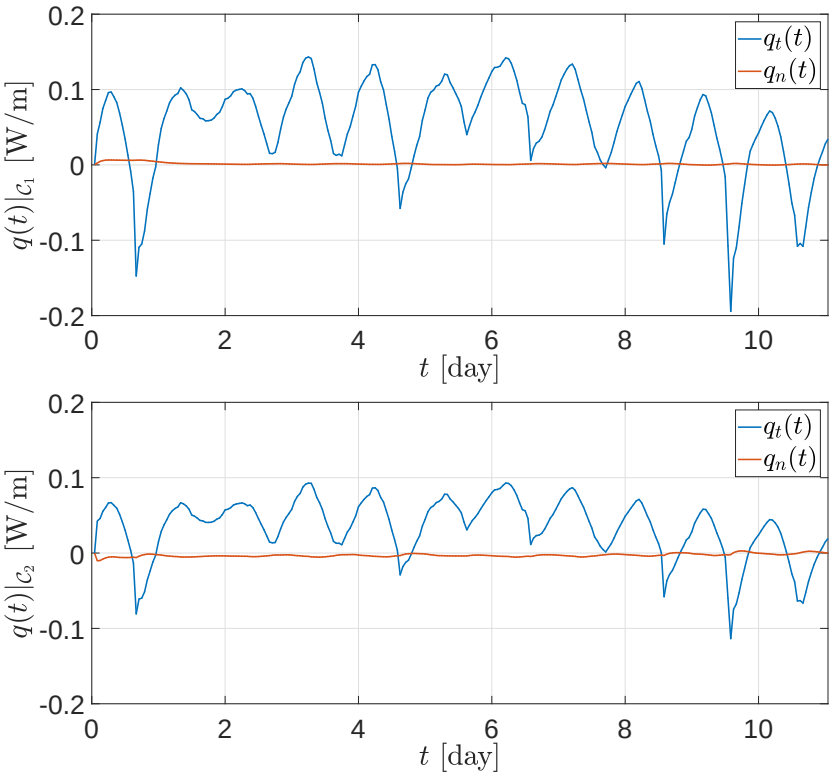

Figure 36: Fluxes along cuts $\mathcal{C}_1$ (upper) and $\mathcal{C}_2$ (bottom).

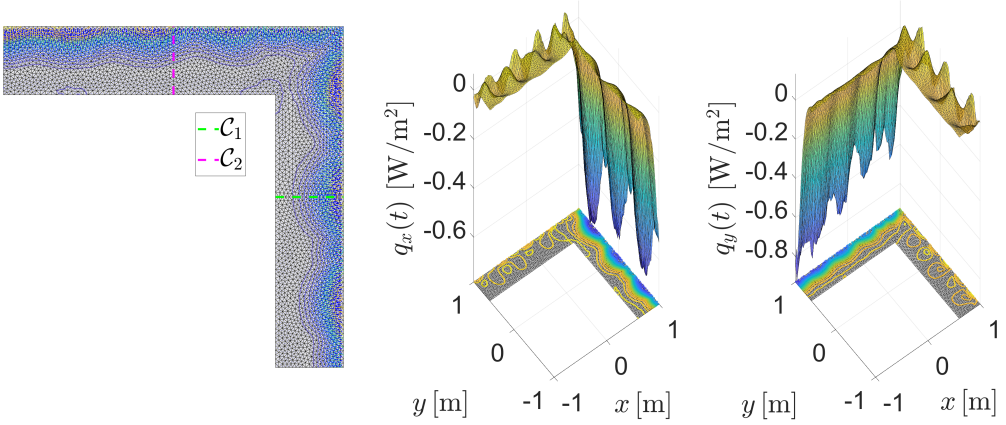

(a) (b) (c)

Figure 37: The position of the cuts $\mathcal{C}_1$ and $\mathcal{C}_2$ with contours of magnitudes of fluxes $\|\mathbf{q}\|$ (a), distribution of individual fluxes q_x (b) and q_y (c) in the domain.

The following figures show the evolution of errors for the extended L-shaped domain on the measured temperature ε_u (see Fig. 38) and on the identified parameters ε_{λ_s} (see Fig. 39) and ε_{c_v} (see Fig. 40). The computation time, number of iterations and errors in the last iteration are listed in Tab. 3 and Tab. 4, respectively. For better overall clarity, each of the errors is further divided into four separate figures containing the results for reference methods Θ, basic and $LSH^2_{0,NM}$ and its modifications solved by various methods.

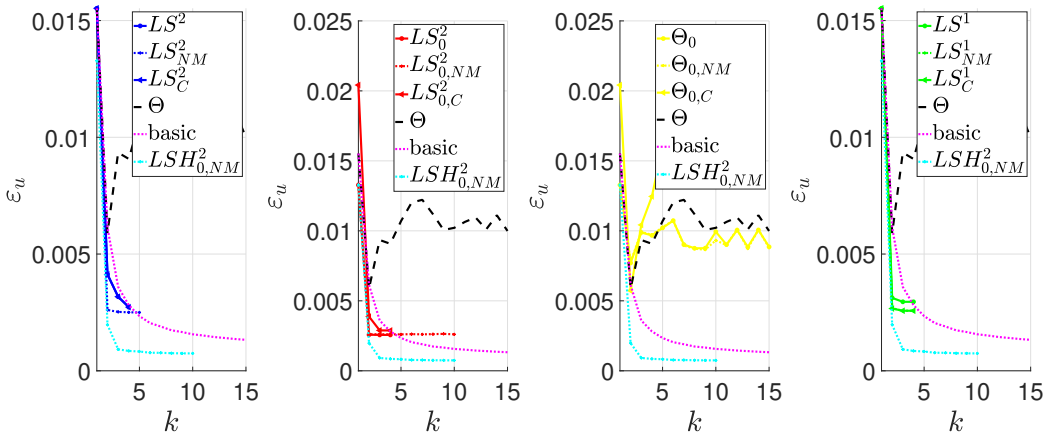

Figure 38: Errors on measured temperatures computed for different approaches; Analysis of the extended L-shaped domain.

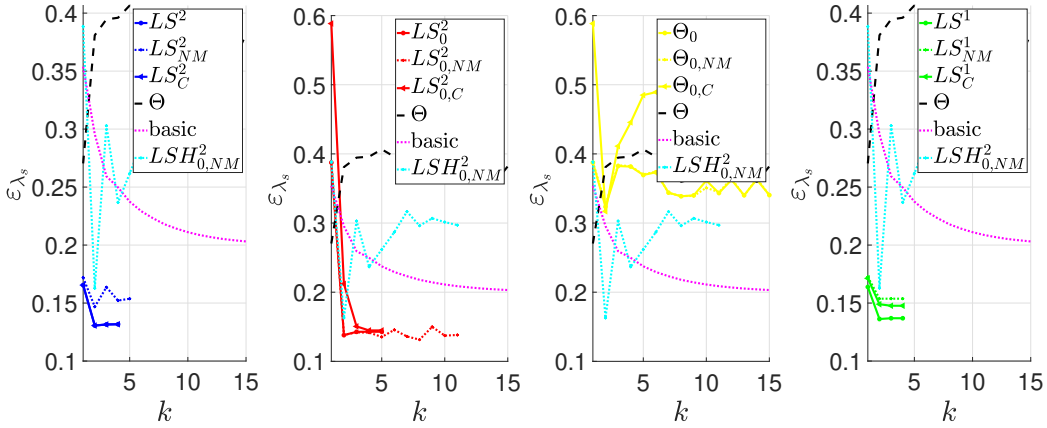

Figure 39: Errors on the identified parameter $\boldsymbol{\lambda}_s$ utilising different approaches for the extended L-shaped domain.

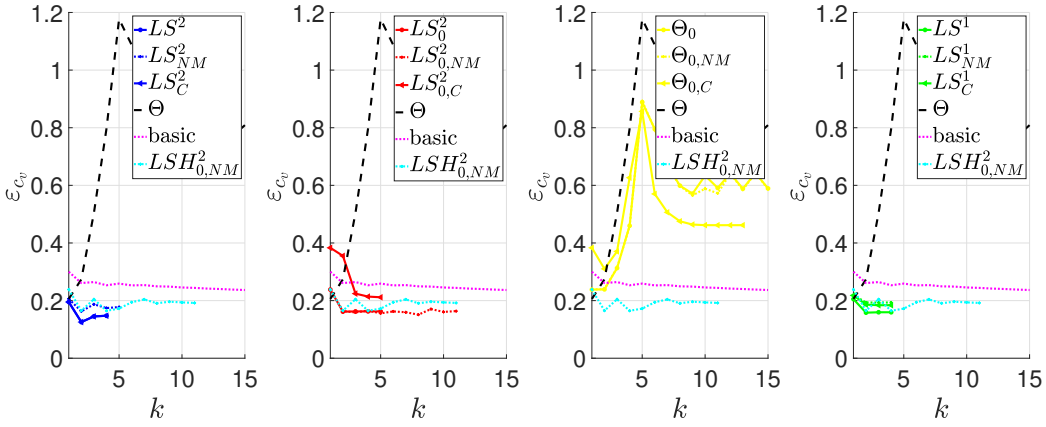

Figure 40: Errors on the identified parameter $\mathbf{c}_v$ utilising different approaches for the extended L-shaped domain.

In this particular example one can notice that the method employing the positivity operator T_p^{exp} without a line-search algorithm does not converge in terms of the observed quantity $\mathbf{u}_m$, i.e. ε_u. On the other hand, $LSH^2_{0,NM}$ converges the fastest and basic the slowest as one would expect. The reason for this is that methods employing line-search algorithm and/or hyper-parameter search modify the one step update $\delta\mathbf{\Theta}_k$ in each iteration in order to achieve lower overall error ε_u. This on one hand prevents the algorithm from divergence but at the same time is directing the overall solution $\mathbf{\Theta}_k$ towards one of the closest local minima. Note that even though the value of ε_u in the last iteration ranges from $\varepsilon_u = 0.00074$ for $LSH^2_{0,NM}$ to $\varepsilon_u = 0.00133$ for the basic method (see Tab. 4). It is in both cases insignificant relative to the expected error of the measuring equipment. In order to support this claim, in each time instance we select the highest value of ratio $|\mathbf{u}_m/\mathrm{F}(\Theta_{\mathrm{rec}})|$ across all nodes located on Γ_m, where $\mathbf{u}_m$ is the measured temperature and $\mathrm{F}(\Theta_{\mathrm{rec}})$ is the model response. The resulting evolution in time is shown in the following figure.

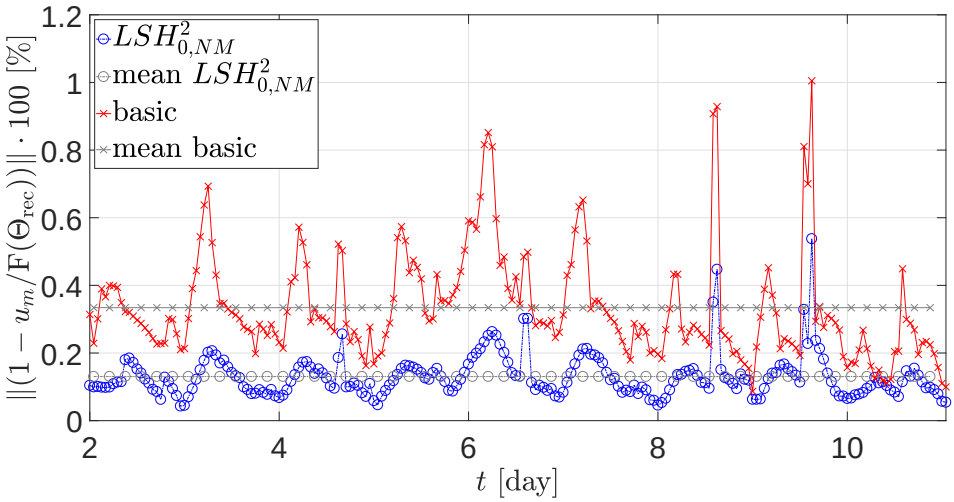

Figure 41: The highest discrepancy across all nodes located on Γ_m in time for extended L-shaped domain.

Convergence towards the local extreme can be observed in particular in Fig. 39, where the error ε_{λ_s} increases sharply after the first iteration which can be associated with finding an opposite direction $\delta\boldsymbol{\Theta}$. More precisely the two consecutive iterations have the property of $\delta\boldsymbol{\Theta}_{k-1} \cdot \delta\boldsymbol{\Theta}_k < 0$, where $\cdot$ is the scalar product, meaning that the newly acquired vector $\delta\boldsymbol{\Theta}_k$ is loosely speaking taking an opposite direction relative to the previous step $\delta\boldsymbol{\Theta}_{k-1}$.

Also from Fig. 39 and Fig. 40, it can be seen that particular choice of the boundary conditions together with the domain shape, measurements and included error lead to the several possible realisations of identified parameter field. Although more sophisticated algorithm is able to find a better overall solution regarding the observed quantity $\mathbf{u}_m$, it does not necessarily lead to better approximation of the underlying field.

In the following table we summarise the total computational time t_{comp} needed for the identification and the number of iterations k for each method. In order to distinguish the identification algorithm performance for the extended and reference domain without the necessity to dive deep into the numbers we introduce the following colour coding: higher values relative to the other solution are coloured in red, lower in green, and unchanged values are left black. The same applies for the table containing errors (see Tab. 4). By comparing the computational times for the reference and extended domains (see the third and the sixth column in Tab. 3), we find that the times do not change fundamentally and are proportionally dependent on the number of iterations. This is because the identification algorithm utilises in both cases identical domain discretisation, i.e. from the identification perspective

	Extended domain			Reference domain		
Method	k	t_{comp} [minutes]	t_{comp}/k	k	t_{comp} [minutes]	t_{comp}/k
LS^2	4	16.21	4.05	4	16.73	4.18
LS^2_{NM}	5	37.61	7.52	6	45.36	7.56
LS^2_C	4	29.66	7.42	4	29.83	7.46
LS^2_0	4	27.23	6.81	4	28.07	7.02
$LS^2_{0,NM}$	10	62.04	6.20	8	51.65	6.46
$LS^2_{0,C}$	4	26.32	6.58	4	27.07	6.77
LS^1	4	26.48	6.62	4	26.38	6.60
LS^1_{NM}	4	26.58	6.65	4	26.81	6.70
LS^1_C	4	26.86	6.71	4	28.03	7.01
Θ	15	100.40	6.69	15	100.86	6.72
Θ_0	15	102.57	6.84	15	101.35	6.76
$\Theta_{0,NM}$	15	107.58	7.17	10	67.78	6.78
$\Theta_{0,C}$	12	76.27	6.36	9	63.08	7.01
basic	15	119.85	7.99	15	120.10	8.01
$LSH^2_{0,NM}$	10	80.57	8.06	4	34.98	8.74

Table 3: Computational times t_{comp} and number of iterations k utilising different approaches for the extended and reference L-shaped domain.

the only difference between these two examples lies in the vector $\mathbf{u}_m$, and thus the discrepancy refers to the standard deviation of the computing equipment. Focusing on the average time per iteration t_{comp}/k, i.e. the fourth or seventh column of Tab. 3, we can say that individual methods are relatively balanced relative to each other and the main differences can be attributed to the convergence of particular method for solving the line search problem. This is especially true in the case of LS^2, LS^2_{NM} and LS^2_C which are essentially the same algorithms with a different minimisation method for the line search, but LS^2_{NM} and LS^2_C have almost twice the computing time compared to LS^2. Note that this behaviour is extremely case dependent since for the other triplets, i.e. $\{LS^2_0, LS^2_{0,NM}, LS^2_{0,C}\}$ and $\{LS^1, LS^1_{NM}, LS^1_C\}$, the computational times are indistinguishable (see Tab. 3).

Focusing on the second table containing errors ε_u, ε_{λ_s} and ε_{c_v} while omitting the results for diverging Θ and its modifications, one can see the colour coding reveals a clear pattern. That is, the results for the reference domain show overall lower errors with an occasional twist in results within 7% in

the case of LS_0^2, $LS_{0,NM}^2$ and LS^1 which is acceptable margin taking into account the ill-posed nature of the problem. Such outcomes are expected, since the identification algorithms are provided with a slightly different boundary conditions forcing it to compensate the mismatch on the identified fields.

	Extended domain			Reference domain		
Method	ε_u	ε_{λ_s}	ε_{c_v}	ε_u	ε_{λ_s}	ε_{c_v}
LS^2	0.00273	0.13173	0.14744	0.00273	0.12355	0.14316
LS_{NM}^2	0.00250	0.15373	0.17762	0.00234	0.13496	0.16189
LS_C^2	0.00273	0.13173	0.14744	0.00273	0.12355	0.14316
LS_0^2	0.00256	0.14280	0.16255	0.00240	0.14855	0.17056
$LS_{0,NM}^2$	0.00260	0.13815	0.16353	0.00249	0.14129	0.16526
$LS_{0,C}^2$	0.00288	0.14472	0.21152	0.00265	0.13597	0.20689
LS^1	0.00295	0.13691	0.15955	0.00243	0.13221	0.17081
LS_{NM}^1	0.00257	0.15376	0.19334	0.00248	0.13556	0.17795
LS_C^1	0.00257	0.14769	0.18402	0.00244	0.13264	0.17164
Θ	0.00999	0.38202	0.80899	0.01200	0.38557	0.89114
Θ_0	0.00886	0.36303	0.64383	0.00985	0.35500	0.63818
$\Theta_{0,NM}$	0.00879	0.36453	0.64491	0.00938	0.34726	0.58946
$\Theta_{0,C}$	0.01802	0.49428	0.46180	0.01851	0.51046	0.46005
basic	0.00133	0.20312	0.23678	0.00113	0.20186	0.23326
$LSH_{0,NM}^2$	0.00074	0.29698	0.19188	0.00053	0.20534	0.17233

Table 4: Errors in last iteration utilising different approaches for the extended and reference L-shaped domain.

As an example of the identified fields we pick the results utilising $LSH_{0,NM}^2$ method, that is the best performing in terms of ε_u and LS^2, which achieves the lowest error on both identified fields. The comparison can be viewed on the following figures.

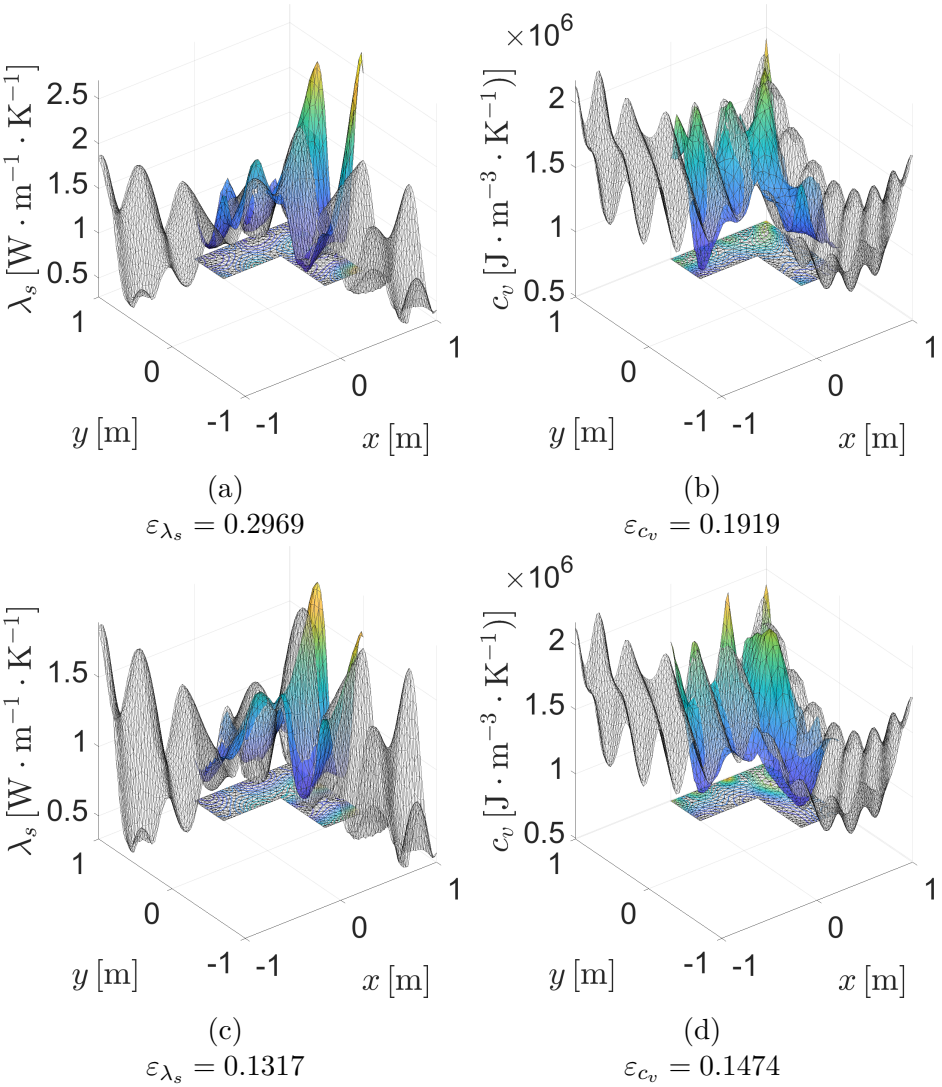

Figure 42: Identified fields for the L-shaped extended domain (a,b) utilising $LSH^2_{0,NM}$ method and (c,d) utilising LS^2 method.

Despite nearly double the error in ε_{λ_s} between these methods, we can observe almost identical fields except of a big spike in the rightmost corner of the identified field reaching a value of approximately 2.5, where the true value is just about 1.5. While still focusing on the same figures, i.e. Fig. 42a and Fig. 42c, one can notice that the $LSH^2_{0,NM}$ tends to overestimate the fluctuations as it falls more aggressively to a local minimum whereas LS^2 is more conservative in its predictions. This can be also seen in the case of c_v in Fig. 42, where the gap between the methods in terms of the error ε_{c_v} is not that significant (see the caption for Fig. 42b and Fig. 42d). In this case

LS^2 provides slightly more definition, i.e. the shape of $c_{v,\mathrm{rec}}$ approximates the underlying field $c_{v,\mathrm{true}}$ better. This is most visible especially in the areas where assumptions on the boundary conditions have been made.

Within this section we provide a second example concerning a similar practical situation, i.e. possibly wrong assumptions on the boundary conditions with a missing measurements. However, in this case we intent to simplify the settings. Similarly to the previous example we perform two sets of computations, where one serves as a reference solution on the non-extended domain. We consider the reference domain to be a rectangle of sides equal to 0.5 m and 2 m, see Fig. 43b. The extended domain is prolonged by 1 m on both sides, see Fig. 43a. Figures 43a and 43b represent the domain-discretisation setup for the scenario considering wrong assumptions on the boundary conditions. Measurements $\mathbf{u}_m$ for the reference solution are calculated using the non-extended domain with the finite element mesh discretisation shown in Fig. 43a and the identification algorithm utilised domain-discretisation shown in Fig. 43b. There are in total $m_n = 98$ measurement nodes located along the boundaries $\partial\Omega_1$ and $\partial\Omega_2$ which correspond to 79.03% representation of the whole boundary $\partial\Omega$ with respect to the reference domain in Fig. 43b. Regarding the boundary conditions, the ambient temperature, i.e. T_1 and T_2 in eq. (4.28), stays the same as in the previous example, see Fig. 35. Such loading settings provide a more clear picture of the directionality of heat fluxes in the domain.

$$\begin{aligned}
\lambda_s(x)\frac{\partial u}{\partial n}(x,t)|_{\partial\Omega_1} &= 10\cdot(u(x,t)-T_1(t))\,,\\
\lambda_s(x)\frac{\partial u}{\partial n}(x,t)|_{\partial\Omega_2} &= 10\cdot(u(x,t)-T_2(t))\,,\\
\lambda_s(x)\frac{\partial u}{\partial n}(x,t)|_{\partial\Omega_3} &= 0,\\
\lambda_s(x)\frac{\partial u}{\partial n}(x,t)|_{\partial\Omega_4} &= 0.
\end{aligned} \tag{4.28}$$

.

The spatial distribution of material fields $\boldsymbol{\lambda}_{s,\mathrm{true}}$ and $\mathbf{c}_{v,\mathrm{true}}$ is identical in shape and only differ in magnitude, see Fig. 43c and 43d. In this particular case we deliberately choose a simpler field but at the same time we maintain its key aspect which is represented by omnidirectional spatial variability. This option promises simplified reading of the results as well as revealing the solver limitations. In order to provide better overall readability of the spatial distributions in Fig. 42c and 42d, the axes are scaled accordingly.

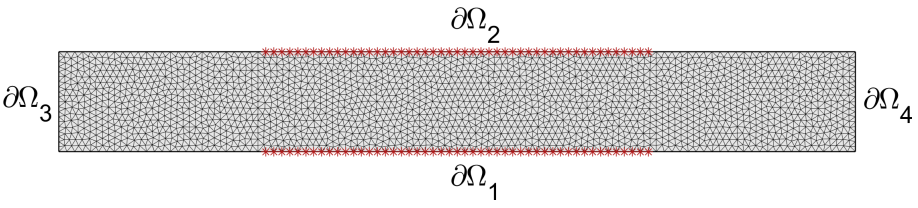

(a) $N_n = 2145$, $N_e = 4048$

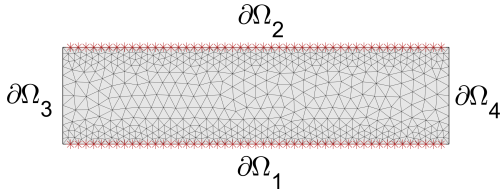

(b) $N_n = 589$, $N_e = 1052$

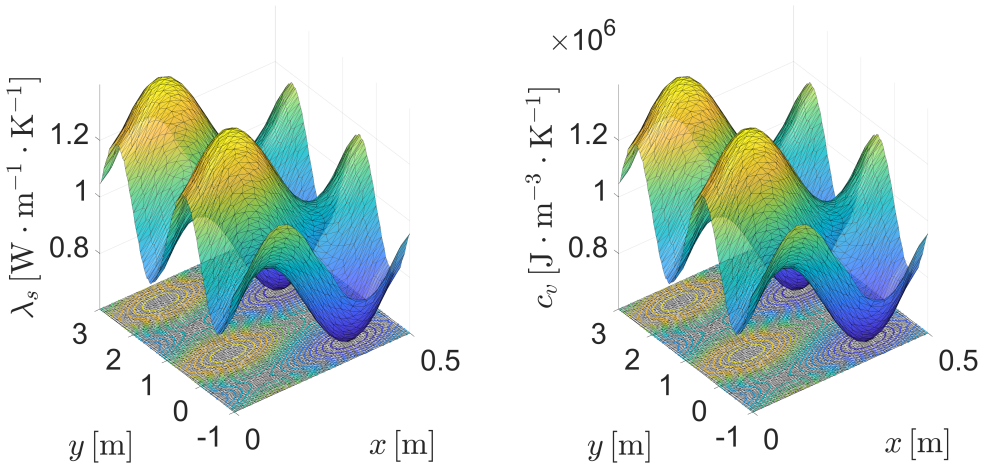

(c) (d)

Figure 43: Rectangular wall domain with discretisation utilised for (a) simulating real measurement and (b) for the identification, (c) distribution of the true thermal conductivity $\lambda_{s,\text{true}}$, (d) distribution of the true volumetric heat capacity $c_{v,\text{true}}$.

In the following figures, one can notice an important phenomena. Even though all methods tend to numerically converge in terms of ε_u, i.e. the model responses $\mathrm{F}(\mathbf{\Phi})$ are approaching the measured temperatures $\mathbf{u}_m$, they have the opposite tendency in the parameters ε_{λ_s} and ε_{c_v} except for methods $LSH^2_{0,NM}$ and the basic method. The divergence in ε_{λ_s} and ε_{c_v} is due to the ambiguity of the identification task resulting from the specific loading-measurement scheme. This is described in more detail in the paragraph above Fig. 47.

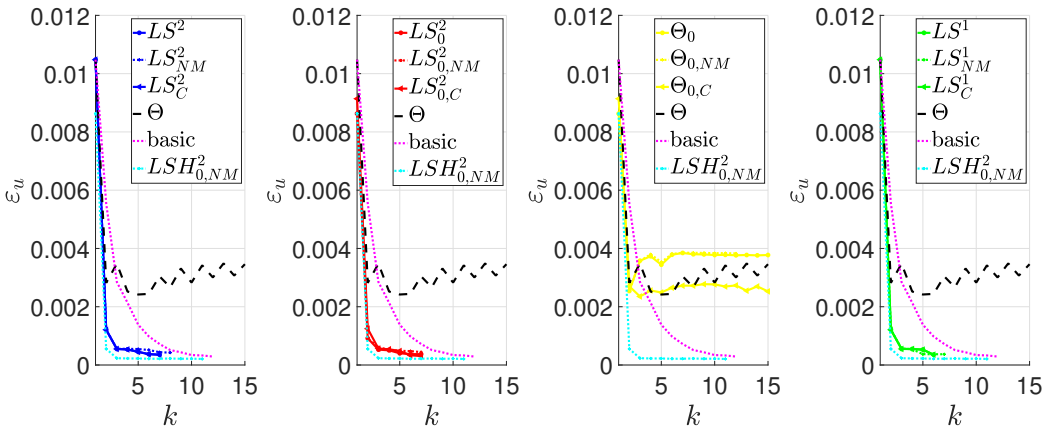

Figure 44: Errors on measured temperatures computed for different approaches; Analysis of the extended rectangular wall domain.

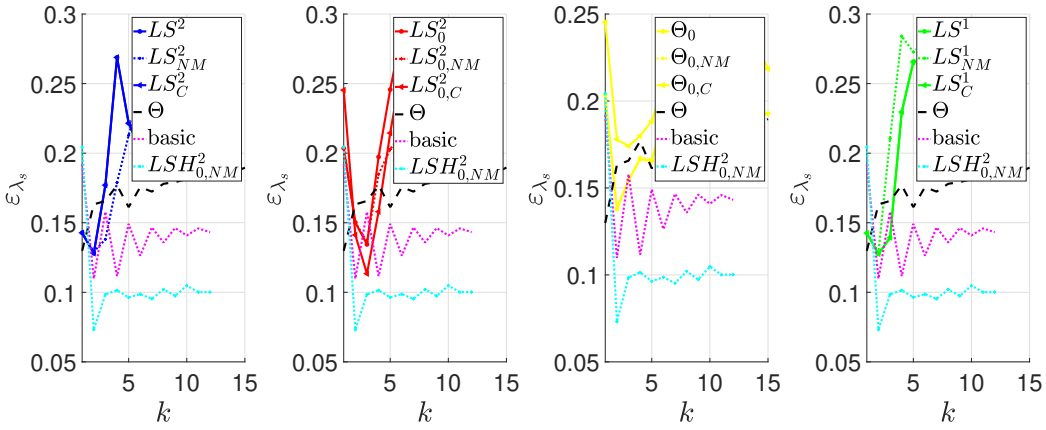

Figure 45: Errors on the identified parameter $\boldsymbol{\lambda}_s$ computed for different approaches; Analysis of the extended rectangular wall domain.

As far as Tab. 5 is concerned, although the colour coding consistently shows faster computational times per iteration in the case of extended domain, upon closer examination we find that the difference between the times it takes to evaluate one iteration for the reference and extended domain is almost indistinguishable. With the exception of method $LSH^2_{0,NM}$, the time difference for all methods is below 10%. This level of deviation may be attributed to the variations in the secondary computations, such as the line search minimisation problem.

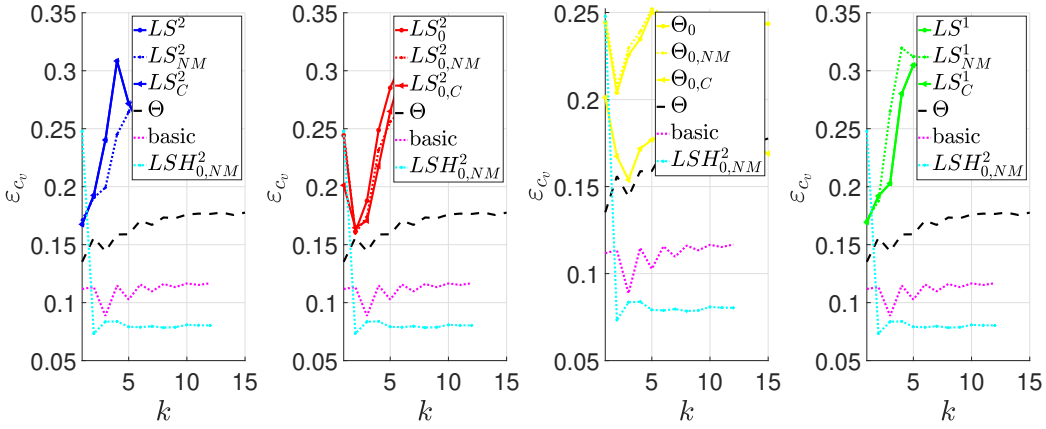

Figure 46: Errors on the identified parameter $\mathbf{c}_v$ computed for different approaches; Analysis of the extended rectangular wall domain.

	Extended domain			Reference domain		
Method	k	t_{comp} [minutes]	t_{comp}/k	k	t_{comp} [minutes]	t_{comp}/k
LS^2	7	37.50	5.36	10	59.32	5.93
LS^2_{NM}	8	45.64	5.71	10	61.89	6.19
LS^2_C	7	41.99	6.00	10	64.78	6.48
LS^2_0	7	41.99	6.00	8	52.53	6.57
$LS^2_{0,NM}$	7	42.37	6.05	8	53.06	6.63
$LS^2_{0,C}$	7	44.72	6.39	6	40.77	6.80
LS^1	6	37.55	6.26	4	26.96	6.74
LS^1_{NM}	7	43.65	6.24	6	40.26	6.71
LS^1_C	6	38.43	6.40	4	27.00	6.75
Θ	15	94.83	6.32	15	101.72	6.78
Θ_0	15	95.55	6.37	15	102.82	6.85
$\Theta_{0,NM}$	12	76.96	6.41	15	103.00	6.87
$\Theta_{0,C}$	15	96.55	6.44	15	102.93	6.86
basic	12	77.43	6.45	12	81.97	6.83
$LSH^2_{0,NM}$	11	73.43	6.68	9	68.52	7.61

Table 5: Computational times t_{comp} and number of iterations k utilising different approaches for the extended and reference wall domain.

Regarding errors ε_u, ε_{λ_s} and ε_{c_v} in Tab. 6, one can see a similar scenario as in the previous example, i.e. results for the reference domain exhibits

lower errors in ε_{λ_s} and ε_{c_v} in comparison to the extended domain. The first exception for this is the $LSH^2_{0,NM}$ method having a significant drop in errors ε_{λ_s} and ε_{c_v} compared to the reference solution. The second exception is represented by the whole family of methods containing $\{\Theta, \Theta_0, \Theta_{0,NM}, \Theta_{0,C}\}$ which is, judged by the evolution of error ε_u, on the very edge of stability and can thus behave unpredictably.

	Extended domain			Reference domain		
Method	ε_u	ε_{λ_s}	ε_{c_v}	ε_u	ε_{λ_s}	ε_{c_v}
LS^2	0.00035	0.20128	0.25024	0.00026	0.16083	0.19929
LS^2_{NM}	0.00042	0.24750	0.29670	0.00035	0.25057	0.29079
LS^2_C	0.00035	0.20128	0.25024	0.00026	0.16083	0.19929
LS^2_0	0.00037	0.28482	0.30608	0.00028	0.20881	0.24368
$LS^2_{0,NM}$	0.00044	0.23188	0.27460	0.00037	0.22237	0.26401
$LS^2_{0,C}$	0.00031	0.27595	0.30693	0.00026	0.26431	0.29066
LS^1	0.00035	0.26698	0.30555	0.00043	0.14525	0.20134
LS^1_{NM}	0.00037	0.28014	0.31685	0.00029	0.26445	0.29638
LS^1_C	0.00035	0.26658	0.30525	0.00043	0.14549	0.20145
Θ	0.00346	0.18960	0.17763	0.00350	0.18688	0.17779
Θ_0	0.00377	0.19305	0.24359	0.00378	0.19542	0.24469
$\Theta_{0,NM}$	0.00383	0.19309	0.24674	0.00383	0.19792	0.24814
$\Theta_{0,C}$	0.00253	0.23328	0.17246	0.00248	0.24041	0.17493
basic	0.00029	0.14318	0.11672	0.00031	0.13257	0.10824
$LSH^2_{0,NM}$	0.00021	0.10017	0.08036	0.00012	0.13321	0.14065

Table 6: Errors in last iteration utilising different approaches for the extended and reference wall domain.

In this example, we show the identified fields based on methods $LS^2_{0,NM}$ and $LSH^2_{0,NM}$. These two approaches distinguish only in choice of the hyper-parameter. Interesting is that their results compared to other examples differ the most. Note that the true fields $\boldsymbol{\lambda}_{s,\text{true}}$ and $\mathbf{c}_{v,\text{true}}$ are depicted in their full size, i.e. even for the extended part of the domain, meanwhile the identified fields occupy only the area of interest. Due to this, the aspect ratio had to be modified so that the fields can be displayed legibly.

The whole picture behind the divergence in ε_{λ_s} and ε_{c_v} in Fig. 45 and 46 can be understood to its full extent only after viewing the resulting identified fields in Fig. 47(a,b). One can notice that the shape of the fields in sections

parallel to the y axis is identified considerably well, while the ambiguity of the identification manifests itself in the direction perpendicular to the y axis. Although individual fields λ_s and c_v are not identified accurately, Fig. 47(a,b) shows a particular pattern indicating that the governing equation in eq. (2.19) is probably not controlled by two individual parameters but rather by a one parameter composed of both. And that is the spatial distribution of the thermal effusivity $e_s = \sqrt{\lambda_s \cdot c_v}$ that carries the information about the thermal energy transfers.

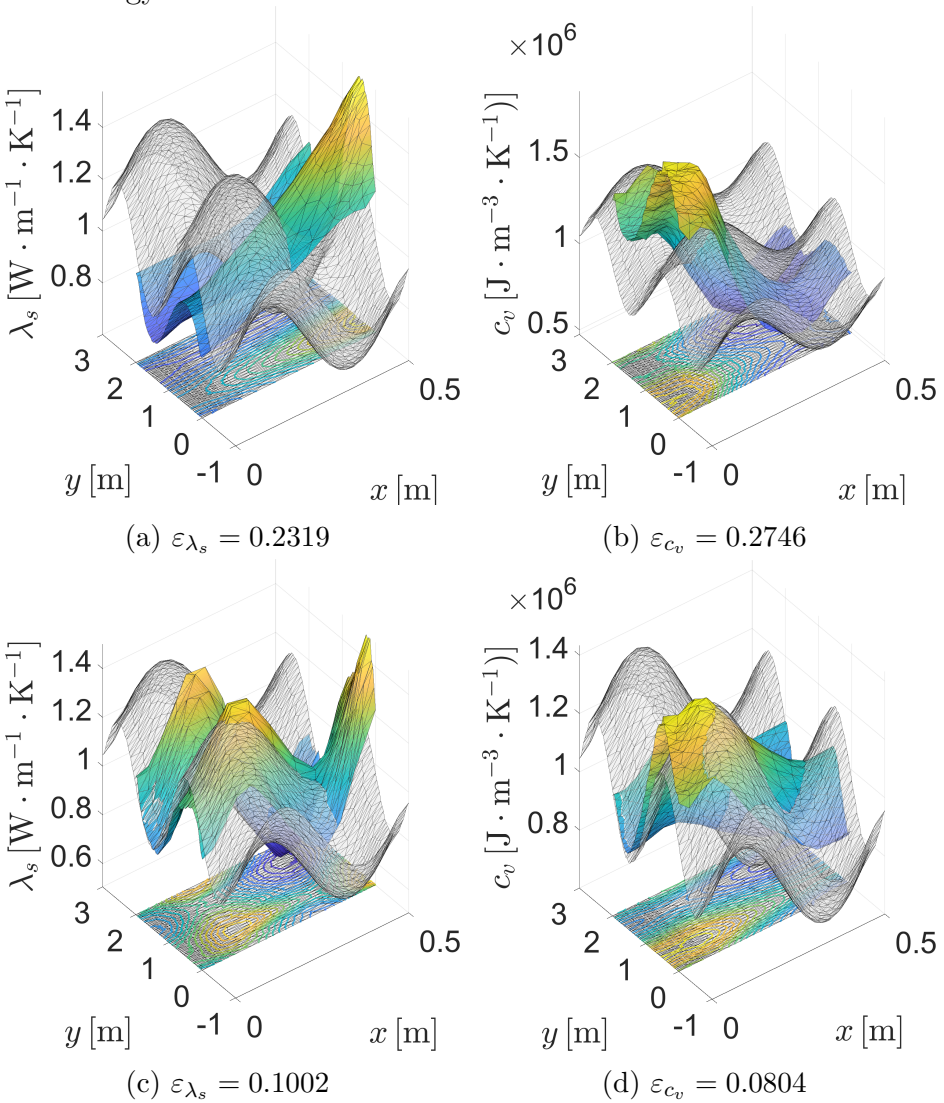

(a) $\varepsilon_{\lambda_s} = 0.2319$ (b) $\varepsilon_{c_v} = 0.2746$

(c) $\varepsilon_{\lambda_s} = 0.1002$ (d) $\varepsilon_{c_v} = 0.0804$

Figure 47: Identified fields for the extended wall domain (a,b) utilising $LS^2_{0,NM}$ method and (c,d) utilising $LSH^2_{0,NM}$ method.

On the other hand, the thermal diffusivity $d = \lambda_s/c_v$, i.e. the measure

of how rapidly the temperature variations can be transmitted through the body, becomes irrelevant. The effect of ambiguity in one direction is present in all of the methods, although in $LSH^2_{0,NM}$ it is very significantly suppressed, which gives $LSH^2_{0,NM}$ an edge over other methods.

As the results indicate, the information about the underlying distribution of $\boldsymbol{\lambda}_s$ and $\mathbf{c}_v$ is entangled within the thermal effusivity. Note that this is the primary reason for convergence in ε_u while the vast majority of methods simultaneously diverges in ε_{λ_s} and ε_{c_v}. In other words, the ambiguity of the problem, where the dominant direction $\delta\boldsymbol{\Phi} = [\delta\boldsymbol{\lambda}_s, \delta\mathbf{c}_v]$ in the identification process is determined by a mutual product of parameters $\boldsymbol{\lambda}_s$ and $\mathbf{c}_v$, represents an unstable degree of freedom in the optimisation task. With this in mind, one could provide the regularisation term in eq. (3.11) with additional prior assumption regarding the mutual relation of the two parameters, i.e. to impose a measure of shape resemblance within the parameters. Such regularisation term could be defined in the following form

$$G_{\text{shape}}(\boldsymbol{\Phi}) = \|L(\phi_1) - L(\phi_2)\|_p = \|L(\lambda_s) - L(c_v)\|_p, \tag{4.29}$$

where L is the regularisation operator with its discrete form defined in eq. (3.12), and $\|\cdot\|_p$ is the ℓ_p norm. In fact, this has a real justification in a number of cases, but it limits or completely eliminates the possibility of identifying shape-differentiated fields such as the ones utilised in the previous example (see Fig. 33c and 33d).

The resulting fields regarding the thermal effusivity $\mathbf{e}_s$ with corresponding errors ε_{e_s} are depicted in the following figure

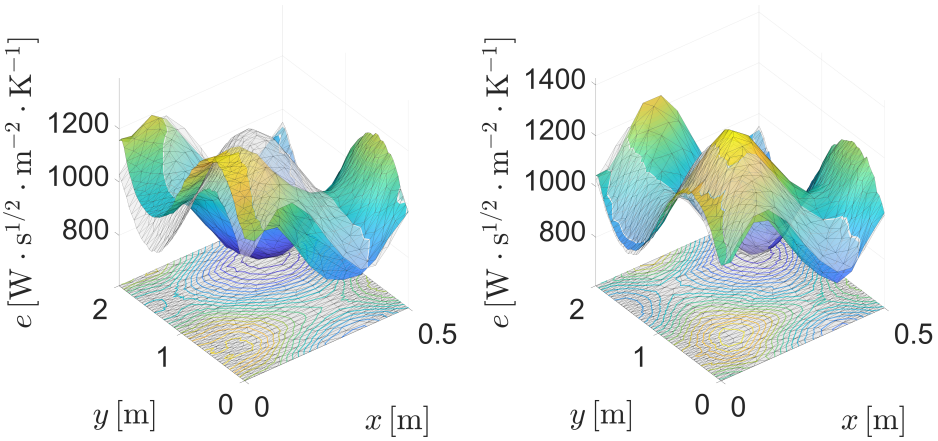

(a) $\varepsilon_{e_s} = 0.0635$

(b) $\varepsilon_{e_s} = 0.0278$

Figure 48: Identified thermal effusivity fields $\mathbf{e}_{s,\text{rec}}$ for the extended wall domain utilising (a) $LS^2_{0,NM}$ method and (b) $LSH^2_{0,NM}$ method.

From the caption below Fig. 48a and 48b one can see that the obtained errors ε_{e_s} are of much lower amplitude than in the case of either ε_{λ_s} or ε_{c_v}. Also visual perception in the case of Fig. 48b gives the impression of almost perfect identification.

4.3.3 Domain related issues

Since this work is mainly focused on the non-invasive identification it is sensible to consider situations, where wrong assumptions have been made on the internal part of the domain under consideration. This includes unpredicted caverns, cracks and hollow areas which are present in the synthetic experiment, but are unknown for the identification process, see for example Fig. 50. A different important aspect when considering domain related issues is also the finite element mesh refinement. In essence the numerical model represented here by the forward operator can not be more accurate or include all of the physical phenomena and imperfections of the real world structure. Therefore if one is not provided with experimental data, the synthetic experiment should always be performed on a more accurate model then the one that is utilised in the identification procedure. In fact one can utilise possibly a non-linear or coupled physics model, but in this work we perform the synthetic experiment with a finer finite element mesh of the same physical model. In order to prevent further bias, the finite element nodes of both meshes do not coincide with each other, i.e. they are not nested. The only exception for this rule are nodes on the boundary $\partial\Omega$ which coincide for both meshes in number and position in space.

We first start with a simple example of the square domain with a side length of 1 m and a centred hole with a diameter of 0.25 m, see Fig. 50. We examine the identification algorithm from two perspectives. The first one is the stability for two loading-measurement scenarios, where the combination #1 includes Fig. 49a with Fig. 50(a,b) and the second scenario combines Fig. 49(b,c) with Fig. 50(c,d). The second perspective is the ability to identify the approximate position of the hole. Note that due to the particular choice of boundary conditions (see eq. (4.30)) the true value of both parameters, i.e. $\lambda_{s,\text{true}}$ and $c_{v,\text{true}}$, in the area covered by the hole is zero. The boundary conditions for both loading-measurement scenarios are set according to eq. (4.30). Other parameters of the numerical solution except of the boundary conditions and domain shape with discretisation (see Fig. 50) are set as follows: the first loading-measurement scenario, i.e. the combination of Fig. 49a and Fig. 50(a,b), comprises $m_t = 125$ distinct time steps and $m_n = 82$ nodes located on the left and right sides of the domain which accounts for 51.25% representation of the whole boundary $\partial\Omega$. The second

loading-measurement scenario consists of a full $m_n = 160$ measurement array, i.e. the observed boundary Γ_m coincides with the free boundary $\partial\Omega$, and a more complex load conditions with $m_t = 425$ distinct time steps (see Fig. 49(b,c)).

$$\begin{aligned}
\lambda_s(x)\frac{\partial u}{\partial n}(x,t)|_{\partial\Omega_1} &= 10\cdot(u(x,t)-T_1(t))\,,\\
\lambda_s(x)\frac{\partial u}{\partial n}(x,t)|_{\partial\Omega_2} &= 10\cdot(u(x,t)-T_2(t))\,,\\
\lambda_s(x)\frac{\partial u}{\partial n}(x,t)|_{\partial\Omega_3} &= 10\cdot(u(x,t)-T_3(t))\,,\\
\lambda_s(x)\frac{\partial u}{\partial n}(x,t)|_{\partial\Omega_4} &= 10\cdot(u(x,t)-T_4(t))\,,\\
\lambda_s(x)\frac{\partial u}{\partial n}(x,t)|_{\partial\Omega_5} &= 0.
\end{aligned} \tag{4.30}$$

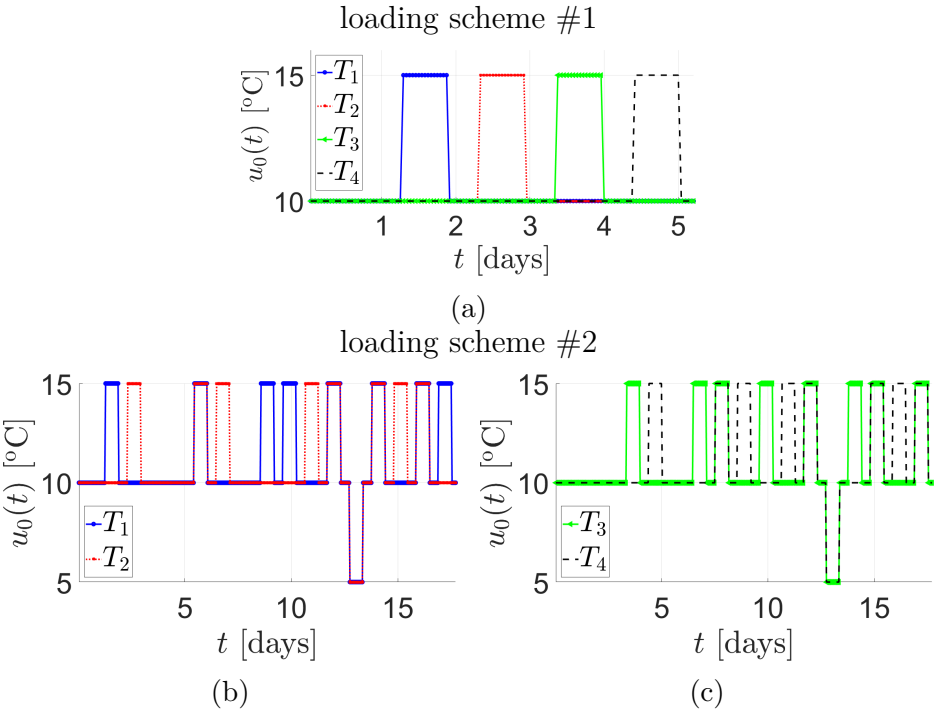

Figure 49: Evolution of boundary conditions in time for the square domain with a hole.

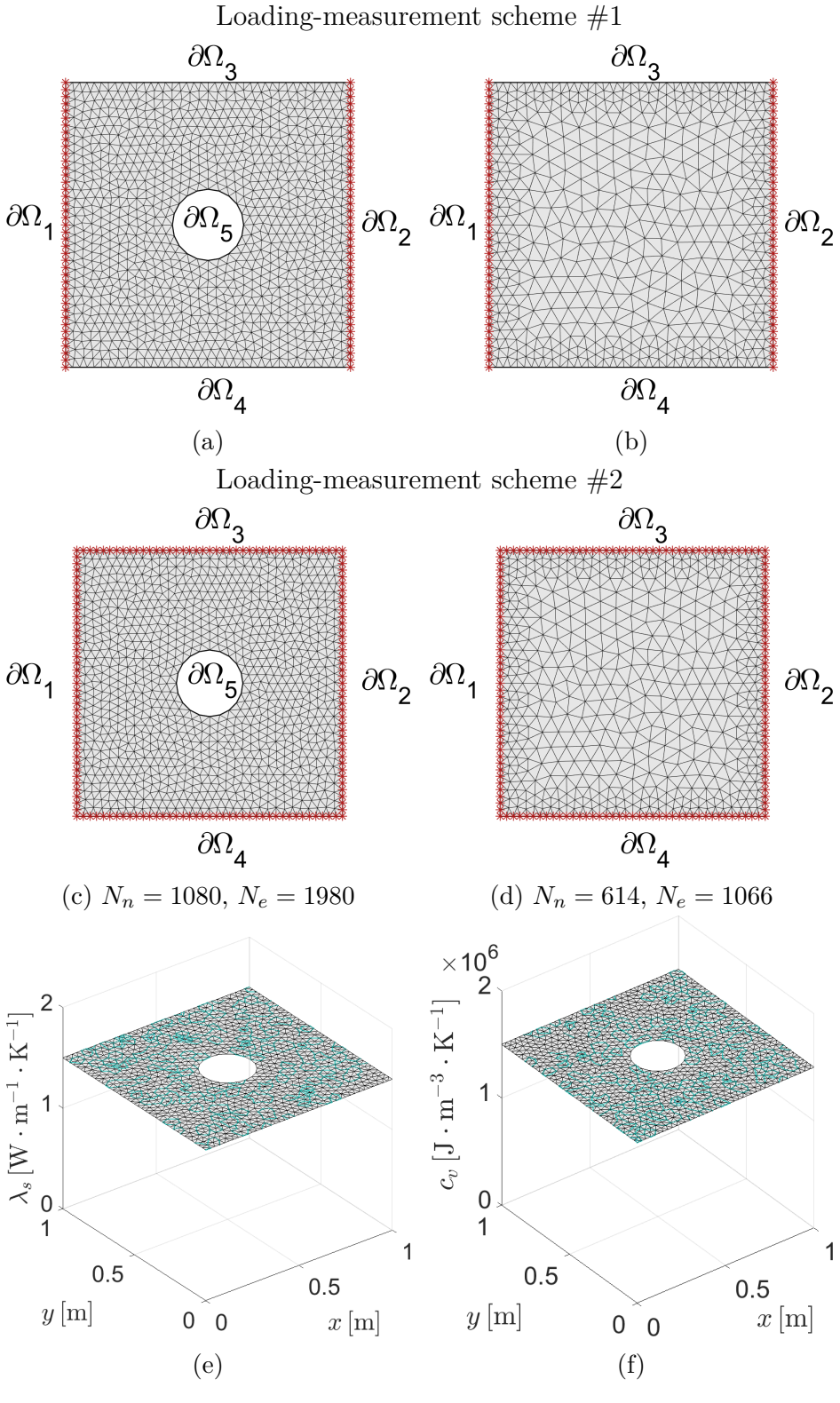

Figure 50: Square domain with discretisation utilised for (a,c) simulating real measurement and (b,d) for the identification, (e) true thermal conductivity $\lambda_{s,\mathrm{true}}$, (f) true volumetric heat capacity $c_{v,\mathrm{true}}$.

Convergence of individual methods for the monitored variable $\mathbf{u}_m$ and the identified fields $\boldsymbol{\lambda}_s$ and $\mathbf{c}_v$ is displayed in Fig. 51 to 53, respectively. The results from the last iteration are summarised in Tab. 7 and 8, and the identified fields for the two selected methods are displayed in Fig. 55 and 56. In order to compare the performance of distinct methods despite the diverging solution for $\boldsymbol{\Theta}$, the vertical axes in following figures are set to log-scale. Method $LSH^2_{0,NM}$ again shows the fastest convergence on the observed variable ε_u although the calculation lasts the longest (see Tab. 7). This is due to the fact that the errors come close to its trigger point of the stopping criteria in eqs. (3.52) to (3.54) but do not pass it.

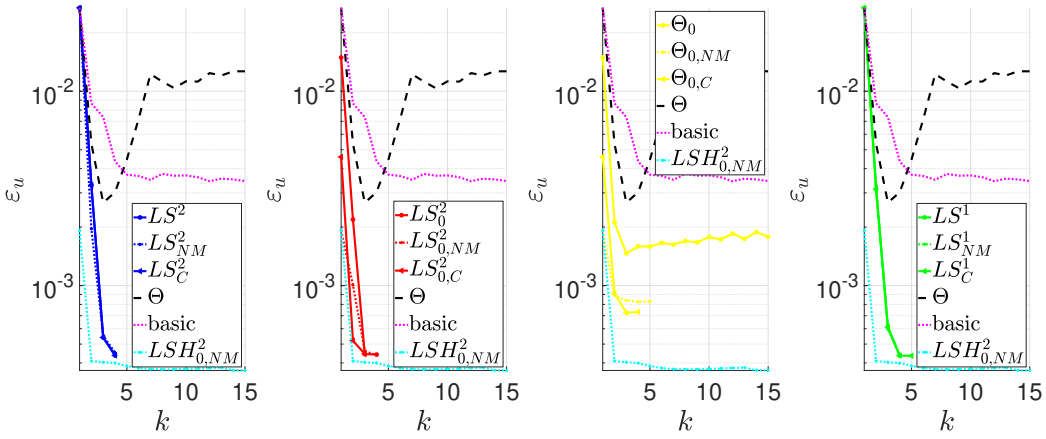

Figure 51: Errors on measured temperatures computed for different approaches; Analysis of the square domain with a hole (loading-measurement scenario #2).

An interesting finding is provided when we look at the difference between the plain method $\boldsymbol{\Theta}$ and its modification $\boldsymbol{\Theta}_0$, $\boldsymbol{\Theta}_{0,NM}$, $\boldsymbol{\Theta}_{0,C}$ in Fig. 51 to 53. The subscript 0 indicated an initial constant shift of the fields $\tilde{\boldsymbol{\Theta}}$ (see Tab. 1) just before the main Gauss-Newton iteration scheme introduces the spatial variability by adding some $\delta\boldsymbol{\Theta}$. In this particular example, where the true fields are close to spatial constants, adjusting the initial guess can be considered as another factor that can potentially prevent the algorithm from divergence. This also implies that the closer the identified field gets to the true one, the more stable the subsequent iteration is.

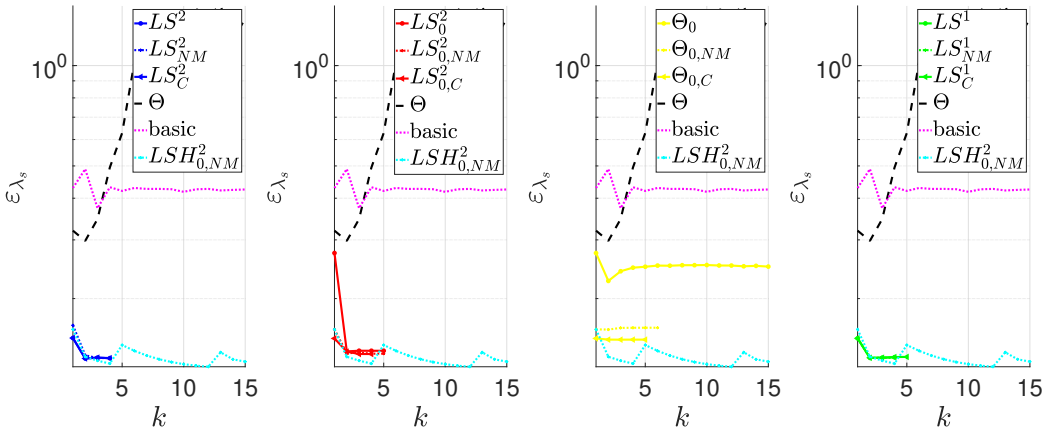

Figure 52: Errors on the identified parameter $\boldsymbol{\lambda}_s$ computed for different approaches; Analysis of the square domain with a hole (loading-measurement scenario #2).

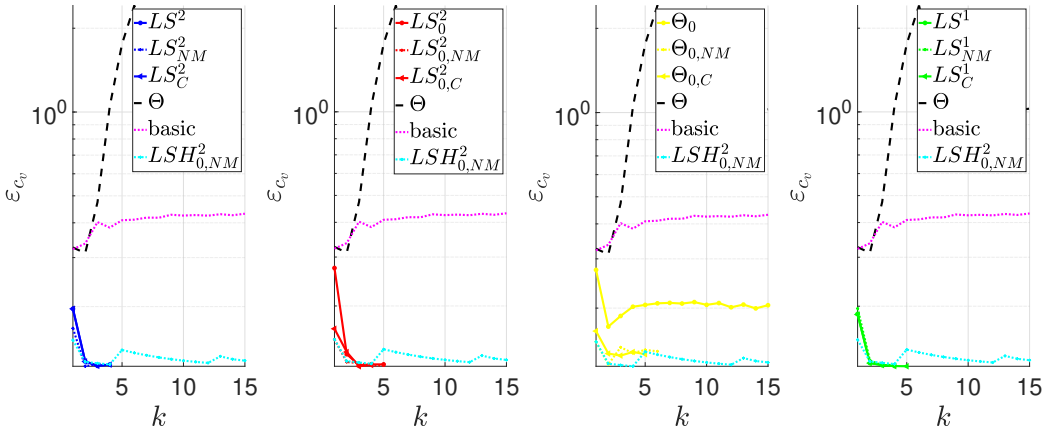

Figure 53: Errors on the identified parameter $\mathbf{c}_v$ computed for different approaches; Analysis of the square domain with a hole (loading-measurement scenario #2).

An important finding, which can be observed for all converging methods, can be found in Tab. 8 and in particular in the magnitude of errors ε_{λ_s} and ε_{c_v}. Although the identification algorithm in the case of loading-measurement scenario #1 is provided with a handful of data in comparison to the loading-measurement scenario #2, the identified fields in both cases reach virtually the same level of errors ε_{λ_s} and ε_{c_v}. This means that additional load conditions and measurements do not necessarily lead to a better performance of the identification algorithm, contrary the stationary model

wherein the plurality of measurements and/or loads resulted in a better approximation of the identified fields. Another important mention concerns the error ε_u and the way it is assessed. As this and previous examples show, it is not appropriate to consider the error ε_u from an absolute value perspective. In our settings the complete image of the error is only linked to the concrete example. If we want to compare the results in columns 2 and 5 in Tab. 8, we have to proceed to a certain normalisation or to express the error ε_u in a different metric. In our case we proceed with the former solution. First, let us revisit the formula for calculation of ε_u, which takes the following form

$$\varepsilon_u = \sqrt{\sum_{i=1}^{m_n \cdot m_t} \delta u_{m,i}^2}. \tag{4.31}$$

From eq. (4.31), one can see that the error magnitude is inherently influenced by the dataset size $m_n \cdot m_t$, which causes the discrepancy in results in columns 2 and 5 in Tab. 8. In order to eliminate the dependence on the size of the dataset, we extract an equivalent of the average error $\bar{\varepsilon}$ from the error ε_u by setting $\delta \mathbf{u}_m = \bar{\varepsilon}\mathbf{1}$, where $\mathbf{1} = [1, \ldots, 1]^T \in \mathbb{R}^{m_n \cdot m_t}$, in the following way

$$\varepsilon_u = \sqrt{\sum_{i=1}^{m_n \cdot m_t} (\bar{\varepsilon}1)^2} = \sqrt{\bar{\varepsilon}^2 \sum_{i=1}^{m_n \cdot m_t} 1} = |\bar{\varepsilon}|\sqrt{m_n \cdot m_t}. \tag{4.32}$$

With the help of the previous equation, we can express a new quantity $\hat{\varepsilon}$ in terms of already known error ε_u and the dataset size $m_n \cdot m_t$ while maintaining the error structure shown in eq. (4.31) in the following way

$$\bar{\varepsilon} = \frac{\varepsilon_u}{\sqrt{m_n \cdot m_t}}. \tag{4.33}$$

Scaling constants for this particular example would be then $1/\sqrt{82 \cdot 125} = 0.0099$ for the setup #1 and $1/\sqrt{160 \cdot 425} = 0.0038$ for the setup #2. After scaling the errors ε_u in Tab. 8 by corresponding factors, the setup #2 with more comprehensive boundary conditions and measurement nodes show for all methods lower level of errors compared to #1.

With regard to the computational times in Tab. 7, one can see that the main difference in #1 compared to #2 lies in the time needed for evaluation of each iteration. This is due to the fact that most of the computational time is devoted to solving the finite element problem. In this particular example the only difference between the setup #1 and #2 regarding the finite element solution is represented by the number of time steps m_t, i.e. one may expect that evaluating model in setup #2 takes approximately $m_t^2/m_t^1 = 425/125 = 3.4$ times longer, which corresponds to the results in Tab. 7.

	Loading-measurement #1			Loading-measurement #2		
Method	k	t_{comp} [minutes]	t_{comp}/k	k	t_{comp} [minutes]	t_{comp}/k
LS^2	6	32.26	5.38	4	70.22	17.56
LS^2_{NM}	6	35.77	5.96	4	69.28	17.32
LS^2_C	6	33.18	5.53	4	69.92	17.48
LS^2_0	5	24.34	4.87	4	70.15	17.54
$LS^2_{0,NM}$	7	33.86	4.84	4	72.19	18.05
$LS^2_{0,C}$	6	31.52	5.25	3	53.10	17.70
LS^1	9	46.82	5.20	4	62.69	15.67
LS^1_{NM}	5	26.61	5.32	4	61.05	15.26
LS^1_C	5	26.75	5.35	5	75.10	15.02
Θ	15	80.07	5.34	15	196.29	13.09
Θ_0	15	78.13	5.21	15	183.53	12.24
$\Theta_{0,NM}$	15	82.46	5.50	5	110.31	22.06
$\Theta_{0,C}$	15	82.07	5.47	4	78.43	19.61
basic	15	109.37	7.29	15	204.84	13.66
$LSH^2_{0,NM}$	12	66.60	5.55	15	293.28	19.55

Table 7: Computational times t_{comp} and number of iterations k utilising different approaches for a square domain with a hole.

The following figures show the elements of the weighting matrix $\mathbf{W} = \mathrm{diag}([\mathbf{w}_1\, \mathbf{w}_2])$, see eq. (3.26), where the individual elements in this particular example correspond to $\mathbf{w}_1 = \mathbf{w}_{\lambda_s}$ and $\mathbf{w}_2 = \mathbf{w}_{c_v}$. This metric scaled by the values of $\mathbf{w}_{\lambda_s}$ or $\mathbf{w}_{c_v}$ (ranging from 1 and 1.5) loses the information about the overall sensitivity and thus shows only relative sensitivity, i.e. one can tell only which locations in space are more or less sensitive with respect to others.

Loading-measurement scheme #1

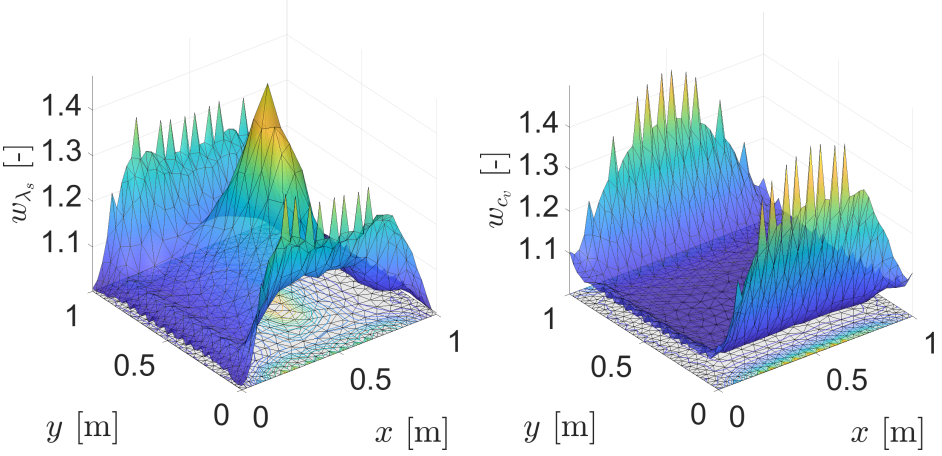

(a) (b)

Loading-measurement scheme #2

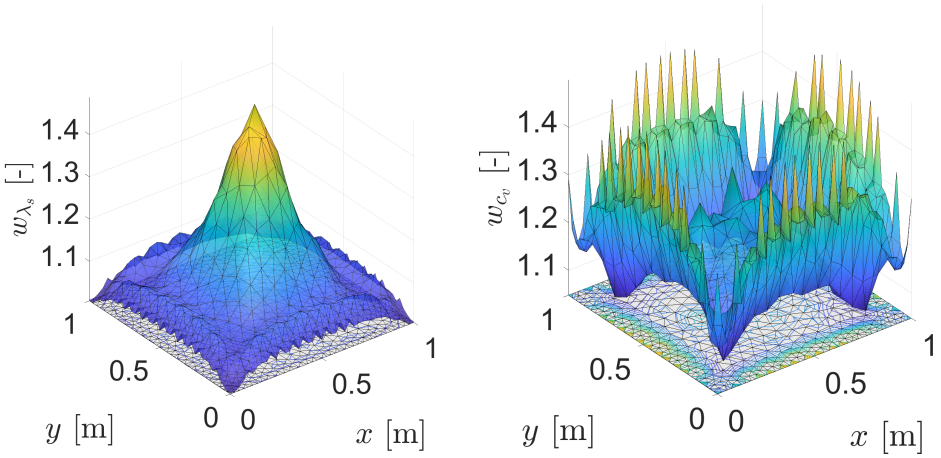

(c) (d)

Figure 54: Visualisation of the weighting matrix elements, i.e. the insensitivity maps w_1 and w_2, in the first iteration.

One can notice that the insensitivity maps $\mathbf{w}_{\lambda_s}$ and $\mathbf{w}_{c_v}$ follow the mea-

	Loading-measurement #1			Loading-measurement #2		
Method	ε_u	ε_{λ_s}	ε_{c_v}	ε_u	ε_{λ_s}	ε_{c_v}
LS^2	0.00025	0.13369	0.13166	0.00044	0.13250	0.12376
LS^2_{NM}	0.00026	0.13381	0.13144	0.00045	0.13271	0.12308
LS^2_C	0.00025	0.13369	0.13166	0.00044	0.13250	0.12376
LS^2_0	0.00024	0.14313	0.13110	0.00044	0.13945	0.12321
$LS^2_{0,NM}$	0.00024	0.14022	0.13218	0.00044	0.13671	0.12229
$LS^2_{0,C}$	0.00024	0.13851	0.13417	0.00044	0.13635	0.12264
LS^1	0.00026	0.13380	0.13177	0.00044	0.13336	0.12201
LS^1_{NM}	0.00025	0.13375	0.13187	0.00044	0.13276	0.12320
LS^1_C	0.00024	0.13385	0.13217	0.00044	0.13366	0.12164
Θ	0.01379	2.10056	2.01515	0.01266	1.38312	1.02749
Θ_0	0.00208	0.21009	0.16325	0.00178	0.25016	0.19779
$\Theta_{0,NM}$	0.00095	0.16832	0.15547	0.00083	0.16351	0.14015
$\Theta_{0,C}$	0.00047	0.14987	0.13721	0.00073	0.15061	0.13685
basic	0.00245	0.41917	0.39059	0.00345	0.42491	0.43121
$LSH^2_{0,NM}$	0.00022	0.12470	0.12035	0.00037	0.12781	0.12662

Table 8: Errors in last iteration utilising different approaches for a square domain with a hole.

surement scheme quite well, i.e. the insensitivity is higher in regions where no measurement nodes are located and vice versa, see in particular w_{λ_s} in Fig. 54(a,c). Interestingly, the area of the circular hole is also revealed in Fig. 54(a,c) as being insensitive to measurements. The insensitivity maps can also be viewed as identifiers of potentially vulnerable areas which needs to be regularised more aggressively. This can be rationalised by the following consideration: in regions where the insensitivity of the particular variable is a relatively higher number, e.g. in Fig. 54c a point with coordinates [0.5 0.5] with a value of ≈ 1.5, the algorithm is forced to alter the magnitude of such variable[24] more radically in order to cause a corresponding changes in the measured quantity $\mathbf{u}_m$. This can cause the solver instability.

In the following figures one can see that despite observing convergence in terms of the error ε_u in the case of basic method (see Fig. 51), the identified fields do not reveal even an approximate location of the inclusion. This is

[24]In this case the algorithm alters the value of λ_s for each element of the finite element mesh.

true for both loading-measurement scenarios, although one can observe the basic approach in Fig. 56(a,c) starts to show similar behaviour as $LSH^2_{0,NM}$ in terms of shape of the identified field for $\boldsymbol{\lambda}_s$.

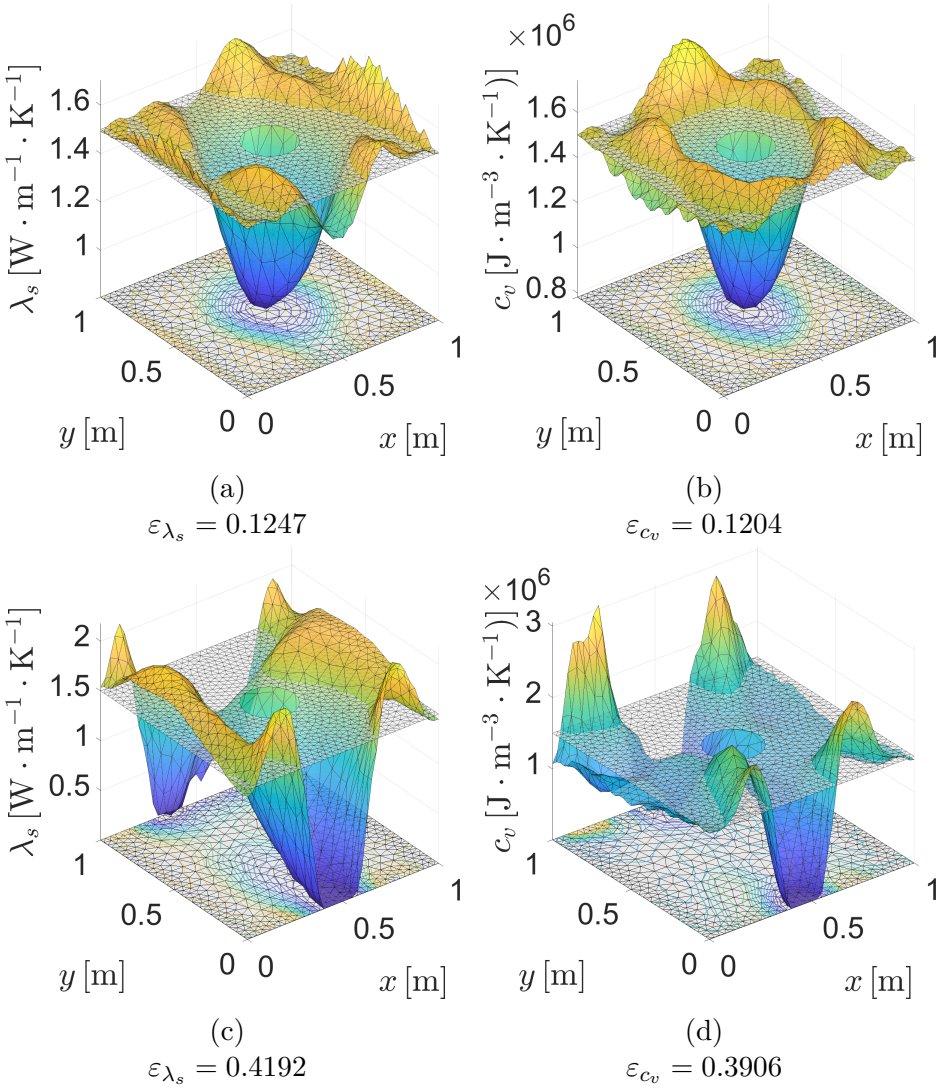

Figure 55: Identified fields for the square domain with a hole for loading-measurement scheme #1 (a,b) utilising $LSH^2_{0,NM}$ method and (c,d) utilising basic method.

On the other hand, looking at the identified fields coming from the $LSH^2_{0,NM}$ method, whether for loading-measurement scheme #1 or #2, a clear definition of the hole with minor oscillations in the surrounding is seen. It is also noticeable that both fields, i.e. $\boldsymbol{\lambda}_{s,\mathrm{rec}}$ and $\mathbf{c}_{v,\mathrm{rec}}$, complement each

other with these oscillations in terms of mutual product $e = \sqrt{\lambda_s \cdot c_v}$, i.e. an identical phenomenon that is present the previous case (see Fig. 48). Although this effect is less evident due to the omnidirectional load and measurement.

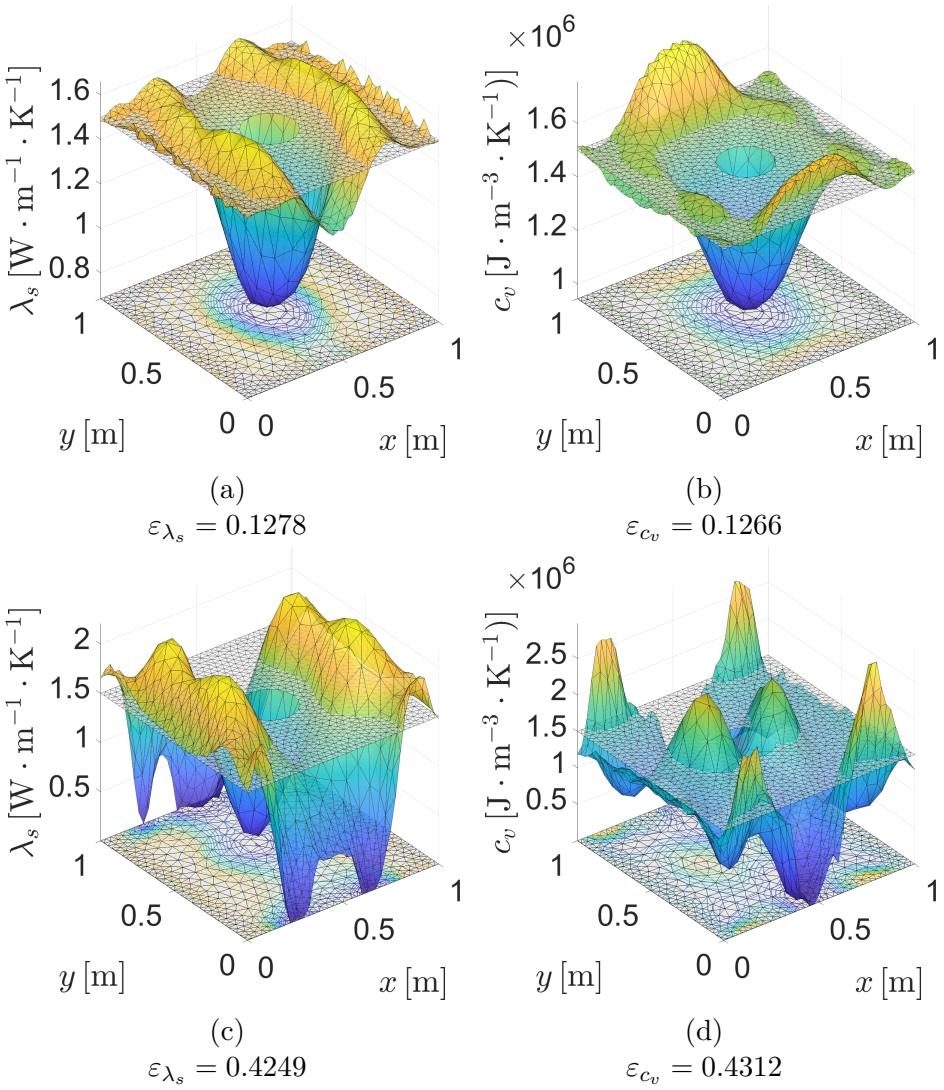

Figure 56: Identified fields for the square domain with a hole for loading-measurement scheme #2 (a,b) utilising $LSH^2_{0,NM}$ method and (c,d) utilising basic method.

For better readability, the following thermal effusivity images are plotted as contour plots for both of the aforementioned methods. Surprisingly, even in this case, the basic method (see Fig. 57a) does not suggest even an

indication of a hole at all. Yet, the identified thermal effusivity field coming from $LSH^2_{0,NM}$ method (see Fig. 57b) exhibits a clear definition of the hole, which also results in a relatively low error of $\varepsilon_{e_s} = 0.09$. In order to better understand Fig. 57, the correct thermal effusivity values are in this case equal to $e_{s,\text{body}} = \sqrt{1.5 \cdot 1.5 \times 10^6} = 1.5 \times 10^3$ and $e_{s,\text{hole}} = \sqrt{0 \cdot 0} = 0$.

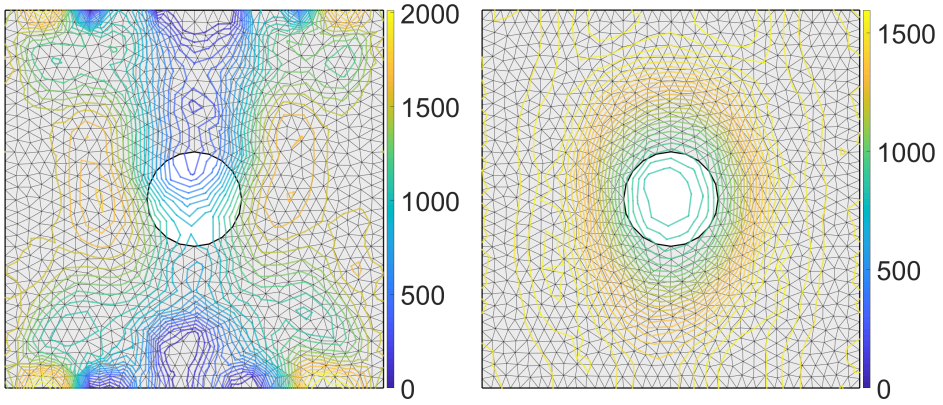

(a) $\varepsilon_{e_s} = 0.3894$ (b) $\varepsilon_{e_s} = 0.0906$

Figure 57: Identified thermal effusivity fields $\mathbf{e}_{s,\text{rec}}$ for the square domain with a circular hole utilising (a) basic method and (b) $LSH^2_{0,NM}$ method.

The next example represents a similar settings to the previous one, however, in this example we want to stress out the ability of the algorithm to identify the underlying fields $\boldsymbol{\lambda}_s$ and $\mathbf{c}_v$ for more complex situations. This is accomplished by modelling two thin ellipsoidal holes representing cracks inside the body. Such task can be considered as very difficult from two perspectives. In the first place the crack width is much smaller with respect to an element size for the finite element mesh utilised in the identification process. The second reason is related to the smoothing nature of the governing equations for which the individual parameters in some parts of the domain likely get exaggerated, smoothed out or spread the effect of the crack into surroundings.

As in the previous example, we perform two separate experiments which differ in loading scheme. The boundary conditions are set in the same way as in the previous example, see eq. (4.30), where $\partial\Omega_5$ corresponds to the boundary of both cracks. The only exception concerns the measurement nodes which are set the same for both loading cases and consist of a full measurement array, i.e. $\Gamma_m = \partial\Omega \backslash \partial\Omega_5$, see Fig. 58.

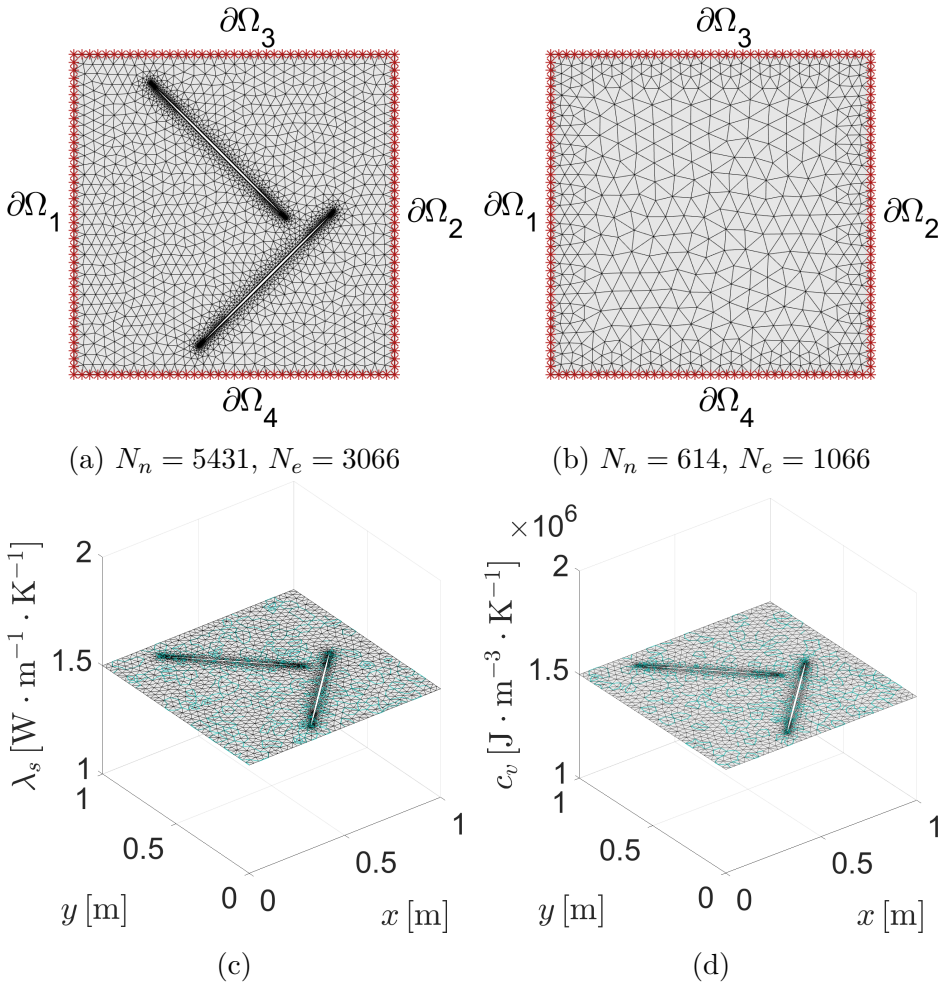

(a) $N_n = 5431$, $N_e = 3066$ (b) $N_n = 614$, $N_e = 1066$

(c) (d)

Figure 58: Square domain with discretisation utilised for (a) simulating real measurement and (b) for the identification, (c) distribution of the true thermal conductivity $\lambda_{s,\mathrm{true}}$, (d) distribution of the true volumetric heat capacity $c_{v,\mathrm{true}}$.

Since the true fields $\boldsymbol{\lambda}_s$ and $\mathbf{c}_v$ for the finite element mesh utilised in the identification algorithm (see Fig. 58b) can not be approximated sufficiently well, we calculate the errors ε_{λ_s} and ε_{c_v} in Tab. 10 and Fig. 60 and 61 with respect to spatially constant fields set to $\lambda_{s,\mathrm{true}} = 1.5$ and $c_{v,\mathrm{true}} = 1.5 \times 10^6$. For this reason, we have to be more cautious when assessing the resulting errors ε_{λ_s}, ε_{c_v} and ε_{e_s}.

By examining the following figures, we can observe that method Θ in its unmodified version is unable to converge in terms of ε_u. However, its variants with the initial search for optimal constant fields, i.e. $\{\Theta_0,\ \Theta_{0,C},\ \Theta_{0,NM}\}$, are able to achieve comparable results with respect to other methods. The

reason for this is that the closer the initial solution is to the true one, the more stable the identification is, regardless of the method used. Otherwise, Fig. 59 provides a standard performance picture of the methods as in previous examples.

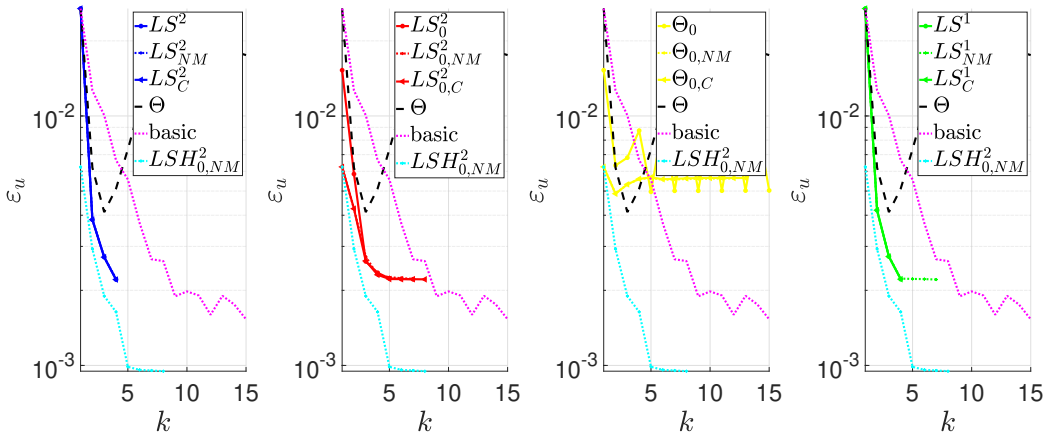

Figure 59: Errors on measured temperatures computed for different approaches; Analysis of the square domain with cracks (load #2).

Since the data in following figures are affected by the particular choice of true fields, the analysis of foregoing results in Fig. 60 and 61 does not provide a straightforward image about the errors and requires individual assessment. It can be viewed as follows: the errors indicate a deviation from the true fields which are set to $\lambda_{s,\text{true}} = 1.5$ and $c_{v,\text{true}} = 1.5 \times 10^6$. These values are correct on almost the entire domain and therefore the results are not completely misleading. Anyway, the irregularity in the form of cracks introduces some fluctuations into the identified fields, which artificially increases the error. On the other hand, fields that are close to the constant spatial distribution, close to $\lambda_{s,\text{rec}} \approx 1.5$ and $c_{v,\text{rec}} \approx 1.5 \times 10^6$, result in a lower overall error.

Looking specifically at Fig. 60 and 61, error values for methods that do not have 0 in subscript and therefore do not employ optimisation for initial estimation of constant fields $\lambda_{s,0}$ and $c_{v,0}$ start with an error ranging approximately from 2×10^{-1} to 3×10^{-1} for both ε_{λ_s} and ε_{c_v}[25]. The only exception is represented by LS^2_0 and Θ_0 methods that use the pure Newton's method, that has often encountered convergence problems, which is one of the reasons for applying other non-gradient methods in order to minimise problems in eq. (3.48) and eq. (3.35).

[25]Note that for $k = 0$, which is not present in the figures, methods without a subscript 0 would start with an error equal to $\varepsilon_{\lambda_s} = \varepsilon_{c_v} = (1.5 - 1)/1.5 = 0.333$ as the starting fields are equal to 1 or 1×10^6.

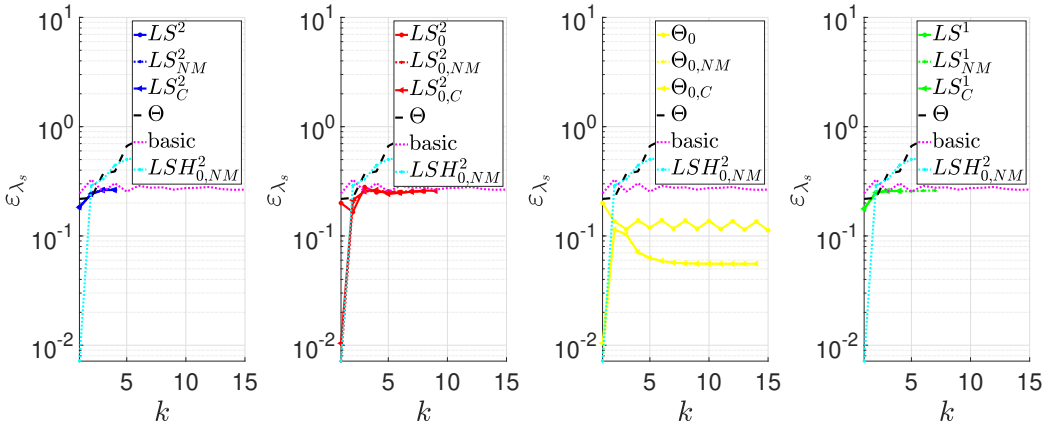

Figure 60: Errors on the identified parameter $\boldsymbol{\lambda}_s$ computed for different approaches; Analysis of the square domain with cracks (load #2).

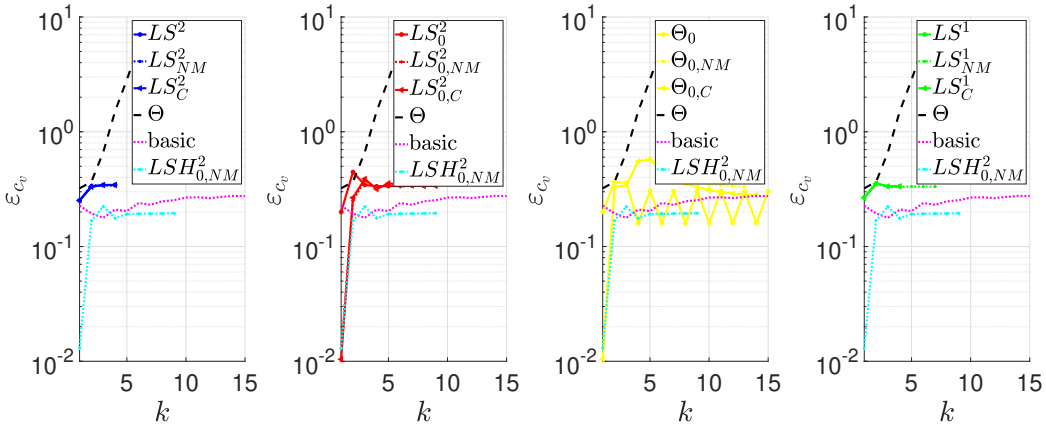

Figure 61: Errors on the identified parameter $\mathbf{c}_v$ computed for different approaches; Analysis of the square domain with cracks (load #2).

The computation times in Tab. 9 are in accordance with the finite element model complexity. The ratio of time needed to evaluate one iteration for setup in load #2 with respect to load #1 approximates to 3.4. This ratio stems from the number of time steps involved in the calculation which is $m_t = 125$ for the setup #1 and $m_t = 425$ in the case of setup #2. The obtained data matches with the previous example, see Tab. 7 and the corresponding description.

	Load #1			Load #2		
Method	k	t_{comp} [minutes]	t_{comp}/k	k	t_{comp} [minutes]	t_{comp}/k
LS^2	9	49.26	5.47	4	75.01	18.75
LS^2_{NM}	7	38.74	5.53	4	68.79	17.20
LS^2_C	9	45.50	5.06	4	69.13	17.28
LS^2_0	6	32.19	5.36	7	124.24	17.75
$LS^2_{0,NM}$	15	81.07	5.40	7	125.29	17.90
$LS^2_{0,C}$	3	17.54	5.85	8	133.97	16.75
LS^1	9	53.93	5.99	4	72.43	18.11
LS^1_{NM}	11	66.92	6.08	7	106.69	15.24
LS^1_C	10	62.34	6.23	4	59.19	14.80
Θ	15	101.58	6.77	15	195.26	13.02
Θ_0	15	83.99	5.60	15	283.52	18.90
$\Theta_{0,NM}$	15	76.83	5.12	12	160.58	13.38
$\Theta_{0,C}$	15	79.32	5.29	13	162.16	12.47
basic	15	95.88	6.39	15	239.69	15.98
$LSH^2_{0,NM}$	12	84.42	7.03	8	197.47	24.68

Table 9: Computational times t_{comp} and number of iterations k utilising different approaches for the square domain with cracks.

Since the results regarding ε_u in the second and the fifth column in Tab. 10 are based on vectors of different sizes and thus are not directly comparable, one can employ comparative factors in the sense of eq. (4.33). The scaling constant[26] with respect to the load setup #1 is equal to $1/\sqrt{160 \cdot 125} = 0.0071$ and $1/\sqrt{160 \cdot 425} = 0.0038$ in the case of load setup #2. Once the scaling is applied, the errors for load setup #2 reach significantly lower levels than in the case of load setup #1.

Because we cannot directly assess the accuracy of the identification in Tab. 10 based solely on the magnitude of errors ε_{λ_s} and ε_{c_v}, we use the error ε_u as a confirmatory factor. This means that since results for ε_u in load setup #2 are lower[27] in all instances, we only need to focus on ε_{λ_s} and ε_{c_v} for load setup #2 marked in red. If we filter out methods that show negligible difference in errors for both load setups, i.e. LS^2_{NM} and basic, and the methods exhibiting some sort of instability, i.e. the whole

[26]The results in the Tab. 10 are not scaled.

[27]We refer to the situation after the resulting errors ε_u were appropriately scaled.

	Load #1			Load #2		
Method	ε_u	ε_{λ_s}	ε_{c_v}	ε_u	ε_{λ_s}	ε_{c_v}
LS^2	0.00179	0.33684	0.35562	0.00221	0.26346	0.34373
LS^2_{NM}	0.00184	0.30909	0.33164	0.00223	0.26681	0.33928
LS^2_C	0.00179	0.33684	0.35562	0.00221	0.26346	0.34373
LS^2_0	0.00182	0.32107	0.34257	0.00222	0.25583	0.33864
$LS^2_{0,NM}$	0.00947	0.05231	0.10078	0.00222	0.25530	0.33802
$LS^2_{0,C}$	0.00971	0.08545	0.01054	0.00221	0.25866	0.33739
LS^1	0.00180	0.29270	0.36872	0.00222	0.25815	0.33461
LS^1_{NM}	0.00183	0.31282	0.33263	0.00221	0.26093	0.33186
LS^1_C	0.00180	0.27821	0.39208	0.00222	0.25840	0.33532
Θ	0.01867	1.11468	3.01882	0.01754	2.48007	2.60391
Θ_0	0.01824	0.16924	0.25475	0.00503	0.13483	0.16067
$\Theta_{0,NM}$	0.00639	0.15495	0.13390	0.00561	0.05544	0.33233
$\Theta_{0,C}$	0.00634	0.15228	0.28935	0.00564	0.05569	0.28038
basic	0.00184	0.29163	0.25679	0.00153	0.26565	0.27499
$LSH^2_{0,NM}$	0.00121	0.37526	0.29744	0.00095	0.53127	0.19486

Table 10: Errors in last iteration utilising different approaches for the square domain with cracks.

family of methods employing the Θ transformation, we are left with methods $LSH^2_{0,NM}$, $LS^2_{0,NM}$ and $LS^2_{0,C}$. Examining the $LSH^2_{0,NM}$ method, we can see that the amplitude of fluctuations for load setup #2, especially in the case of λ_s (see Fig. 63a and 64a), are amplified with respect to load setup #1. This clearly leads to an increased error in ε_{λ_s} as shown in Tab. 10, but at the same time it does not indicate the accuracy of the identification. However, taking into account the error ε_u, we can conclude that the increased level of fluctuations in λ_s in the load setup #2 leads to overall lower error in ε_u and hence a better approximation of the underlying field. On the other hand, methods $LS^2_{0,NM}$ and $LS^2_{0,C}$ for load setup #1 reach the lowest errors for ε_{λ_s} and ε_{c_v}. In this particular example it means that the identified fields are close to constants $[\lambda_{s,\text{rec}} \approx 1.5,\ c_{v,\text{rec}} \approx 1.5 \times 10^6]$. Considering the magnitude of ε_u, we can conclude that lower level of errors ε_{λ_s} and ε_{c_v} is not due to a more accurate approximation of the underlying fields, but rather due to a wrong setup of the true fields for which the errors are calculated.

In the following figures we present in total nine contour plots representing

the influence and the potential moves of the line search algorithm of the $LSH^2_{0,NM}$ method for this concrete example. The caption underneath each subplot indicates the corresponding iteration number of the Gauss-Newton method, whereas $k = 0$ stands for a situation, when the line search algorithm is utilised to explore the available search space for the optimal magnitude of initial fields with a constant spatial distribution. In other words, the expression in eq. (3.48) for $k = 0$ turns into the following minimisation problem

$$\begin{aligned} \boldsymbol{\beta}_{\min} &= \min_{\beta_1,\beta_2} f(\boldsymbol{\Phi}_0\boldsymbol{\beta}), \\ &= \min_{\beta_1,\beta_2} \|\delta\mathbf{u}(\boldsymbol{\Phi}_0\boldsymbol{\beta})\|_2 + G(\boldsymbol{\Phi}_0\boldsymbol{\beta}), \\ &= \min_{\beta_1,\beta_2} \|\mathbf{u}_m - \mathrm{F}\left(\boldsymbol{\Phi}_0\boldsymbol{\beta}\right)\|_2, \end{aligned} \tag{4.34}$$

where in the case of transient heat transfer the term $\boldsymbol{\Phi}_0 = [\boldsymbol{\phi}_{0,1},\, \boldsymbol{\phi}_{0,2}] = [\boldsymbol{\lambda}_{s,0},\, \mathbf{c}_{v,0}] = [\mathbf{1}, 1 \times 10^6 \cdot \mathbf{1}]$ and $\boldsymbol{\beta} = \mathrm{diag}([\beta_1, \beta_2])$. This means that the parameter β_1 controls $\boldsymbol{\phi}_1 = \boldsymbol{\lambda}_s$ and β_2 is modifies the parameter $\boldsymbol{\phi}_2 = \mathbf{c}_v$. Note that the regularisation term $G(\cdot)$ in the aforementioned expression vanquishes for constant fields due to the property of regularisation operator $\mathbf{L}$, see eq. (3.11) for the expanded form of the function $G(\cdot)$ and eq. (3.12) for the definition of the regularisation operator. The contour plots for $k = 1, \ldots, 8$ then utilise a formula in eq. (3.51) in order to search for an optimal $\boldsymbol{\beta}_{\min}$.

The dotted diagonal lines in Fig. 62 indicate all possible movements for a plain LS^1 method, i.e. a situation when $\beta_1 = \beta_2$. The red dot marks the spot for a case when $\delta\boldsymbol{\Theta}$ is not being altered by a line search algorithm meaning that $\beta_1 = \beta_2 = 1$. In the case of $k = 0$, the red dot marks a point for an initial expert guess of $\boldsymbol{\lambda}_{s,0} = \mathbf{1}$ and $\mathbf{c}_{v,0} = 1 \times 10^6 \cdot \mathbf{1}$. The yellow diamond marks the minimum achieved for a pure line search algorithm with a single degree of freedom, i.e. LS^1 where $\beta_1 = \beta_2$, and the blue cross represents the full LS^2 method with two degrees of freedom, i.e. LS^2 where β_1 and β_2 are treated independently. Before we get into the description of individual plots in Fig. 62, we remark that in the case of $LSH^2_{0,NM}$, there are actually two layers of the line search algorithm adopted and even in the case of $\beta_1 = \beta_2 = 1$, the parameters $\boldsymbol{\kappa} = \mathrm{diag}([\kappa_1, \kappa_2])$ controlling the magnitude of the regularisation term are still being optimised. Also, it is worth mentioning that each plot in Fig. 62 starts from an already adjusted solution from the previously acquired step $k - 1$ marked by a blue cross. Without this compounding, we would obtain slightly different images, where positions of the red dot, yellow diamond and blue cross would be more scattered in the $\boldsymbol{\beta}$ domain. However, this effect virtually cumulates tiny, almost indistinguishable, adjustments, which in the end result into a possibly very different identified fields.

By examining the contour plot for $k = 0$, we see that the optimum point lies at the coordinates $\beta_1 = \beta_2 \approx 1.5$. Note that the optimal point landed on the dotted line just by a coincidence caused by the particular choice of the

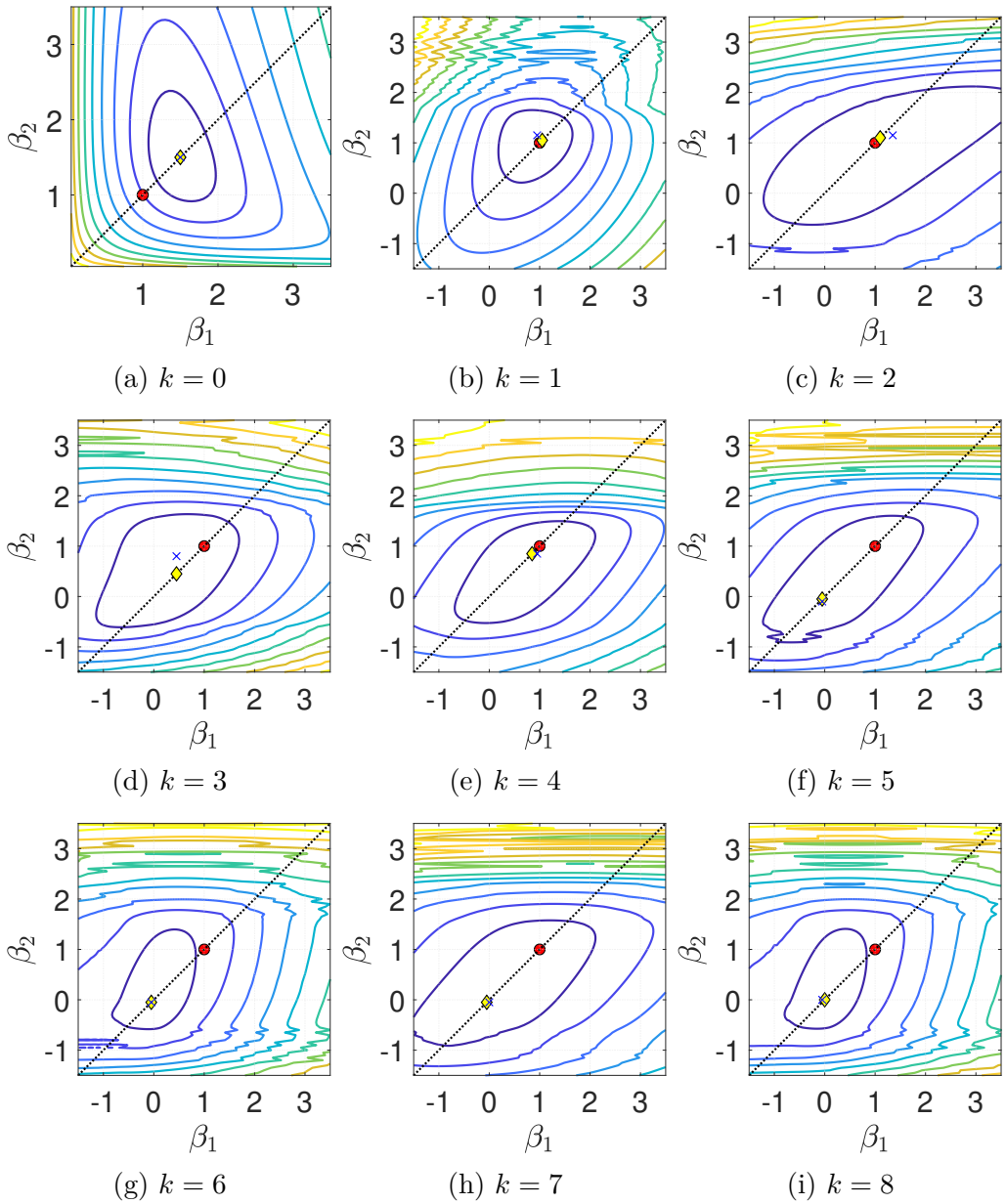

(a) $k = 0$ (b) $k = 1$ (c) $k = 2$

(d) $k = 3$ (e) $k = 4$ (f) $k = 5$

(g) $k = 6$ (h) $k = 7$ (i) $k = 8$

Figure 62: Contour plots of the objective function f evaluated for various combinations of β_1 and β_2.

initial fields $\boldsymbol{\lambda}_{s,0} = \mathbf{1}$ and $\mathbf{c}_{v,0} = 1 \times 10^6 \cdot \mathbf{1}$ and the true fields, which are

mostly equal to $\boldsymbol{\lambda}_{s,\text{true}} = 1.5 \cdot \mathbf{1}$ and $\mathbf{c}_{v,\text{true}} = 1.5 \times 10^6 \cdot \mathbf{1}$.

In the next four iterations, i.e. $k = 1, \ldots, 4$, the optimum is found relatively close to $\beta_1 \approx 1 \wedge \beta_2 \approx 1$, meaning the direction $\delta\boldsymbol{\Theta}$ coming directly from the Gauss-Newton algorithm is very close to the actual local minima in a given iteration. However, from the fifth iteration, i.e. $k = 5$, the LS^1 and LS^2, strongly suppress further progress by setting the constants β_1 and β_2 close to zero. This basically happens when the direction $\delta\boldsymbol{\Theta}_k$, proposed by the Gauss-Newton method, does is nowhere near to the vector $\delta\bar{\boldsymbol{\Theta}}_k = \boldsymbol{\Theta}_{\text{true}} - \boldsymbol{\Theta}_k$. In mathematical terms, the algorithm is forced to set the constants β_1 and β_2 to zero, when the fields $\delta\bar{\boldsymbol{\Theta}}_k$ and $\delta\boldsymbol{\Theta}_k$ are perpendicular to each other, i.e. when $\delta\bar{\boldsymbol{\Theta}}_k \cdot \delta\boldsymbol{\Theta}_k \to 0$. In such situation, there is no room for improvement in terms of minimisation of the objective function. Note that in k-th iteration, one can always achieve at least the same level of error as in the iteration $k-1$ simply by setting $\beta_1 = \beta_2 = 0$.

One can also spot a zig-zag patterns, particularly pronounced in the case of $k = 1$, which appear in the direction of β_1 in the region of $\beta_2 > 2$. This indicates an activation of the positivity operator eq. (3.51) due to negative values of variable β_2. Note that in case one would pass a material field containing negative numbers into the finite element solver, it would cause the task to be singular with corresponding implications for the evaluation of the objective function. Therefore, even though it seems the positivity operator causes some non-smoothness, it regularises in fact an otherwise discontinuous function, which is particularly advantageous in minimising such a function. All in all, although the contributions of the line search method are very mild in the individual iterations, the overall effect is very noticeable. This is particularly evident in methods $\Theta_{0,NM}$ and $LS^2_{0,NM}$ (see Tab. 10), where the only difference is the use of line search algorithm in $LS^2_{0,NM}$. In our case, this method serves several purposes. First of all, it is about increasing the stability of the whole task and preventing divergence. Secondary properties are the increased accuracy of the solution and the possibility of faster convergence.

From the visual comparison of the identified fields, whether in Fig. 63 or Fig. 64, we can see at a glance that the task is particularly difficult, since large variations in the identified fields can be observed. Also, the difference in resulting fields between the load setups is very subtle, indicating the impartiality of boundary conditions in the identification process. When analysing the resulting data from an unbiased point of view, i.e. if we do not know the distribution of true fields $\lambda_{s,\text{true}}$ and $c_{v,\text{true}}$, one can see that in the case of thermal conductivity $\lambda_{s,\text{rec}}$ the identified field significantly drops in the surrounding of cracks (see for example Fig. 63c). However, this phenomenon is not replicated in case of the volumetric capacity $c_{v,\text{rec}}$ (see Fig. 63d), although we know that in this case the true field of volumetric capacity should

acquire the same shape as the thermal conductivity.

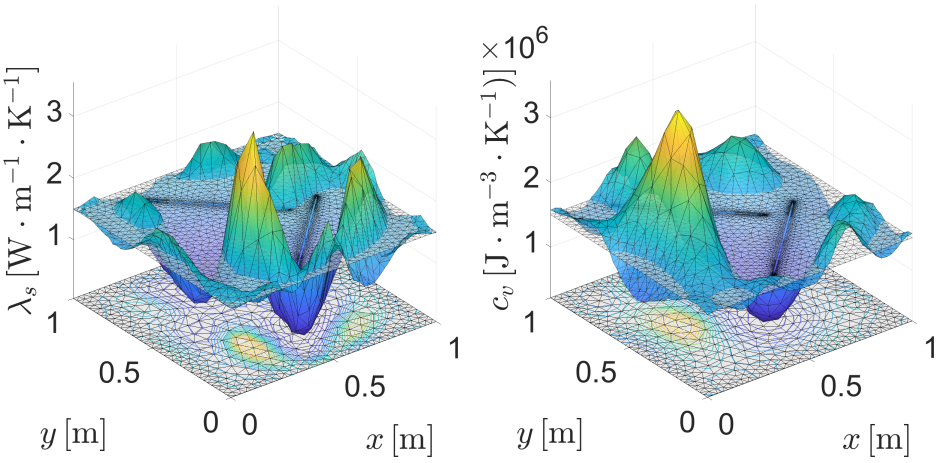

(a)
$\varepsilon_{\lambda_s} = 0.3753$

(b)
$\varepsilon_{c_v} = 0.2974$

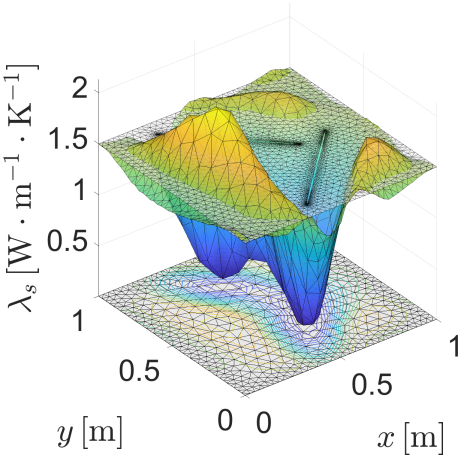

(c)
$\varepsilon_{\lambda_s} = 0.2916$

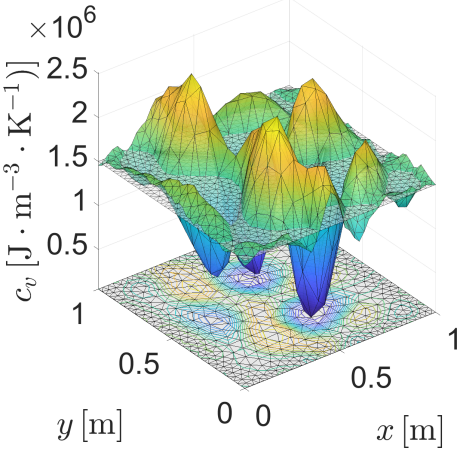

(d)
$\varepsilon_{c_v} = 0.2568$

Figure 63: Identified fields for the square domain with cracks for loading-measurement scheme #1 (a,b) utilising $LSH^2_{0,NM}$ method and (c,d) utilising basic method.

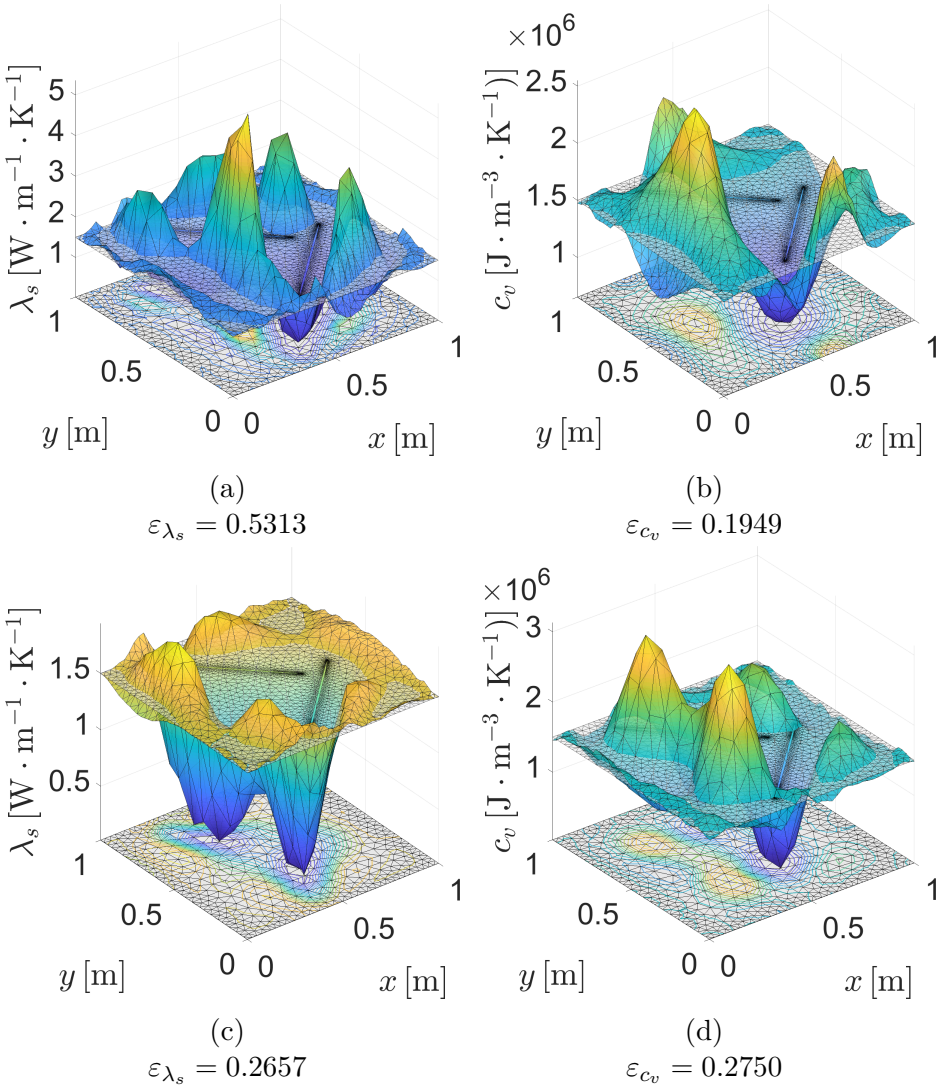

(a) $\varepsilon_{\lambda_s} = 0.5313$

(b) $\varepsilon_{c_v} = 0.1949$

(c) $\varepsilon_{\lambda_s} = 0.2657$

(d) $\varepsilon_{c_v} = 0.2750$

Figure 64: Identified fields for the square domain with cracks for loading-measurement scheme #2 (a,b) utilising $LSH^2_{0,NM}$ method and (c,d) utilising basic method.

In the following figures, we show contour plots of thermal effusivity e_s utilising basic and $LSH^2_{0,NM}$ method for load setup #2. Note that the error ε_{e_s} is still being calculated with respect to $\lambda_{s,\mathrm{true}} = 1.5$ and $c_{v,\mathrm{true}} = 1.5 \times 10^6$, and thus expresses rather the degree of fluctuations around the constant $e_{s,\mathrm{true}} = \sqrt{\lambda_{s,\mathrm{true}} \cdot c_{v,\mathrm{true}}} = 1.5 \times 10^3$. The correct values of the thermal effusivity are in fact equal to $e_{s,\mathrm{body}} = \sqrt{1.5 \cdot 1.5 \times 10^6} = 1.5 \times 10^3$ and $e_{s,\mathrm{crack}} = \sqrt{0 \cdot 0} = 0$. We can see that both methods performed relatively well in terms of precision of $e_{s,\mathrm{body}}$. However, method $LSH^2_{0,NM}$ was a bit

more aggressive and achieved substantially higher resolution, whereas in basic method, the secondary fluctuations are spread further into the domain.

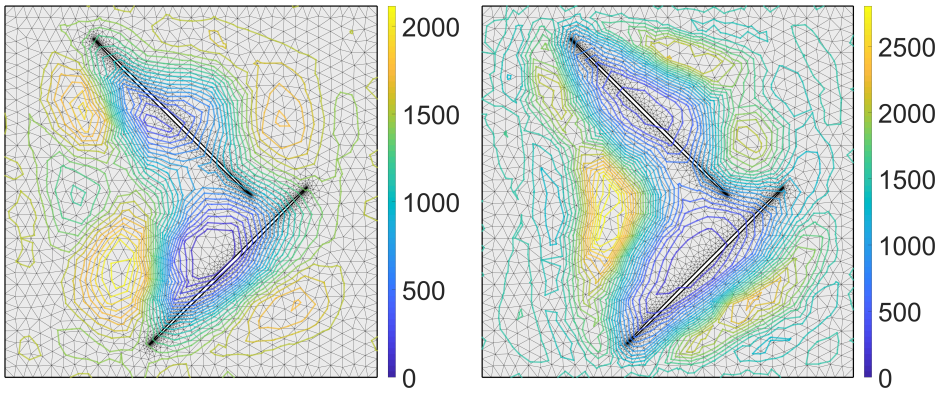

(a) $\varepsilon_{e_s} = 0.2057$ (b) $\varepsilon_{e_s} = 0.2536$

Figure 65: Identified thermal effusivity fields $\mathbf{e}_{s,\mathrm{rec}}$ for the square domain with cracks utilising (a) basic method and (b) $LSH^2_{0,NM}$ method.

Likewise to the previous example, if we are about to judge the algorithm performance from the perspective of solver stability, we can conclude that all of the methods with the exception of Θ are able to converge in both, the measured temperatures and the parameter fields. Assessing the second perspective, i.e. the ability to localise cracks, is a bit more complicated. In this case, the ability of the algorithm to identify individual parameter fields is inadequate. However, the position and direction of cracks is embedded in the thermal effusivity field. This is especially true for the $LSH^2_{0,NM}$ method, which is the only one that can also indicate the direction of cracks.

5 Summary and future work

In this work, we show the possibilities of identifying material fields by using only boundary, non-invasive measurements. First, we recapitulate the standard procedure of EIT used in medical imaging extended with a numerical analysis of partial data reconstruction, which is discussed in section 4.1. Following the same principles as in the Calderón's inverse problem, in section 4.2 we develop a steady-state model applicable in civil engineering, namely the general transport model (GTM) governed by a linear elliptic equation. This model is suitable to describe for example heat transport, groundwater flow or electrostatics. In particular, we are interested in the problems of heat transfer in civil engineering and so the individual examples are chosen so that they correspond to common building structures in terms of material properties, load and domain shapes. Moreover, we employ only the simple regularised Gauss-Newton method and focus on the impact of loading and measurement on the resulting identified field. Despite the inaccuracies in certain situations, e.g. insufficiency of data, non-smooth material field, the Gauss-Newton method proves to be stable and flexible solver for such tasks. This method can handle the reconstruction for CEM and GTM with a very limited data for various domains and material properties.

Subsequently, we focus our attention on a more attractive issue, represented by the transient problem in heat transport. The identification procedure for non-stationary model is first compared to a steady-state problem with identical inputs using the same Gauss-Newton method, except that it is extended by additional parameter. The results in Fig. 21 and 22 then indicate that the information about the underlying material parameters is to some extent embedded even in the first few time snapshots of the boundary Γ_m. This particular example reveals the potential to avoid imposing a predefined set of load cases as it is required in the classical EIT or thermal tomography and, on the contrary, to utilise natural changes in ambient temperature. This assumption is successfully numerically verified by identifying the material parameters in a structural detail representing a building corner subjected to a real climatic conditions over several consecutive days. In this case, the identification is evaluated with a deterministic and probabilistic solver. Due to the high computational complexity in the latter approach, we introduce a random field theory. This concept effectively reduces the number of variables for description of the heterogeneity, which in turn leads to computationally tractable problem. However, the reduced computational complexity is redeemed by the necessity to define additional parameters in the form of correlation length ρ and smoothness parameter ν. These parameters ultimately determine the shape of the identified fields and by selecting

the correlation length ρ we limit the amount of spatial fluctuations contained therein. On the one hand, this may appear to be a disadvantage, due to the increased demands on the end users, who should then be aware of meaning or be able to come up with an expert estimate of these parameters. On the other hand, we can perceive these parameters as an advantage because they can serve as high[28] or low[29] frequency filters. The results reported here indicate that the proposed algorithm based on the Bayesian inference is capable of identifying a heterogeneous material field from boundary measurements utilising only a few eigenmodes. Moreover, the obtained results are compared with those provided by a standard deterministic identification approach used in thermal tomography. To summarise the results, Fig. 31 displays the comparisons of average errors in both the parameter fields as well as in the temperature fields for all the studied correlation lengths. It is clearly visible that all graphs start from an almost identical value of error, i.e. the error when only the first mode is utilised, that is very similar for all correlation lengths. Furthermore, some graphs start to differ significantly with an increasing number included eigenmodes. With no doubt, for some specific correlation lengths, namely $\rho = 0.25$ and $\rho = 0.50$, the amount of error in parameter fields converges quickly towards the amount of error for a deterministic solution. This confirms that the proposed methodology has the potential for an efficient reduction in dimensionality in the solution of the Calderón problem. However, the results also reveal the enormous significance in the appropriate choice of correlation length ρ in material properties. The wrong correlation length choice may completely inhibit the solver to converge towards a deterministic solution. Moreover, the effect of smoothness parameter ν was neglected in this study as being significantly less important than the correlation length ρ. We perceive the ability to naturally involve the measurement error in the calculation as the greatest advantage of the probabilistic approach. Whereas in the deterministic method that incorporates the influence of errors, one often generates a set of random samples and performs the whole inverse procedure for each individual sample separately. This is on one hand very computationally demanding task, however, individual samples are not dependent on each other and so the task can be solved in parallel. Therefore, from our perspective we are not able to determine the best identification method. The choice of particular method boils down to a personal preference, expertise, hardware availability, specific problem being solved and the interest in concrete methods.

[28] This can be achieved using $1, \ldots, m$ eigenmodes in the computation.

[29] On contrary to the high frequency filter, in this case one would utilise $m, \ldots, N_n$ eigenmodes in the computation with an appropriate scaling of corresponding eigenvalues.

In sections 4.3.2 and 4.3.3 we deal with practical tasks and examine the errors that are inevitably included in the calculation. Due to the computational complexity and number of examples, we perform all computations in these sections with the help of the deterministic solver and its modifications which are briefly outlined in Tab. 1. The identified fields for the first two examples (see Fig. 42 and 47) are concerned with inaccurate boundary conditions, and their influence on the parameter identification. This introduces additional fluxes causing the resulting fields to deteriorate. Although the difference in errors ε_{λ_s} and ε_u between the reference and extended domain might get up to 50% (see Tab. 4 or Tab. 6), it is mainly due to the fact that the metric utilised to evaluate the errors ε_{λ_s} and ε_u, i.e. eqs. (4.14) and (4.15), tends to exaggerate the errors. Moreover, even though the basic and $LSH^2_{0,NM}$ methods exhibit higher errors for the extended domain in all monitored variables, Fig. 41 shows that the maximum errors during the experiment are still well below the resolution of commonly available sensors. The discrepancy in the identified fields can be therefore attributed to the overall ambiguity of the task itself rather than to the solver inability to describe the underlying fields, which is most significant in Fig. 47 and 48. In the next set of examples, we focus on the detection of hollow areas and/or defects in the structure. In this case, the basic deterministic method fails to identify the underlying fields. On the other hand, $LSH^2_{0,NM}$ is able to locate the hollow area quite well and simultaneously achieve the lowest overall errors among other methods, see Tab. 8. This is true for both loading scenarios, see Fig. 55 and 56. Regarding the examples dealing with cracks in the domain, we utilise a FEM mesh, which deliberately does not match the size of the cracks. The resulting fields in Fig. 63 and 64 partially indicate the position of the cracks. However, the truly interesting results are shown for the thermal effusivity in Fig. 65. Given the conditions under which the identification is performed, we consider the results in Fig. 65 to be surprisingly good. For both categories of examples in sections 4.3.2 and 4.3.3, we are able to achieve satisfactory results, which confirm the suitability of the model and inverse methods for identifying material parameters in civil engineering. The most consistent results across various examples are achieved by $LSH^2_{0,NM}$ method, which in every case achieves the lowest amount of error on the measured quantity ε_u. In addition, it has the advantage that it does not require any internal parameter[30] to be tuned by the user. Although the evaluation of individual steps in $LSH^2_{0,NM}$ method is computationally more demanding, the resulting computational times are not significantly different from other methods.

[30]Represented by a particular choice of the hyper-parameter $\boldsymbol{\kappa}$.

Regarding the future research in probabilistic method, we think it is necessary to focus more on a detailed elaboration of the effects of covariance function on a Karhunen-Loève expansion. From our point of view, we see two main directions of the following research. This can be accomplished by a study providing guidelines for selecting the number of eigenmodes m and correlation length ρ in order to reach a desired level of error in the description of some field with fluctuations containing certain frequencies. The second option is to include the parameters (m, ρ, ν) in the identification algorithm as free parameters. This option is not entirely straightforward, because the actual calculation of the eigenmodes is computationally demanding and their re-calculation in each iteration of the MCMC algorithm would result in a computationally intractable problem. Therefore, some approximation or a surrogate model would have to be built in order to harness the additional computational complexity.

In general, further work has to be devoted to clarifying the causes of ambiguity of the task, which manifests itself especially in the examples in Fig. 48 and 65 and partly also in Fig. 57. In these cases, the thermal effusivity e_s becomes the governing parameter of the equation in 2.19. Although one would naturally expect that if the equation has only one parameter, it should be the thermal diffusivity d_s. This finding is of crucial importance, since the way of loading and measurements determines parameters which can be identified. One could in essence predict the accuracy which could be achieved for particular settings or design an experiment in order to reach desired accuracy or identify a particular parameter. The experiment of an extended wall in Fig. 47 and 48 would be for example suitable in situation when one is interested in identifying of the thermal effusivity e_s. Because of this, we suppose that the interchangeability of DTN and NTD maps in transient problem does not hold any more. In continuation of this work we also intend to study the mutual ratio of terms $\rho_s c_p \frac{\partial u}{\partial t}$ and $\nabla \cdot (\lambda_s \nabla u)$ in eq. (2.19) and their influence on the identified fields. In our opinion, the representation of both terms, expressed by the mutual ratio, represents another essential information when determining the ability to identify individual fields. From a general perspective, a further extension of the presented work would be the identification of the parameter fields for coupled heat and moisture problem. For this purpose a Künzel's diffusion model would be suitable, because it is (i) relatively simple as it involves only a handful of material parameters, (ii) sufficiently accurate to describe the behaviour of structures under regular operation conditions, but is still (iii) complex enough to demonstrate the feasibility of the developed methodology towards the real-world applications. Knowledge of such parameters is particularly useful in describing degradation processes [102] and therefore such methodology could represent

an essential tool for comprehensive and yet non-destructive analysis of historical structures.

In oppose to electrical impedance tomography where the crucial part of successful material field identification is based on a precise position of the measurement electrodes together with the boundary shape and knowledge of the load conditions[31], in our application the problems might arise from insufficient space-time variability of the environmental factors leading to ambiguity of the task subsequently to unwanted artefacts in the identified fields.

[31]Especially in the electrical impedance tomography, where the electrodes are placed on a human body, the boundary shape and electrodes are in a continuous motion due to the patient breath and movement.

References

[1] G. Alessandrini and M. Di Cristo. Stable determination of an inclusion by boundary measurements. *SIAM journal on mathematical analysis*, 37(1):200–217, 2005.

[2] A. Allers and F. Santosa. Stability and resolution analysis of a linearized problem in electrical impedance tomography. *Inverse problems*, 7(4):515–533, 1991.

[3] K. Y. Aristovich, B. C. Packham, H. Koo, G. S. Santos, A. McEvoy, and D. S. Holder. Imaging fast electrical activity in the brain with electrical impedance tomography. *NeuroImage*, 124, Part A:204–213, 2016.

[4] K. Astala, K. Päivärinta, and M. Lassas. Calderóns' inverse problem for anisotropic conductivity in the plane. *Communications in Partial Differential Equations*, 30(1-2):207–224, 2005.

[5] M. Bachmayr. *Iterative Total Variation Methods for Nonlinear Inverse Problems*. PhD thesis, University of Linz, Master Thesis, 2007.

[6] V. F. Bakirov, R. A. Kline, and W. P. Winfree. Discrete variable thermal tomography. In *AIP Conference Proceedings*, volume 700 (1), pages 469–476, 2004.

[7] H. Baltes and B. Hoenders. Inverse problems in optics. In *1979 Antennas and Propagation Society International Symposium*, volume 17, pages 225–227, 1979.

[8] D. C. Barber and B. H. Brown. Applied potential tomography. *Journal of Physics E: Scientific Instruments*, 17(9):723, 1984.

[9] K. J. Bathe. *Finite element procedures*. Prentice Hall, 2006.

[10] Z. P. Bažant, Z. Bittnar, M. Jirásek, and J. Mazars. *Fracture and Damage in Quasibrittle Structures: Experiment, modeling and computation*. CRC Press, 2004.

[11] Z. P. Bažant and R. L'Hermite. *Mathematical modeling of creep and shrinkage of concrete*. Wiley New York, 1988.

[12] C. A. Berenstein and T. E. Casadio. Inversion formulas for the k -dimensional radon transform in real hyperbolic spaces. *Duke Mathematical Journal*, 62(3):613–631, 04 1991.

[13] J. Bikowski, K. Knudsen, and J. L. Mueller. Direct numerical reconstruction of conductivities in three dimensions using scattering transforms. *Inverse Problems*, 27(1):1–19, 2010.

[14] R. S. Blue. *Real-time three-dimensional electrical impedance tomography.* Phd thesis, R.P.I, Troy, 1997.

[15] R. S. Blue, D. Isaacson, and J. C. Newell. Real-time three-dimensional electrical impedance imaging. *Physiological measurement*, 21(1):15–26, 2000.

[16] B. Borden. Mathematical problems in radar inverse scattering. *Inverse Problems*, 18(1):R1, 2002.

[17] A. Borsic, B. M. Graham, A. Adler, and W. R. B. Lionheart. In vivo impedance imaging with total variation regularization. *IEEE transactions on medical imaging*, 29(1):44–54, 2010.

[18] A. Borsic, W. R. B. Lionheart, and C. N. McLeod. Generation of anisotropic-smoothness regularization filters for EIT. *IEEE Transactions on Medical Imaging*, 21(6):579–587, 2002.

[19] B. H. Brown, D. C. Barber, and A. D. Seagar. Applied potential tomography: Possible clinical applications. *Clinical Physics and Physiological Measurement*, 6(2):109–121, 1985.

[20] R. M. Brown and G. A. Uhlmann. Uniqueness in the inverse conductivity problem for nonsmooth conductivities in two dimensions. *Communications in Partial Differential Equations*, 22(5-6):1009–1027, 1997.

[21] A. P. Calderón. On an inverse boundary value problem. *Seminar on Numerical Analysis and Its Applications to Continuum Physics: Rio de Janeiro*, 12:67–73, 1980.

[22] A. P. Calderón. On an inverse boundary value problem. *Computational & Applied Mathematics*, 25:133–138, 00 2006.

[23] S. Campana and S. Piro. *Seeing the Unseen Geophysics and Landscape Archaeology.* Taylor & Francis, 2008.

[24] M. Cheney, D. Isaacson, J. C. Newell, S. Simske, and J. Goble. NOSER: An algorithm for solving the inverse conductivity problem. *International Journal of Imaging Systems and Technology*, 2(2):66–75, 1990.

[25] K. S. Cheng, D. Isaacson, J. C. Newell, and D. G. Gisser. Electrode models for electric current computed tomography. *IEEE Transactions on Biomedical Engineering*, 36(9):918–924, 1989.

[26] V. Cherepenin, A. Karpov, A. Korjenevsky, V. Kornienko, A. Mazaletskaya, D. Mazourov, and D. Meister. A 3D electrical impedance tomography (EIT) system for breast cancer detection. *Physiological Measurement*, 22(1):9–18, 2001.

[27] M. H. Choi, T. J. Kao, D. Isaacson, G. J. Saulnier, and J. C. Newell. A simplified model of mammography geometry for breast cancer imaging with electrical impedance tomography. In *The* 26^{th} *Annual International Conference of the IEEE Engineering in Medicine and Biology Society*, volume 1, pages 1310–1313, 2004.

[28] D. L. Colton and R. Kress. *Inverse acoustic and electromagnetic scattering theory*, volume 93. Springer Science & Business Media, 2012.

[29] I. J. D. Craig and J. C. Brown. *Inverse Problems in Astronomy: A Guide to Inversion Strategies for Remotely Sensed Data*, volume 1. Adam Hilger, Ltd., 1986.

[30] T. Dai and A. Adler. Electrical impedance tomography reconstruction using L1 norms for data and image terms. In *Engineering in Medicine and Biology Society, 2008. EMBS 2008. 30th Annual International Conference of the IEEE*, pages 2721–2724, 2008.

[31] W. Daily, A. Ramirez, D. LaBrecque, and W. Barber. Electrical resistance tomography experiments at the oregon graduate institute. *Journal of Applied Geophysics*, 33(4):227–237, 1995.

[32] W. Daily, A. Ramirez, D. LaBrecque, and J. Nitao. Electrical resistivity tomography of vadose water movement. *Water Resources Research*, 28(5):1429–1442, 1992.

[33] J. B. Drake. *Climate Modeling for Scientists and Engineers*. SIAM, 2014.

[34] A. Gelman, J. Carlin, H. S. Stern, D. Dunson, A. Vehtari, and D. Rubin. *Bayesian data analysis*. Chapman and Hall/CRC, 2013.

[35] R. G. Ghanem and P. D. Spanos. Stochastic finite elements: a spectral approach, 2003.

[36] P. E. Gill and W. Murray. Algorithms for the solution of the non-linear least-squares problem. *SIAM Journal on Numerical Analysis*, 15(5):977–992, 1978.

[37] B. M. Graham. *Enhancements in Electrical Impedance Tomography (EIT) Image Reconstruction for 3D Lung Imaging*. Phd thesis, School of Informtation Technology, University of Ottawa, 2007.

[38] A. Greenleaf, M. Lassas, and G. Uhlmann. Anisotropic conductivities that cannot be detected by EIT. *Physiological Measurement*, 24(2):413–419, 2003.

[39] Ch. W. Groetsch. *Inverse problems in the mathematical sciences*, volume 52. Springer, 1993.

[40] S. J. Hamilton, M. Lassas, and S. Siltanen. A direct reconstruction method for anisotropic electrical impedance tomography. *Inverse Problems*, 30(7):1–30, 2014.

[41] H. O. Hartley. The modified gauss-newton method for the fitting of non-linear regression functions by least squares. *Technometrics*, 3(2):269–280, 1961.

[42] J. Havelka and J. Sýkora. Application of Calderón's inverse problem in civil engineering. *Applications of Mathematics*, accepted for publication, 2018.

[43] R. P. Henderson and J. G. Webster. An impedance camera for spatially specific measurements of the thorax. *IEEE Transactions on Biomedical Engineering*, BME-25(3):250–254, 1978.

[44] D. S. Holder. *Electrical Impedance Tomography: Methods, History and Applications (Series in Medical Physics and Biomedical Engineering)*. Series in Medical Physics and Biomedical Engineering. Taylor & Francis, 1^{st} edition, 2004.

[45] C. Huang and S. Chin. A two-dimensional inverse problem in imaging the thermal conductivity of a non-homogeneous medium. *International Journal of Heat and Mass Transfer*, 43(22):4061–4071, 2000.

[46] S. M. Huang, A. B. Plaskowski, C. G. Xie, and M. S. Beck. Capacitance-based tomographic flow imaging system. *Electronics Letters*, 24(7):418–419, 1988.

[47] T. J. R. Hughes. *The finite element method: linear static and dynamic finite element analysis*. Courier Corporation, 2012.

[48] A. J. Jaworski and T. Dyakowski. Application of electrical capacitance tomography for measurement of gas-solids flow characteristics in a pneumatic conveying system. *Measurement Science and Technology*, 12(8):1109–1119, 2001.

[49] M. Jirásek and Z. P. Bažant. *Inelastic analysis of structures*. John Wiley & Sons, 2002.

[50] M. R. Jones, A. Tezuka, and Y. Yamada. Thermal tomographic detection of inhomogeneities. *Journal of Heat Transfer*, 117(4):969–975, 1995.

[51] C. E. Kenig and M. Salo. The Calderón problem with partial data on manifolds and applications. *Analysis & PDE*, 6(8):2003–2048, 2014.

[52] C. E. Kenig, J. Sjöstrand, and G. Uhlmann. The Calderón problem with partial data. *Annals of Mathematics*, 165(2):567–591, 2007.

[53] A. Kirsch. *An Introduction to the Mathematical Theory of Inverse Problems*. Applied Mathematical Sciences 120. Springer-Verlag New York, 2 edition, 2011.

[54] K. Knudsen. The Calderón problem with partial data for less smooth conductivities. *Communications in Partial Differential Equations*, 31(1):57–71, 2006.

[55] K. Knudsen, M. Lassas, J. L. Mueller, and S. Siltanen. Regularized D-bar method for the inverse conductivity problem. *Inverse Problems and Imaging*, 3(4):599–624, 2009.

[56] H. M. Künzel. *Simultaneous Heat and Moisture Transport in Building Components*. PhD thesis, Fraunhofer Institute of Building Physics, 1995.

[57] T. G. Kolda, R. M. Lewis, and V. J. Torczon. Optimization by direct search: New perspectives on some classical and modern methods. *SIAM Review*, 45:385–482, 2003.

[58] V. Kolehmainen. *Novel approaches to image reconstruction in diffusion tomography*. Phd thesis, Kuopion University, 2001.

[59] V. Kolehmainen, J. P. Kaipio, and H. R. B. Orlande. Reconstruction of thermal conductivity and heat capacity using a tomographic approach. *International Journal of Heat and Mass Transfer*, 50(25-26):5150–5160, 2007.

[60] V. Kolehmainen, J. P. Kaipio, and H. R. B. Orlande. Reconstruction of thermal conductivity and heat capacity using a tomographic approach. *International Journal of Heat and Mass Transfer*, 51(7):1866–1876, 2008.

[61] A. Kučerová and J. Sýkora. Uncertainty updating in the description of coupled heat and moisture transport in heterogeneous materials. *Applied Mathematics and Computation*, 2011.

[62] A. Kučerová, J. Sýkora, B. Rosić, and H. G. Matthies. Acceleration of uncertainty updating in the description of transport processes in heterogeneous materials. *Journal of Computational and Applied Mathematics*, 236(18):4862–4872, 2012.

[63] O. A. Ladyženskaja, V. A. Solonnikov, and N. N. Ural'ceva. *Linear and Quasi-linear Equations of Parabolic Types*. American Mathematical Society, 1968.

[64] C. Lanczos. *Linear Differential Operators*. Society for Industrial and Applied Mathematics, 1996.

[65] R. E. Langer. An inverse problem in differential equations. *Bulletin of the American Mathematical Society*, 39(10):814–820, 1933.

[66] S. Leonhardt and B. Lachmann. Electrical impedance tomography: the holy grail of ventilation and perfusion monitoring? *Intensive Care Medicine*, 38(12):1917–1929, 2012.

[67] W. R. B. Lionheart. Conformal uniqueness results in anisotropic electrical impedance imaging. *Inverse Problems*, 13(1):125–134, 1997.

[68] W. R. B. Lionheart. EIT reconstruction algorithms: pitfalls, challenges and recent developments. *Physiological Measurement*, 25(1):125–142, 2004.

[69] W. K. Liu, A. Mani, and T. Belytschko. Finite element methods in probabilistic mechanics. *Probabilistic Engineering Mechanics*, 2(4):201 – 213, 1987.

[70] M. Lombardo, J. Zeman, M. Šejnoha, and G. Falsone. Stochastic modeling of chaotic masonry via mesostructural characterization. *International Journal for Multiscale Computational Engineering*, 7(2):171–185, 2009.

[71] L. B. Lucy. Astronomical Inverse Problems. In *Reviews in Modern Astronomy*, volume 7 of *Reviews in Modern Astronomy*, pages 31–50, 1994.

[72] Y. Mamatjan, A. Borsic, D. Gürsoy, and A. Adler. Experimental/clinical evaluation of EIT image reconstruction with $\ell 1$ data and image norms. *Journal of Physics: Conference Series*, 434(1):1–4, 2013.

[73] Y. M. Marzouk and H. N. Najm. Dimensionality reduction and polynomial chaos acceleration of bayesian inference in inverse problems. *Journal of Computational Physics*, 228(6):1862–1902, 2009.

[74] H. G. Matthies. *Encyclopedia of Computational Mechanics*, chapter Uncertainty Quantification with Stochastic Finite Elements. John Wiley & Sons, Ltd., 2007.

[75] H. G. Matthies, A. Litvinenko, B. V. Rosic, and E. Zander. Bayesian parameter estimation via filtering and functional approximations. *arXiv preprint arXiv:1611.09293*, 2016.

[76] J. L. Melsa and D. L. Cohn. *Decision and estimation theory*. New York : McGraw-Hill, 1978.

[77] B. Minasny and A. B. McBratney. The matérn function as a general model for soil variograms. *Geoderma*, 128(3):192–207, 2005.

[78] J. L. Mueller, D. Isaacson, and J. C. Newell. Reconstruction of conductivity changes due to ventilation and perfusion from EIT data collected on a rectangular electrode array. *Physiological Measurement*, 22(1):97–106, 2001.

[79] J. L. Mueller and S. Siltanen. Direct reconstructions of conductivities from boundary measurements. *SIAM Journal on Scientific Computing*, 24(4):1232–1266, 2003.

[80] A. I. Nachman. Global uniqueness for a two-dimensional inverse boundary value problem. *Annals of Mathematics*, 143(1):71–96, 1996.

[81] J. A. Nelder and R. Mead. A simplex method for function minimization. *The Computer Journal*, 7(4):308–313, 1965.

[82] J. Nocedal and S. Wright. *Numerical Optimization*. Springer Series in Operations Research and Financial Engineering. Springer New York, 2006.

[83] M. Noel and B. Xu. Archaeological investigation by electrical resistivity tomography: a preliminary study. *Geophysical Journal International*, 107(1):95–102, 1991.

[84] E. R. Pike, J. G. McWhirter, M. Bertero, and Ch. de Mol. Generalised information theory for inverse problems in signal processing. In *IEE Proceedings F (Communications, Radar and Signal Processing)*, volume 131, pages 660–667. IET, 1984.

[85] K. Prasad and R. B. Howard. Coupled fire dynamics and thermal response of complex building structures. *Proceedings of the Combustion Institute*, 30(2):2255 – 2262, 2005.

[86] K. Rektorys. *Variational Methods in Math, Sci. and Eng.* D. Reidel, 1980.

[87] B. Rosić, A. Kučerová, J. Sỳkora, O. Pajonk, A. Litvinenko, and H. G. Matthies. Parameter identification in a probabilistic setting. *Engineering Structures*, 50:179–196, 2013.

[88] B. Rosić and H. G. Matthies. Computational approaches to inelastic media with uncertain parameters. *Journal of the Serbian Society for Computational Mechanics*, 2(1):28–43, 2008.

[89] L. I. Rudin, S. Osher, and E. Fatemi. Nonlinear total variation based noise removal algorithms. *Physica D: Nonlinear Phenomena*, 60(1-4):259–268, 1992.

[90] M. Salo. *Calderón problem*. Lecture notes, University of Helsinki, 2008.

[91] F. Santosa. *Inverse problems of acoustic and elastic waves*, volume 14. SIAM, 1984.

[92] F. Santosa and M. Vogelius. A backprojection algorithm for electrical impedance imaging. *SIAM Journal on Applied Mathematics*, 50(1):216–243, 1990.

[93] O. Scherzer. *Handbook of Mathematical Methods in Imaging*. Springer-Verlag New York, 2 edition, 2015.

[94] S. Siltanen, J. Mueller, and D. Isaacson. An implementation of the reconstruction algorithm of A. Nachman for the 2d inverse conductivity problem. *Inverse Problems*, 16(3):681–699, 2000.

[95] L. D. Slater, A. Binley, and D. Brown. Electrical imaging of fractures using ground-water salinity change. *Ground Water*, 35(3):436–442, 1997.

[96] L. B. Slichter. The interpretation of the resistivity prospecting method for horizontal structures. *Physics*, 4(9):307–322, 1933.

[97] J. Snoek, H. Larochelle, and R. P. Adams. Practical bayesian optimization of machine learning algorithms. In *Advances in neural information processing systems*, pages 2951–2959, 2012.

[98] E. Somersalo, M. Cheney, and D. Isaacson. Existence and uniqueness for electrode models for electric current computed tomography. *SIAM Journal on Applied Mathematics*, 52(4):1023–1040, 1992.

[99] E. Somersalo, M. Cheney, D. Isaacson, and E. Isaacson. Layer stripping: a direct numerical method for impedance imaging. *Inverse problems*, 7(6):899–926, 1991.

[100] E. Somersalo, J. P. Kaipio, M. J. Vauhkonen, D. Baroudi, and S. Järvenpää. Impedance imaging and Markov chain Monte Carlo methods. In *Optical Science, Engineering and Instrumentation'97*, pages 175–185. International Society for Optics and Photonics, 1997.

[101] G. Strang and G. J. Fix. *An analysis of the finite element method*, volume 212. Prentice-hall Englewood Cliffs, NJ, 1973.

[102] J. Sýkora. Modeling of degradation processes in historical mortars. *Advances in Engineering Software*, 70:203–214, 2014.

[103] J. Sylvester. An anisotropic inverse boundary value problem. *Communications on Pure and Applied Mathematics*, 43(2):201–232, 1990.

[104] J. Sylvester and G. Uhlmann. A uniqueness theorem for an inverse boundary value problem in electrical prospection. *Communications on Pure and Applied Mathematics*, 39(1):91–112, 1986.

[105] J. Sylvester and G. Uhlmann. A global uniqueness theorem for an inverse boundary value problem. *Annals of Mathematics*, 125(1):153–169, 1987.

[106] J. Syren. *Theoretical and numerical analysis of the Dirichlet-to-Neumann map in EIT*. PhD thesis, University of Helsinki, Master Thesis, 2016.

[107] A. Tarantola. *Inverse problem theory and methods for model parameter estimation*. SIAM, 2005.

[108] A. Tarantola. *Inverse Problem Theory and Methods for Model Parameter Estimation*. Society for Industrial and Applied Mathematics, 2005.

[109] T. Tidswell, A. Gibson, R. H. Bayford, and D. S. Holder. Three-dimensional electrical impedance tomography of human brain activity. *NeuroImage*, 13(2):283–294, 2001.

[110] J. M. Toivanen, V. Kolehmainen, T. Tarvainen, H. R. B. Orlande, and J. P. Kaipio. Simultaneous estimation of spatially distributed thermal conductivity, heat capacity and surface heat transfer coefficient in thermal tomography. *International Journal of Heat and Mass Transfer*, 55(25-26):7958–7968, 2012.

[111] J. M. Toivanen, T. Tarvainen, J. M. J. Huttunen, T. Savolainen, H. R. B. Orlande, J. P. Kaipio, and V. Kolehmainen. 3d thermal tomography with experimental measurement data. *International Journal of Heat and Mass Transfer*, 78:1126–113, 2014.

[112] M. Th. Van Genuchten. A closed-form equation for predicting the hydraulic conductivity of unsaturated soils. *Soil science society of America journal*, 44(5):892–898, 1980.

[113] M. Vauhkonen. *Electrical impedance tomography and prior information*. Phd thesis, Kuopio University, 1997.

[114] M. Vauhkonen, W. R. B. Lionheart, L. M. Heikkinen, P. J. Vauhkonen, and J. P. Kaipio. A MATLAB package for the EIDORS project to reconstruct two-dimensional eit images. *Physiological Measurement*, 22(1):107–111, 2001.

[115] A. J. Wilkinson, E. W. Randall, D. Durrett, T. Naidoo, and J. J. Cilliers. The design of a 1000 frames/second ERT data capture system and calibration techniques employed. In 3^{rd} *World Congress on Industrial Process Tomography. Banff*, 2003.

[116] D. Wipf and B. Rao. ℓ_0-norm minimization for basis selection. In *Proceedings of the 17th International Conference on Neural Information Processing Systems*, NIPS'04, pages 1513–1520. MIT Press, 2004.

[117] W. Q. Yang and L. Peng. Image reconstruction algorithms for electrical capacitance tomography. *Measurement Science and Technology*, 14(1):1–14, 2003.

[118] O. C. Zienkiewicz and R. L. Taylor. *The finite element method*, volume 3. McGraw-hill London, 1977.

A Synthetic material fields

Identification computations are performed with synthetic true parameter fields, i.e. thermal conductivity λ_s and volumetric heat capacity c_v, generated by a known function. Specifically we utilise the following functions

$$\lambda_s^{(1)}(x,y) = \frac{1}{15}\Big[\mathrm{abs}\Big(5 + 3x^2 + 2y - yx - 5y\sin(x/0.075) + \ldots + 10x\cos(10y)\Big) + 5\Big], \tag{A.1}$$

$$c_v^{(1)}(x,y) = 850 \cdot \Big[5(50x^3 + 100x^2 + 150y^2 - 100yx + 100y) + \ldots + 500 + 300\cos(10\pi xy) - 300\sin(6\pi x)\Big]. \tag{A.2}$$

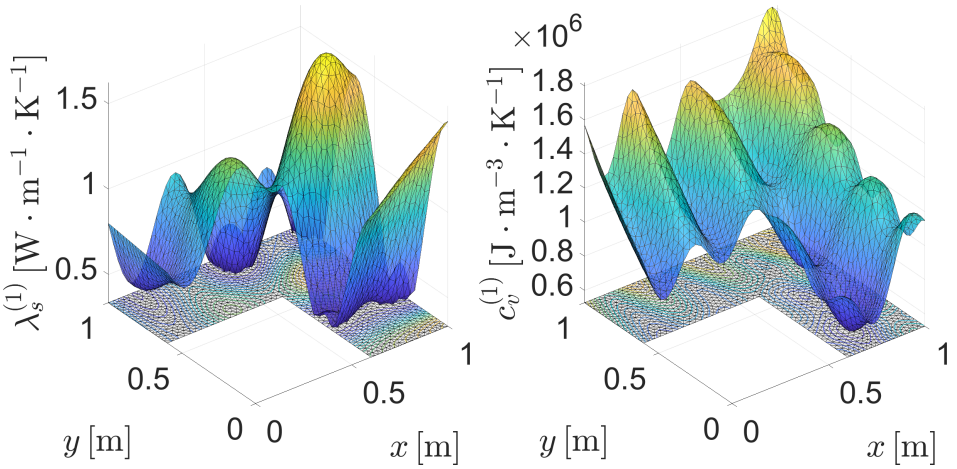

Figure 66: (a) Thermal conductivity $\lambda_s^{(1)}$ generated by function in eq. (A.1), (b) volumetric capacity $c_v^{(1)}$ generated by function in eq. (A.2).

$$\lambda_s^{(2)}(x,y) = 1 + 0.5 \cdot \Big[(x \geq 0.7 \wedge x \leq 0.9) \wedge (y \geq 0.1 \wedge y \leq 0.6)\Big] + \ldots + 0.2\ (x - y \leq 0), \tag{A.3}$$

$$c_v^{(2)}(x,y) = 1 \times 10^6 \cdot \Big\{0.7 + 0.6 \cdot \Big[(x \geq 0.7 \wedge x \leq 0.9) \wedge (y \geq 0.1 \wedge y \leq 0.6)\Big] + \ldots + 0.3 \cdot (x - y \leq 0)\Big\}, \tag{A.4}$$

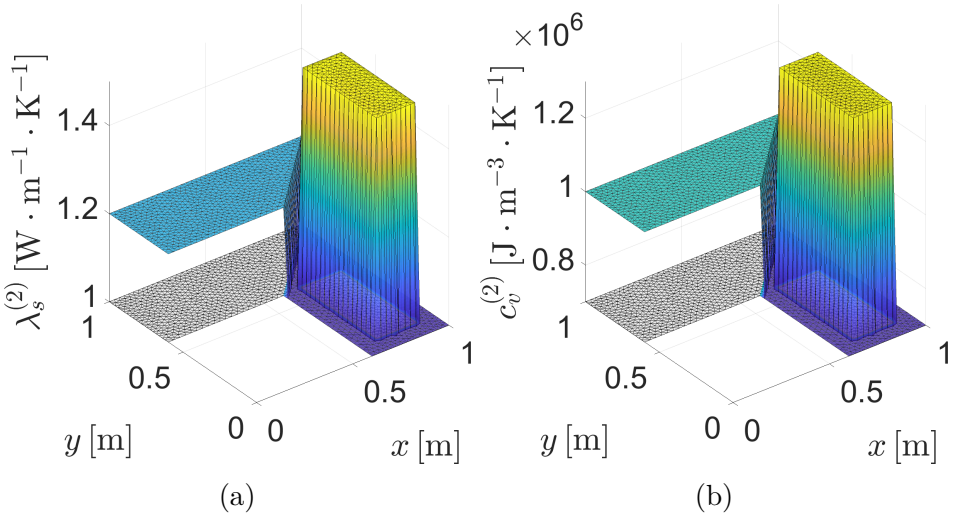

Figure 67: (a) Thermal conductivity $\lambda_s^{(2)}$ generated by function in eq. (A.3), (b) volumetric capacity $c_v^{(2)}$ generated by function in eq. (A.4).

$$\begin{aligned}\lambda_s^{(3)}(x,y) = \sigma(x,y) = 20 + \ldots \\ + 20 \cdot \Big[\big(x > 0.6 \wedge x < 0.8\big) \wedge \big(y > 0.6 \wedge y < 0.8\big)\Big] - \ldots \\ - 15 \cdot \Big[\big(x > 0.8 \wedge x < 1\big) \wedge \big(y > 0.1 \wedge y < 0.3\big)\Big], \end{aligned} \tag{A.5}$$

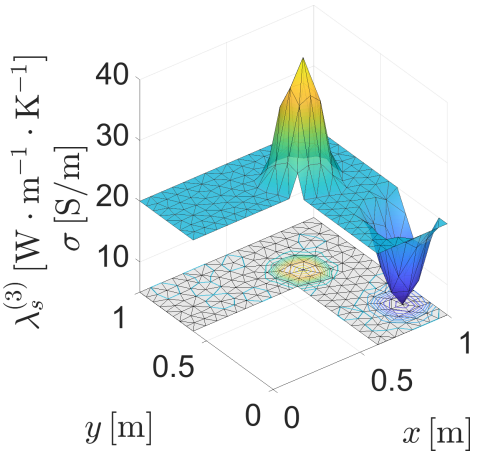

Figure 68: Thermal conductivity $\lambda_s^{(3)}$ and electrical conductivity σ generated by function in eq. (A.5).

$$\lambda_s(x,y) = 1 + 0.5\Big[\Big((x+0.25)^2 + (y+0.15)^2\Big) \leq 0.101^2\Big] + \ldots + \Big[\Big((x-0.2)^2 + (y-0.05)^2\Big) \leq 0.201^2\Big], \tag{A.6}$$

$$c_v(x,y) = 1 \times 10^6 \cdot \Big\{0.8 + 0.4\Big[\Big((x+0.25)^2 + (y+0.15)^2\Big) \leq 0.101^2\Big] + \ldots + 0.8\Big[\Big((x-0.2)^2 + (y-0.05)^2\Big) \leq 0.201^2\Big]\Big\}, \tag{A.7}$$

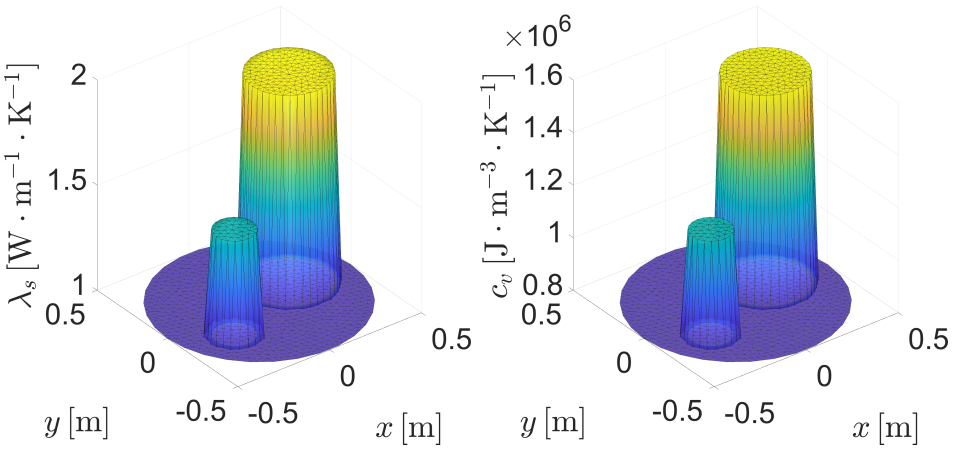

(a) (b)

Figure 69: (a) Thermal conductivity $\lambda_s^{(1)}$ generated by function in eq. (A.6), (b) volumetric capacity $c_v^{(1)}$ generated by function in eq. (A.7).

$$\lambda_s(x,y) = 1 + 0.5\Big[\Big((x-0.25)^2 + (y-0.25)^2\Big) \leq 0.101^2\Big] + \ldots + \Big[\Big((x-0.6)^2 + (y-0.5)^2\Big) \leq 0.151^2\Big], \tag{A.8}$$

$$c_v(x,y) = 1 \times 10^6 \cdot \Big\{0.8 + 0.4\Big[\Big((x-0.25)^2 + (y-0.25)^2\Big) \leq 0.101^2\Big] + \ldots + 0.8\Big[\Big((x-0.6)^2 + (y-0.5)^2\Big) \leq 0.151^2\Big]\Big\}, \tag{A.9}$$

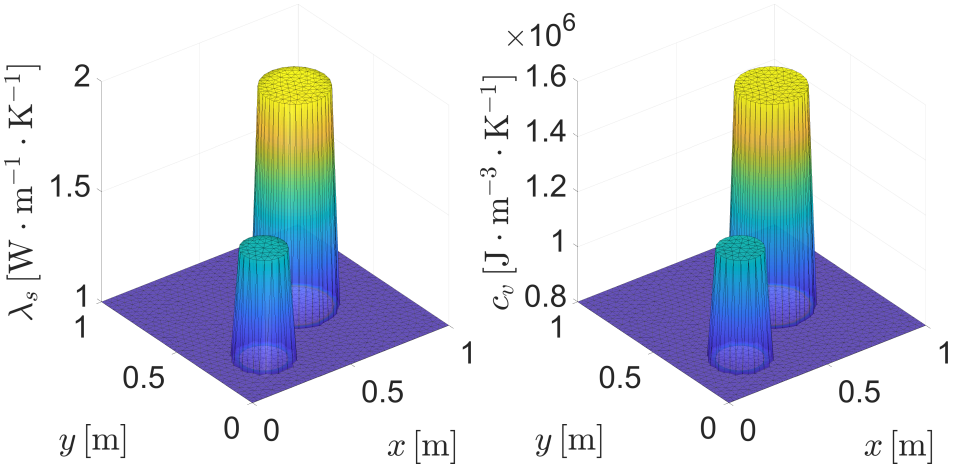

(a) (b)

Figure 70: (a) Thermal conductivity $\lambda_s^{(1)}$ generated by function in eq. (A.6), (b) volumetric capacity $c_v^{(1)}$ generated by function in eq. (A.7).

$$\lambda_s(x, y) = 1 + 0.2 \sin(2\pi x), \tag{A.10}$$

$$c_v(x, y) = 1 \times 10^6 \cdot \Big\{1 + 0.2 \sin(2\pi x)\Big\}, \tag{A.11}$$

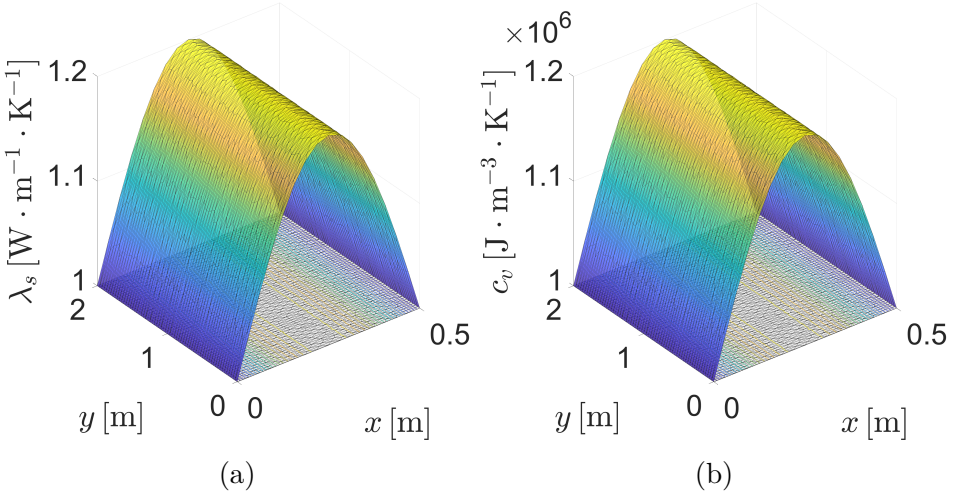

(a) (b)

Figure 71: (a) Thermal conductivity $\lambda_s^{(1)}$ generated by function in eq. (A.10), (b) volumetric capacity $c_v^{(1)}$ generated by function in eq. (A.11).

$$\lambda_s(x, y) = 1 + 0.2 \sin(2\pi x), \tag{A.12}$$

$$c_v(x, y) = 1 \times 10^6 \cdot \Big\{1 + 0.2 \sin(2\pi x)\Big\}. \tag{A.13}$$

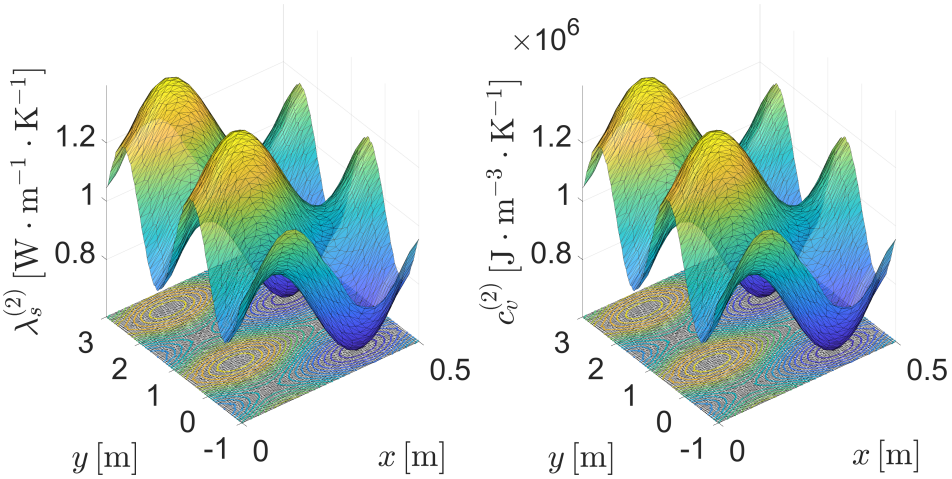

Figure 72: (a) Thermal conductivity $\lambda_s^{(2)}$ generated by function in eq. (A.12), (b) volumetric capacity $c_v^{(2)}$ generated by function in eq. (A.13).

B Differential operators

We utilise first and second order differential operators applied on the scalar field $f : \mathbb{R}^n \to \mathbb{R}$ that is a function of n variables which are sorted in a vector $\mathbf{\Phi} = [\phi_1, \phi_2, \ldots, \phi_n]$. In particular gradient of the field f, evaluated at the point $\widehat{\mathbf{\Phi}}$ is denoted in the following way

$$\boldsymbol{\nabla} \left(f(\mathbf{\Phi})\right)|_{\widehat{\mathbf{\Phi}}} = \boldsymbol{\nabla} \left(f(\widehat{\mathbf{\Phi}})\right) = \boldsymbol{\nabla} \left(f(\widehat{\mathbf{\Phi}})\right) = \begin{bmatrix} \dfrac{\partial f(\widehat{\mathbf{\Phi}})}{\partial \phi_1} \\ \dfrac{\partial f(\widehat{\mathbf{\Phi}})}{\partial \phi_2} \\ \vdots \\ \dfrac{\partial f(\widehat{\mathbf{\Phi}})}{\partial \phi_n} \end{bmatrix}, \tag{B.1}$$

where the vector form of the differential operator $\boldsymbol{\nabla}$ with respect to the individual elements of $\mathbf{\Phi} = [\phi_1, \phi_2, \ldots, \phi_n]$ can be expressed in the following

way

$$\boldsymbol{\nabla} = \begin{bmatrix} \dfrac{\partial}{\partial \phi_1} \\ \dfrac{\partial}{\partial \phi_2} \\ \vdots \\ \dfrac{\partial}{\partial \phi_n} \end{bmatrix}. \tag{B.2}$$

Common symbols for Hessian of the scalar field f can be denoted by the following notations

$$\mathbf{H}(f) = \boldsymbol{\nabla}^2(f) = \boldsymbol{\Delta}(f) = \boldsymbol{\nabla}\boldsymbol{\nabla}^T(f). \tag{B.3}$$

As it can be recognised in the last expression of eq. (B.3) the derivation of Hessian elements can be approached as an application of the gradient to the transposed gradient applied on the scalar function f. The Hessian of a scalar field f at some point $\mathbf{d} = (\mathbf{d}_1, \ldots, \mathbf{d}_{N_p})$ forms a following matrix of second partial derivatives

$$\boldsymbol{\nabla}\boldsymbol{\nabla}^T\left(f(\boldsymbol{\Phi})\right) = \begin{bmatrix} \dfrac{\partial}{\partial \phi_1} \\ \dfrac{\partial}{\partial \phi_2} \\ \vdots \\ \dfrac{\partial}{\partial \phi_N} \end{bmatrix} \begin{bmatrix} \dfrac{\partial}{\partial \phi_1} & \dfrac{\partial}{\partial \phi_2} & \cdots & \dfrac{\partial}{\partial \phi_N} \end{bmatrix} \left(f(\boldsymbol{\Phi})\right) \tag{B.4}$$

$$= \begin{bmatrix} \dfrac{\partial^2 f(\boldsymbol{\Phi})}{\partial \phi_1^2} & \dfrac{\partial^2 f(\boldsymbol{\Phi})}{\partial \phi_1 \partial \phi_2} & \cdots & \dfrac{\partial^2 f(\boldsymbol{\Phi})}{\partial \phi_1 \partial \phi_n} \\ \dfrac{\partial^2 f(\boldsymbol{\Phi})}{\partial \phi_2 \partial \phi_1} & \dfrac{\partial^2 f(\boldsymbol{\Phi})}{\partial \phi_2^2} & \cdots & \dfrac{\partial^2 f(\boldsymbol{\Phi})}{\partial \phi_2 \partial \phi_n} \\ \vdots & \vdots & \ddots & \vdots \\ \dfrac{\partial^2 f(\boldsymbol{\Phi})}{\partial \phi_n \partial \phi_1} & \dfrac{\partial^2 f(\boldsymbol{\Phi})}{\partial \phi_n \partial \phi_2} & \cdots & \dfrac{\partial^2 f(\boldsymbol{\Phi})}{\partial \phi_n^2} \end{bmatrix} \tag{B.5}$$